

**Density-matrix renormalization-group studies of  
spin, boson and fermion systems with  
symmetry-protected topological phases**

**Inauguraldissertation**

zur

Erlangung des akademischen Grades eines

Doktors der Naturwissenschaften  
(Dr. rer. nat.)

der

Mathematisch-Naturwissenschaftlichen Fakultät

der

Universität Greifswald

vorgelegt von

Florian Lange

geboren am 15. Februar 1991

in Schleswig

Greifswald, 1. August 2019

Dekan:	Prof. Dr. Werner Weitschies
1. Gutachter:	Prof. Dr. Holger Fehske
2. Gutachter:	Prof. Dr. Eric Jeckelmann
3. Gutachter:	Prof. Dr. Fabian Heidrich-Meisner
Tag der Promotion:	1. November 2019





# Contents

<b>1</b>	<b>Summary</b>	<b>1</b>
1.1	Introduction . . . . .	1
1.2	Numerical method . . . . .	3
1.3	Symmetry-protected topological order and criticality . . . . .	9
1.4	Response to external fields . . . . .	17
1.5	Conclusion . . . . .	22
<b>2</b>	<b>Thesis articles</b>	<b>25</b>
2.3	Article I — Exotic criticality in the dimerized spin-1 $XXZ$ chain with single-ion anisotropy . . . . .	29
2.4	Article II — Quantum phase transitions in the dimerized extended Bose-Hubbard model . . . . .	47
2.1	Article III — Ising tricriticality in the extended Hubbard model with bond dimerization . . . . .	55
2.2	Article IV — Critical behavior of the extended Hubbard model with bond dimerization . . . . .	63
2.5	Article V — Anyonic Haldane Insulator in One Dimension . . . . .	69
2.6	Article VI — Strongly repulsive anyons in one dimension . . . . .	75
2.7	Article VII — Finite-temperature dynamic structure factor of the spin-1 $XXZ$ chain with single-ion anisotropy . . . . .	85
2.8	Manuscript VIII — Dynamic response of spin-2 bosons in one-dimensional optical lattices . . . . .	93
2.9	Article IX — Spin transport through a spin-1/2 $XXZ$ chain contacted to fermionic leads . . . . .	99
2.10	Article X — Driving $XXZ$ spin chains: Magnetic-field and boundary effects . . . . .	109
2.11	Technical Report XI — Block-Lanczos density-matrix renormalization-group study of the spin transport in Heisenberg chains coupled to leads . . . . .	117
	<b>Bibliography</b>	<b>131</b>
	<b>Scientific contributions</b>	<b>139</b>
	<b>Erklärung</b>	<b>143</b>
	<b>Acknowledgement</b>	<b>145</b>



# 1 Summary

## 1.1 Introduction

This thesis contains numerical studies of strongly correlated systems in one dimension, with a focus on topological phases. Here, zero-temperature phases are called topological, when the ground state cannot be adiabatically connected to a site-factorizable state [1, 2]. As topological phases are not characterized by symmetry breaking and local order parameters, there has been much effort in finding hidden orders that distinguish them from topologically trivial phases [3–5]. In one-dimensional systems of bosons or spins, only symmetry-protected topological (SPT) phases are possible, i.e., the distinction from phases with trivial topological order depends on the conservation of certain symmetries in the Hamiltonian [6, 7]. Such one-dimensional bosonic SPT phases have been analyzed using the framework of matrix-product states (MPS) [8], which has led to their systematic classification depending on the symmetry group of the model [6, 7, 9, 10]. Through a Jordan-Wigner transformation, these results also apply to fermions [10, 11].

Matrix-product states are the variational ansatz underlying the density-matrix renormalization group (DMRG) for ground-state calculations [12, 13]. What makes them useful is that they can be manipulated conveniently which enables efficient numerical algorithms, and that the MPS ansatz is quite generally applicable as long as the model is one-dimensional. In fact, there is strong evidence that all gapped ground states in one dimension can be accurately represented by MPS [14]. This has been exploited to find the above-mentioned classification of SPT states. Besides the original DMRG algorithm for ground-state calculations, there are various MPS techniques that make it possible to also determine dynamical [15–18] and finite-temperature [19, 20] properties with high accuracy.

While topological phases in one dimension are by now well-understood theoretically, there are only few experimental realizations. The most prominent example for SPT order in one dimension is probably the gapped Haldane phase of antiferromagnetic spin-1 chains [21], which is characterized by gapless spin-1/2 edge states and non-local string order [22–24]. It has been observed experimentally in quasi one-dimensional magnets that behave approximately as collections of independent chains [25, 26]. Examples are compounds with  $\text{Ni}^{2+}$ -ions such as  $\text{Ni}(\text{C}_2\text{H}_8\text{N}_2)_2\text{NO}_2(\text{ClO}_4)$  (NENP).

Another type of system in which one-dimensional physics can be realized are optical lattices. They consist of interfering laser beams which act as a periodic potential for the cold neutral atoms loaded into it. By using strong potentials along two directions, the system becomes effectively one-dimensional [27, 28]. There has been much interest in optical lattices due to the high level of control over the engineered Hamiltonians. The realization of SPT phases in particular could allow for a better experimental analysis of their characteristic properties, for example through measurements of string order parameters [29, 30]. So far, experiments have been reported mostly on systems corre-

sponding to non-interacting SPT models [31]. Typical interacting models associated with optical-lattice systems are the Fermi- and Bose-Hubbard models, which have only topologically trivial phases. However, SPT phases appear for more general Hamiltonians that may also become feasible to implement [32]. The extended Bose-Hubbard model with nearest-neighbor interaction exhibits, for a density of one particle per site, a phase diagram similar to that of the antiferromagnetic spin-1 chain, including a topological Haldane phase [33, 34]. The extended fermionic Hubbard model, on the other hand, does not have a Haldane phase. Instead, SPT states can be obtained by adding an explicit dimerization which induces a Peierls insulator [35, 36] interpolating between the SPT states of the non-interacting Su-Schrieffer-Heeger model and the dimerized spin-1/2 Heisenberg chain [37].

In this thesis, we numerically investigate one-dimensional spin and generalized Hubbard Hamiltonians, that are expected to be relevant for quasi one-dimensional magnets and cold atoms in optical lattices. While the basic models are well-understood, it is worthwhile to study the effect of perturbations that may occur either naturally or could be artificially engineered. We concentrate on systems exhibiting SPT order, particularly those related to the spin-1 Haldane chain. In our calculations, we mainly use MPS-based techniques such as the DMRG, which are briefly described in Sec. 1.2.

Section 1.3 deals with ground-state phase diagrams. We first investigate the effect of dimerization on the spin-1 XXZ chain with single-ion anisotropy, as well as on the extended Bose- and Fermi-Hubbard chains. Mapping out the phase diagrams of these models, we find no SPT states besides the known Haldane and Peierls phases. The properties of the phase transitions change, however. In addition to the Ising and Gaussian universality classes, we find in each model critical points belonging to the more exotic tricritical Ising universality class. The critical properties can be understood within a field-theoretical picture, which we confirm numerically by calculating the critical exponents of various correlation functions.

Recently, it was proposed that optical lattices may be able to realize an anyon-Hubbard model which, in a sense, interpolates between fermions and bosons through a statistical angle  $\theta$  [38]. We confirm the existence of a Haldane phase in the extended anyon-Hubbard model with nearest-neighbor interaction, and determine its SPT order with MPS techniques. The extent of this Haldane phase depends strongly on the statistical angle  $\theta$ . Notably, it vanishes toward the pseudo-fermion limit of the anyons.

In Sec. 1.4, we investigate dynamical properties of spin chains using time-dependent MPS techniques. We first calculate the dynamic spin structure factor for the spin-1 XXZ chain with single-ion anisotropy and for a spin-2 chain expected to describe bosons in optical lattices. For the spin-1 chain we also consider finite temperatures, in which case additional features due to intraband scattering appear [39]. Response functions such as the dynamic structure factor are valuable since the quantities used to characterize the phases and phase transitions theoretically, for example topological order parameters or entanglement properties, may not be easily accessible experimentally. The dynamic structure factor, on the other hand, can be measured in scattering experiments [40–42]. It is also interesting from a theoretical perspective as it contains detailed information about the excitations.

Lastly, in light of recent experiments on the spin injection into magnetic insulators [43, 44], we investigate the spin conductance of finite-length spin chains connected



to metallic leads. Our focus is on the spin-1/2 XXZ chain which exhibits ballistic transport in the gapless phase. We analyze the dependence of the spin conductance on the spin-chain and interface properties, and relate the results to previous studies of charge-transport in inhomogeneous fermion chains. The effect of an external homogeneous magnetic field is also studied.

## 1.2 Numerical method

Throughout this thesis, we use the DMRG [12] and the infinite DMRG [45] (iDMRG) for ground-state calculations. These techniques can be understood as variational methods in the space of MPS and infinite MPS (iMPS), respectively [13]. In the following, we review some important facts about (i)MPS and the associated numerical algorithms. We also briefly summarize the application of MPS in the classification of SPT orders.

**Matrix-product states** An arbitrary pure quantum state on a lattice of  $N$  sites can be written as  $|\psi\rangle = \sum_{\boldsymbol{\sigma}} c_{\boldsymbol{\sigma}} |\boldsymbol{\sigma}\rangle$ , where  $\boldsymbol{\sigma} = (\sigma_1, \sigma_2, \dots, \sigma_N)$  is a multi-index denoting the state on each site, and  $c_{\boldsymbol{\sigma}}$  are complex coefficients with normalization  $\sum_{\boldsymbol{\sigma}} |c_{\boldsymbol{\sigma}}|^2 = 1$ . In an MPS, the coefficients are decomposed into matrix products as follows:

$$c_{\boldsymbol{\sigma}} = A^{[1]\sigma_1} A^{[2]\sigma_2} \dots A^{[N]\sigma_N}, \quad \begin{array}{c} c_{\boldsymbol{\sigma}} \\ \text{---} \\ \sigma_1 \quad \sigma_2 \quad \dots \quad \sigma_N \end{array} = \begin{array}{c} A^{[1]} \quad A^{[2]} \quad \dots \quad A^{[N]} \\ \circ \text{---} \circ \text{---} \dots \text{---} \circ \\ \sigma_1 \quad \sigma_2 \quad \dots \quad \sigma_N \end{array}. \quad (1)$$

The state is thus defined by specifying a set of  $\chi_{j-1} \times \chi_j$  matrices  $A^{[j]\sigma_j}$  for each site  $j$ , with the numbers  $\chi_j$  called the bond dimensions. Obviously,  $\chi_0 = \chi_N = 1$  so that Eq. (1) yields a scalar. The explicit site index  $[j]$  will be left out in the following if it is already indicated by the physical index  $\sigma_j$ . It is often advantageous to regard the set of matrices at a site as a rank-three tensor. We have included the typical graphical representation in which a tensor is depicted as a geometrical shape with an outgoing line for each index, and connected lines correspond to contracted indices. Every state can be written as an MPS if there are no restrictions on the bond dimensions  $\chi_j$ . In practical calculations, however, the bond dimensions of the MPS are bounded by some maximum number  $\chi$ , which generally introduces an error. The success of the DMRG is due to the fact that one-dimensional ground states are usually accurately described by MPS with moderate bond dimensions of the order of a few hundreds.

An MPS representation of a quantum state is not unique. Typically, one imposes one of the conditions

$$\left( \sum_{\sigma_j} A^{\sigma_j \dagger} A^{\sigma_j} \right)_{\alpha\beta} = \delta_{\alpha\beta}, \quad \left( \sum_{\sigma_j} A^{\sigma_j} A^{\sigma_j \dagger} \right)_{\alpha\beta} = \delta_{\alpha\beta}, \quad (2)$$

which are called left and right normalization, respectively. If for some  $\ell$  all tensors  $j \leq \ell$  are left-normalized, then the states  $|\alpha\rangle_L^\ell = (A^{\sigma_1} A^{\sigma_2} \dots A^{\sigma_\ell})_\alpha |\sigma_1, \dots, \sigma_\ell\rangle$  form an orthonormal system. An analogous statement holds for right-normalized tensors and the states  $|\alpha\rangle_R^\ell = (A^{\sigma_{\ell+1}} A^{\sigma_{\ell+2}} \dots A^{\sigma_N})_\alpha |\sigma_{\ell+1}, \dots, \sigma_N\rangle$ . The normalization conditions can always be achieved through singular-value decompositions without increasing the bond dimensions. For each bond  $(\ell, \ell + 1)$ , one can bring the MPS to a form that describes

a Schmidt decomposition for the corresponding bipartition:

$$|\psi\rangle = \sum_{\alpha=1}^{\chi_\ell} \Lambda_\alpha |\alpha\rangle_L^\ell |\alpha\rangle_R^\ell \quad \begin{array}{c} \overbrace{\quad\quad\quad}^{|\alpha\rangle_L^\ell} \quad \Lambda \quad \overbrace{\quad\quad\quad}^{|\alpha\rangle_R^\ell} \\ \circ_{\sigma_1} \cdots \circ_{\sigma_\ell} \text{---} \diamond \text{---} \circ_{\sigma_{\ell+1}} \cdots \circ_{\sigma_N} \end{array}, \quad (3)$$

where  $\Lambda = \text{diag}(\Lambda_1, \Lambda_2, \dots, \Lambda_{\chi_\ell})$  is an additional diagonal  $\chi_\ell \times \chi_\ell$  matrix that contains the Schmidt values. There is also an alternative MPS representation introduced by Vidal [16], in which the Schmidt decompositions for every bond is included:

$$|\psi\rangle = \sum_{\sigma} \Gamma^{\sigma_1} \Lambda^{[1]} \Gamma^{\sigma_2} \Lambda^{[2]} \dots \Gamma^{\sigma_N} |\sigma\rangle \quad \begin{array}{c} \Gamma^{[1]} \quad \Lambda^{[1]} \quad \Gamma^{[2]} \quad \dots \\ \circ \text{---} \diamond \text{---} \circ \text{---} \diamond \text{---} \dots \text{---} \diamond \text{---} \circ \end{array}. \quad (4)$$

Here, the tensors formed by the matrices  $\Lambda^{[j-1]} \Gamma^{\sigma_j}$  are left-normalized and those formed by  $\Gamma^{\sigma_j} \Lambda^{[j]}$  are right-normalized. Since the bond dimension places a limit on the Schmidt number, MPS are in a sense low-entanglement approximations.

Ground states of gapped short-ranged Hamiltonians are generally expected to fulfill area laws for the von Neumann entanglement entropy  $S = -\text{Tr}[\rho \ln(\rho)]$  of the reduced density matrix  $\rho$  [46]. For the bipartition in Eq. (3), the entanglement entropy is  $S = -\sum_{\alpha=1}^{\chi_\ell} \Lambda_\alpha^2 \ln(\Lambda_\alpha^2)$ . The system is said to fulfill an area law when in the thermodynamic limit the entanglement entropy for a subsystem is proportional its surface. For one-dimensional systems, it means that the entanglement entropy saturates when the size of the subsystem is increased. This has been proven for unique gapped ground states under the condition of finite range and finite strength of the interactions [14]. The bound on the entanglement entropy implies that the state can be accurately approximated by an MPS with finite bond dimension even in the thermodynamic limit. Critical ground states do not fulfill an area law and the entanglement entropy instead grows logarithmically with the size of the subsystem [47]. Nevertheless, the computational complexity scales polynomially with the system size which is preferable to the exponential increase for exact diagonalization [48].

Instead of simulating large finite systems with MPS it can be more efficient to work directly in the thermodynamic limit by using iMPS [45, 49]. In an iMPS, the translation invariance is exploited by making the  $\Gamma$  and  $\Lambda$  tensors in the representation of Eq. (4) independent of the unit cell. Such a state can be written as

$$|\psi\rangle = \sum_{\sigma} \dots \Lambda^{[N]} \Gamma^{[1]\sigma_j} \Lambda^{[1]} \dots \Gamma^{[N]\sigma_{j+N-1}} \Lambda^{[N]} \Gamma^{[1]\sigma_{j+N}} \dots |\sigma\rangle, \quad (5)$$

where  $N$  is the size of the unit cell. Only a finite number of tensors needs to be contracted to evaluate expectation values because of the normalizations imposed on the tensors. Assuming for simplicity  $N = 1$ , two-point correlation functions  $\langle \psi | \hat{O}_{j+r} \hat{O}_j | \psi \rangle$  are given graphically by

$$\langle \psi | \hat{O}_{j+r} \hat{O}_j | \psi \rangle = \begin{array}{c} \Lambda \quad \Gamma \quad \dots \\ \circ \text{---} \diamond \text{---} \circ \text{---} \diamond \text{---} \dots \text{---} \diamond \text{---} \circ \\ \Lambda \quad \Gamma^* \quad \dots \end{array} \quad \begin{array}{c} \circ \text{---} \diamond \text{---} \circ \text{---} \diamond \text{---} \dots \text{---} \diamond \text{---} \circ \\ \circ \text{---} \diamond \text{---} \circ \text{---} \diamond \text{---} \dots \text{---} \diamond \text{---} \circ \end{array}. \quad (6)$$

By defining the (left) transfer matrix  $T = \sum_{\sigma} \Lambda \Gamma^{\sigma} \otimes (\Lambda \Gamma^{\sigma})^{\dagger}$  we may write the correlation function as  $\langle \psi | \hat{O}_{j+r} \hat{O}_j | \psi \rangle = v_L T^{r-1} v_R$ , where  $v_L$  and  $v_R$  are vectors obtained by reshaping the matrices  $\sum_{\sigma, \sigma'} \Gamma^{\sigma'} \Lambda^2 \Gamma^{\sigma} \langle \sigma' | \hat{O}_j | \sigma \rangle$  and  $\sum_{\sigma, \sigma'} \Lambda \Gamma^{\sigma} \Lambda^2 \Gamma^{\sigma'} \Lambda \langle \sigma' | \hat{O}_{j+r} | \sigma \rangle$ , respectively. Since  $T$  is a finite-dimensional matrix this indicates that all correlation functions decay exponentially for long enough distances, which is a clear sign that iMPS are not able to describe critical states faithfully in the thermodynamic limit. Let  $\lambda_n$  with  $n = 1, 2, \dots$  be the eigenvalues of  $T$ , sorted in descending order regarding their absolute values. We have  $|\lambda_n| \leq 1$  since otherwise correlation functions would diverge for  $r \rightarrow \infty$ . Moreover, there must be an eigenvalue  $\lambda_1 = 1$  because  $\langle \psi | \psi \rangle = 1$ . From the orthogonalization of the tensors follows that the corresponding left eigenvector is the identity matrix, while the right eigenvector is the reduced density matrix. Infinite MPS which have only one eigenvalue of magnitude 1 are called *pure*. Their connected correlation functions all decay to zero for long distances with an effective correlation length  $\xi_{\text{MPS}} = -1/\ln(|\lambda_2|)$  that is determined by the second-largest eigenvalue of  $T$ . When there is more than one eigenvalue of magnitude 1, which is the case for superpositions of different symmetry-broken states, the state can be uniquely decomposed into a sum of pure iMPS [50].

At a critical point the physical correlation length diverges while  $\xi_{\text{MPS}}$  of an iMPS approximation of the ground state is finite. The effective correlation length  $\xi_{\text{MPS}}$  gives an indication up to which length the powerlaw decay of correlations is accurately reproduced [45]. When the bond dimension  $\chi$  is increased,  $\xi_{\text{MPS}}$  grows roughly with a powerlaw that depends on the universality class of the critical point [51].

**Density-matrix renormalization group** The primary application of MPS is as a ground-state ansatz in the DMRG [12, 13]. One tries to find the MPS which minimizes the energy  $\langle \psi | \hat{H} | \psi \rangle / \langle \psi | \psi \rangle$  for some Hamiltonian  $\hat{H}$  under the constraint that the bond dimensions  $\chi_j$  are all smaller than some number  $\chi$ . The basic idea of the DMRG in the MPS formalism is to break down the global energy minimization into a series of much smaller minimization problems in which only one or two of the tensors  $A^{[j]}$  are modified. In doing so, left and right normalizations of the remaining tensors are used to simplify the problem. Here, we discuss the traditional two-site algorithm.

Let us assume we have an MPS in which for some  $\ell$  all tensors  $A^{[j]}$  with  $j < \ell$  ( $j > \ell + 1$ ) are left-normalized (right-normalized), i.e.,

$$|\psi\rangle = \sum_{\alpha=1}^{\chi_{\ell-1}} \sum_{\beta=1}^{\chi_{\ell+1}} \sum_{\sigma_{\ell} \sigma_{\ell+1}} \Phi_{\alpha \sigma_{\ell}, \beta \sigma_{\ell+1}} |\alpha\rangle_L^{\ell-1} |\sigma_{\ell}\rangle |\sigma_{\ell+1}\rangle |\beta\rangle_R^{\ell+1}, \quad (7)$$

where the tensor for two sites  $\ell$  and  $\ell+1$  were combined into a single tensor  $\Phi_{\alpha \sigma_{\ell}, \beta \sigma_{\ell+1}} = (A^{\sigma_{\ell}} A^{\sigma_{\ell+1}})_{\alpha \beta}$ . The states  $|\alpha\rangle_L^{\ell-1} |\sigma_{\ell}\rangle |\sigma_{\ell+1}\rangle |\beta\rangle_R^{\ell+1}$  form an orthonormal basis of a subspace of the total Hilbert space. As a step toward the determination of the ground state one minimizes the energy in this subspace using some standard iterative algorithm, which yields a new tensor  $\Phi'$ . In order to restore the MPS structure of the state,

a singular-value decomposition is carried out:

$$\Phi'_{\alpha\sigma_\ell, \beta\sigma_{\ell+1}} = \sum_{\gamma} U_{\alpha\sigma_\ell, \gamma} D_{\gamma} V_{\gamma, \beta\sigma_{\ell+1}}^{\dagger}, \quad \text{---}\overset{\Phi'}{\text{---}}\text{---} = \text{---}\overset{U}{\circ}\overset{D}{\diamond}\overset{V^{\dagger}}{\circ}\text{---}. \quad (8)$$

Here,  $D_{\gamma}$  are the singular values and  $U$  and  $V$  are, when the indices are combined as indicated, matrices with orthogonal columns. By identifying  $A_{\alpha\gamma}^{\sigma_\ell} = U_{\alpha\sigma_\ell, \gamma}$ ,  $A_{\gamma\beta}^{\sigma_{\ell+1}} = V_{\gamma, \beta\sigma_{\ell+1}}^{\dagger}$  and  $\Lambda_{\gamma} = D_{\gamma}$  we obtain a Schmidt decomposition as in Eq. (3), since the new  $A_{\alpha\gamma}^{\sigma_\ell}$  and  $A_{\gamma\beta}^{\sigma_{\ell+1}}$  are left- and right-normalized, respectively. However, the Schmidt rank can be larger than the initial bond dimension  $\chi_\ell$ , possibly by a factor equal to the dimension of the single-site Hilbert space. To fulfill the bound on the bond dimension, the Schmidt rank needs to be truncated down to  $\chi$ . The best approximation regarding the Euclidean norm is obtained by dropping the smallest Schmidt values, or equivalently, the eigenvalues of the reduced density matrix with the smallest weight. The total weight of the discarded eigenvalues, which is called the truncation error, is often used as a measure for the accuracy of a DMRG calculation.

To proceed, one sets  $\ell \leftarrow \ell + 1$  or  $\ell \leftarrow \ell - 1$  and repeats the steps described above. The ground-state approximation is obtained iteratively by updating each tensor in turn, moving from one end of the system to the other and back, which is called a sweep. Typically, of the order of 10 sweeps are necessary to achieve acceptable convergence.

In an iMPS, each tensor appears an infinite number of times, so that a different approach is needed to minimize the energy. An efficient method is the iDMRG which is related to the infinite-system algorithm sometimes used to initialize the finite-system DMRG [12, 45]. Assume we have an MPS that approximates the ground state for a finite system. It can be brought to a form that shows the Schmidt decomposition at the center bond:  $|\psi\rangle = \sum_{\alpha} \Lambda_{\alpha} |\alpha\rangle_L |\alpha\rangle_R$ . In each step of the iDMRG, a unit cell is inserted in the center of the system by replacing the matrix of Schmidt values  $\Lambda$  with the tensors for a new unit cell of  $N$  sites, i.e.,  $|\psi'\rangle = \sum_{\alpha} \sum_{\sigma_1, \dots, \sigma_N} (A^{\sigma_1} \dots A^{\sigma_N})_{\alpha\beta} |\alpha\rangle_L |\sigma_1, \dots, \sigma_N\rangle |\beta\rangle_R$ . The energy is then minimized with the tensors  $A^{[1]}, \dots, A^{[N]}$  as free parameters through restricted DMRG sweeps that only run over the new sites in the center. In the thermodynamic limit where translation invariance holds, the state  $|\psi'\rangle$  will have a Schmidt decomposition equivalent to that at the center of the previous state  $|\psi\rangle$ , if we cut the system at one of the bonds connecting the new unit cell to rest of the system. Combining for simplicity the sites of the unit cell, the tensors  $\Gamma^{\sigma_1, \dots, \sigma_N} = \Lambda^{-1} A^{\sigma_1} \dots A^{\sigma_N} \Lambda^{-1}$  and  $\Lambda$  thus can be used to define an iMPS as in Eq. (4), that approximates the ground state in the thermodynamic limit. In the iDMRG, the limit of an infinite system is approached by successively inserting sites in the middle of the system and keeping track of the convergence of the iMPS defined by the last-added tensors.

**Time evolution** If an MPS ground state is evolved in time following some perturbation, the bond dimension required for an accurate MPS representation will typically increase and eventually become prohibitively large. For short times, however, an MPS description is still feasible. The accessible time scales strongly depend on the nature of the perturbation. A global quench leads to a linear growth of the entanglement entropy [52] corresponding to potentially exponentially increasing bond dimension. Local perturbations cause at most logarithmic increase of the entanglement entropy so that

longer times can be reached [53, 54]. The latter case occurs in the calculation of dynamic response functions such as the dynamic structure factor. For this task, the time-evolution of MPS is currently one of the most efficient techniques in one dimension [55].

There are multiple ways to carry out the time evolution in a numerical simulation. Generally applicable are the matrix-product operator (MPO) technique of Ref. [56] and methods based on the time-dependent variational principle [57]. We used the time-evolving block decimation (TEBD) [16] which, unless swap gates are employed [20], requires the Hamiltonian to have at most nearest-neighbor terms. Advantages of the TEBD algorithm are that it is fast and allows for easy parallelization. In the TEBD, the time-evolution operator is approximated by a Suzuki-Trotter decomposition [58]. Assume we have a Hamiltonian that is a sum of nearest-neighbor terms  $\hat{H} = \sum_j \hat{h}_{j,j+1}$ . The time-evolution operator in a first-order Suzuki-Trotter decomposition is then

$$e^{-it\hat{H}} = \left[ \left( \prod_{j \text{ odd}} e^{-i(t/n)\hat{h}_{j,j+1}} \right) \left( \prod_{j \text{ even}} e^{-i(t/n)\hat{h}_{j,j+1}} \right) \right]^n + \mathcal{O}(t^2/n^2), \quad (9)$$

where  $n$  is the number of time steps. In practical calculations, one usually uses second- or fourth-order formulas that are constructed similarly. Each individual term  $e^{-i(t/n)\hat{h}_{j,j+1}}$  only affects two tensors and thus can be efficiently applied to the MPS using local updates like in the DMRG. For each two-site operator, appropriate left- and right-normalizations of the MPS tensors are necessary to ensure a controlled truncation of the bond dimension. By using the MPS representation of Eq. (4) it is possible to apply all odd or even terms simultaneously [49]. This parallel update scheme is allowed, because each factor  $e^{-i(t/n)\hat{h}_{j,j+1}}$  in the Suzuki-Trotter approximation is unitary and thus, neglecting truncation errors, only changes the Schmidt values at the bond it acts on.

**Finite temperature** Density operators of mixed states can be represented by MPO, which are straightforward generalizations of MPS with an additional physical index for each tensor [19]. However, there is no efficient way to ensure the required positive semi-definiteness in an MPO [59]. One therefore often uses a purification ansatz instead, where the density operator  $\hat{\rho}$  is obtained as the reduced density operator of a pure state  $|\psi\rangle$  in an enlarged system, so that  $\hat{\rho}$  is positive semi-definite by construction [19]. By adding an auxiliary Hilbert space  $\mathcal{H}_{\text{aux}}$  which is a copy of the physical space  $\mathcal{H}_{\text{phys}}$  one can always write  $\hat{\rho} = \text{Tr}_{\text{aux}}(|\psi\rangle\langle\psi|)$ , where  $|\psi\rangle \in \mathcal{H}_{\text{phys}} \otimes \mathcal{H}_{\text{aux}}$  and  $\text{Tr}_{\text{aux}}$  denotes the partial trace over  $\mathcal{H}_{\text{aux}}$ . The expectation value of an operator  $\hat{O}$  is then calculated via  $\text{Tr}(\hat{\rho}\hat{O})/\text{Tr}(\hat{\rho}) = \langle\psi|\hat{O}|\psi\rangle/\langle\psi|\psi\rangle$ . On the right side of this relation,  $\hat{O}$  acts trivially on the auxiliary space.

In order to analyze finite-temperature properties of a Hamiltonian  $\hat{H}$ , we need to find a purification for the thermal density operator  $\hat{\rho}_\beta = e^{-\beta\hat{H}}/\text{Tr}(e^{-\beta\hat{H}})$ , where  $\beta$  is the inverse temperature. This is done by starting from a trivial infinite-temperature purification  $|\psi_0\rangle$  and then applying small imaginary time steps  $e^{-\delta\tau\hat{H}}$  that each lower the temperature by  $2\delta\tau$ . A simple choice for the infinite-temperature purification that can be directly constructed is, up to a normalization,  $|\psi_0\rangle = \prod_j (\sum_{\sigma_j} |\sigma_j\rangle_{\text{phys}} |\sigma_j\rangle_{\text{aux}})$ , i.e., the physical and auxiliary sites are grouped in pairs that form maximally entangled

states. In the MPS representation, the paired sites are chosen to be nearest neighbors. The imaginary time-steps are applied to the physical part of the system using similar techniques as for real-time evolution.

As the temperature is lowered, the bond dimensions of the MPS purification needs to be increased to maintain an accurate representation of the state. It has been shown that in the thermodynamic limit the required bond dimension saturates for gapped systems, while it scales polynomially in the inverse temperature  $\beta$  in the gapless case [60].

Real-time evolution following a quench or a perturbation by an operator is simulated in similar fashion as for pure states by applying small real-time steps  $e^{-i\delta t \hat{H}}$  to the physical part. The limitations are also similar, i.e., the required bond dimension grows with the simulated time and restricts the calculations to relatively short time scales.

**Symmetry-protected topological order in matrix-product states** In addition to having applications in numerical algorithms, MPS are helpful as a theoretical tool to classify the gapped phases of one-dimensional systems [6, 7, 9, 10]. Here, two points in the space of finite-ranged Hamiltonians are said to belong to different phases when they cannot be smoothly connected without crossing a phase transition. A phase transition is defined as a point where the gap closes or where the derivative of the ground-state energy has a discontinuity [61]. It is known that MPS can accurately represent one-dimensional gapped ground states in the thermodynamic limit, and that every MPS is the unique ground state of a finite-ranged and gapped parent Hamiltonian with the same symmetry [50]. This justifies a classification of gapped phases by determining which MPS are connected by a smooth path of gapped parent Hamiltonians [7]. In the following, we summarize the results of such an analysis.

The definition of phases depends on the symmetries imposed on the Hamiltonian. Two ground states in different phases may be distinguished by the spontaneous breaking of these symmetries. However, it is also possible that two ground states do not break any symmetry yet cannot be smoothly connected by Hamiltonians as long as certain symmetries are kept intact, and in that sense also belong to different phases. A subclass of such phases consist of states distinguished by SPT order. Non-trivial SPT order means that the phase does not include a site-factorizable state. The main use of the MPS classification is that it allows to identify the possible types of SPT order depending on the symmetries of the Hamiltonian.

We now assume that the ground state is given by a pure iMPS as in Eq. (5) with bond dimension  $\chi$  and a one-site unit cell. The starting point for the classification in the presence of symmetries is the equation [62]

$$\sum_{\sigma'} \Sigma_{\sigma\sigma'} \Gamma^{\sigma'} = e^{i\varphi} U^\dagger \Gamma^\sigma U, \quad \begin{array}{c} \Gamma \\ \circ \\ \text{---} \\ \square \\ \Sigma \end{array} = \begin{array}{c} U^\dagger \quad \Gamma \quad U \\ \square \quad \circ \quad \square \end{array} \cdot e^{i\varphi}, \quad (10)$$

where  $U$  is a unitary  $\chi \times \chi$  matrix that commutes with  $\Lambda$ , and  $\varphi \in \mathbb{R}$ . This equation relates a local symmetry operation represented by a unitary matrix  $\Sigma$  acting on the physical index of the tensor, to a matrix  $U$  acting on the bond index. Similar expressions hold for time-reversal and inversion symmetries, where the matrices on the left-hand side are the complex conjugate  $\Gamma^{\sigma'*}$  and the transpose  $\Gamma^{\sigma'T}$ , respectively [9].

We now consider multiple local symmetries defined by matrices  $\Sigma_g$ . Consistency

with the symmetry group leads to certain constraints on the corresponding matrices  $U_g$  and the phase factors  $e^{i\varphi_g}$ . Here, we focus on the matrices  $U_g$  which are important for the definition of SPT phases. For only local symmetries, the matrices  $U_g$  form a projective representation of the symmetry group, i.e.,  $U_g U_h = e^{i\alpha(g,h)} U_{gh}$ , where  $e^{i\alpha(g,h)}$  is a phase factor, and the corresponding local transformation matrices are assumed to satisfy  $\Sigma_g \Sigma_h = \Sigma_{gh}$ . It has been shown that two MPS are in the same phase if their  $U$  matrices form equivalent projective representations. For example, the group  $\mathbb{Z}_2 \times \mathbb{Z}_2$  has two classes of projective representations and thus supports two symmetric phases [9]. They can be identified by considering the matrices  $U_g$  and  $U_h$  for two different elements, which must satisfy

$$U_g U_h = \pm U_h U_g. \quad (11)$$

The sign distinguishes between trivial (+) and non-trivial (−) SPT order.

Time-reversal  $\mathcal{T}$  and inversion  $\mathcal{I}$  symmetries do not fall into this description. Instead, their matrices satisfy

$$U_{\mathcal{T}} = \pm U_{\mathcal{T}}^T, \quad U_{\mathcal{I}} = \pm U_{\mathcal{I}}^T, \quad (12)$$

where the minus sign again corresponds to non-trivial SPT order. The combination of time-reversal, inversion and local symmetries leads to additional phase labels beyond the ones for the individual symmetries, which will not be discussed here [10].

The conditions on the  $U$  matrices for non-trivial SPT order imply, through the relation  $[U, \Lambda] = 0$ , that each Schmidt value in  $\Lambda$  has an even degeneracy [9]. This shows that the phase does indeed not include a site-factorizable state. The degeneracy can also be used as a signature of SPT phases in DMRG calculations, though it does not indicate the type of SPT order. As described in Ref. [63], however, it is possible to obtain the  $U$  matrices for an iMPS numerically and thereby unambiguously determine the protecting symmetries.

### 1.3 Symmetry-protected topological order and criticality

The Haldane phase realized by the spin-1 Heisenberg chain is one the most famous examples of topological order in one dimension. A more general model is the spin-1 XXZ chain with single-ion anisotropy:

$$\hat{H}_{XXZ,D} = J \sum_j \left[ \frac{1}{2} (\hat{S}_j^+ \hat{S}_{j+1}^- + \hat{S}_j^- \hat{S}_{j+1}^+) + \Delta \hat{S}_j^z \hat{S}_{j+1}^z \right] + D \sum_j (\hat{S}_j^z)^2, \quad (13)$$

which for  $J, \Delta > 0$  also includes topologically trivial phases, a phase with spontaneously broken symmetry, and different types of phase transitions. Because many of the models studied in this thesis are related to this spin chain, we briefly review its ground-state phase diagram [64, 65]. For a strong on-site anisotropy, the system is in the large- $D$  phase without broken symmetries. The ground state in the limit  $D \rightarrow \infty$  becomes the product state  $\prod_j |0\rangle_j$ , where the number indicates the eigenstate in the eigenbasis of  $\hat{S}_j^z$ . Accordingly, the large- $D$  phase is topologically trivial. When the anisotropy parameter  $\Delta$  is large, the ground state belongs to the Néel phase with long-range

antiferromagnetic order that spontaneously breaks symmetries of the Hamiltonian. Like the large- $D$  phase, it is topologically trivial since it includes the limit  $\Delta \rightarrow \infty$  where the two degenerate ground states are the product states  $\prod_j |\pm(-1)^j\rangle$ . Finally, between the large- $D$  and Néel phases is the SPT Haldane phase. It is symmetric and therefore the distinction from the large- $D$  phase is not possible through a local order parameter that measures symmetry breaking. Nevertheless, it is a separate phase since it has non-trivial SPT order. The protecting symmetries for the Haldane phase are time-reversal  $\mathcal{T}$ , bond-centered inversion  $\mathcal{I}$  and the  $\mathbb{Z}_2 \times \mathbb{Z}_2$  group of  $\pi$  spin rotations around two orthogonal axes [9]. Characteristics of the Haldane phase are gapless spin-1/2 edge states [23], and non-local string order [22]. These features are not protected by all symmetries mentioned above, however. If there is only inversion symmetry  $\mathcal{I}$ , they may disappear for parameters in the phase [24].

The transitions between the Haldane phase and the large- $D$  and Néel phases are continuous and belong to the Gaussian and Ising universality class, respectively [64, 66]. For large  $\Delta$  and  $D$  values, there is also a direct transition between the large- $D$  and the Néel phase, which is of first order. Ising universality refers to the fact that the effective field theory describing the asymptotic behavior of correlation functions is the same as that for the finite-temperature phase transition in the classical two-dimensional Ising model [61]. Gaussian universality means that the system is described by the Luttinger liquid field theory which, for example, also applies to the gapless phase of interacting spinless fermions in one-dimension. An important difference between the two cases is that the critical exponents that can occur in the Ising universality class are discrete, while in the Gaussian class they depend on a parameter  $K \in (0, \infty)$  which may vary continuously along a phase-transition line.

To experimentally investigate the SPT and critical properties of the model it would be advantageous to have a realization in an optical lattice. Likely easier to implement in such a setup than the spin-1 chain is the extended Bose-Hubbard model which exhibits many of the same phenomena [33, 34]. The Hamiltonian of the extended Bose-Hubbard model is

$$\hat{H}_{\text{EBHM}} = -t \sum_j (\hat{b}_j^\dagger \hat{b}_{j+1} + \hat{b}_{j+1}^\dagger \hat{b}_j) + \frac{U}{2} \sum_j \hat{n}_j (\hat{n}_j - 1) + V \sum_j \hat{n}_j \hat{n}_{j+1}. \quad (14)$$

We assume a density  $\rho = 1$  of one particle per site and  $U, V > 0$ . Because of the local repulsion, we can approximately truncate the local Hilbert spaces to states with particle number  $n < 3$  and identify the states  $|n\rangle \leftrightarrow |S^z + 1\rangle$ . By ignoring the difference in the commutation relations of the spin and boson operators and making the replacements  $\hat{b}_j \rightarrow \hat{S}_j^-$ ,  $\hat{b}_j^\dagger \rightarrow \hat{S}_j^+$  and  $\hat{n}_j \rightarrow \hat{S}_j^z + 1$ , we end up with the Hamiltonian in Eq. (13) up to a minus factor in the hopping term which is not significant as can be removed by a unitary transformation  $e^{i\pi \sum_j \text{odd } \hat{S}_j^z}$  or  $e^{i\pi \sum_j \text{odd } \hat{n}_j}$ . While this is a rough approximation, it has been shown numerically that the phase diagram of the extended Bose-Hubbard model is indeed very similar to that of the spin chain, with Mott insulator, Haldane insulator and density-wave phases replacing the large- $D$ , Haldane, and Néel phases, respectively. In contrast to the spin model, where the analogous phase occurs only for negative  $\Delta$ , there is a gapless superfluid phase in the regime of weak interaction [34]. Furthermore, to arrive at the spin-1 chain model, we dropped terms of the Hamiltonian that break the protecting symmetries of the Haldane phase except the bond-centered inversion  $\mathcal{I}$ .



Taking into account the unitary transformation needed to adjust the hopping sign, it follows that the Haldane insulator of the extended Bose-Hubbard model is protected by the modified inversion symmetry  $\mathcal{I}' = e^{i\pi \sum_j \hat{n}_j} \mathcal{I}$  [9]. String order and edge states thus cannot be used to define the bosonic Haldane phase.

**Dimerization** As a first extension, we study the effect of dimerization which here refers to an alternating strength of the nearest-neighbor hopping or exchange-interaction terms. There are different possible sources for dimerization in one-dimensional systems. For half-filled fermion systems or analogous spin chains it can occur as a result of spontaneous symmetry breaking because of the Peierls instability. Additionally, there are materials with dimerization due to the crystal structure [67]. In optical lattices, dimerization has been implemented by superimposing two regular lattices with different wavelengths [68].

We begin by discussing the dimerized spin-1 chain with Hamiltonian

$$\hat{H} = \hat{H}_{XZX,D} + J\delta \sum_j (-1)^j \left[ \frac{1}{2} (\hat{S}_j^+ \hat{S}_{j+1}^- + \hat{S}_j^- \hat{S}_{j+1}^+) + \Delta \hat{S}_j^z \hat{S}_{j+1}^z \right] \quad (15)$$

(see Article I). Basic features of the phase diagram can be anticipated from the known results for the model with  $\delta = 0$ . Since the large- $D$ , Haldane and Néel phases are gapped, they will be stable against a small dimerization. Furthermore, the protecting symmetries of the Haldane phase are not broken so that the distinction between large- $D$  and Haldane phase must remain. For very strong dimerization, there is a transition to a phase which includes a fully dimerized state. Unlike in the spin-1/2 case, however, this is not an SPT phase. It is in fact the large- $D$  phase in the general model with both dimerization and single-ion anisotropy.

To determine the phase for a set of parameters  $(\Delta, D/J, \delta)$  numerically, we calculate an iMPS approximation of the ground state with the iDMRG and then extract local and topological order parameters. The locations of the phase transition are also confirmed by calculating the correlation length of the iMPS which remains finite but shows a sharp peak as the parameters are varied through a critical point. Figure 1 shows the resulting phase diagram for dimerization  $\delta = 0.1$ . There are still large- $D$ , Haldane and Néel phases, but the Haldane phase shrinks as  $\delta$  is increased and eventually vanishes in the parameter range studied. The numerical calculations show that no additional phases appear even for large  $\delta$ .

The effect on the phase transitions is more significant. In contrast to the model without dimerization, the transition between the large- $D$  and the Néel phase is partially continuous. The continuous part is in the Ising universality class [69] except for the point where the transition becomes of first order. There, the ground state belongs to the tricritical Ising universality class, which has only few known realizations in realistic Hamiltonians. Note, that such a point does not occur in the model with  $D = 0$ .

An efficient way to identify the universality classes numerically is through the calculation of the central charge  $c$ . This is a quantity from conformal field theory, which we here simply use as a label for the different universality classes [70]. For the phase transitions we encounter, the central charges are  $c = 1/2$  (Ising),  $c = 7/10$  (tricritical Ising) and  $c = 1$  (Gaussian). To calculate the central charge  $c$  one can exploit

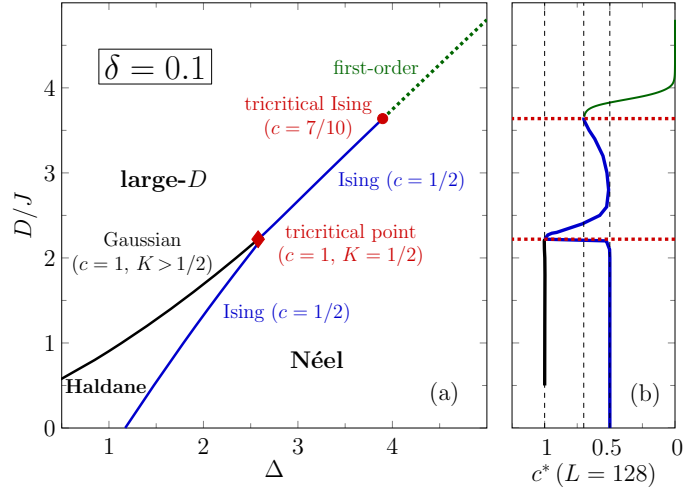


**Figure 1:** Phase diagram of the spin-1 XXZ chain with single-ion anisotropy and dimerization  $\delta = 0.1$  calculated with the iDMRG. Panel (b) shows the measure for the central charge  $c^*(L)$  defined in Eq. (17) for  $L = 128$  along the phase transition lines.

that it appears in the scaling of the entanglement entropy  $S(\ell)$  with the size  $\ell$  of the subsystems in the bipartition. For a large system with  $L$  sites and periodic boundary conditions at criticality, the following relation holds for the von Neumann entanglement entropy between a contiguous block of  $\ell$  sites and the rest of the system [47]:

$$S(\ell) = \frac{c}{3} \ln \left[ \frac{L}{\pi} \sin \left( \frac{\pi \ell}{L} \right) \right] + s_1, \quad (16)$$

where  $s_1$  is a non-universal constant. Since we consider dimerized systems, the above equation applies only for even and odd bonds separately. Taking this into account, we define a quantity [71]

$$c^*(L) = 3 \frac{[S(L/2 - 2) - S(L/2)]}{\ln\{\cos[\pi/(L/2)]\}} \quad (17)$$

that becomes equal to the central charge in the thermodynamic limit for critical systems, i.e.,  $\lim_{L \rightarrow \infty} c^*(L) = c$ . In gapped systems, including first-order phase transitions,  $\lim_{L \rightarrow \infty} c^*(L) = 0$  because of the area law. While periodic boundary conditions are more difficult to handle with MPS-based methods, they avoid boundary corrections to Eq. (16) which would hinder the calculation of  $c$  [72].

The correct universality classes of the phase transitions could already be guessed from the central charge  $c$ . However, this does not tell us the relation between the effective field theory and the lattice model, which is necessary to make predictions for the correlation functions. An analytical derivation of the field theory is helpful in this regard. The effective field theory for the Hamiltonian (15) can be obtained starting from an exactly solvable point in the bilinear-biquadratic model with an additional nearest-neighbor term  $\propto (\hat{\mathbf{S}}_j \hat{\mathbf{S}}_{j+1})^2$  [66]. We do not discuss the resulting field theory here and only state the predictions for the correlations functions. For the Ising and

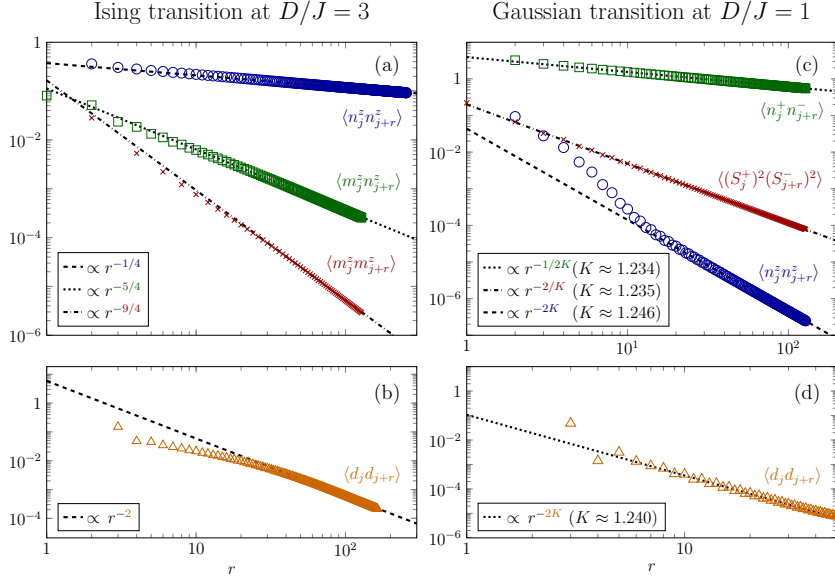


**Figure 2:** Correlation functions at the two phase-transition points belonging to the Ising (a,b) and Gaussian (c,d) universality classes. The symbols are iDMRG results, the solid lines fits according to the critical exponents in Eq. (18).

Gaussian phase transitions, we have the asymptotic behavior

Ising	Gaussian	
$\langle \hat{n}_j^z \hat{n}_{j+r}^z \rangle \sim r^{-1/4},$	$\langle \hat{n}_j^z \hat{n}_{j+r}^z \rangle \sim r^{-2K},$	(18)
$\langle \hat{m}_j^z \hat{m}_{j+r}^z \rangle \sim r^{-9/4},$	$\langle \hat{m}_j^z \hat{m}_{j+r}^z \rangle \sim r^{-2},$	
$\langle \hat{m}_j^z \hat{n}_{j+r}^z \rangle \sim r^{-5/4},$	$\langle (\hat{S}_j^+)^2 (\hat{S}_{j+r}^-)^2 \rangle \sim r^{-2/K},$	
$\langle \hat{d}_j \hat{d}_{j+r} \rangle \sim r^{-2} + \text{const.},$	$\langle \hat{n}_j^\alpha \hat{n}_{j+r}^\alpha \rangle \sim r^{-1/2K}, \quad \alpha = x, y,$	
	$\langle \hat{d}_j \hat{d}_{j+r} \rangle \sim r^{-2K} + \text{const.},$	

where  $\hat{n}_j^\alpha = (-1)^j (\hat{S}_j^\alpha - \hat{S}_{j+1}^\alpha)/2$ ,  $\hat{m}_j^\alpha = (\hat{S}_j^\alpha + \hat{S}_{j+1}^\alpha)/2$  and  $\hat{d}_j = (-1)^j (\hat{S}_j \hat{S}_{j+1} - \hat{S}_{j+1} \hat{S}_{j+2})$  are the operators for staggered magnetization, smoothed magnetization and dimerization, respectively. The Luttinger liquid parameter along the Gaussian line is  $K \leq 1/2$ , with  $K = 1/2$  at the tricritical point.

Our numerical approach to analyze the phase transitions is as follows. First, we use the iDMRG to find the transition lines with high accuracy. We then switch to finite-system DMRG with periodic boundary conditions to calculate  $c^*(L)$  along the transitions. This indicates where the different types of phase transition occur and in particular allows us to locate the tricritical Ising point with  $c = 7/10$ . Finally, the field-theoretical predictions for various critical exponents are checked by iDMRG calculations. The behavior of the central charge is shown in Fig. 1(b), the correlation functions in Fig. 2. For all correlation functions and both Ising and Gaussian transitions, the critical exponents agree with the field-theory predictions in Eq. (18).

Dimerization in the extended Bose-Hubbard model (14) at density  $\rho = 1$  should have a similar effect on the phase diagram as in the spin-1 chain because of the relation

between the models. We confirm in Article II by numerical calculations that this is indeed the case, i.e., the Haldane insulator phase shrinks with increasing dimerization and there is a continuous Ising line between Mott insulator and charge-density wave phases that terminates at a tricritical Ising point.

We also study the effect of dimerization on the extended Fermi-Hubbard model with nearest-neighbor interaction (see Articles III and IV). Without dimerization, the model has an extended spin-density-wave phase with gapless spin excitations. A small dimerization immediately opens a gap in the spectrum and the spin-density-wave phase is replaced by an SPT Peierls insulator phase [35]. If sites connected by a weak bond are regarded as a single site, the Peierls insulator is protected by similar symmetries as the Haldane phase of spin-1 chains, i.e., bond-centered inversion, an antiunitary symmetry, and an on-site  $\mathbb{Z}_2 \times \mathbb{Z}_2$  symmetry [36, 37]<sup>1</sup>. The phase transition between Peierls insulator and a long-range ordered charge-density wave phase is known to partially belong to the Ising universality class [35, 73] but we show that it also includes a tricritical Ising point where it turns first order. We calculate the critical exponents for both Ising and tricritical Ising transitions and find good agreement with field-theory predictions. It should be noted that a narrow bond-order wave phase exists, as a result of spontaneous symmetry breaking, already in the extended Hubbard model without explicit dimerization [74]. In the phase diagram with dimerization, this bond-order-wave phase appears to mark a first-order transition between two different SPT phases.

**Anyon-Hubbard models and the anyonic Haldane insulator** Anyons are defined by the property that the many-body wave function picks up a complex phase factor  $e^{i\theta}$  under particle exchange. They thus interpolate between fermions ( $\theta = \pi$ ) and bosons ( $\theta = 0$ ). No anyonic elementary particles exist but quasiparticles in a solid may obey anyonic exchange statistics. From topological arguments follows that anyons cannot occur in space dimensions three or higher [75]. Furthermore, in one dimension the exchange of particles is not possible without them passing through each other, which appears to leave only two-dimensional systems as candidates. Nevertheless, a type of anyonic system can be defined in one dimension by deforming the exchange relations of the creation and annihilation operators of the particles [76]. In the lattice models we consider, this takes the form:

$$\hat{a}_j \hat{a}_\ell^\dagger - e^{-i\theta \text{sgn}(j-\ell)} \hat{a}_\ell^\dagger \hat{a}_j = \delta_{j\ell}, \quad \hat{a}_j \hat{a}_\ell - e^{-i\theta \text{sgn}(j-\ell)} \hat{a}_\ell \hat{a}_j = 0, \quad (19)$$

where  $\text{sgn}(x)$  is the sign function with  $\text{sgn}(0) = 0$ , and  $\theta$  is called the statistical phase. For  $\theta = 0$ , Eqs. (19) turn into the usual bosonic commutation relations, while for  $\theta = \pi$ , they resemble the fermionic anticommutation relations. However, even for  $\theta = \pi$  the particles are not truly fermions since they obey bosonic statistics on-site.

One of the simplest models of one-dimensional anyons is the anyon-Hubbard model [38]. Its Hamiltonian has the same form as that of the Bose-Hubbard model but the creation and annihilation operators obey the anyon statistics defined by Eqs. (19). We consider an extended anyon-Hubbard model with nearest-neighbor interactions,

---

<sup>1</sup> The SPT phase of the dimerized Hubbard chain has also been referred to as *Haldane phase* [37]. We use the term *Peierls insulator* to distinguish it from the Haldane insulator phase of the extended Bose-Hubbard model.

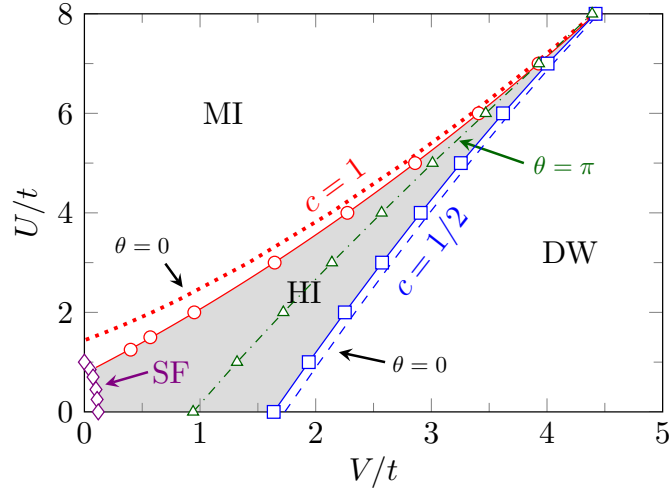


**Figure 3:** Phase diagram of the extended anyon-Hubbard model for  $\theta = \pi/4$  at density  $\rho = 1$ . As in the extended Bose-Hubbard model  $\theta = 0$ , we find a Mott insulator (MI), a Haldane insulator (HI), a density-wave (DW) and a superfluid (SF) phase. The values of the central charge  $c$  at the phase transitions are unchanged. For comparison, the phase boundaries are also shown for  $\theta = 0$  and  $\theta = \pi$ .

which is the anyon version of Eq. (14). With a generalized Jordan-Wigner transformation

$$\hat{a}_j = \hat{b}_j e^{i\theta \sum_{\ell=1}^{j-1} \hat{n}_\ell}, \quad (20)$$

where  $\hat{b}_j$  is a boson annihilation operator, the modification of the exchange relations can equivalently be expressed as a change of the Hamiltonian. While the interaction terms are not affected since  $\hat{n}_j = \hat{a}_j^\dagger \hat{a}_j = \hat{b}_j^\dagger \hat{b}_j$ , the hopping terms get a density-dependent phase factor:

$$\hat{H}_{\text{EAHM}} = -t \sum_j (\hat{b}_j^\dagger \hat{b}_{j+1} e^{i\theta \hat{n}_j} + \text{H.c.}) + \frac{U}{2} \sum_j \hat{n}_j (\hat{n}_j - 1) + V \sum_j \hat{n}_j \hat{n}_{j+1}. \quad (21)$$

Importantly, the above bosonic representation is the basis for several proposals to implement the anyon-Hubbard model in optical lattices [38, 77, 78].

The anyon-Hubbard model ( $V = 0$ ) has already been investigated at length using the DMRG and analytical techniques. We supplement the previous studies in two respects. For the Mott-insulator phase of the anyon-Hubbard model, we use strong-coupling perturbation theory to obtain expressions for the  $\theta$  dependence of various quantities and confirm their range of validity with DMRG calculations (see Article VI). Moreover, we study the extended anyon-Hubbard model (21) with nearest-neighbor interaction and analyze its phase diagram at density  $\rho = 1$  (see Article V). In the following, we discuss only the results for the extended anyon-Hubbard model.

The phase diagram of the extended anyon-Hubbard model is presented in Fig. 3. When  $\theta$  is increased from 0 to  $\pi$ , the Haldane insulator phase becomes gradually smaller

and eventually disappears at least for repulsive interactions. This is in accordance with the naive expectation that the anyons resemble fermions for  $\theta = \pi$ , which do not realize a Haldane phase in the extended Hubbard model. Apart from that, the phase diagram is mostly unchanged compared with that of the extended Bose-Hubbard model. The additional effort to implement the hopping phase experimentally therefore seems hardly worthwhile. From a theoretical point of view, however, the existence of the anyonic Haldane insulator is interesting since the hopping phase in Eq. (21) breaks the modified inversion symmetry

$$\mathcal{I}' = e^{i\pi \sum_j \hat{n}_j} \mathcal{I} \quad (22)$$

that protects the bosonic Haldane insulator phase. Here,  $\mathcal{I}$  is the regular bond-centered inversion. Since  $\mathcal{I}$  is a symmetry only for  $\theta = 0$  or  $\theta = \pi$ , it is not obvious that the Haldane insulator survives in the anyonic model. When a symmetry-breaking perturbation is added it will usually lift the clear distinction between the phases differing only by the corresponding SPT order. For example, a correlated-hopping term  $\propto [(\hat{n}_j - 1)\hat{b}_j^\dagger \hat{b}_{j+1} + \text{H.c.}]$  has been shown to open a small gap at the transition between Mott and Haldane insulator [34]. Our main result for the model (21) is that the Haldane insulator phase is robust under the specific perturbation corresponding by the change from bosons to anyons. The reason is that not only the modified inversion symmetry  $\mathcal{I}'$  protects the Haldane phase but also a combination of local, time-reversal and inversion symmetries. Namely, in addition to the  $U(1)$  symmetry

$$\mathcal{R}(\varphi) = e^{i\varphi \sum_j \hat{n}_j}, \quad \varphi \in [0, 2\pi) \quad (23)$$

corresponding to particle-number conservation, there is a symmetry

$$\mathcal{K} = e^{i\theta \sum_j \hat{n}_j (\hat{n}_j - 1)/2} \mathcal{I} \mathcal{T}, \quad (24)$$

where  $\mathcal{I}$  is a bond-centered inversion and  $\mathcal{T}$  the time-reversal operation (complex conjugation). We find that if both symmetries (23) and (24) are present, an SPT phase can exist which is a generalization of the Haldane insulator for bosons. The analysis is

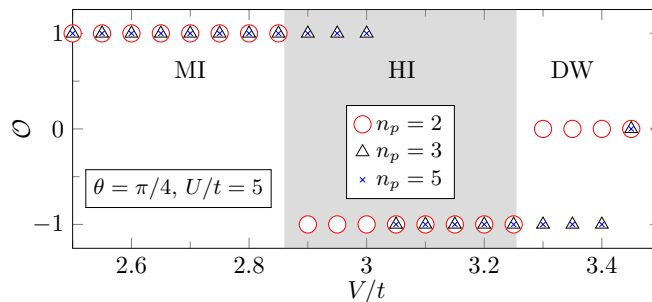


**Figure 4:** Topological order parameter calculated numerically using the iDMRG ground states in the Mott insulator (MI), Haldane insulator (HI) and density-wave (DW) phases. A value  $\mathcal{O} = 1$  ( $\mathcal{O} = -1$ ) indicates a topologically trivial (non-trivial) state, while  $\mathcal{O} = 0$  means that the symmetry is spontaneously broken.

based on Eq. (10) which describes the effect of the symmetry operations on the tensors of an iMPS.

It turns out that regarding the SPT classification of phases,  $\mathcal{K}$  behaves much like an additional local  $\mathbb{Z}_2$  symmetry. An important point is that unlike time-reversal and inversion symmetries separately, the symmetry  $\mathcal{K}$  by itself does not lead to an SPT phase since  $\mathbb{Z}_2$  has only one class of projective representation. However, when the particle conservation is taken into account, we have the constraint that the corresponding  $U$  matrices [see Eq. (10)] must form a projective representation of the symmetry group formed by  $\mathcal{R}(\varphi)$  and  $\mathcal{K}$ , which is  $U(1) \times \mathbb{Z}_2$ . This is analogous to the spin rotation symmetry of the Hamiltonians in Eqs. (13) and (15). It is known that it suffices to consider the subgroup  $\mathbb{Z}_2 \times \mathbb{Z}_2$  that permits two different phases [79]. Here, this subgroup corresponds to  $\mathcal{K}$  and  $\mathcal{R}(\pi)$  which is the particle-number conservation modulo 2. We have the constraint  $U_{\mathcal{K}}U_{\mathcal{R}(\pi)} = \pm U_{\mathcal{R}(\pi)}U_{\mathcal{K}}$  and thus, following Ref. [63], define the order parameter

$$\mathcal{O} = \frac{1}{\chi} \text{Tr}(U_{\mathcal{K}}U_{\mathcal{R}(\pi)}U_{\mathcal{K}}^\dagger U_{\mathcal{R}(\pi)}^\dagger), \quad (25)$$

where  $\chi$  is the bond dimension of the iMPS. A value  $\mathcal{O} = 1$  ( $\mathcal{O} = -1$ ) indicates trivial (non-trivial) SPT order.

Numerical calculations yield  $\mathcal{O} = 1$  in the large- $D$  phase and  $\mathcal{O} = -1$  in the Haldane phase [see Fig. 4]. The Haldane insulator in the extended anyon-Hubbard model is therefore indeed protected by the combination of the symmetries  $\mathcal{R}^z(\pi)$  and  $\mathcal{K}$ . This also holds in the bosonic limit  $\theta = 0$ . However, in that case, the weaker condition of symmetry under  $\mathcal{I}'$  defined in Eq. (22) is sufficient.

## 1.4 Response to external fields

We now turn our attention to dynamical quantities that describe the response of the system to external perturbations. Namely, we calculate the dynamic structure factor and the spin conductance for different types of spin chains. Symmetry-protected topological order can appear through edge excitations for open boundaries, but is otherwise not directly related to these quantities.

**Dynamic spin structure factor** The dynamic spin structure factor is the space and time Fourier transformed spin-spin correlation function. When the Hamiltonian is isotropic, it is sufficient to consider one component, e.g.,

$$S^{zz}(k, \omega) = \frac{1}{2\pi} \int dt \sum_r e^{i(kr - \omega t)} \langle \hat{S}_{j+r}^z(t) \hat{S}_j^z(0) \rangle. \quad (26)$$

The Lehmann representation of the dynamic spin structure factor at zero temperature is  $S^{zz}(k, \omega) = \sum_{n>0} |\langle \psi_n | \hat{S}^z(k) | \psi_0 \rangle|^2 \delta(\omega - E_n + E_0)$ , where  $|\psi_n\rangle$  are the energy eigenstates sorted by their eigenvalues  $E_n$ , and  $\hat{S}^z(k) = \frac{1}{\sqrt{N}} \sum_j e^{ikj} \hat{S}_j^z$  for a system with  $N$  sites and periodic boundary conditions. By determining  $S^{zz}(k, \omega)$ , one can therefore gain insight into the excitation spectrum. A numerical calculation of  $S^{zz}(k, \omega)$  is more involved than DMRG techniques that directly target the lowest-lying excited states. However,

$S^{zz}(k, \omega)$  contains additional information about higher excitations and the momentum dependence. It is also directly measurable in scattering experiments [40, 42].

There are several MPS-based techniques to calculate  $S^{zz}(k, \omega)$  [15, 18, 80]. We use a time-evolution scheme following Refs. [17, 81, 82]. First, the equilibrium state is approximated by an MPS  $|\psi_0\rangle$ . This is simply a DMRG ground-state calculation for zero temperature. For finite temperatures, the MPS is a purification of the density matrix obtained by imaginary time-evolution. The equilibrium state is then perturbed by applying the spin operator  $\hat{S}_j^z$  and subsequently evolved in time:  $|\psi(t)\rangle = e^{-it\hat{H}} \hat{S}_j^z |\psi_0\rangle$ . After each few time steps the matrix elements  $\langle \psi_0 | \hat{S}_{j+r}^z | \psi(t) \rangle$  with the starting state can be calculated to obtain the time-dependent spin-spin correlation function.

The resolution in energy space after the Fourier transformation is determined by the maximum simulated time, which is limited by the growth of the bond dimension required to accurately represent the state  $|\psi(t)\rangle$ . Different techniques have been devised to extend the accessible time scales [83]. A straightforward approach is to spread the time-evolution to two states [84],  $|\psi_A(t)\rangle = e^{-it\hat{H}} \hat{S}_j^z |\psi_0\rangle$  and  $|\psi_B(-t)\rangle = e^{it\hat{H}} \hat{S}_{j+r}^z |\psi_0\rangle$ , and calculate  $\langle \psi_B(-t) | \psi_A(t) \rangle$ . This is equal to  $\langle \psi_0 | \hat{S}_{j+r}^z | \psi(2t) \rangle$  and thus doubles the reached time for fixed maximum bond dimension, though the evaluation of the expectation value becomes slightly more expensive. A major drawback of this scheme is that both operators in the correlation function are fixed. To obtain the dynamic structure factor we need the correlation functions for a wide range of distances  $r$ , and naively each  $r$  value requires a separate simulation. We show in the following how this can be circumvented when infinite boundary conditions are used.

Let us assume we have a state of the form

$$|\psi_A\rangle = \sum_{\sigma} \dots \Lambda \Gamma^{\sigma_0} A^{[1]\sigma_1} A^{[2]\sigma_2} \dots A^{[N]\sigma_N} \Gamma^{\sigma_{N+1}} \Lambda \dots |\sigma\rangle, \quad (27)$$

which is referred to as an MPS with infinite boundary conditions [82, 85, 86]. Equation (27) describes an MPS in the thermodynamic limit whose tensors  $\Lambda$  and  $\Gamma$  are uniform, except for a finite window of  $N$  sites, where it has site-dependent tensors  $A$ . For the calculation of the dynamic structure factor, we set  $|\psi_A\rangle = e^{-it\hat{H}} \hat{S}_{N/2}^z |\psi_0\rangle$ . The idea behind the infinite boundary conditions in Eq. (27) is that it suffices to up-

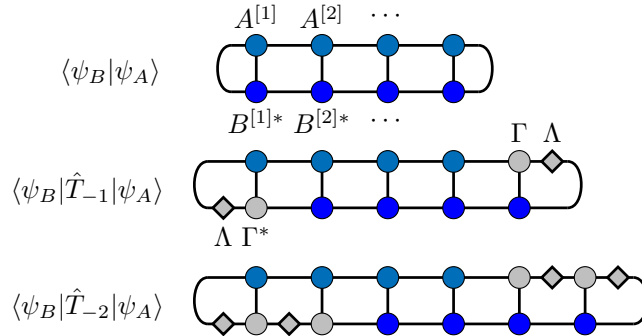


**Figure 5:** Graphical representation of Eq.(28). The blue symbols represent the tensors in the finite window that distinguishes between  $|\psi_A\rangle$  and  $|\psi_B\rangle$  while the gray tensors represent the iMPS unit cell.



date only the  $A$  tensors during the time-evolution as long as the perturbation has not reached the edges of the window. As described above, longer times are reached by introducing a second state  $|\psi_B\rangle = e^{it\hat{H}}\hat{S}_{N/2}^z|\psi_0\rangle$  which is evolved backwards in time. The state  $|\psi_B\rangle$  is also given as an MPS with infinite boundaries but it has different tensors inside the window, which we denote by  $B$  instead of  $A$ . We can determine the local correlation function by evaluating the overlap of the two states  $\langle\psi_B|\psi_A\rangle = \sum_{\sigma} \text{Tr}(A^{[1]\sigma_1}\dots A^{[N]\sigma_N} B^{[N]\sigma_N\dagger}\dots B^{[1]\sigma_1\dagger})$ . This is also true for open boundary conditions. An advantage of infinite boundary conditions is that the correlation function for other distances  $r$  is simply obtained by shifting the states against each other and calculating

$$\langle\psi_B|\hat{T}_{-r}|\psi_A\rangle = \sum_{\sigma} \text{Tr}\left(A^{[1]\sigma_{1-r}}\dots A^{[N]\sigma_{N-r}}\left(\prod_{d=1}^r \Gamma^{\sigma_{N-r+d}\Lambda}\right)B^{[N]\sigma_N\dagger}\dots B^{[1]\sigma_1\dagger}\left(\prod_{d=1}^r \Gamma^{\sigma_{1-d}\Lambda}\right)\right), \quad (28)$$

where the operator  $\hat{T}_{-r}$  translates the state by  $r$  sites to the left [see Fig. 27]. Therefore, the time-evolution needs to be carried out only for two states. When the unit cell consist of more than one site, the number of necessary states increases.

We apply this method to two different systems, the spin-1 XXZ chain with single-ion anisotropy (see Article VII), and a spin-2 chain that describes the small-hopping limit of a spinful Bose-Hubbard model (see Manuscript VIII). As an example, we show results for the spin-1 system in the Haldane phase at finite temperature, which was recently studied with a different MPS approach using open boundary conditions [39].

Since the Hamiltonian of the spin-1 XXZ in Eq. (13) chain does not have the full spin-rotation symmetry we also need

$$S^{+-}(k, \omega) = \frac{1}{4\pi} \int dt \sum_r e^{i(kr - \omega t)} \langle \hat{S}_{j+r}^+(t) \hat{S}_j^-(0) \rangle. \quad (29)$$

to completely specify the dynamic spin structure factor. The dynamic response function of the spin-1 Heisenberg chain ( $\Delta = 1, D = 0$ ) at zero-temperature consists mostly of a gapped magnon band with a minimum at momentum  $k = \pi$  [87]. Figure 6 displays our finite-temperature results for the Heisenberg chain with additional single-ion anisotropies  $D/J = -0.04$  and  $D/J = 0.2$ . The finite temperature leads to a significant broadening of the magnon line, while the effect of the single-ion anisotropy is negligible for the considered  $D$  values. In contrast to simulations with open boundaries, zero-energy edge excitations do not appear. However, there is an additional signature below the magnon excitations, which corresponds to intraband magnon scattering and thus only appears for finite temperatures [39]. We observe similar intraband scattering also in the large- $D$  and Néel phases, where the elementary excitations are different.

**Spin transport** In the study of the transport in spin chains, the focus has been primarily on the relation between integrability and the spin Drude weight  $D_S$  which is the weight of the zero-frequency contribution to the real part of the spin conductivity [88]. It distinguishes ballistic conductors with infinite conductivity ( $D_S > 0$ ) from normal

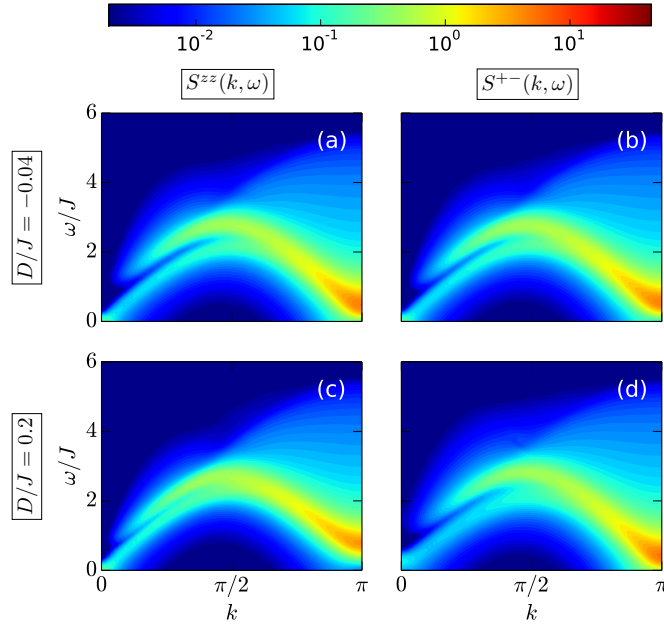


**Figure 6:** Dynamic spin structure factor of the spin-1 chain (13) in the Haldane phase for  $\Delta = 1$  and two values of the single-ion anisotropy  $D$ . The temperature is  $T/J = 0.4$ . A Gaussian broadening with  $\sigma/J = 0.1$  has been applied.

conductors and insulators ( $D_S = 0$ ). The most thoroughly investigated model in this context is probably the spin-1/2 XXZ chain with Hamiltonian

$$\hat{H}_{XXZ} = J \sum_j \left[ \frac{1}{2} (\hat{S}_j^+ \hat{S}_{j+1}^- + \hat{S}_j^- \hat{S}_{j+1}^+) + \Delta \hat{S}_j^z \hat{S}_{j+1}^z \right], \quad (30)$$

which is realized in several quasi one-dimensional materials [89]. It was shown for both zero and finite temperature that  $D_S > 0$  in the gapless phase for  $|\Delta| < 1$ , and  $D_S = 0$  in the gapped phase for  $|\Delta| > 1$  [90–96].

Less-studied than the properties of the bulk chain, is the effect of leads and interfaces on the spin transport. We use the time-evolution of MPS to investigate the spin transport in the spin-1/2 XXZ chain, but instead of a uniform spin chain, we consider a junction consisting of two semi-infinite metallic leads and a finite-length spin chain with  $N_S$  sites (see Article IX, Article X, and Technical Report XI). The main quantity of interest in this setup is the conductance  $G = I/V$  which describes the current  $I$  induced by a potential difference  $V$  between the leads. As shown in the following, the inclusion of metallic leads affects the spin transport significantly.

We summarize the setup used in Article IX, the one in Article X is only slightly different. The total Hamiltonian  $\hat{H} = \hat{H}_{XXZ} + \hat{H}_L + \hat{H}_c$  contains, in addition to the spin-chain Hamiltonian  $H_{XXZ}$ , a part for the leads

$$\hat{H}_L = -t \sum_{a=l,r} \sum_{\sigma=\uparrow,\downarrow} \sum_{j>1} [\hat{c}_{j\sigma a}^\dagger \hat{c}_{j+1,\sigma a} + \hat{c}_{j+1,\sigma a}^\dagger \hat{c}_{j\sigma a}] \quad (31)$$

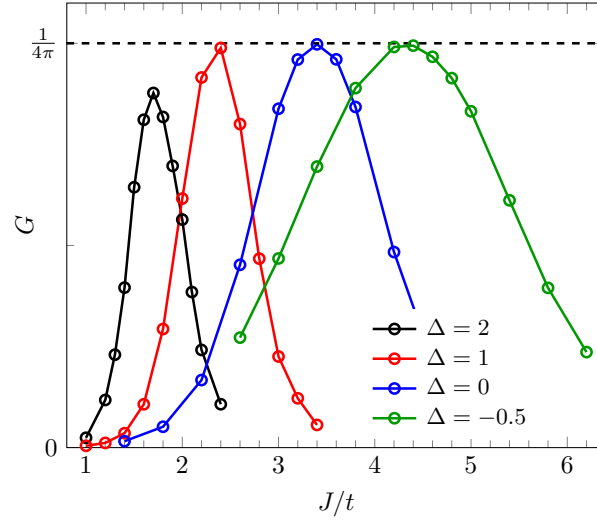


**Figure 7:** Spin conductance  $G$  for the junction described by Eq. (30-32) for spin voltage  $V/t = 0.2$  and  $N_S = 8$  sites in the spin chain.

that describes two chains of non-interacting spinful fermions, and a term

$$\begin{aligned} \hat{H}_c = & \frac{J'}{2} \left[ \hat{c}_{1\uparrow l}^\dagger \hat{c}_{1\downarrow l} \hat{S}_1^- + \hat{c}_{1\downarrow l}^\dagger \hat{c}_{1\uparrow l} \hat{S}_1^+ + \Delta (\hat{c}_{1\uparrow l}^\dagger \hat{c}_{1\uparrow l} - \hat{c}_{1\downarrow l}^\dagger \hat{c}_{1\downarrow l}) \hat{S}_1^z \right] \\ & + \frac{J'}{2} \left[ \hat{c}_{1\uparrow r}^\dagger \hat{c}_{1\downarrow r} \hat{S}_{N_S}^- + \hat{c}_{1\downarrow r}^\dagger \hat{c}_{1\uparrow r} \hat{S}_{N_S}^+ + \Delta (\hat{c}_{1\uparrow r}^\dagger \hat{c}_{1\uparrow r} - \hat{c}_{1\downarrow r}^\dagger \hat{c}_{1\downarrow r}) \hat{S}_{N_S}^z \right] \end{aligned} \quad (32)$$

that couples the first and last sites of the spin chain to the left and right leads, respectively. For simplicity, we assume that this exchange coupling has the same amplitude as that in the spin chain, i.e.,  $J' = J$ . To drive a spin current, an inhomogeneous magnetic field with a constant gradient in the spin chain is switched on, which adds the following term to the Hamiltonian:

$$\begin{aligned} \hat{H}_V = & \frac{V}{2} \sum_{j>1} (\hat{c}_{j\uparrow l}^\dagger \hat{c}_{j\uparrow l} - \hat{c}_{j\downarrow l}^\dagger \hat{c}_{j\downarrow l}) + \sum_j \left( -\frac{V}{N_S + 1} j + \frac{V}{2} \right) \hat{S}_j^z \\ & - \frac{V}{2} \sum_{j>1} (\hat{c}_{j\uparrow r}^\dagger \hat{c}_{j\uparrow r} - \hat{c}_{j\downarrow r}^\dagger \hat{c}_{j\downarrow r}). \end{aligned} \quad (33)$$

The spin current  $I$  flowing through the spin chain in the steady state defines the conductance  $G = I/V$ .

To determine the conductance  $G$  of the junction at zero temperature, we truncate the leads to a finite number of sites and approximate the ground state with the DMRG. The spin-voltage term  $\hat{H}_V$  is then turned on and the state evolved in time with a TEBD method. From the time-dependence of the current through the spin chain, the steady-state value is extrapolated to estimate the spin conductance  $G$  [97, 98].

Figure 7 shows the calculated spin conductance  $G$  at spin voltage  $V/t = 0.2$  as a function of  $J/t$  for multiple values of the anisotropy parameter  $\Delta$ . For each  $\Delta$ , the spin conductance  $G$  has a single peak. While the position and width of the peak depend on  $\Delta$ , its maximum is nearly the same for the parameters in the gapless phase. For

$\Delta = 2$ , in the gapped Néel phase, we find a smaller conductance maximum. It decreases further when the length  $N_S$  of the spin chain is increased (see Article IX). In all cases,  $G$  falls off to zero away from the peak.

The observed behavior for the spin conductance is quite similar to that of the charge conductance in inhomogeneous chains of interacting fermions. There, the transport behavior has been understood qualitatively using an inhomogeneous Luttinger liquid model with local backscattering terms. The backscattering terms cause the linear conductance to vanish at zero temperature [99, 100]. However, there can be parameters in the underlying lattice model for which they disappear in the effective Luttinger liquid Hamiltonian [101, 102]. At such conducting fixed points, the linear conductance is equal to that of the leads [103, 104]. In our system, the spin-conductance peaks seem to correspond to similar conducting fixed points that are reached by fine-tuning the model parameters near the interface. This is plausible, since both the gapless spin chain and the spin sector of the leads are separately described by Luttinger liquid Hamiltonians [105]. The maximum spin conductance in the gapless phase indeed agrees with the value  $G = 1/(4\pi)$  expected for non-interacting leads. Note that for a uniform spin chain without leads, the conductance would depend on  $\Delta$  [100].

Although we only carried out numerical simulations for zero temperature, the qualitative behavior of the spin conductance should also be valid for low finite temperatures. Based on the results for the Luttinger liquid model [100, 101], we expect that the width of the conductance peaks [cf. Fig. 7] increases with temperature, so that the effect of the interfaces becomes less severe. The conductance also depends on the value of the spin voltage  $V$ , with sharper peaks occurring for smaller  $V$ . Figure 7 shows results for an intermediate value  $V/t = 0.2$ . To instead obtain the linear conductance, one could numerically evaluate the corresponding Kubo formula with MPS techniques [106, 107].

Finally, let us comment on the effect of a homogeneous magnetic-field term  $h \sum_j \hat{S}_j^z$  already present in the equilibrium, which is discussed in Article X. For  $\Delta > 1$ , a large-enough  $h$  causes a phase transition from the gapped into a gapless phase. In this field-induced gapless phase, we also find a conducting fixed point that is independent of the precise value of  $h$ . There, the low- $V$  spin conductance  $G$  as a function of  $h$  exhibits roughly a step-like behavior when passing through the phase transition, which agrees with the naive expectation for the two phases based on their bulk transport behavior. Away from the conducting fixed point,  $G$  shows several peaks as  $h$  is varied through the points where level crossings in the spin chain occur. This is reminiscent of the Coulomb blockade effect for charge transport [108].

## 1.5 Conclusion

Using matrix-product-state (MPS) techniques, in particular the (infinite) density-matrix renormalization group and time-evolution methods, we studied various aspects of strongly correlated one-dimensional systems. The considered models are generalizations of Heisenberg spin chains and (Bose-)Hubbard models relevant for quasi one-dimensional magnets and optical lattices.

In the first part, we investigated ground-state phase diagrams regarding symmetry-protected topological (SPT) order and critical properties. We analyzed the effect of an explicit dimerization on the spin-1 XXZ chain with single-ion anisotropy and the related

extended Bose-Hubbard model at a density of one particle per site, which both exhibit an SPT Haldane phase. Since the dimerization conserves the protecting symmetries, it does not immediately destroy the SPT order. However, as the strength of the dimerization is increased, the extent of the Haldane phase becomes smaller. There is also a qualitative change regarding the type of phase transitions. For finite dimerization, part of the transition between the large- $D$  and the Néel phase (or the analogous phases in the extended Bose-Hubbard model) becomes first order and a point belonging to the tricritical Ising universality class appears. Such a tricritical Ising point was also found in the extended Fermi-Hubbard model with dimerization. The overall phase diagram of the fermionic model differs from that for bosons, however. In particular, it is known that there is no analogous Haldane phase but an SPT Peierls insulator. With this in mind, we investigated how the phase diagram of the extended Bose-Hubbard model changes when the particle statistics are smoothly deformed, i.e., we considered anyons instead of bosons. The resulting extended anyon-Hubbard model also has a Haldane insulator phase, which shrinks the further the model is perturbed from the bosonic limit. Since the change to anyons breaks the protecting symmetry of the bosonic Haldane phase, the existence of the anyonic Haldane phase is a non-trivial result. Using an MPS calculation of topological order parameters, we showed how the symmetry protection for anyons differs from that for bosons.

In the second part of this thesis, we studied dynamical properties of spin chain models, using the time-evolution of MPS. We considered two different physical quantities, the dynamic structure factor which describes neutron-scattering experiments in solids, and the spin conductance, which determines the spin current in response to a magnetic-field gradient. The dynamic structure factor was calculated for the spin-1 XXZ chain with on-site anisotropy, and for a more exotic spin-2 chain that emerges as an effective description of spinful bosons in optical lattices. While the dynamic structure factor for the spin-1 chain has been calculated before and its basic features are known, our results are new in that the simulations are directly in the thermodynamic limit and at finite temperature. We also introduced a more efficient scheme to evaluate the expectations values when using MPS in the thermodynamic limit. For the spin conductance, we focused on the spin-1/2 XXZ chain, which is an ideal spin conductor in the gapless regime. Instead of a homogeneous chain whose spin transport properties are already well-understood, we investigated a junction with metallic leads. The interface generally strongly reduces the conductance at zero temperature. For fine-tuned parameters, however, the linear conductance matches that of the leads. Overall, the behavior of the spin conductance resembles that previously observed for charge transport of inhomogeneous fermion chains which is explained in terms of a generic effective Luttinger liquid Hamiltonian.



## 2 Thesis articles

### Author Contribution

#### Article I:

“*Exotic criticality in the dimerized spin-1 XXZ chain with single-ion anisotropy*”

S. Ejima, T. Yamaguchi, F. H. L. Essler, F. Lange, Y. Ohta and H. Fehske , *SciPost Phys.* **5**, 059 (2018).

S. Ejima, F. H. L. Essler, H. Fehske and F. Lange outlined the scope and strategy of the calculation. The numerical calculation was performed by S. Ejima, F. Lange and T. Yamaguchi. F. H. L. Essler performed the field-theory calculation. S. Ejima, F. H. L. Essler and H. Fehske wrote the manuscript which was edited by all authors.

#### Article II:

“*Quantum phase transitions in the dimerized extended Bose-Hubbard model*”

K. Sugimoto, S. Ejima, F. Lange and H. Fehske , *Phys. Rev. A* **99**, 012122 (2019). Copyright (2019) by the American Physical Society.

S. Ejima, F. Lange and H. Fehske outlined the scope and strategy of the calculation. The calculation was performed by S. Ejima, F. Lange and K. Sugimoto. S. Ejima, F. Lange and K. Sugimoto wrote the manuscript which was edited by all authors.

#### Article III:

“*Ising tricriticality in the extended Hubbard model with bond dimerization*”

S. Ejima, F. H. L. Essler, F. Lange, and H. Fehske, *Phys. Rev. B* **93**, 235118 (2016). Copyright (2016) by the American Physical Society.

All authors outlined the scope and strategy of the calculation. The numerical calculation was performed by S. Ejima and F. Lange. F. H. L. Essler performed the field-theory calculation. S. Ejima and F. H. L. Essler wrote the manuscript which was edited by all authors.

#### Article IV:

“*Critical behavior of the extended Hubbard model with bond dimerization*”

S. Ejima , F. Lange, F. H. L. Essler , H. Fehske, *Physica B* **536**, 474 (2018). Copyright (2017) by Elsevier.

All authors outlined the scope and strategy of the calculation. The numerical calculation was performed by S. Ejima and F. Lange. F. H. L. Essler performed the field-theory calculation. S. Ejima and F. H. L. Essler wrote the manuscript which was edited by all authors.

**Article V:**

“*Anyonic Haldane Insulator in One Dimension*”

F. Lange, S. Ejima, and H. Fehske, *Phys. Rev. Lett.* **118**, 120401 (2017). Copyright (2017) by the American Physical Society.

All authors outlined the scope and strategy of the calculation. The calculation was performed by S. Ejima and F. Lange. All authors wrote the manuscript.

**Article VI:**

“*Strongly repulsive anyons in one dimension*”

F. Lange, S. Ejima, and H. Fehske, *Phys. Rev. A* **95**, 063621 (2017). Copyright (2017) by the American Physical Society.

All authors outlined the scope and strategy of the calculation. The calculation was performed by S. Ejima and F. Lange. All authors wrote the manuscript.

**Article VII:**

“*Finite-temperature dynamic structure factor of the spin-1 XXZ chain with single-ion anisotropy*”

F. Lange, S. Ejima, and H. Fehske, *Phys. Rev. B* **97**, 060403(R) (2018). Copyright (2018) by the American Physical Society.

All authors outlined the scope and strategy of the calculation. The calculation was performed by F. Lange. H. Fehske and F. Lange wrote the manuscript which was edited by all authors.

**Manuscript VIII:**

“*Dynamic response of spin-2 bosons in one-dimensional optical lattices*”

F. Lange, S. Ejima, and H. Fehske, submitted to *Phys. Rev. A*

All authors outlined the scope and strategy of the calculation. The calculation was performed by F. Lange. H. Fehske and F. Lange wrote the manuscript which was edited by all authors.

**Article IX:**

“*Spin transport through a spin-1/2 XXZ chain contacted to fermionic leads*”

F. Lange, S. Ejima, T. Shirakawa, S. Yunoki, and H. Fehske, *Phys. Rev. B* **97**, 245124 (2018). Copyright (2018) by the American Physical Society.

All authors outlined the scope and strategy of the calculation. The calculation was performed by F. Lange. H. Fehske and F. Lange wrote the manuscript which was edited by all authors.

**Article X:**

“*Driving XXZ spin chains: Magnetic-field and boundary effects*”

F. Lange, S. Ejima, and H. Fehske, *Europhys. Lett.* **125**, 17001 (2019). Copyright (2019) by the Europhysics Letters Association.

All authors outlined the scope and strategy of the calculation. The calculation was performed by F. Lange. H. Fehske and F. Lange wrote the manuscript which was edited by all authors.



---

**Technical Report XI:**

*“Block-Lanczos density-matrix renormalization-group study of the spin transport in Heisenberg chains coupled to leads”*

F. Lange, S. Ejima, and H. Fehske, to be submitted

All authors outlined the scope and strategy of the calculation. F. Lange performed the calculation and wrote the manuscript.

Confirmed:

---

(Prof. Dr. Holger Fehske)

Greifswald, August 1, 2019

---

(Florian Lange)

Greifswald, August 1, 2019



## Exotic criticality in the dimerized spin-1 $XXZ$ chain with single-ion anisotropy

Satoshi Ejima<sup>1\*</sup>, Tomoki Yamaguchi<sup>2</sup>, Fabian H. L. Essler<sup>3</sup>,  
Florian Lange<sup>1</sup>, Yukinori Ohta<sup>2</sup> and Holger Fehske<sup>1</sup>

<sup>1</sup> Institute of Physics, University Greifswald, 17489 Greifswald, Germany

<sup>2</sup> Department of Physics, Chiba University, Chiba 263-8522, Japan

<sup>3</sup> The Rudolf Peierls Centre for Theoretical Physics, Oxford University, Oxford OX1 3NP, UK

\* [ejima@physik.uni-greifswald.de](mailto:ejima@physik.uni-greifswald.de)

### Abstract

We consider the dimerized spin-1  $XXZ$  chain with single-ion anisotropy  $D$ . In absence of an explicit dimerization there are three phases: a large- $D$ , an antiferromagnetically ordered and a Haldane phase. This phase structure persists up to a critical dimerization, above which the Haldane phase disappears. We show that for weak dimerization the phases are separated by Gaussian and Ising quantum phase transitions. One of the Ising transitions terminates in a critical point in the universality class of the dilute Ising model. We comment on the relevance of our results to experiments on quasi-one-dimensional anisotropic spin-1 quantum magnets.



Copyright S. Ejima *et al.*

This work is licensed under the Creative Commons

[Attribution 4.0 International License](https://creativecommons.org/licenses/by/4.0/).

Published by the SciPost Foundation.

Received 05-10-2018

Accepted 03-12-2018

Published 07-12-2018

doi:[10.21468/SciPostPhys.5.6.059](https://doi.org/10.21468/SciPostPhys.5.6.059)



Check for updates

### Contents

<b>1</b>	<b>Introduction</b>	<b>2</b>
<b>2</b>	<b>Ground-state phase diagram</b>	<b>3</b>
<b>3</b>	<b>Field-theory approach</b>	<b>4</b>
3.1	Renormalization group analysis	5
3.2	Quantum phase transitions	6
3.2.1	$D$ -LD $\Leftrightarrow$ D-AFM phase transition line	6
3.2.2	D-H $\Leftrightarrow$ D-AFM phase transition line	7
3.2.3	D-H $\Leftrightarrow$ D-LD phase transition line	7
<b>4</b>	<b>DMRG analysis</b>	<b>8</b>
4.1	Quantum phase transitions	8
4.1.1	$D$ -LD $\Leftrightarrow$ D-AFM and D-H $\Leftrightarrow$ D-AFM Ising phase transition lines	8
4.1.2	D-H $\Leftrightarrow$ D-LD phase transition line	9
4.2	Topological order parameters	10
<b>5</b>	<b>Relevance to experiments</b>	<b>11</b>

<b>6 Summary and Conclusions</b>	<b>11</b>
<b>A Low-energy projections of operators</b>	<b>13</b>
A.1 Integrating out the bosonic degrees of freedom	13
A.2 Integrating out the fermionic degrees of freedom	14
<b>B Determination of phase boundaries</b>	<b>14</b>
<b>C Ground-state phase diagram for strong dimerization</b>	<b>15</b>
<b>References</b>	<b>16</b>

## 1 Introduction

It is well established that quantum effects in one-dimensional antiferromagnetic (AFM) spin systems lead to interesting physical phenomena. While a uniform Heisenberg chain is gapless for half-integer spins, an exotic ground state with a finite gap appears for integer spins [1]. For spins  $S = 1$ , this Haldane phase can be understood in the framework of the Affleck-Kennedy-Lieb-Tasaki model [2, 3], whose exact ground state can be constructed in terms of valence bonds, i.e., singlet pairs of  $S = 1/2$  spins. Meanwhile, the Haldane phase is recognized as a symmetry-protected topological (SPT) state [4, 5] and attracts continued attention from both theoretical and experimental points of view. For instance, the Haldane gap was confirmed experimentally in a compound with  $\text{Ni}^{2+}$  ions  $\text{Ni}(\text{C}_2\text{H}_8\text{N}_2)_2\text{NO}_2(\text{ClO}_4)$  [6, 7], in which a small value of the single-ion anisotropy  $D$  was reported [8]. A minimal model for the description of such anisotropic spin-1 chains is

$$\hat{H}_{XXZ,D} = J \sum_j (\hat{\mathbf{S}}_j \cdot \hat{\mathbf{S}}_{j+1})_\Delta + D \sum_j (\hat{S}_j^z)^2, \quad (1)$$

where  $(\hat{\mathbf{S}}_j \cdot \hat{\mathbf{S}}_{j+1})_\Delta = \hat{S}_j^x \hat{S}_{j+1}^x + \hat{S}_j^y \hat{S}_{j+1}^y + \Delta \hat{S}_j^z \hat{S}_{j+1}^z$ . Assuming a positive exchange parameter  $J > 0$  and  $\Delta > 0$ , the ground-state phase diagram exhibits three gapped phases [9]. At the isotropic point ( $D = 0$  and  $\Delta = 1$ ) the model is in a Haldane phase. A sufficiently strong single-ion anisotropy  $D/J$  induces a Gaussian quantum phase transition (QPT) with central charge  $c = 1$  to a topologically trivial large- $D$  (LD) phase. On the other hand, increasing  $\Delta$  for fixed  $D = 0$  from the isotropic point leads to a Ising QPT with  $c = 1/2$  to a long-range ordered AFM phase. At larger values of  $\Delta$  and  $D$  there is a first order transition between the LD and AFM phases.

A natural extension of the spin-1 XXZ chain (1) is the introduction of an explicit bond alternation

$$\hat{H} = \hat{H}_{XXZ,D} + J \sum_j \delta(-1)^j (\hat{\mathbf{S}}_j \cdot \hat{\mathbf{S}}_{j+1})_\Delta. \quad (2)$$

Interestingly this model realizes dimerized versions of the same three phases as the one described by Eq. (1), namely, dimerized Haldane (D-H), AFM (D-AFM) and LD (D-LD) phases. The case  $D = 0$  has been studied previously [10, 11] and it was found that the D-H to D-LD transition is again of the Gaussian type, but the *entire* D-AFM-phase boundary, including the transition to the D-LD phase, belongs to the Ising universality class. A key question is how the

criticality at the phase boundary changes, if both  $D$  and  $\delta$  are finite. Earlier studies of half-filled Hubbard-type models realizing SPT insulating and long-range ordered (charge-density-wave) phases [12–14] indicated a transition line that is separated into continuous Ising and first-order QPTs. The meeting point of these lines belongs to the tricritical Ising universality class with  $c = 7/10$ , which can be described by the second minimal model of conformal field theory [15, 16].

In this paper, we determine and analyze the ground-state phase diagram of the extended model (2) by means of field theory and matrix-product-state based density-matrix renormalization group (DMRG) [17, 18] techniques, focusing on the quantum criticality at the phase boundaries. By calculating the central charge  $c$ , we provide compelling evidence for the existence of a critical point in the tricritical Ising universality class. Field-theory predictions for the phases and the nature of the phase boundaries of the model (2) with both single-ion anisotropy  $D$  and bond alternation  $\delta$  are shown to be in excellent agreement with numerical simulations. Finally, we discuss the relevance of our results to experiments on dimerized spin-1 materials [19].

## 2 Ground-state phase diagram

Let us first describe the numerical method we have used to determine the phase boundaries of the model (2). By means of the infinite DMRG (iDMRG) [20] a characteristic correlation length  $\xi_\chi$  can be calculated. While this  $\xi_\chi$  is always finite for fixed bond dimension  $\chi$ , it strongly peaks at a critical point and therefore allows for an accurate determination of QPT points, see Appendix B. This approach was already applied to half-filled Hubbard-type models [12–14].

In order to identify the different continuous phase transitions occurring in the model (2), we calculate the corresponding central charges  $c$  via the entanglement entropy. For a critical system with  $L$  sites and periodic boundary conditions, the von Neumann entanglement entropy of a contiguous block of  $\ell$  sites with the rest of the system is  $S_L(\ell) = \frac{c}{3} \ln \left[ \frac{L}{\pi} \sin \left( \frac{\pi \ell}{L} \right) \right] + s_1$ , where  $s_1$  is a non-universal constant [21]. An accurate determination of the central charge is possible by using the relation [13, 22]

$$c^*(L) \equiv \frac{3[S_L(L/2-2) - S_L(L/2)]}{\ln\{\cos[\pi/(L/2)]\}}, \quad (3)$$

where in view of the explicit dimerization the doubled unit cell has been taken into account. Calculating the central charge numerically via Eq. (3), the universality classes of the QPT points are confirmed; this is demonstrated in Appendix B.

For iDMRG simulations typical truncation errors are  $10^{-12}$ , using bond dimensions  $\chi$  up to 1600. In the case of finite-system DMRG calculations with periodic boundary conditions, e.g., by estimating the central charge via Eq. (3), the maximal truncation errors are about  $10^{-9}$ , with  $\chi$  up to 6000.

Figure 1(a) shows the ground-state phase diagram of the model (2) for  $\delta = 0.1$ . For weak dimerization, the D-H phase survives between the D-LD and D-AFM phases. In contrast to the model without dimerization, however, the transition between the D-LD and D-AFM phases is continuous below a critical end point  $(\Delta_{ce}, D_{ce}/J) \simeq (3.90, 3.64)$ . Like the D-H  $\rightleftharpoons$  D-AFM line, this part of the transition belongs to the Ising universality class with central charge  $c = 1/2$ , except for the critical end point, which belongs to the universality class of the tricritical Ising model with  $c = 7/10$ . A tricritical Ising point at which the transition becomes first order is not observed in the dimerized model without single-ion anisotropy, simply because in this case the transition between the D-LD and D-AFM phases is always continuous. At the phase boundaries involving the Haldane phase, the universality classes are the same as in the non-

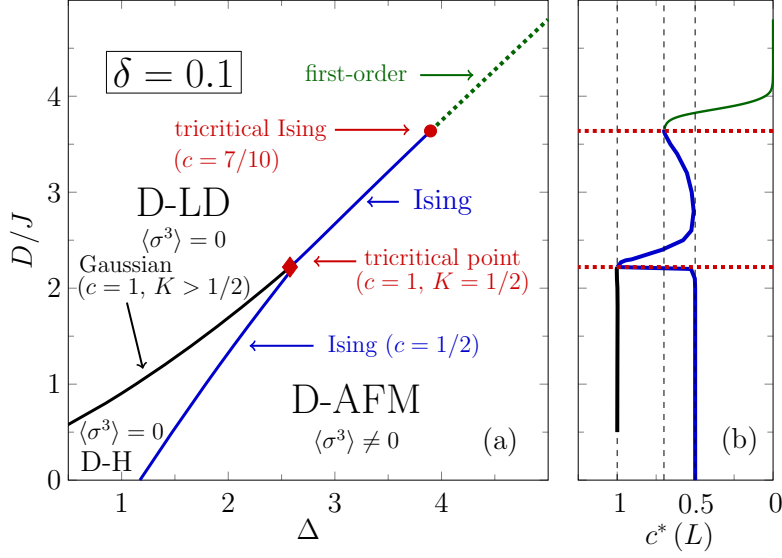


Figure 1: (a): Ground-state phase diagram of the model (2) for  $\delta = 0.1$ . The error bar of the tricritical (Ising) point is smaller than the symbol size.  $\langle \sigma^3 \rangle$  denotes the third Ising order parameter, determining the Ising QPT between the D-H or D-LD phase and the D-AFM phase. (b): Numerically obtained central charge  $c^*(L)$  on various phase transition lines from Eq. (3) with  $L = 128$  and periodic boundary conditions.

dimerized model. Now the tricritical point, where the Haldane phase vanishes, is at  $(\Delta_{\text{tr}}, D_{\text{tr}}/J) \simeq (2.58, 2.22)$ . For  $\delta \neq 0$ , the central charge at this point is  $c = 1$ .

In the following, combining field theory and DMRG, we discuss various QPTs, including the direct Ising transition from the D-LD to the D-AFM phase.

### 3 Field-theory approach

In order to obtain a field-theory description of the model in the vicinity of the various phase transition lines we consider the Hamiltonian

$$\hat{H}_{\text{FT}} = \hat{H} - J \sum_j (1 - \alpha) (\hat{\mathbf{S}}_j \cdot \hat{\mathbf{S}}_{j+1})_{\Delta'}^2, \quad (4)$$

which differs from Eq. (2) by an additional biquadratic exchange term. A field-theory description of the model (4) can be constructed in the vicinity of the Takhtajan-Babujian point [23, 24] ( $\alpha = 0$ ,  $\delta = 0$ ,  $D = 0$ ,  $\Delta = 1$  and  $\Delta' = 1$ ) following Ref. [25]. This leads to a Hamiltonian density of the form

$$\hat{\mathcal{H}} = \sum_{a=1}^3 \frac{i v_a}{2} [\hat{L}_a \partial_x \hat{L}_a - \hat{R}_a \partial_x \hat{R}_a] - i m_a \hat{R}_a \hat{L}_a + \sum_{a=1}^3 g_a \hat{j}^a \hat{j}^a + \lambda \hat{\sigma}^1 \hat{\sigma}^2 \hat{\sigma}^3, \quad (5)$$

where  $\hat{L}_a$  and  $\hat{R}_a$  are left and right moving Majorana fermions,  $\hat{\sigma}^a$  are three Ising order parameter fields and

$$\hat{j}^a = -(i/2) \epsilon^{abc} [\hat{L}_b \hat{L}_c + \hat{R}_b \hat{R}_c]. \quad (6)$$

The parameter  $\lambda$  in  $\hat{\mathcal{H}}$  is proportional to the dimerization  $\delta$  and by virtue of the U(1) symmetry of the microscopic Hamiltonian (4) we have  $v_1 = v_2$ ,  $m_1 = m_2 \equiv m$ , and  $g_1 = g_2 \equiv g$ .

The masses  $m$  and  $m_3$  are functions of  $D$  and  $\alpha$ . The functional form of this dependence is only known in the vicinity of the Takhtajan–Babujian point and in what follows we therefore take  $m_3$  and  $m$  as free parameters, which we adjust in order to recover the structure of the phase diagram obtained by DMRG. Our main working assumption is that the field theory (4) remains a good description of the low-energy degrees of freedom in the vicinity of the various phase transition lines in the microscopic model even far away in parameter space from the Takhtajan–Babujian point. We note that an alternative way of deriving a field theory proposed by Schulz [26] leads to equivalent results. A third approach would be to develop a field-theory description around the SU(3) symmetric point of the spin-1 chain [27–30], but we do not pursue this here. The relation between lattice spin operators and continuum fields is

$$\hat{S}_j^a \sim \hat{M}^a(x) + (-1)^j \hat{n}^a(x), \quad (7)$$

where  $x = ja_0$  ( $a_0$  is the lattice spacing). The smooth components of the spin operators are proportional to the currents  $\hat{M}^a(x) \propto \hat{J}^a(x)$ , while  $\hat{n}^a(x)$  are expressed in terms of Ising order and disorder operators as

$$\hat{n}^x(x) \propto \hat{\sigma}^1(x) \hat{\mu}^2(x) \hat{\mu}^3(x), \quad (8)$$

$$\hat{n}^y(x) \propto \hat{\mu}^1(x) \hat{\sigma}^2(x) \hat{\mu}^3(x), \quad (9)$$

$$\hat{n}^z(x) \propto \hat{\mu}^1(x) \hat{\mu}^2(x) \hat{\sigma}^3(x). \quad (10)$$

In order to facilitate comparisons between field-theory and iDMRG results for the lattice model it is useful to define lattice operators

$$\hat{m}_j^\alpha = \frac{\hat{S}_j^\alpha + \hat{S}_{j+1}^\alpha}{2}, \quad \hat{n}_j^\alpha = (-1)^j \frac{\hat{S}_j^\alpha - \hat{S}_{j+1}^\alpha}{2}. \quad (11)$$

At long distances we have

$$\hat{m}_j^\alpha \approx \hat{M}^\alpha(x), \quad \hat{n}_j^\alpha \approx \hat{n}^\alpha(x). \quad (12)$$

It is convenient to use the U(1) symmetry to bosonize

$$\hat{L}_1 + i\hat{L}_2 \sim \frac{1}{\sqrt{\pi a_0}} e^{-i\sqrt{4\pi}\hat{\varphi}_L}, \quad \hat{R}_1 + i\hat{R}_2 \sim \frac{1}{\sqrt{\pi a_0}} e^{i\sqrt{4\pi}\hat{\varphi}_R}. \quad (13)$$

In terms of the corresponding canonical Bose field  $\hat{\Phi} = \hat{\varphi}_L + \hat{\varphi}_R$  and the dual field  $\hat{\Theta} = \hat{\varphi}_R - \hat{\varphi}_L$  the field theory (5) reads:

$$\hat{\mathcal{H}} = \hat{\mathcal{H}}_3 + \hat{\mathcal{H}}_B + \hat{\mathcal{H}}_{\text{int}}, \quad (14)$$

$$\hat{\mathcal{H}}_3 = \frac{iv_3}{2} [\hat{L}_3 \partial_x \hat{L}_3 - \hat{R}_3 \partial_x \hat{R}_3] - im_3 \hat{R}_3 \hat{L}_3, \quad (15)$$

$$\hat{\mathcal{H}}_B = \frac{v}{2} \left[ \frac{1}{K} (\partial_x \hat{\Phi})^2 + K (\partial_x \hat{\Theta})^2 \right] - \frac{m}{\pi a_0} \cos \sqrt{4\pi} \hat{\Phi}, \quad (16)$$

$$\hat{\mathcal{H}}_{\text{int}} = \frac{2ig}{\pi a_0} \cos(\sqrt{4\pi} \hat{\Phi}) \hat{L}_3 \hat{R}_3 + \lambda' \sin(\sqrt{\pi} \hat{\Phi}) \hat{\sigma}^3, \quad (17)$$

where  $K$  is the Luttinger liquid (LL) parameter.

### 3.1 Renormalization group analysis

The most relevant perturbation is always the dimerization, and concomitantly at weak coupling the  $\lambda'$  term reaches strong coupling first under the renormalization group (RG) flow. This results in a non-zero dimerization

$$\langle \hat{d} \rangle \equiv \left\langle \frac{1}{L} \sum_j \hat{D}_j \right\rangle \neq 0, \quad \hat{D}_j = (-1)^j \hat{S}_j \cdot \hat{S}_{j+1}. \quad (18)$$

For later convenience we define a lattice version of the normal-ordered dimerization operator

$$\hat{d}_j = \frac{\hat{D}_j + \hat{D}_{j+1}}{2} - \langle \hat{d} \rangle. \quad (19)$$

To see what happens after the dimerization perturbation has reached strong coupling we consider the next most relevant operators, which are the Majorana mass term and the cos-term in the bosonic sector. Assuming that we have  $m > 0$ , what happens then depends on the sign of the Majorana mass term  $m_3$ . If it is positive the third Ising model is in its disordered phase  $\langle \hat{\sigma}^3(x) \rangle = 0$ , while  $m_3 < 0$  implies that  $\langle \hat{\sigma}^3(x) \rangle \neq 0$ . In the latter case the strong coupling RG fixed point is amenable to a mean-field analysis. The term  $\hat{\mathcal{H}}_{\text{int}}$  coupling the bosonic and fermionic sectors can be decoupled, e.g.

$$\hat{\sigma}^3(x) \sin(\sqrt{\pi}\Phi(x)) \rightarrow \langle \hat{\sigma}^3(x) \rangle \sin(\sqrt{\pi}\hat{\Phi}(x)) + \hat{\sigma}^3(x) \langle \sin(\sqrt{\pi}\hat{\Phi}(x)) \rangle. \quad (20)$$

This leads to a mean-field description in terms of an Ising model in a longitudinal field and a double sine-Gordon model [31, 32]

$$\begin{aligned} \hat{\mathcal{H}}_{\text{MF}} = & \frac{iv_3}{2} [\hat{L}_3 \partial_x \hat{L}_3 - \hat{R}_3 \partial_x \hat{R}_3] - i\tilde{m}_3 \hat{R}_3 \hat{L}_3 + h\hat{\sigma}^3 + \frac{v}{2} \left[ \frac{1}{K} (\partial_x \hat{\Phi})^2 + K (\partial_x \hat{\Theta})^2 \right] \\ & - \frac{\tilde{m}}{\pi a_0} \cos(\sqrt{4\pi}\hat{\Phi}) + \tilde{\lambda} \sin(\sqrt{\pi}\hat{\Phi}), \end{aligned} \quad (21)$$

where

$$\begin{aligned} \tilde{\lambda} &= \lambda' \langle \hat{\sigma}^3 \rangle, \quad h = \lambda' \langle \cos(\sqrt{4\pi}\hat{\Phi}) \rangle, \\ \tilde{m} &= m + 2ig \langle \hat{R}_3 \hat{L}_3 \rangle, \quad \tilde{m}_3 = m_3 + \frac{2g}{\pi a_0} \langle \cos(\sqrt{4\pi}\hat{\Phi}) \rangle. \end{aligned} \quad (22)$$

The classical ground state of the double sine-Gordon model is obtained by solving

$$\frac{2\tilde{m}}{\pi} \sin(\sqrt{4\pi}\hat{\Phi}_c) + \tilde{\lambda} \cos(\sqrt{\pi}\hat{\Phi}_c) = 0. \quad (23)$$

Importantly, this tells us that for  $\tilde{m} > 0$  we have

$$\langle \cos(\sqrt{\pi}\hat{\Phi}(x)) \rangle \neq 0, \quad (24)$$

which in turn implies that

$$\langle \hat{n}^z(x) \rangle \propto \langle \hat{\sigma}^3(x) \cos(\sqrt{\pi}\hat{\Phi}) \rangle \neq 0. \quad (25)$$

Hence the strong coupling RG fixed point describes a phase where antiferromagnetic order coexists with dimerization. This is the D-AFM phase identified above by the DMRG.

In the other phases the RG fixed points again occur at strong coupling but cannot be analyzed in terms of a simple mean-field argument. However, the field theory nevertheless allows for a description of the various transition lines as shown in what follows.

## 3.2 Quantum phase transitions

### 3.2.1 D-LD $\Leftrightarrow$ D-AFM phase transition line

This corresponds to the situation where the bosonic sector remains gapped, while the third Ising model undergoes a transition between a disordered phase  $\langle \hat{\sigma}^3 \rangle = 0$  on the D-LD side and an ordered phase  $\langle \hat{\sigma}^3 \rangle \neq 0$  on the D-AFM side of the phase diagram. As a result the D-LD  $\Leftrightarrow$  D-AFM phase transition is in the universality class of the two-dimensional Ising model.



In the vicinity of the transition we may project onto the low-energy Ising degrees of freedom following e.g. Ref. [33]. Details are given in Appendix A. This yields

$$\hat{m}_j^z \Big|_{\text{low}} = A \partial_x \hat{\sigma}^3(x) + \dots, \quad (26)$$

$$\hat{n}_j^z \Big|_{\text{low}} = B \hat{\sigma}^3(x) + \dots, \quad (27)$$

$$\hat{d}_j \Big|_{\text{low}} = iC \hat{R}_3(x) \hat{L}_3(x) + \dots. \quad (28)$$

Along the phase transition line we thus have

$$\langle \hat{n}_j^z \hat{n}_{j+\ell}^z \rangle = B^2 \ell^{-1/4} + \dots, \quad (29)$$

$$\langle \hat{m}_j^z \hat{n}_{j+\ell}^z \rangle = -\frac{AB}{4} \ell^{-5/4} + \dots, \quad (30)$$

$$\langle \hat{m}_j^z \hat{m}_{j+\ell}^z \rangle = \frac{5A^2}{16} \ell^{-9/4} + \dots, \quad (31)$$

and

$$\langle \hat{d}_j \hat{d}_{j+\ell} \rangle = C^2 \ell^{-2} + \dots. \quad (32)$$

The predictions (29)–(32) are compared to iDMRG simulations below.

### 3.2.2 D-H $\Leftrightarrow$ D-AFM phase transition line

The D-AFM to D-H transition is described by the same scenario as discussed above, since it also belongs to the Ising universality class with  $c = 1/2$ . Accordingly, Eqs. (29)–(32) are valid on this transition line as well.

### 3.2.3 D-H $\Leftrightarrow$ D-LD phase transition line

As we cross from the D-AFM into the D-H phase at fixed  $\Delta$  by increasing  $D$  the (effective) Majorana mass  $m_3$  increases. Assuming that this relation continues to hold, the characteristic energy scale in the Majorana sector can eventually become large compared to that of the bosonic sector and it is then justified to integrate out the Majorana sector. This leads to an effective low-energy description in terms of a sine-Gordon model

$$\hat{\mathcal{H}}_{\text{low}} = \frac{v}{2} \left[ \frac{1}{K} (\partial_x \hat{\Phi})^2 + K (\partial_x \hat{\Theta})^2 \right] - \frac{m^*}{\pi a_0} \cos(\sqrt{4\pi} \hat{\Phi}). \quad (33)$$

The main effect of integrating out the Majorana sector is the renormalization of the sine-Gordon coupling. Importantly,  $m^*$  can vanish for particular values of  $D$ , which corresponds to a phase transition line described by a LL characterized by the LL parameter  $K$ . The low-energy projections of the lattice spin operators along this line are

$$\hat{d}_j \Big|_{\text{low}} = A_D \cos(\sqrt{4\pi} \hat{\Phi}(x)) + \dots, \quad (34)$$

$$\hat{n}_j^z \Big|_{\text{low}} = A_z \sin(\sqrt{4\pi} \hat{\Phi}(x)) + \dots, \quad (35)$$

$$\hat{n}_j^x \Big|_{\text{low}} = A_x \cos(\sqrt{\pi} \hat{\Theta}(x)) + \dots, \quad (36)$$

$$(S_j^+)^2 \Big|_{\text{low}} = A_2 e^{i\sqrt{4\pi} \hat{\Theta}(x)} + \dots, \quad (37)$$

$$\hat{m}_j^x \Big|_{\text{low}} = \frac{a_0}{\sqrt{\pi}} \partial_x \hat{\Phi}(x) + \dots. \quad (38)$$

This gives the following field-theory predictions for power-law decays of two-point functions

$$\langle \hat{n}_j^z \hat{n}_{j+\ell}^z \rangle = \frac{A_z^2}{2} \ell^{-2K} + \dots, \quad (39)$$

$$\langle \hat{n}_j^\alpha \hat{n}_{j+\ell}^\alpha \rangle = \frac{A_x^2}{2} \ell^{-1/2K} + \dots, \quad \alpha = x, y, \quad (40)$$

$$\langle (\hat{S}_j^+)^2 (\hat{S}_{j+\ell}^-)^2 \rangle = A_2^2 \ell^{-2/K} + \dots, \quad (41)$$

$$\langle \hat{m}_j^z \hat{m}_{j+\ell}^z \rangle = \frac{K}{2\pi^2} \ell^{-2} + \dots, \quad (42)$$

$$\langle \hat{d}_j \hat{d}_{j+\ell} \rangle = \frac{A_D^2}{2} \ell^{-2K} + \dots \quad (43)$$

## 4 DMRG analysis

In this section, we examine various two-point correlation functions of the lattice Hamiltonian (2) using iDMRG in order to prove the field-theory predictions described in the last section. Then, the topological properties of each phase are discussed by simulating topological order parameters.

### 4.1 Quantum phase transitions

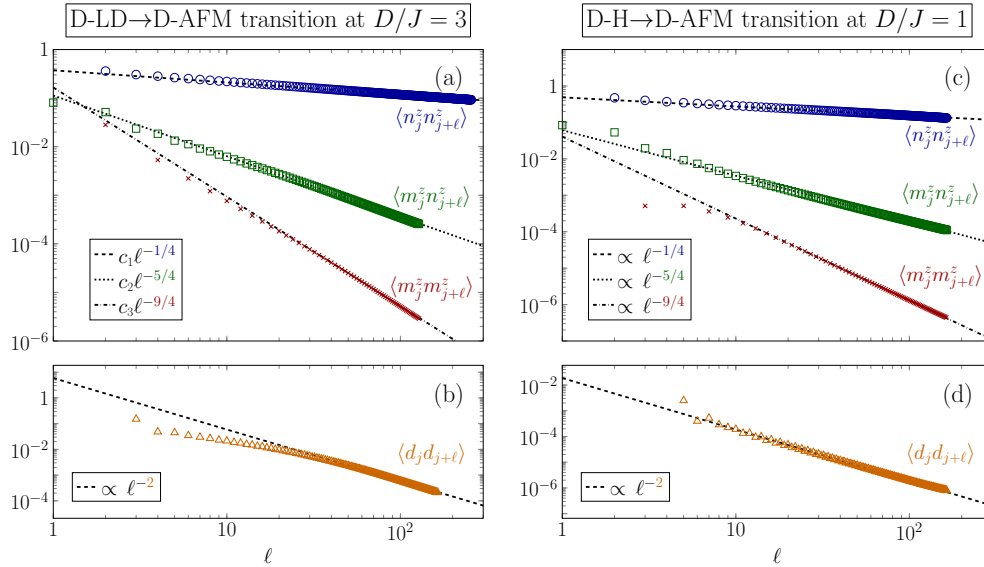


Figure 2: The connected longitudinal spin-spin (upper panels) and dimerization (lower panels) two-point functions at the Ising transition point for fixed  $D/J = 3$  (left panels) and  $D/J = 1$  (right panels) with  $\delta = 0.1$ , obtained by iDMRG with  $\chi = 1600$ . Correlation functions (symbols) show a power-law decay in accordance with the field-theory predictions Eqs. (29)–(32) [lines].

#### 4.1.1 D-LD $\rightleftharpoons$ D-AFM and D-H $\rightleftharpoons$ D-AFM Ising phase transition lines

For fixed  $D/J = 3$  and  $\delta = 0.1$  the Ising QPT occurs at  $\Delta_c \simeq 3.303$  between D-LD and D-AFM phases as extracted from correlation length  $\xi_\chi$ . At this transition point various two-point

functions can be computed by iDMRG. Here,  $\chi = 1600$ . As shown in Fig. 2(a) field-theory predictions for diverse two-point functions of  $z$ -component spin operators (29)–(31) can be proved by iDMRG. Figure 2(b) demonstrates that also the dimer-dimer correlation function is in agreement with the power-law behavior according to Eq. (32) for large distances  $\ell \gg 1$ .

The relations between the coefficients in Eqs. (29)–(32) can be verified by fitting the iDMRG data to the field-theory predictions. For instance, in the case of the D-LD $\rightleftharpoons$ D-AFM transition at  $D/J = 3$  [Fig. 2(a)], we obtain  $c_1 \simeq 0.381$  ( $B \simeq 0.617$ ) and  $c_3 \simeq 0.158$  ( $A \simeq 0.711$ ), i.e.,  $AB/4 \simeq 0.110$ , which is in good agreement with  $c_2 \simeq 0.114$  from Eq. (30).

Along the Ising critical line separating the D-H and D-AFM phases the long-distance behavior of these correlation functions determined by iDMRG is again in excellent agreement with field-theory predictions, cf. Eqs. (29)–(32). A representative example is shown in Figs. 2(c) and (d) for  $D/J = 1$  and  $\Delta_c \simeq 1.789$ .

#### 4.1.2 D-H $\rightleftharpoons$ D-LD phase transition line

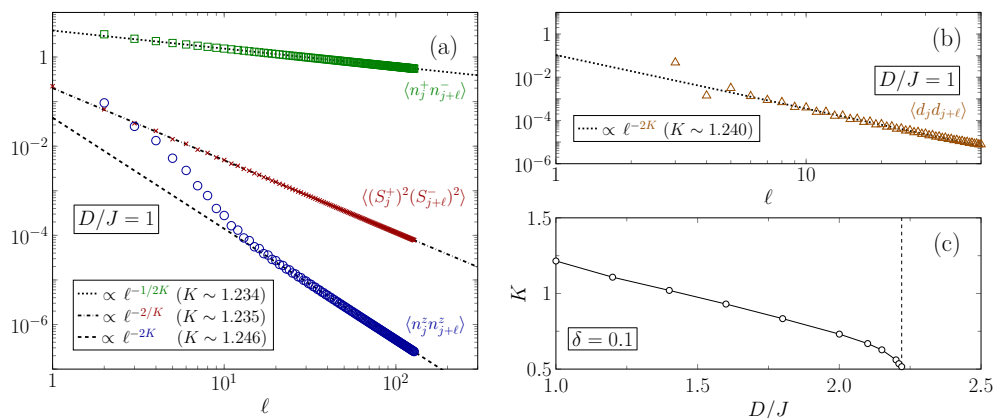


Figure 3: Spin-spin (a) and dimer-dimer (b) correlation functions at the  $c = 1$  transition for  $D/J = 1$  and  $\delta = 0.1$  computed by iDMRG with bond dimension  $\chi = 1600$ . The extracted values of the LL parameter  $K$  are in good agreement. (c) Extrapolated values of LL parameters  $K$  via  $S(q)$  of Eq. (44) on the  $c = 1$  transition line for  $\delta = 0.1$ , obtained by DMRG with up to  $L = 1024$  sites and open boundary conditions.

Along the line of Gaussian QPTs separating the D-H and D-LD phases the exponents characterizing the long-distance behavior of correlation functions depends on the LL parameter  $K$  as described in Eqs. (39)–(41) and (43). In order to facilitate a comparison to the field-theory results we therefore require the LL parameter  $K$ . For fixed  $D/J = 1$  the Gaussian transition occurs at  $\Delta_c \simeq 1.135$ . In Figs. 3(a) and (b) we show numerical results of correlation functions obtained by iDMRG. The values of LL parameters extracted from the fits to Eqs. (39)–(41) and (43) show reasonable agreement with each other.

These values can also be extracted from the long-distance behavior of the smooth part of the spin-spin correlation function (42), that is, the LL parameter determines the amplitude of the correlation function but not the exponent. We calculate the longitudinal spin correlation function and isolate the smooth component from a Fourier transformed structure factor

$$S(q) = \frac{1}{L} \sum_{j\ell} e^{iq(j-\ell)} \left( \langle \hat{S}_j^z \hat{S}_\ell^z \rangle - \langle \hat{S}_j^z \rangle \langle \hat{S}_\ell^z \rangle \right) \quad (44)$$

for  $q \approx 0$ , where  $q = 2\pi/L$ . The LL parameter is determined as  $K = \lim_{q \rightarrow 0} \pi S(q)/q$  [34]. Figure 3(c) shows the results for the Luttinger parameter  $K$  on the  $c = 1$  line for  $\delta = 0.1$ .

At  $\Delta = 1$  we have  $K = 1.215$ , in reasonable agreement with the values obtained from the exponents of correlation functions in Figs. 3(a) and (b). Following the Gaussian transition line by increasing  $\Delta$  and  $D/J$  the Luttinger parameter decreases and takes the value  $K \simeq 1/2$  at the point when the Gaussian line merges with the line of Ising QPTs.

## 4.2 Topological order parameters

Let us now explore the topological properties of the phases of the model (2). Following Vidal [35], we use the infinite matrix-product-state representation formed by  $\chi \times \chi$  matrices  $\Gamma_\sigma$  and a positive real, diagonal matrix  $\Lambda$ :

$$|\psi\rangle = \sum_{\dots\sigma_j, \sigma_{j+1}\dots} \dots \Lambda \Gamma_{\sigma_j} \Lambda \Gamma_{\sigma_{j+1}} \dots |\dots\sigma_j, \sigma_{j+1}, \dots\rangle, \quad (45)$$

where the index  $\sigma$  labels the basis states of the local Hilbert spaces. The  $\Gamma_\sigma$  and  $\Lambda$  are assumed to be in the canonical form:

$$\sum_{\sigma} \Gamma_{\sigma} \Lambda^2 \Gamma_{\sigma}^{\dagger} = \mathbb{1} = \sum_{\sigma} \Gamma_{\sigma}^{\dagger} \Lambda^2 \Gamma_{\sigma}. \quad (46)$$

If  $|\psi\rangle$  is invariant under an internal symmetry represented by a unitary matrix  $\Sigma_{\sigma\sigma'}$ , then the transformed  $\Gamma_\sigma$  matrices satisfy [5, 36]

$$\sum_{\sigma'} \Sigma_{\sigma\sigma'} \Gamma_{\sigma'} = e^{i\theta} U^{\dagger} \Gamma_{\sigma} U. \quad (47)$$

Here  $U$  is a unitary matrix that commutes with  $\Lambda$ , and  $e^{i\theta}$  is a phase factor. In the case of time reversal symmetry (inversion symmetry),  $\Gamma_\sigma$  on the left-hand side is replaced by its complex conjugate  $\Gamma_\sigma^{\dagger}$  (its transpose  $\Gamma_\sigma^T$ ). Exploiting the properties of the matrices  $U$  each SPT phase can be classified [5]: In the case of time reversal (inverse) symmetry the matrices satisfy  $U_T U_T^* = \pm \mathbb{1}$  ( $U_I U_I^* = \pm \mathbb{1}$ ), and the sign can be used to distinguish different SPT phases. In presence of a  $\mathbb{Z}_2 \times \mathbb{Z}_2$  symmetry the order parameter is given by

$$O_{\mathbb{Z}_2 \times \mathbb{Z}_2} = \frac{1}{\chi} \text{Tr} (U_x U_z U_x^{\dagger} U_z^{\dagger}), \quad (48)$$

where we use the symmetry operations  $\hat{R}^x = \exp(i\pi \sum_j \hat{S}_j^x)$  and  $\hat{R}^z = \exp(i\pi \sum_j \hat{S}_j^z)$  to calculate  $U_x$  and  $U_z$ .

In the presence of dimerization the unit cell consists of two sites, which we have to block together in order to apply the above description. For the model (2), blocking sites across weak bonds gives the same values of the order parameters as blocking across strong bonds. Figure 4 shows the iDMRG results for the order parameters in case of inverse and  $\mathbb{Z}_2 \times \mathbb{Z}_2$  symmetries. If  $U_x$  and  $U_z$  commute ( $O_{\mathbb{Z}_2 \times \mathbb{Z}_2} = 1$ ), the system is in a trivial phase, i.e., a site-factorizable LD state, whereas if they anticommute ( $O_{\mathbb{Z}_2 \times \mathbb{Z}_2} = -1$ ), the system realizes a non-trivial Haldane state. If the symmetry is broken, we set  $O_{\mathbb{Z}_2 \times \mathbb{Z}_2} = 0$ . Obviously, the order parameter  $O_{\mathbb{Z}_2 \times \mathbb{Z}_2}$  changes its sign only if a phase transition occurs between D-LD and D-H phases.  $O_I$  behaves similarly to  $O_{\mathbb{Z}_2 \times \mathbb{Z}_2}$ , i.e.,  $O_I = \pm 1$  for the two symmetric phases, and  $O_I = 0$  in the D-AFM phase.

To summarize this subsection, dimerization does not affect the topological properties of the system (2), so that the D-H (D-LD) phase remains a non-trivial (trivial) SPT phase as in the system without dimerization (1).

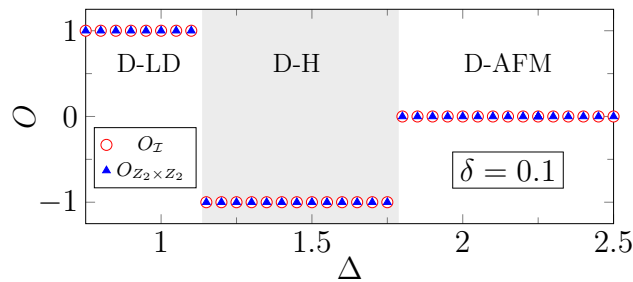


Figure 4: Topological order parameters for inversion symmetry  $O_I$  and  $\mathbb{Z}_2 \times \mathbb{Z}_2$  spin rotation symmetry  $O_{\mathbb{Z}_2 \times \mathbb{Z}_2}$  at  $D/J = 1$  and  $\delta = 0.1$ .

## 5 Relevance to experiments

Let us finally relate our findings with experimental results. There are several realizations of spin-1 bond-alternating chains, such as  $\text{Ni}(\text{C}_9\text{H}_24\text{N}_4)(\text{NO}_2)\text{ClO}_4$  [37, 38] and  $[\text{Ni}(333\text{-tet})(\mu\text{-N}_3)_n](\text{ClO}_4)_n$  [39–41]. Most remarkably, in the latter material a logarithmic decrease of the susceptibility was observed at low temperature, indicating a vanishing excitation gap [19]. Comparing quantum Monte-Carlo simulations with experimental data suggested that the material is described by a Hamiltonian of the form (2) with  $\delta = 0.25$ ,  $\Delta = 1$  and  $D/J = 0$ . Totsuka *et al.* [42] determined the critical point for  $D = 0$  numerically and obtained  $\delta_c = 0.25 \pm 0.01$  and  $c = 1$ , while results by Kitazawa and Nomura [11] suggested that  $\delta_c = 0.2598$ . Importantly these parameter sets are close to the location of the point where the Gaussian and Ising phase transitions merge [10, 11].

In the following, we therefore determine the ground-state phase diagram of the model (2) for  $\delta = 0.25$  and reexamine the magnetic susceptibility of the above mentioned nickel compound using the infinite time-evolving block decimation (iTEBD) [35]. Figure 5(a) displays the corresponding phase diagram of the model (2). Although the extent of the Haldane phase is significantly reduced, the Gaussian and Ising transition lines can still be detected numerically. As shown in Fig. 5(b) the experimental data of the magnetic susceptibility for  $[\text{Ni}(333\text{-tet})(\mu\text{-N}_3)_n](\text{ClO}_4)_n$  can be fitted most successfully for  $\Delta = 1$  and  $D/J = 0.02$ , taking the reported small single-ion anisotropy  $D/J < 0.1$  [19] into account. On the other hand, the numerical data at the Gaussian transition point for fixed  $\Delta = 1$  deviates from experimental ones in the lower-temperature regime. Thus, this nickel compound may be even closer to the Ising transition line than to the  $c=1$  transition line considered so far. It would be interesting to investigate signatures of the Ising QPT experimentally, e.g., by inelastic neutron scattering, where the corresponding dynamical structure factor can be calculated numerically, see Ref. [43].

## 6 Summary and Conclusions

In this work we investigated the ground-state phase diagram and quantum criticality of the dimerized spin-1  $XXZ$  chain with single-ion anisotropy  $D$ , employing a combination of analytical and numerical techniques. For weak dimerization ( $\delta \lesssim 0.26$ ) and single-ion anisotropy, the symmetry-protected topological Haldane phase survives and the transition between the D-LD and D-AFM phases, which is always of first order in the absence of dimerization, becomes partially continuous. The continuous section of the transition line belongs to the Ising universality class with central charge  $c = 1/2$ . With increasing the magnitude of  $D$ , this Ising line terminates at a tricritical Ising point with  $c = 7/10$ , above which the phase transition becomes first order. A comprehensive description of the phases and phase boundaries can be

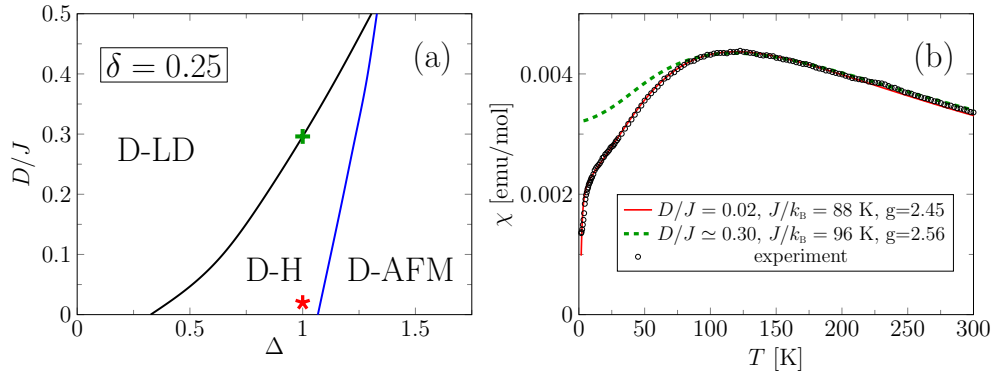


Figure 5: (a) Ground-state phase diagram of the model (2) for  $\delta = 0.25$ . The red star denotes the parameter set corresponding to the Ni compound  $[\text{Ni}(333\text{-tet})(\mu\text{-N}_3)_n](\text{ClO}_4)_n$ , and the green cross gives the Gaussian transition point  $[(D/J)_c \simeq 0.296]$  for fixed  $\Delta = 1$ . (b) Temperature dependence of the magnetic susceptibility of the powdered sample for  $[\text{Ni}(333\text{-tet})(\mu\text{-N}_3)_n](\text{ClO}_4)_n$  (circles) taken from Ref. [19]. The red solid line is the iTEBD data for  $\Delta = 1$ ,  $D/J = 0.02$  and  $\delta = 0.25$  with  $J/k_B = 88$  K and  $g = 2.45$ . For comparison, we also show the iTEBD result at the Gaussian transition for fixed  $\Delta = 1$  (green dashed line).

achieved by a bosonization-based field theory including three Majorana fermions. The field-theory predictions for various correlation functions have been confirmed by numerical iDMRG calculations.

Finally, we have revisited the experimental results for the Ni compound  $[\text{Ni}(333\text{-tet})(\mu\text{-N}_3)_n](\text{ClO}_4)_n$  showing gapless behavior and have demonstrated that the corresponding parameter set might be not only in the vicinity of the Gaussian transition line but also very close to the Ising transition line. Further experimental research for this material, such as neutron scattering, would be desirable.

## Acknowledgements

We thank M. Hagiwara for useful discussions and providing us with their experimental data. The iDMRG simulations were performed using the ITensor library [44].

**Funding information** This work was supported by the Deutsche Forschungsgemeinschaft (Germany) under Grant No. FE 398/8-1 (FL), by the EPSRC under Grant No. EP/N01930X (FHLE) and the National Science Foundation under Grant No. NSF PHY-1748958 (FHLE). FHLE is grateful to the Erwin Schrödinger International Institute for Mathematics and Physics for hospitality and support during the programme on *Quantum Paths*. TY acknowledges support by a Chiba University SEEDS Fund and YO acknowledges support by a Grant-in-Aid for Scientific Research (Grant No. 17K05530) from JSPS of Japan. HF is grateful to the Los Alamos National Laboratory for hospitality and support.

## A Low-energy projections of operators

Let us denote the Euclidean action corresponding to the Hamiltonian density (14) by

$$S = S_3 + S_B + S_{\text{int}}, \quad (49)$$

where  $S_3$  and  $S_B$  involve only Ising and bosonic degrees of freedom respectively and  $S_{\text{int}}$  describes the interaction between the two sectors. In the regimes where the mass scale associated with  $S_3$  is much smaller (larger) than the one associated with  $S_B$  and where  $S_{\text{int}}$  can be treated as a perturbation, we may integrate out the bosonic (fermionic) degrees of freedom, see e.g. Ref. [33].

### A.1 Integrating out the bosonic degrees of freedom

This case pertains to the transition lines between the D-AFM phase and the D-LD and D-H phases. In these cases the low-energy projection of a general local operator is given by

$$\hat{O}\Big|_{\text{low}} = \int \mathcal{D}\Phi e^{-S_B} e^{-S_{\text{int}}} \hat{O} = \langle \hat{O} \rangle_{\Phi} - \langle S_{\text{int}} \hat{O} \rangle_{\Phi} + \dots, \quad (50)$$

where  $\langle \rangle_{\Phi}$  denotes the average with respect to the bosonic action  $S_B$ . As we have assumed that the parameter  $m$  is positive, we have

$$\langle \sin(\sqrt{4\pi}\Phi) \rangle_{\Phi} = 0. \quad (51)$$

This implies that the low-energy projection of the dimerization operator is

$$\begin{aligned} \hat{D}_j\Big|_{\text{low}} &\sim -\langle S_{\text{int}} \hat{\sigma}^3(x) \sin(\sqrt{\pi}\hat{\Phi}(x)) \rangle_{\Phi} + \dots \\ &= -\lambda' \int d\tau dy \hat{\sigma}^3(x) \hat{\sigma}^3(y, \tau) \langle \sin(\sqrt{\pi}\hat{\Phi}(x, 0)) \sin(\sqrt{\pi}\hat{\Phi}(y, \tau)) \rangle_{\Phi} + \dots \\ &= \langle \hat{d} \rangle + iC\hat{R}_3(x)\hat{L}_3(x) + \dots \end{aligned} \quad (52)$$

In the last line we have used that the expectation value in the bosonic sector decays exponentially in the Euclidean distance  $r = \sqrt{(x-y)^2 + v^2\tau^2}$ ,

$$\langle \sin(\sqrt{\pi}\hat{\Phi}(x, 0)) \sin(\sqrt{\pi}\hat{\Phi}(y, \tau)) \rangle_{\Phi} \propto e^{-r/\xi}, \quad (53)$$

which in turn allows us to employ the operator product expansion in the Ising sector

$$\hat{\sigma}^3(x) \hat{\sigma}^3(y, \tau) = \left(\frac{a_0}{r}\right)^{\frac{1}{4}} [1 - i\pi r \hat{R}_3(x) \hat{L}_3(x)] + \dots \quad (54)$$

Finally we have fixed the constant part in the low-energy projection by using that it must give the correct expectation value of the dimerization operator. Similarly we obtain

$$\begin{aligned} \hat{M}_j^z\Big|_{\text{low}} &\sim -\lambda' \int d\tau dy \hat{\sigma}^3(y, \tau) \langle \partial_x \hat{\Phi}(x, 0) \sin(\sqrt{\pi}\hat{\Phi}(y, \tau)) \rangle_{\Phi} + \dots \\ &= A \partial_x \hat{\sigma}^3(x) + \dots \end{aligned} \quad (55)$$

The leading contribution to the low-energy projection of  $\hat{n}_j^z$  occurs at order  $\hat{O}(\lambda')^0$  of our procedure and gives

$$\begin{aligned} \hat{n}_j^z\Big|_{\text{low}} &\sim B' \langle \cos(\sqrt{\pi}\hat{\Phi}(x)) \rangle_{\Phi} \hat{\sigma}^3(x) + \dots \\ &= B \hat{\sigma}^3(x) + \dots \end{aligned} \quad (56)$$

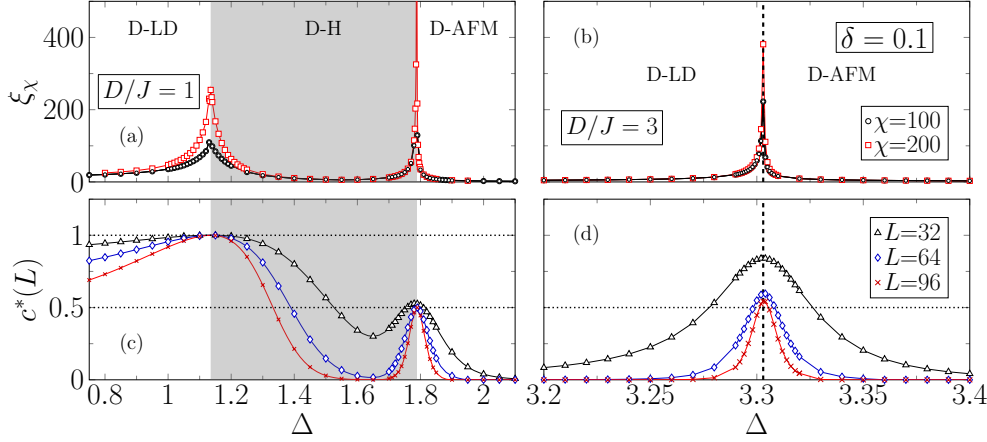


Figure 6: Correlation length  $\xi_\chi$  (upper panels) and central charge  $c^*(L)$  (lower panels) for fixed  $D/J = 1$  (left panels) and 3 (right panels) with  $\delta = 0.1$ .

## A.2 Integrating out the fermionic degrees of freedom

This case pertains to the transition line between the D-LD and D-H phases. Here we have

$$\hat{O}\Big|_{\text{low}} = \int \mathcal{D}\hat{R}_3 \mathcal{D}\hat{L}_3 e^{-S_3 - S_{\text{int}}} \hat{O} = \langle \hat{O} \rangle_3 - \langle S_{\text{int}} \hat{O} \rangle_3 + \dots, \quad (57)$$

where  $\langle \rangle_3$  denotes the average with respect to the Majorana action  $S_3$ . On the transition line we have  $m_3 > 0$  which implies

$$\langle \hat{\mu}^3(x) \rangle_3 \neq 0. \quad (58)$$

An immediate consequence of (58) is that

$$\hat{n}_j^x \Big|_{\text{low}} \sim \cos(\sqrt{\pi} \hat{\Phi}(x)) \langle \hat{\mu}^3(x) \rangle_3 + \dots \quad (59)$$

The low-energy projections of other operators can be worked out as before

$$\begin{aligned} \hat{n}_j^z \Big|_{\text{low}} &\sim -\lambda' B' \int dy d\tau \langle \hat{\sigma}^3(x, 0) \hat{\sigma}^3(y, \tau) \rangle_3 \sin(\sqrt{\pi} \hat{\Phi}(x, 0)) \cos(\sqrt{\pi} \hat{\Phi}(y, \tau)) \\ &= A_2 \sin(\sqrt{4\pi} \hat{\Phi}(x)) + \dots \end{aligned} \quad (60)$$

Here we have used that

$$\langle \hat{\sigma}^3(x, 0) \hat{\sigma}^3(y, \tau) \rangle_3 \propto e^{-r/\zeta}, \quad (61)$$

which permits us to employ operator product expansions in the bosonic sector. The projection of the dimerization operator is

$$\begin{aligned} \hat{D}_j \Big|_{\text{low}} &\sim -\lambda' \int d\tau dy \langle \hat{\sigma}^3(x) \hat{\sigma}^3(y, \tau) \rangle_3 \sin(\sqrt{\pi} \hat{\Phi}(x, 0)) \sin(\sqrt{\pi} \hat{\Phi}(y, \tau)) + \dots \\ &= \langle \hat{d} \rangle + D \cos(\sqrt{4\pi} \hat{\Phi}) + \dots \end{aligned} \quad (62)$$

## B Determination of phase boundaries

In this section, we explain how the QPT points and their universality classes are determined within the (i)DMRG method. Since the QPTs are the only points in the considered parameter



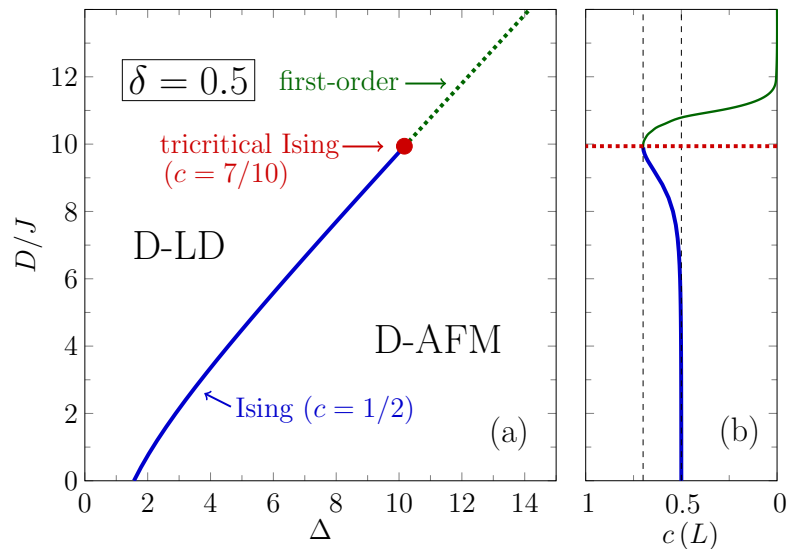


Figure 7: (a) Phase diagram of the model (2) for  $\delta = 0.5$ . D-LD $\rightleftharpoons$ D-AFM phase boundary of the continuous Ising transition terminates at a tricritical Ising point. Beyond this point, the QPT becomes first order. (b) Central charge  $c(L)$  on the D-LD $\rightleftharpoons$ D-AFM phase boundaries obtained numerically for  $L = 128$  and periodic boundary conditions.

region where the system becomes critical, they are easily obtained by simulating the correlation length  $\xi_\chi$ , as demonstrated in Figs. 6(a) and (b) for  $\delta = 0.1$  with fixed  $D/J = 1$  and 3, respectively. The divergence of the physical correlation length at a QPT is reflected by a pronounced peak of  $\xi_\chi$  whose height increases with the bond dimension  $\chi$ . From the peak positions for large enough  $\chi$ , we pinpoint the phase transition with an accuracy of at least three digits. For  $D/J = 1$  the transitions occur at  $\Delta_{c1} \simeq 1.135$  and  $\Delta_{c2} \simeq 1.789$  [see Fig. 6(a)], while there is only one Ising transition at  $\Delta_c \simeq 3.303$  [see Fig. 6(b)].

The central charge  $c^*(L)$  calculated by DMRG also exhibits a peak structure around the critical points [see Figs. 6(c) and (d)]. These peaks become more distinct with increasing system size  $L$ . From the heights of the peaks at large  $L$ , we obtain the central charges  $c = 1$  and  $c = 1/2$ , which are consistent with Gaussian- and Ising-type transitions, respectively. Moreover, the positions of the peaks agree with the QPT points estimated from the correlation length.

## C Ground-state phase diagram for strong dimerization

With increasing dimerization the D-H phase is reduced, and it disappears for  $\delta \gtrsim 0.26$  [11] if we limit ourselves to the parameter region  $J > 0$  and  $\delta > 0$ . Figure 7(a) for  $\delta = 0.5$  demonstrates such a situation consisting of only D-LD and D-AFM phases, separated by continuous and first-order transition lines. At the meeting of these transition lines the numerically obtained central charge indicates  $c = 7/10$  [Fig. 7(b)], suggesting that this point belongs to the tricritical Ising universality class.

## References

- [1] F. D. M. Haldane, *Nonlinear field theory of large-spin Heisenberg antiferromagnets: Semiclassically quantized solitons of the one-dimensional easy-axis Néel state*, Phys. Rev. Lett. **50**, 1153 (1983), doi:[10.1103/PhysRevLett.50.1153](https://doi.org/10.1103/PhysRevLett.50.1153).
- [2] I. Affleck, T. Kennedy, E. H. Lieb and H. Tasaki, *Rigorous results on valence-bond ground states in antiferromagnets*, Phys. Rev. Lett. **59**, 799 (1987), doi:[10.1103/PhysRevLett.59.799](https://doi.org/10.1103/PhysRevLett.59.799).
- [3] I. Affleck, *Quantum spin chains and the Haldane gap*, J. Phys.: Condens. Matter **1**, 3047 (1989), doi:[10.1088/0953-8984/1/19/001](https://doi.org/10.1088/0953-8984/1/19/001).
- [4] Z.-C. Gu and X.-G. Wen, *Tensor-entanglement-filtering renormalization approach and symmetry-protected topological order*, Phys. Rev. B **80**, 155131 (2009), doi:[10.1103/PhysRevB.80.155131](https://doi.org/10.1103/PhysRevB.80.155131).
- [5] F. Pollmann, A. M. Turner, E. Berg and M. Oshikawa, *Entanglement spectrum of a topological phase in one dimension*, Phys. Rev. B **81**, 064439 (2010), doi:[10.1103/PhysRevB.81.064439](https://doi.org/10.1103/PhysRevB.81.064439).
- [6] W. J. L. Buyers, R. M. Morra, R. L. Armstrong, M. J. Hogan, P. Gerlach and a. K. Hirakawa, *Experimental evidence for the Haldane gap in a spin-1 nearly isotropic, antiferromagnetic chain*, Phys. Rev. Lett. **56**, 371 (1986), doi:[10.1103/PhysRevLett.56.371](https://doi.org/10.1103/PhysRevLett.56.371).
- [7] J. P. Renard, M. Verdaguer, L. P. Regnault, W. A. C. Erkelens, J. Rossat-Mignod and W. G. Stirling, *Presumption for a quantum energy gap in the quasi-one-dimensional  $S = 1$  Heisenberg antiferromagnet  $\text{Ni}(\text{C}_2\text{H}_8\text{N}_2)_2\text{NO}_2(\text{ClO}_4)$* , Europhys. Lett. **3**, 945 (1987), doi:[10.1209/0295-5075/3/8/013](https://doi.org/10.1209/0295-5075/3/8/013).
- [8] T. Delica, K. Kopinga, H. Leschke and K. K. Mon, *Thermal properties of chains of antiferromagnetically coupled spins with  $s=1$ : Numerical evidence of the Haldane gap at nonzero temperatures*, Europhys. Lett. **15**, 55 (1991), doi:[10.1209/0295-5075/15/1/010](https://doi.org/10.1209/0295-5075/15/1/010).
- [9] W. Chen, K. Hida and B. C. Sanctuary, *Ground-state phase diagram of  $S=1$  XXZ chains with uniaxial single-ion-type anisotropy*, Phys. Rev. B **67**, 104401 (2003), doi:[10.1103/PhysRevB.67.104401](https://doi.org/10.1103/PhysRevB.67.104401).
- [10] A. Kitazawa, K. Nomura and K. Okamoto, *Phase diagram of  $S=1$  bond-alternating XXZ chains*, Phys. Rev. Lett. **76**, 4038 (1996), doi:[10.1103/PhysRevLett.76.4038](https://doi.org/10.1103/PhysRevLett.76.4038).
- [11] A. Kitazawa and K. Nomura, *Critical properties of  $S=1$  bond-alternating XXZ chains and hidden  $Z_2 \times Z_2$  symmetry*, J. Phys. Soc. Jpn. **66**, 3944 (1997), doi:[10.1143/JPSJ.66.3944](https://doi.org/10.1143/JPSJ.66.3944).
- [12] F. Lange, S. Ejima and H. Fehske, *Criticality at the Haldane-insulator charge-density-wave quantum phase transition*, Phys. Rev. B **92**, 041120 (2015), doi:[10.1103/PhysRevB.92.041120](https://doi.org/10.1103/PhysRevB.92.041120).
- [13] S. Ejima, F. H. L. Essler, F. Lange and H. Fehske, *Ising tricriticality in the extended Hubbard model with bond dimerization*, Phys. Rev. B **93**, 235118 (2016), doi:[10.1103/PhysRevB.93.235118](https://doi.org/10.1103/PhysRevB.93.235118).
- [14] S. Ejima, F. Lange, F. H. L. Essler and H. Fehske, *Critical behavior of the extended Hubbard model with bond dimerization*, Phys. B: Condens. Matter **536**, 474 (2018), doi:[10.1016/j.physb.2017.09.001](https://doi.org/10.1016/j.physb.2017.09.001).

- [15] D. Friedan, Z. Qiu and S. Shenker, *Conformal invariance, unitarity, and critical exponents in two dimensions*, Phys. Rev. Lett. **52**, 1575 (1984), doi:[10.1103/PhysRevLett.52.1575](https://doi.org/10.1103/PhysRevLett.52.1575).
- [16] D. Friedan, Z. Qiu and S. Shenker, *Superconformal invariance in two dimensions and the tricritical Ising model*, Phys. Lett. B **151**, 37 (1985), doi:[10.1016/0370-2693\(85\)90819-6](https://doi.org/10.1016/0370-2693(85)90819-6).
- [17] S. R. White, *Density matrix formulation for quantum renormalization groups*, Phys. Rev. Lett. **69**, 2863 (1992), doi:[10.1103/PhysRevLett.69.2863](https://doi.org/10.1103/PhysRevLett.69.2863).
- [18] U. Schollwöck, *The density-matrix renormalization group in the age of matrix product states*, Ann. Phys. **326**, 96 (2011), doi:[10.1016/j.aop.2010.09.012](https://doi.org/10.1016/j.aop.2010.09.012).
- [19] M. Hagiwara, Y. Narumi, K. Kindo, M. Kohno, H. Nakano, R. Sato and M. Takahashi, *Experimental verification of the gapless point in the  $S=1$  antiferromagnetic bond alternating chain*, Phys. Rev. Lett. **80**, 1312 (1998), doi:[10.1103/PhysRevLett.80.1312](https://doi.org/10.1103/PhysRevLett.80.1312).
- [20] I. P. McCulloch, *Infinite size density matrix renormalization group, revisited* (2008), [arXiv:0804.2509](https://arxiv.org/abs/0804.2509).
- [21] P. Calabrese and J. Cardy, *Entanglement entropy and quantum field theory*, J. Stat. Mech.: Theor. Exp. P06002 (2004), doi:[10.1088/1742-5468/2004/06/P06002](https://doi.org/10.1088/1742-5468/2004/06/P06002).
- [22] S. Nishimoto, *Tomonaga-Luttinger-liquid criticality: Numerical entanglement entropy approach*, Phys. Rev. B **84**, 195108 (2011), doi:[10.1103/PhysRevB.84.195108](https://doi.org/10.1103/PhysRevB.84.195108).
- [23] L. A. Takhtajan, *The picture of low-lying excitations in the isotropic Heisenberg chain of arbitrary spins*, Phys. Lett. A **87**, 479 (1982), doi:[10.1016/0375-9601\(82\)90764-2](https://doi.org/10.1016/0375-9601(82)90764-2).
- [24] H. M. Babujian, *Exact solution of the one-dimensional isotropic Heisenberg chain with arbitrary spins  $S$* , Phys. Lett. A **90**, 479 (1982), doi:[10.1016/0375-9601\(82\)90403-0](https://doi.org/10.1016/0375-9601(82)90403-0).
- [25] A. M. Tsvelik, *Field-theory treatment of the Heisenberg spin-1 chain*, Phys. Rev. B **42**, 10499 (1990), doi:[10.1103/PhysRevB.42.10499](https://doi.org/10.1103/PhysRevB.42.10499).
- [26] H. J. Schulz, *Phase diagrams and correlation exponents for quantum spin chains of arbitrary spin quantum number*, Phys. Rev. B **34**, 6372 (1986), doi:[10.1103/PhysRevB.34.6372](https://doi.org/10.1103/PhysRevB.34.6372).
- [27] I. Affleck, *Critical behaviour of  $SU(n)$  quantum chains and topological non-linear  $\sigma$ -models*, Nucl. Phys. B **305**, 582 (1988), doi:[10.1016/0550-3213\(88\)90117-4](https://doi.org/10.1016/0550-3213(88)90117-4).
- [28] C. Itoi and M.-H. Kato, *Extended massless phase and the Haldane phase in a spin-1 isotropic antiferromagnetic chain*, Phys. Rev. B **55**, 8295 (1997), doi:[10.1103/PhysRevB.55.8295](https://doi.org/10.1103/PhysRevB.55.8295).
- [29] R. Assaraf, P. Azaria, M. Caffarel and P. Lecheminant, *Metal-insulator transition in the one-dimensional  $SU(N)$  Hubbard model*, Phys. Rev. B **60**, 2299 (1999), doi:[10.1103/PhysRevB.60.2299](https://doi.org/10.1103/PhysRevB.60.2299).
- [30] S. R. Manmana, A. M. Läuchli, F. H. L. Essler and F. Mila, *Phase diagram and continuous pair-unbinding transition of the bilinear-biquadratic  $S=1$  Heisenberg chain in a magnetic field*, Phys. Rev. B **83**, 184433 (2011), doi:[10.1103/PhysRevB.83.184433](https://doi.org/10.1103/PhysRevB.83.184433).
- [31] M. Fabrizio, A. O. Gogolin and A. A. Nersisyan, *Critical properties of the double-frequency sine-Gordon model with applications*, Nucl. Phys. B **580**, 647 (2000), doi:[10.1016/S0550-3213\(00\)00247-9](https://doi.org/10.1016/S0550-3213(00)00247-9).

- [32] G. Delfino and G. Mussardo, *Non-integrable aspects of the multi-frequency sine-Gordon model*, Nucl. Phys. B **516**, 675 (1998), doi:[10.1016/S0550-3213\(98\)00063-7](https://doi.org/10.1016/S0550-3213(98)00063-7).
- [33] Y.-J. Wang, F. H. L. Essler, M. Fabrizio and A. A. Nersesyan, *Quantum criticalities in a two-leg antiferromagnetic  $S=1/2$  ladder induced by a staggered magnetic field*, Phys. Rev. B **66**, 024412 (2002), doi:[10.1103/PhysRevB.66.024412](https://doi.org/10.1103/PhysRevB.66.024412).
- [34] S. Ejima, F. Gebhard and S. Nishimoto, *Tomonaga-Luttinger parameters for doped Mott insulators*, Europhys. Lett. **70**, 492 (2005), doi:[10.1209/epl/i2005-10020-8](https://doi.org/10.1209/epl/i2005-10020-8).
- [35] G. Vidal, *Classical simulation of infinite-size quantum lattice systems in one spatial dimension*, Phys. Rev. Lett. **98**, 070201 (2007), doi:[10.1103/PhysRevLett.98.070201](https://doi.org/10.1103/PhysRevLett.98.070201).
- [36] D. Pérez-García, M. M. Wolf, M. Sanz, F. Verstraete and J. I. Cirac, *String order and symmetries in quantum spin lattices*, Phys. Rev. Lett. **100**, 167202 (2008), doi:[10.1103/PhysRevLett.100.167202](https://doi.org/10.1103/PhysRevLett.100.167202).
- [37] A. Escuer, R. Vicente and X. Solans, *Syntheses of several kinds of one-dimensional nickel(II)-nitrito complexes: a new  $\mu$ -nitritonickel(II) alternating chain*, J. Chem. Soc., Dalton Trans. **4**, 531 (1997), doi:[10.1039/A603070J](https://doi.org/10.1039/A603070J).
- [38] M. Hagiwara, H. Tsujii, C. R. Rotundu, B. Andraka, Y. Takano, N. Tateiwa, T. C. Kobayashi, T. Suzuki and S. Suga, *Tomonaga-Luttinger liquid in a quasi-one-dimensional  $S=1$  antiferromagnet observed by specific heat measurements*, Phys. Rev. Lett. **96**, 147203 (2006), doi:[10.1103/PhysRevLett.96.147203](https://doi.org/10.1103/PhysRevLett.96.147203).
- [39] R. Vicente, A. Escuer, J. Ribas and X. Solans, *The first nickel(II) alternating chain with two different end-to-end azido bridges*, Inorg. Chem. **31**, 1726 (1992), doi:[10.1021/ic00035a041](https://doi.org/10.1021/ic00035a041).
- [40] A. Escuer, R. Vicente, J. Ribas, M. Salah El Fallah, X. Solans and M. Font-Bardia, *Trans-[Ni(333-tet)( $\mu$ -N<sub>3</sub>)<sub>n</sub>](ClO<sub>4</sub>)<sub>n</sub> and cis-[Ni(333-tet)( $\mu$ -N<sub>3</sub>)<sub>n</sub>](PF<sub>6</sub>)<sub>n</sub>: Two novel kinds of structural nickel(II) chains with a single azido bridge. Magnetic behavior of an alternating  $S = 1$  chain with  $\alpha = 0.46$* , Inorg. Chem. **33**, 1842 (1994), doi:[10.1021/ic00087a019](https://doi.org/10.1021/ic00087a019).
- [41] A. Escuer, R. Vicente, X. Solans and M. Font-Bardia, *Crystal structure and magnetic properties of [Ni<sub>2</sub>(dpt)<sub>2</sub>( $\mu$ -ox)( $\mu$ -N<sub>3</sub>)<sub>n</sub>](PF<sub>6</sub>)<sub>n</sub>: A new strategy to obtain  $S = 1$  alternating chains*, Inorg. Chem. **33**, 6007 (1994), doi:[10.1021/ic00104a007](https://doi.org/10.1021/ic00104a007).
- [42] K. Totsuka, Y. Nishiyama, N. Hatano and M. Suzuki, *Isotropic spin-1 chains with bond alternation: analytic and numerical studies*, J. Phys.: Condens. Matter **7**, 4895 (1995), doi:[10.1088/0953-8984/7/25/014](https://doi.org/10.1088/0953-8984/7/25/014).
- [43] S. Ejima and H. Fehske, *Comparative density-matrix renormalization group study of symmetry-protected topological phases in spin-1 chain and Bose-Hubbard models*, Phys. Rev. B **91**, 045121 (2015), doi:[10.1103/PhysRevB.91.045121](https://doi.org/10.1103/PhysRevB.91.045121).
- [44] ITensor, <http://itensor.org/>.

## Quantum phase transitions in the dimerized extended Bose-Hubbard model

Koudai Sugimoto,<sup>1</sup> Satoshi Ejima,<sup>2</sup> Florian Lange,<sup>2</sup> and Holger Fehske<sup>2</sup>

<sup>1</sup>*Center for Frontier Science, Chiba University, Chiba 263-8522, Japan*

<sup>2</sup>*Institut für Physik, Universität Greifswald, D-17489 Greifswald, Germany*



(Received 23 November 2018; published 28 January 2019)

We present an unbiased numerical density-matrix renormalization group study of the one-dimensional Bose-Hubbard model supplemented by nearest-neighbor Coulomb interaction and bond dimerization. It places the emphasis on the determination of the ground-state phase diagram and shows that, besides dimerized Mott and density-wave insulating phases, an intermediate symmetry-protected topological Haldane insulator emerges at weak Coulomb interactions for filling factor one, which disappears, however, when the dimerization becomes too large. Analyzing the critical behavior of the model, we prove that the phase boundaries of the Haldane phase to Mott insulator and density-wave states belong to the Gaussian and Ising universality classes with central charges  $c = 1$  and  $c = 1/2$ , respectively, and merge in a tricritical point. Interestingly we can demonstrate a direct Ising quantum phase transition between the dimerized Mott and density-wave phases above the tricritical point. The corresponding transition line terminates at a critical end point that belongs to the universality class of the dilute Ising model with  $c = 7/10$ . At even stronger Coulomb interactions the transition becomes first order.

DOI: [10.1103/PhysRevA.99.012122](https://doi.org/10.1103/PhysRevA.99.012122)

### I. INTRODUCTION

Over the past years, ultracold atoms in optical lattices have become a fascinating tool to explore strongly correlated many-body systems and thereby provide also valuable insights into complex phenomena in solid-state systems [1–3]. Ultracold-atom-based quantum simulators have already been used, e.g., to observe the transition from a superfluid (SF) to a Mott insulator (MI) phase for bosons [4], to realize the crossover between Bose-Einstein condensation and Bardeen-Cooper-Schrieffer pairing [5], or to modulate the range of interactions in quantum systems [6,7].

One of the targeted model systems for ultracold atoms is the Bose-Hubbard model (BHM), which has been intensively studied from a theoretical point of view. Quite recently, triggered by the observation of a symmetry-protected-topological (SPT) Haldane phase in the spin-1 Heisenberg chain [8–10], the related Haldane insulator (HI) phase in the extended BHM (EBHM) with longer-range repulsion [11] has attracted significant attention.

Including a bond dimerization, which can also be realized in optical lattices [12], the physical properties of the spin-1 chain change drastically, e.g., the Haldane phase shrinks rapidly when the dimerization increases and eventually even disappears [13,14]. In this work, we explore the effect of the bond dimerization  $\delta$  in the EBHM using the density-matrix renormalization group (DMRG) technique [15,16]. We especially demonstrate that a direct continuous transition takes place between the dimerized MI and density-wave (DW) phases, instead of the first-order transition observed in the pure EBHM ( $\delta = 0$ ).

The paper is structured as follows: Section II introduces the EBHM with bond dimerization, as well as the numerical techniques for its investigation. The physical quantities of interest will be defined in Sec. III. Section IV presents the

ground-state phase diagram of the dimerized EBHM for  $\rho = 1$  and classifies the phase boundaries. Some results for band filling factor  $\rho = 1/2$  can be found in Appendix A. Section V summarizes our results and gives a brief outlook.

### II. MODEL AND METHOD

As outlined above, we consider the EBHM with an additional explicit bond dimerization  $\delta$ ,

$$\hat{H} = \hat{H}_{\text{EBHM}} - t \sum_j \delta (-1)^j (\hat{b}_{j+1}^\dagger \hat{b}_j + \text{H.c.}), \quad (1)$$

where the EBHM Hamiltonian is given by

$$\begin{aligned} \hat{H}_{\text{EBHM}} = & -t \sum_j (\hat{b}_{j+1}^\dagger \hat{b}_j + \text{H.c.}) + U \sum_j \hat{n}_j (\hat{n}_j - 1)/2 \\ & + V \sum_j \hat{n}_j \hat{n}_{j+1}. \end{aligned} \quad (2)$$

Here  $\hat{b}_j^\dagger$  ( $\hat{b}_j$ ) creates (annihilates) a boson at site  $j$  of a one-dimensional lattice, and  $\hat{n}_j = \hat{b}_j^\dagger \hat{b}_j$  is the corresponding particle number operator. The transfer amplitude  $t$  enables the bosons to hop between neighboring lattice sites, whereas the on-site (nearest-neighbor) Coulomb repulsion  $U$  ( $V$ ) tends to localize the particles by establishing an MI (a DW) ground state, at least when the number of bosons  $N$  equals the number of lattice sites  $L$ , i.e.,  $\rho = N/L = 1$ . In this case, a finite dimerization should also promote an insulating state but now with alternating strong and weak bonds.

The ground-state phase diagram of the pure BHM, where  $V = 0$  and  $\delta = 0$ , has only two phases, an SF and an MI [17], which are separated by a Kosterlitz-Thouless phase transition at  $t/U \simeq 0.305$  for  $\rho = 1$  [18]. Adding now  $V$  and restricting the maximum number of bosons per site  $n_b$  to

be two, the EBHM can be approximately mapped onto the spin-1  $XXZ$  model with single-ion anisotropy, whereby the bosonic operators  $\hat{b}_j^+$ ,  $\hat{b}_j^-$ , and  $\hat{n}_j$  will be replaced by the spin-1 operators  $\hat{S}_j^+$ ,  $\hat{S}_j^-$ , and  $\hat{S}_j^z + 1$ , respectively [19]. As a result, an SPT Haldane insulator appears between the MI and DW phases for intermediate couplings [11,20], which resembles the gapped Haldane phase of the quantum spin-1 Heisenberg chain [8]. We note that the HI phase continues to exist if one includes higher boson numbers  $n_b > 2$  [21,22]. In the DMRG calculations, a finite maximum number of bosons per site  $n_b$  must be used. All results for  $\rho = 1$  in the main text are obtained with  $n_b = 4$ .

To explore the effects of the dimerization in the full model (1), we employ the matrix-product-state-based infinite DMRG (iDMRG) technique [23]. The iDMRG provides us with unbiased numerical data directly in the thermodynamic limit. Hence the phase boundaries can be obtained without any finite-size scaling procedure. On the other hand, we determine the critical behavior by tracking the central charge along the quantum phase transition (QPT) lines through the use of the more standard DMRG technique for finite systems with periodic boundary conditions (PBC). The quantum phase transition itself is characterized by various excitation gaps obtained by combining DMRG and infinite matrix-product-state representation at the boundaries of the system [24,25].

### III. SYSTEM CHARACTERIZATION

Now we present the physical quantities of interest and explain how they can be simulated within the (i)DMRG framework.

#### A. Entanglement spectrum, central charge, and correlation length

To determine SPT states in the model (1), we discuss the so-called entanglement spectrum  $\varepsilon_\alpha$  [26], which can be extracted from the Schmidt decomposition. Dividing the system with  $L$  sites into two subblocks,  $\mathcal{H} = \mathcal{H}_\ell \otimes \mathcal{H}_{L-\ell}$ , and considering the reduced density matrix  $\rho_\ell = \text{Tr}_{L-\ell}[\rho]$  of a sub-block of (arbitrary) length  $\ell < L$ , the entanglement spectrum is given by the singular values  $\lambda_\alpha$  of  $\rho_\ell$  as  $\varepsilon_\alpha = -2 \ln \lambda_\alpha$ . If we split the system into two semi-infinite pieces during the iDMRG simulations, the entanglement levels  $\varepsilon_\alpha$  show a characteristic degeneracy in the SPT phase, as has been demonstrated for the Haldane phase of the spin-1 chain [10].

The entanglement spectrum also yields valuable information about the criticality of the system. For the von Neumann entanglement entropy,  $S_L(\ell) = -\sum_\alpha \lambda_\alpha^2 \ln \lambda_\alpha^2$ , field theory predicts that

$$S_L(\ell) = \frac{c}{3} \ln \left[ \frac{L}{\pi} \sin \left( \frac{\pi \ell}{L} \right) \right] + s_1 \quad (3)$$

in a critical system with PBC [27]. In Eq. (3),  $c$  is the central charge and  $s_1$  is a nonuniversal constant. Employing a doubled unit cell, in view of the explicit dimerization, the central charge can be calculated very efficiently from the relation [28]

$$c^*(L) = \frac{3[S_L(L/2 - 2) - S_L(L/2)]}{\ln\{\cos[\pi/(L/2)]\}}. \quad (4)$$

In addition, within an iDMRG calculation, the correlation length  $\xi_\chi$  can be obtained from the second-largest eigenvalue of the transfer matrix for some bond dimension  $\chi$  [16,23]. While the physical correlation length diverges when the system becomes critical,  $\xi_\chi$  stays finite during the numerical simulations due to the finite bond dimension. Nevertheless,  $\xi_\chi$  can be utilized to determine the phase transition point because it develops a pronounced maximum with increasing  $\chi$  near the critical point. Putting these criteria together, the QPT can be determined with high precision.

#### B. Excitation gaps

To determine the criticality of the QPTs one can simulate various excitation gaps of the model (1), just as for the EBHM [11,20,21]. For instance, in the EBHM, the single-particle gap

$$\Delta_{\text{sp}} = E_0(N+1) + E_0(N-1) - 2E_0(N) \quad (5)$$

closes at the MI-HI transition, and the neutral gap

$$\Delta_n = E_1(N) - E_0(N) \quad (6)$$

vanishes at the MI-HI and HI-DW transitions, where  $\Delta_n$  closes linearly in the latter case, indicating a critical exponent  $\nu = 1$  of the Ising universality class. In Eqs. (5) and (6),  $E_0$  ( $E_1$ ) denotes the ground-state energy (energy of the first excited state) of the finite  $L$ -site system with fixed boson number.

#### C. Density-wave order parameter

By analogy with the charge-density-wave order parameter of the fermionic Hubbard-type models [29,30], a (dimerized) DW state in the model (1) can be characterized by a nonvanishing expectation value of the operator

$$\hat{m}_{\text{DW}} = \frac{1}{L} \sum_j (-1)^j (\hat{n}_j - 1). \quad (7)$$

Most importantly, analyzing  $\langle \hat{m}_{\text{DW}} \rangle$  close to the Ising or the tricritical Ising transitions points provides the critical exponent  $\beta$  [30].

### IV. NUMERICAL RESULTS FOR $\rho = 1$

#### A. Ground-state phase diagram

Figure 1 presents the ground-state phase diagram of the EBHM with an explicit bond dimerization  $\delta = 0.25$  and  $n_b = 4$  obtained by iDMRG. For the considered weak dimerization, we observe, just as for the EBHM ( $\delta = 0$ ), an HI between the MI and DW states, but now these phases exhibit a finite bond dimerization, i.e., actually we have D-HI, D-MI, and D-DW states. For weak onsite and nearest-neighbor repulsions, an SF phase appears. Additionally, there may be a region of phase separation for  $U/t < 2$ , as observed in the model without dimerization [31]. Here, however, we restrict ourselves to the parameter regime  $U/t \geq 2$  in order to concentrate on the study of D-MI, D-HI, and D-DW phases and the transitions between them.

Also the universality classes of the QPT between the D-HI and the D-MI (D-HI and D-DW) phases are the same as for the EBHM, where they are characterized by a central charge

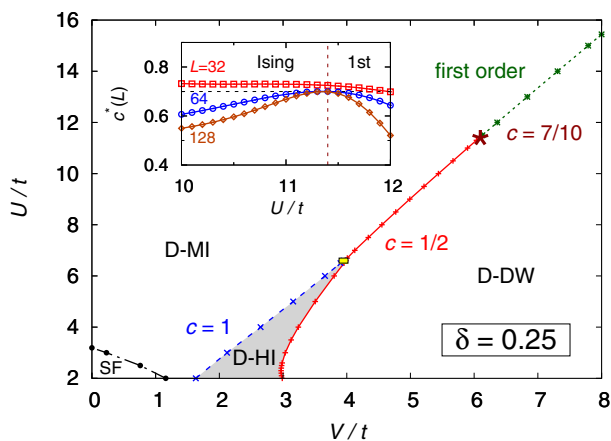


FIG. 1. IDMRG ground-state phase diagram of the dimerized EBHM (1) for  $U/t \geq 2$  with  $\delta = 0.25$  and  $n_b = 4$ . Here the blue dashed line gives the D-MI  $\rightleftharpoons$  D-HI phase boundary; the red solid line denotes the continuous Ising phase transition. Both lines merge at the tricritical point located inside the small rectangle which is enlarged in Fig. 4(c) (see also the discussions in the text). The QPT is continuous (first order) below (above) the critical end point  $(V/t, U/t)_{ce}$  marked by the star symbol [there we obtain for the central charge  $c^*(L) \simeq 0.7$  from Eq. (4) as  $L \rightarrow \infty$  on the D-MI  $\rightleftharpoons$  D-DW transition line, see inset]. In the weak  $(V, U)$ -coupling regime an SF phase is formed.

$c = 1$  ( $c = 1/2$ ). The relevant difference is that now the transition between the D-MI and D-DW phases is continuous below a critical end point  $(V/t, U/t)_{ce}$  [which roughly is  $(11.4, 6.08)$  for  $\delta = 0.25$ ]. The continuous transition also belongs to the Ising universality class, except for the critical end point, which belongs to the universality class of the dilute Ising model with  $c = 7/10$ . This will be confirmed numerically below.

### B. D-HI $\rightleftharpoons$ D-MI and D-HI $\rightleftharpoons$ D-DW quantum phase transitions

We now investigate the nature of the SPT D-HI state and its phase boundaries in more detail. Figure 2(a) displays the behavior of the central charge  $c^*(L)$  as a function of  $V/t$  at fixed  $U/t = 4$ , which is obtained by evaluating Eq. (4) by DMRG for up to  $L = 96$  sites with PBC. Increasing the system size, two peaks develop, which indicates the D-MI  $\rightleftharpoons$  D-HI and D-HI  $\rightleftharpoons$  D-DW transitions. For  $L = 96$ , we find  $c^* \simeq 1.000$  ( $c^* \simeq 0.503$ ) at  $V_{c1}/t \simeq 2.65$  ( $V_{c2}/t \simeq 3.24$ ), which points toward a Gaussian (an Ising) QPT. The corresponding entanglement spectrum  $\varepsilon_\alpha$  [Fig. 2(b)] underlines that a nontrivial topological phase is realized for  $V_{c1} < V < V_{c2}$ , because the entanglement levels show the characteristic degeneracy demonstrated previously for the Haldane phase of the spin-1 chain [10].

Figure 2(c) clearly shows the different behavior of the excitation gaps in the diverse insulator phases, as well as at their phase boundaries: The single-particle gap  $\Delta_{sp}$  is finite throughout the phase diagram, except for the D-HI  $\rightleftharpoons$  D-MI QPT, whereas the neutral gap  $\Delta_n$  closes both at the D-MI  $\rightleftharpoons$  D-HI and D-HI  $\rightleftharpoons$  D-DW QPTs. At the D-HI  $\rightleftharpoons$  D-DW transition  $\Delta_n$  closes linearly, which reflects the critical exponent  $\nu = 1$  of the Ising universality class. Nevertheless, the D-HI phase and its phase boundaries display the same behavior as for the

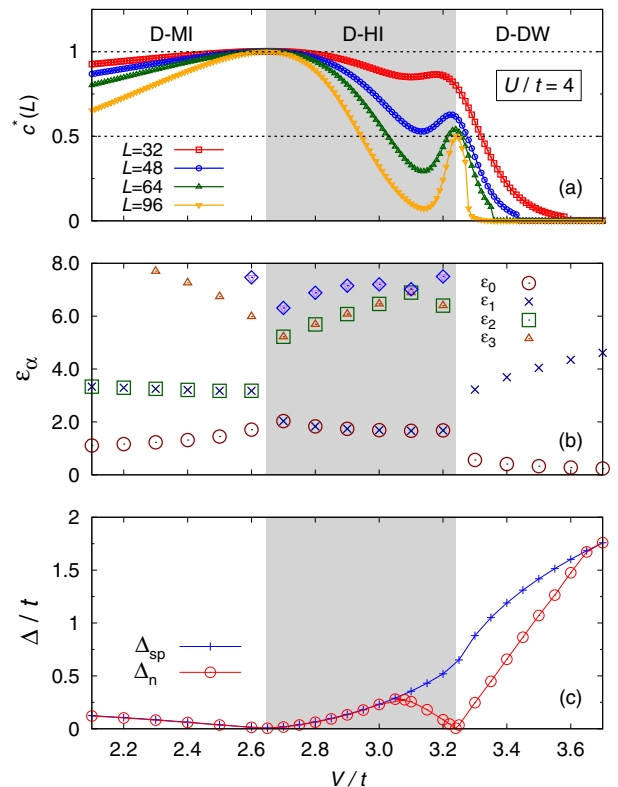


FIG. 2. Central charge (a), entanglement spectrum (b), and excitation gaps (c) of the dimerized EBHM (1) as a function of  $V/t$  at fixed  $U/t = 4$ , where  $\rho = 1$  and  $n_b = 4$ . A central charge  $c = 1$  ( $c = 1/2$ ) indicates the D-HI  $\rightleftharpoons$  D-MI (D-HI  $\rightleftharpoons$  D-DW) transition. The D-HI phase is marked in gray.

nondimerized EBHM. Note that the D-HI phase disappears at the tricritical point  $(V/t, U/t)_{tr}$  [which is located at  $(4.1, 6.9)$  for  $\delta = 0.25$ ], where the central charge becomes 1.

### C. D-MI $\rightleftharpoons$ D-DW Ising transition

The most significant effect of the dimerization is the direct Ising transition between the D-MI and D-DW phases which could not be observed in the pure EBHM. Figure 3(a) displays the central charge  $c^*(L)$ , obtained from Eq. (4) by DMRG. Obviously, in the vicinity of the D-MI  $\rightleftharpoons$  D-DW transition, a peak develops which gets sharper if the system size  $L$  is increased. Fixing  $U/t = 9$ , we find  $c^* \simeq 0.526$  at  $V_c \simeq 4.99$ , indicating that the QPT belongs to the Ising universality class. Since the D-HI phase is absent, the entanglement spectrum  $\varepsilon_\alpha$  is no longer degenerate [in the remaining D-MI and D-DW phases, cf. Fig. 3(b)]. Figure 3(c) gives the excitation gaps for  $U/t = 9$ . Again, the single-particle gap  $\Delta_{sp}$  stays finite, and the neutral gap  $\Delta_n$  closes at the D-MI  $\rightleftharpoons$  D-DW transition point linearly, i.e.,  $\nu = 1$  (Ising universality class).

As already pointed out, the continuous Ising transition line between D-MI and D-DW phases terminates at the tricritical Ising transition point. The inset of Fig. 1 shows how a pronounced maximum develops in the central charge  $c^*$  on the D-MI  $\rightleftharpoons$  D-DW transition line as  $L$  increases. We obtain

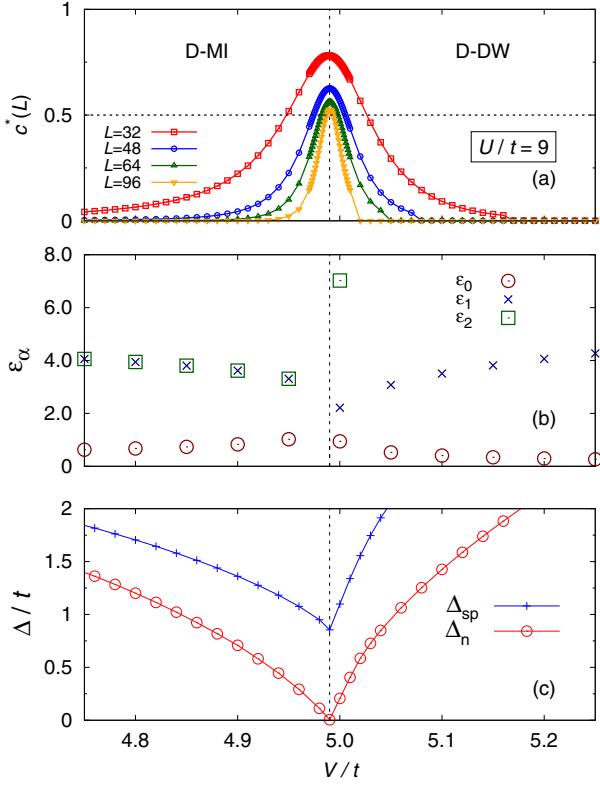


FIG. 3. Central charge (a), entanglement spectrum (b), and excitation gaps (c) of the model (1) as a function of  $V/t$  for fixed  $U/t = 9$  with  $\rho = 1$  and  $n_b = 4$ . The data indicate a D-MI  $\rightleftharpoons$  D-DW transition with  $c = 1/2$ .

$c^* \simeq 0.699$  at the critical end point  $(V/t, U/t)_{ce} \simeq (6.083, 11.4)$ , in agreement with the prediction of field theory for the universality class of the dilute Ising model,  $c = 7/10$ .

#### D. Tricritical regime

To investigate the surroundings of the tricritical point where the D-HI phase vanishes, and determine the value of  $(V/t, U/t)_{tr}$  with maximum precision, we calculated the correlation length  $\xi_\chi$  varying  $V/t$ , at fixed  $U/t$ , above and below the tricritical point. Here a single-peak, respectively, two-peak structure, would be expected. From Fig. 4(a) it seems, however, that in the immediate vicinity of the tricritical point a three-peak structure appears. That is, the DW order parameter  $\langle m_{DW} \rangle$  becomes finite not only for  $V > V_{c3}$  but also for  $V_{c1} < V < V_{c2}$  [see Fig. 4(b)], where  $V_{c1} < V_{c2} < V_{c3}$  denote the positions of three peaks. Plotting the position of these peaks when  $U/t$  is changed, we obtain the strongly zoomed-in phase diagram depicted in Fig. 4(c). According to this figure, the D-DW phase penetrates between the D-MI and the D-HI phase near the tricritical point  $(V/t, U/t)_{tr}$ . Since this re-entrance behavior of the D-DW phase is found numerically in a very limited parameter range only, and  $V_{c2}$  still shifts in the direction of  $V_{c1}$  as  $\chi$  increases [see Fig. 4(a)], it would be highly desirable to explore this region or behavior more

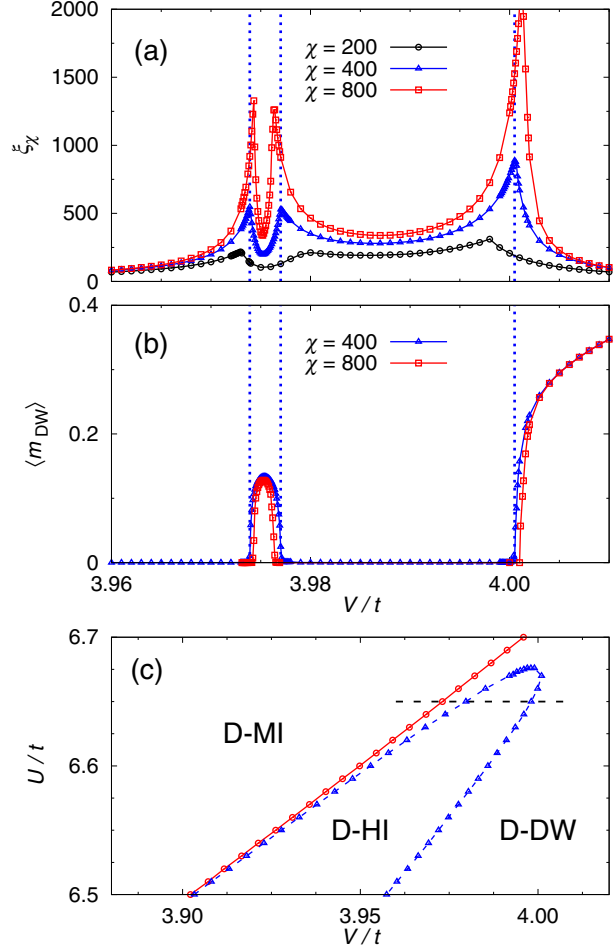


FIG. 4. (a) Three-peak structure of the correlation length  $\xi_\chi$  of the dimerized EBHM with  $\delta = 0.25$  and  $U/t = 6.65$ .  $\chi$  gives the bond dimension used in iDMRG. (b) Corresponding behavior of the DW order parameter  $\langle m_{DW} \rangle$ . Note that  $\langle m_{DW} \rangle$  is finite not only for  $V/t \gtrsim 4.00$  but also for  $3.974 \lesssim V/t \lesssim 3.977$ . The dotted lines denote the QPT points with  $\chi = 400$ . (c) Zoomed-in phase diagram in the immediate vicinity of the tricritical point. The dashed line illustrates the parameter scan performed in panels (a) and (b). Note that the parameter region of panel (c) is equal to the size of the rectangle in Fig. 1.

thoroughly, e.g., accompanying our iDMRG calculations by field theory, which is beyond the scope of this work, however.

#### V. SUMMARY AND CONCLUSIONS

In this work we explored the ground-state phase diagram of the extended Bose-Hubbard model with bond dimerization for filling factor  $\rho = 1$  by means of various density-matrix renormalization group techniques. Most notably, we prove the existence of a symmetry-protected-topological (dimerized) HI which separates—at sufficiently weak Coulomb interactions and dimerization—MI and DW states. In addition, we demonstrate a direct Ising transition line between the MI and DW phases for larger Coulomb interactions, which terminates at a



tricritical Ising point (end point) with central charge  $c = 7/10$ , where it becomes first order.

The phase diagram of the nondimerized model for  $\rho = 1$  can be understood by analogy to the spin-1  $XXZ$  chain with single-ion anisotropy, with the MI, HI, and DW phases corresponding to the large- $D$ , Haldane, and Néel phases, respectively. In particular, it follows that the HI phase is a symmetry-protected-topological phase, which is protected by a modified bond-centered inversion symmetry [10]. Since this symmetry is respected by the explicit dimerization, the distinction between MI and HI survives in the dimerized model. For weak Coulomb repulsions  $U$  and  $V$ , the system realizes an SF phase, just as for filling factor  $\rho = 1/2$ , where no MI exists at all in the absence of dimerization. If the onsite repulsion  $U$  is sufficiently large in the latter case, adding a small bond dimerization opens an energy gap so that the system passes into a symmetry-protected-topological dimerized MI phase (see Appendix A).

We wish to stress that it is extremely difficult to obtain numerical results with sufficient accuracy in the immediate vicinity of the tricritical point. In consequence, it remains an open question whether the observed intervening dimerized DW will survive the limit of infinite bond dimensions in the infinite density-matrix renormalization group simulation, or the tricritical point will be simply shifted to somewhat greater

values of the Coulomb interactions. In order to clarify this issue, an elaborate bosonization-based field theory would be very helpful. Recently, a field theory analysis was carried out in the dimerized spin-1  $XXZ$  chain [32], where the re-entrance behavior of the dimerized Néel phase might also occur.

Equally interesting would be an experimental realization of the dimerized extended Bose-Hubbard model by ultracold atomic gases in optical lattices in order to prove or disprove our theoretical predictions regarding the criticality and non-trivial topological properties.

#### ACKNOWLEDGMENTS

We thank T. Yamaguchi for fruitful discussions. K.S. is grateful for the hospitality at the University of Greifswald. F.L. was supported by Deutsche Forschungsgemeinschaft (Germany) through Project No. FE 398/8-1. The iDMRG simulations were performed using the ITensor library [33].

#### APPENDIX: CASE $\rho = 1/2$

At vanishing dimerization and a boson filling factor  $\rho = 1/2$ , a Kosterlitz-Thouless transition occurs between the SF and DW phases, in close analogy to the metal-insulator transition of the fermionic extended Hubbard model at quarter filling [34,35]. At finite bond dimerization  $\delta$  one expects that the SF phase gives way to an SPT D-MI phase [36]. Then a continuous Ising phase transition might occur between

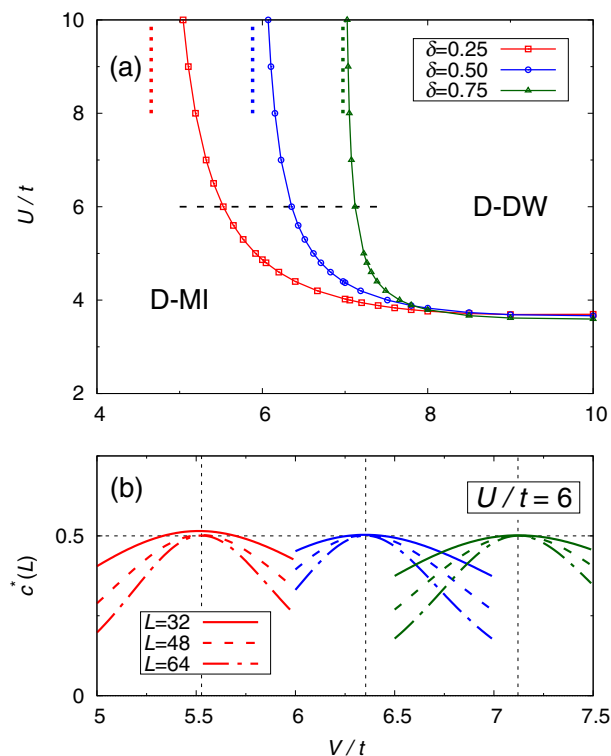


FIG. 5. (a) Ground-state phase diagram of the dimerized EBHM with  $\rho = 1/2$  and  $n_b = 2$ . Data obtained by iDMRG. The dotted lines denote the QPT point with same value of  $\delta$  in the spin-1/2 chain (A1). (b) Central charge  $c^*(L)$  as a function of  $V/t$  at fixed  $U/t = 6$ , calculated [along the dashed line in panel (a)] by finite-system DMRG with PBC.

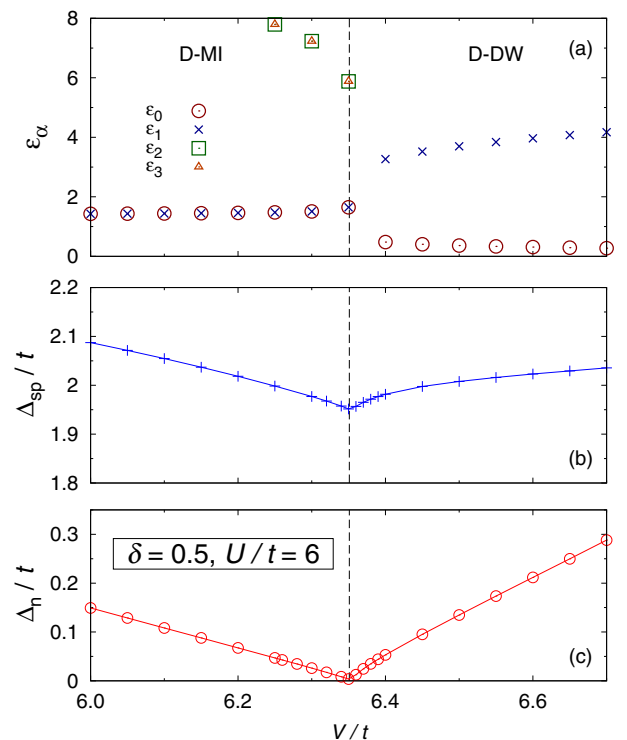


FIG. 6. Entanglement spectrum (a), single-particle gap (b), and neutral gap (c) in the dimerized EBHM with  $\delta = 0.5$  and  $n_b = 2$  at  $U/t = 6$ . The dashed line marks the Ising QPT point at  $V_c/t \simeq 6.351$ .

the SPT D-MI and the D-DW (just as in the charge sector of the quarter-filled extended Hubbard model with explicit dimerization [37,38]). It is well known that the model (1) with  $\rho = 1/2$  can be mapped onto the spin-1/2 dimerized  $XXZ$  model if we take the limit  $U \gg t, V$  and consider only the two lowest Fock states per site  $|0\rangle$  and  $|1\rangle$ . In this case, one may replace  $\hat{b}_j^+$ ,  $\hat{b}_j$ , and  $\hat{n}_j$  by spin-1/2 operators  $\hat{S}_j^+$ ,  $\hat{S}_j^-$ , and  $\hat{S}_j^z + 1/2$ , respectively [39], so that the Hamiltonian (1) becomes

$$\hat{H} = -t \sum_j [1 + \delta(-1)^j] (\hat{S}_j^+ \hat{S}_{j+1}^- + \hat{S}_j^- \hat{S}_{j+1}^+) + V \sum_j \hat{S}_j^z \hat{S}_{j+1}^z. \quad (\text{A1})$$

By taking this limit and  $\delta \rightarrow \pm 1$ , the ground state in the D-MI phase can be adiabatically connected to a fully dimerized state with “singlets” at every second bond, which implies that the D-MI is an SPT phase protected by inversion symmetry about the strong bonds. This is in contrast to the D-HI for  $\rho = 1$ , which is protected by inversion about both strong and weak bonds, and the D-MI for  $\rho = 1$ , which is a topologically trivial phase.

Figure 5(a) displays the ground-state phase diagram for a maximum number of bosons per site  $n_b = 2$  and different bond dimerizations  $\delta = 0.25, 0.50$ , and  $0.75$ . Only D-MI and D-DW phases appear. The phase boundaries for different  $\delta$

approximately coincide for strong nearest-neighbor interactions  $V/t > 8$ . In the limit  $V \rightarrow \infty$ , the ground state in the D-DW phase becomes a product state with alternating empty and single-occupied sites. The lowest-lying excited state then consists of a single double-occupied site with energy  $U$  and two domain walls with energies  $-2(t + \delta)$  and  $-2(t - \delta)$ . Accordingly, the D-DW state should break down at  $U/t = 4$  for all dimerizations. For smaller  $U/t$ , phase separation should occur since the D-MI phase is prohibited by the strong nearest-neighbor repulsion. The critical value  $U/t = 4$  roughly agrees with our numerical results for  $V/t \lesssim 10$ . However, in the parameter region studied, the D-DW borders only on the D-MI and no phase separation is observed.

The universality class of the QPT between the D-MI and the D-DW is deduced from the central charge  $c^*(L)$  [Eq. (4)] by DMRG with PBC. The observed value  $c^* \simeq 0.5$  indicates that the transition belongs to the Ising universality class in two dimensions.

Other static properties of the dimerized EBHM are given by Fig. 6 for a bond dimerization  $\delta = 0.5$  and  $U/t = 6$ . Since the D-MI with doubled unit cell is a nontrivial SPT phase, the D-MI entanglement spectrum exhibits the characteristic degeneracy, which is lifted in the D-DW phase. Figure 6(b) gives the single-particle gap for the same parameter set, which has a minimum at the Ising transition point. As in the case of  $\rho = 1$ , the neutral gap  $\Delta_n$  closes linearly at the Ising transition point [see Fig. 6(c)], yielding the critical exponent  $\nu = 1$  of the Ising universality class.

- 
- [1] I. Bloch, J. Dalibard, and W. Zwerger, *Rev. Mod. Phys.* **80**, 885 (2008).
- [2] I. Bloch, J. Dalibard, and S. Nascimbène, *Nat. Phys.* **8**, 267 (2012).
- [3] C. Gross and I. Bloch, *Science* **357**, 995 (2017).
- [4] M. Greiner, O. Mandel, T. Esslinger, T. W. Hänsch, and I. Bloch, *Nature* **415**, 39 (2002).
- [5] W. Zwerger (ed.), *The BCS-BEC Crossover and the Unitary Fermi Gas* (Springer, Berlin, 2012).
- [6] S. Baier, M. J. Mark, D. Petter, K. Aikawa, L. Chomaz, Z. Cai, M. Baranov, P. Zoller, and F. Ferlaino, *Science* **352**, 201 (2016).
- [7] R. Landig, L. Hruby, N. Dogra, M. Landini, R. Mottl, T. Donner, and T. Esslinger, *Nature* **532**, 476 (2016).
- [8] F. D. M. Haldane, *Phys. Rev. Lett.* **50**, 1153 (1983).
- [9] Z.-C. Gu and X.-G. Wen, *Phys. Rev. B* **80**, 155131 (2009).
- [10] F. Pollmann, A. M. Turner, E. Berg, and M. Oshikawa, *Phys. Rev. B* **81**, 064439 (2010).
- [11] E. G. Dalla Torre, E. Berg, and E. Altman, *Phys. Rev. Lett.* **97**, 260401 (2006).
- [12] M. Atala, M. Aidelsburger, J. T. Barreiro, D. Abanin, T. Kitagawa, E. Demler, and I. Bloch, *Nat. Phys.* **9**, 795 (2013).
- [13] A. Kitazawa, K. Nomura, and K. Okamoto, *Phys. Rev. Lett.* **76**, 4038 (1996).
- [14] A. Kitazawa and K. Nomura, *J. Phys. Soc. Jpn.* **66**, 3944 (1997).
- [15] S. R. White, *Phys. Rev. Lett.* **69**, 2863 (1992).
- [16] U. Schollwöck, *Ann. Phys.* **326**, 96 (2011).
- [17] T. D. Kühner, S. R. White, and H. Monien, *Phys. Rev. B* **61**, 12474 (2000).
- [18] S. Ejima, H. Fehske, and F. Gebhard, *Europhys. Lett.* **93**, 30002 (2011).
- [19] E. Altman and A. Auerbach, *Phys. Rev. Lett.* **89**, 250404 (2002).
- [20] E. Berg, E. G. Dalla Torre, T. Giamarchi, and E. Altman, *Phys. Rev. B* **77**, 245119 (2008).
- [21] S. Ejima, F. Lange, and H. Fehske, *Phys. Rev. Lett.* **113**, 020401 (2014).
- [22] S. Ejima and H. Fehske, *Phys. Rev. B* **91**, 045121 (2015).
- [23] I. P. McCulloch, [arXiv:0804.2509](https://arxiv.org/abs/0804.2509).
- [24] H. N. Phien, G. Vidal, and I. P. McCulloch, *Phys. Rev. B* **86**, 245107 (2012).
- [25] F. Lange, S. Ejima, and H. Fehske, *Phys. Rev. B* **92**, 041120 (2015).
- [26] H. Li and F. D. M. Haldane, *Phys. Rev. Lett.* **101**, 010504 (2008).
- [27] P. Calabrese and J. Cardy, *J. Stat. Mech.* (2004) P06002.
- [28] S. Nishimoto, *Phys. Rev. B* **84**, 195108 (2011).
- [29] S. Ejima, F. H. L. Essler, F. Lange, and H. Fehske, *Phys. Rev. B* **93**, 235118 (2016).
- [30] S. Ejima, F. Lange, F. H. Essler, and H. Fehske, *Physica B: Condensed Matter* **536**, 474 (2018).
- [31] G. G. Batrouni, V. G. Rousseau, R. T. Scalettar, and B. Grémaud, *Phys. Rev. B* **90**, 205123 (2014).

- [32] S. Ejima, T. Yamaguchi, F. H. L. Essler, F. Lange, Y. Ohta, and H. Fehske, *SciPost Phys.* **5**, 059 (2018).
- [33] <http://itensor.org/>.
- [34] F. Mila and X. Zotos, *Europhys. Lett.* **24**, 133 (1993).
- [35] S. Ejima, F. Gebhard, and S. Nishimoto, *Europhys. Lett.* **70**, 492 (2005).
- [36] F. Grusdt, M. Höning, and M. Fleischhauer, *Phys. Rev. Lett.* **110**, 260405 (2013).
- [37] M. Tsuchiizu and E. Orignac, *J. Phys. Chem. Solids* **63**, 1459 (2002).
- [38] S. Ejima, F. Gebhard, and S. Nishimoto, *Phys. Rev. B* **74**, 245110 (2006).
- [39] E. Altman and A. Auerbach, *Phys. Rev. Lett.* **81**, 4484 (1998).





## Ising tricriticality in the extended Hubbard model with bond dimerization

Satoshi Ejima,<sup>1</sup> Fabian H. L. Essler,<sup>2</sup> Florian Lange,<sup>1,3</sup> and Holger Fehske<sup>1</sup>

<sup>1</sup>*Institut für Physik, Ernst-Moritz-Arndt-Universität Greifswald, 17489 Greifswald, Germany*

<sup>2</sup>*The Rudolf Peierls Centre for Theoretical Physics, Oxford University, Oxford OX1 3NP, United Kingdom*

<sup>3</sup>*Computational Condensed Matter Physics Laboratory, RIKEN, Wako, Saitama 351-0198, Japan*

(Received 5 April 2016; published 10 June 2016)

We explore the quantum phase transition between Peierls and charge-density-wave insulating states in the one-dimensional, half-filled, extended Hubbard model with explicit bond dimerization. We show that the critical line of the continuous Ising transition terminates at a tricritical point, belonging to the universality class of the tricritical Ising model with central charge  $c = 7/10$ . Above this point, the quantum phase transition becomes first order. Employing a numerical matrix-product-state based (infinite) density-matrix renormalization group method we determine the ground-state phase diagram, the spin and two-particle charge excitations gaps, and the entanglement properties of the model with high precision. Performing a bosonization analysis we can derive a field description of the transition region in terms of a triple sine-Gordon model. This allows us to derive field theory predictions for the power-law (exponential) decay of the density-density (spin-spin) and bond-order-wave correlation functions, which are found to be in excellent agreement with our numerical results.

DOI: [10.1103/PhysRevB.93.235118](https://doi.org/10.1103/PhysRevB.93.235118)

### I. INTRODUCTION

Ising tricriticality emerges at the end point of a continuous line of Ising quantum phase transitions, above which a first-order transition occurs. In 1+1 dimensions, it is described by a conformal field theory (CFT) and more precisely the second minimal model of central charge  $c = 7/10$  [1,2]. Interestingly, the tricritical Ising model (TIM) exhibits space-time supersymmetry. Until recently, there were only a few known condensed matter realizations of the TIM such as the Blume-Capel model [3–5] or the so-called golden chain with Fibonacci anions [6]. In the last couple of years, other realizations were found in lattice models with interacting Majorana fermions [7,8], and in an extended Hubbard model (EHM) with on-site ( $U$ ) and nearest-neighbor ( $V$ ) Coulomb interactions, in a case where an (somewhat artificial) alternating ferromagnetic spin interaction ( $J$ ) was added [9]. In this model, the  $U$  and  $V$  terms induce respectively fluctuating spin-density-wave (SDW) and charge-density-wave (CDW) order. The  $J$  term promotes the formation of spin-1 moments (out of two spins on neighboring sites) and the build-up of a symmetry-protected topological (SPT) state [10], in close analogy to the spin-1 XXZ chain. As a result, the SDW gives way to a Haldane insulator (HI), and a quantum phase transition takes place between the HI and the CDW when  $V$  increases. If this HI-CDW Ising transition line meets a first-order transition line, a tricritical Ising point appears.

Another, perhaps more realistic, model system, attracting a lot of attention, is the half-filled EHM with explicit bond dimerization [11,12]. Here the formation of an SPT phase might be triggered by the Peierls instability. Indeed, the ground-state phase diagram, obtained within a (perturbative) weak-coupling approach [11], contains besides the CDW a bond-dimerized phase. In order to distinguish this phase from the bond-order-wave (BOW) phase in the EHM [13,14], which arises as a result of spontaneous symmetry breaking, we will call it a *Peierls insulator* (PI) in the following. The quantum phase transition line between the insulating CDW and PI phases belongs to the universality class of the two-dimensional

Ising model [11,12], and has been argued to terminate in a tricritical point, where the phase transition changes from continuous to first order. The existence and universality class of the tricritical point is an open question however. To address this issue, not only a numerical study should be possible (e.g., along the lines of Ref. [9]), but also a field theoretical analysis, based on the results of Ref. [12].

The aim of the present work is to establish the tricritical Ising universality class at the tricritical point on the PI-CDW transition line of the half-filled EHM with staggered bond dimerization, using both a matrix-product-state (MPS) based numerical density-matrix renormalization group (DMRG) technique [15] and a bosonization approach [16,17] combined with a field theoretical analysis.

The outline of this paper is as follows. In Sec. II, we introduce and motivate the model Hamiltonian under investigation. Section III presents our DMRG results, in particular the ground-state phase diagram, the excitation gaps, and the entanglement entropy. Section IV describes the field theoretical approach and makes predictions for the quantum critical line, as well as for the density-density, spin-spin, and bond-order-wave correlations (see also Appendix), which can be used to analyze our numerical data. We conclude in Sec. V.

### II. MODEL

The Hamiltonian of the EHM is defined as

$$\begin{aligned} \hat{H}_{\text{EHM}} = & -t \sum_{j\sigma} (\hat{c}_{j\sigma}^\dagger \hat{c}_{j+1\sigma} + \text{H.c.}) \\ & + U \sum_j \left( \hat{n}_{j\uparrow} - \frac{1}{2} \right) \left( \hat{n}_{j\downarrow} - \frac{1}{2} \right) \\ & + V \sum_j (\hat{n}_j - 1)(\hat{n}_{j+1} - 1), \end{aligned} \quad (1)$$

where  $\hat{c}_{j\sigma}^\dagger$  ( $\hat{c}_{j\sigma}$ ) creates (annihilates) an electron with spin  $\sigma = \uparrow, \downarrow$  in a Wannier orbital centered around site  $j$ ,

$\hat{n}_{j\sigma} = \hat{c}_{j\sigma}^\dagger \hat{c}_{j\sigma}$ , and  $\hat{n}_j = \hat{n}_{j\uparrow} + \hat{n}_{j\downarrow}$ . For  $V = 0$ , the ground state has fluctuating SDW order (there is no long-range order, but the dominant correlations are of SDW type) with gapless spin and gapped charge excitations  $\forall U > 0$  [17]. In the regime  $V/U \lesssim 1/2$ , the ground state remains a SDW, but acquires  $2k_F$ -CDW order when  $V/U \gtrsim 1/2$ . The SDW and CDW phases are separated by a narrow BOW phase below the critical end point [18–22]. The BOW phase exhibits spontaneous breaking of translational symmetry and is characterized by a staggered modulation of the kinetic energy density. Adding a staggered ferromagnetic spin interaction,  $\hat{H}_J = J \sum_{j=1}^{L/2} \hat{S}_{2j-1} \hat{S}_{2j}$  with  $\hat{S}_j = (1/2) \sum_{\sigma\sigma'} \hat{c}_{j\sigma}^\dagger \sigma_{\sigma\sigma'} \hat{c}_{j\sigma'}$ , to the 1D EHM, the alternating spin exchange tends to form spin-1 moments with the result that the SPT HI [10] replaces the Mott insulating and BOW states of the EHM at small  $V/U$  [9].

In the following, we ask whether a similar scenario holds for the half-filled EHM with staggered bond dimerization:

$$\hat{H} = \hat{H}_{\text{EHM}} + \hat{H}_\delta, \quad (2)$$

$$\hat{H}_\delta = -t \sum_{j\sigma} \delta(-1)^j (\hat{c}_{j\sigma}^\dagger \hat{c}_{j+1\sigma} + \text{H.c.}). \quad (3)$$

It was previously shown that in the large- $U$  limit the low-lying excitations of (2) are chargeless spin triplet and spin singlet excitations [16,23–28], whose dynamics is described by a spin-Peierls Hamiltonian.

For finite  $U$ , the Tomonaga-Luttinger liquid parameters have been determined at and near commensurate band fillings [29], by means of DMRG calculations. In the weak electron-electron interaction regime, perturbative [30,31] and renormalization group [11,32,33] approaches determined that the system realizes PI and CDW phases at half-filling. Exploiting DMRG and field theory, it was shown that the transition between these two phases belongs to the universality class of the two-dimensional Ising model [11,12].

### III. DMRG TREATMENT

In this section, we examine the ground-state properties of the 1D lattice Hamiltonian (2) with a high accuracy by means of the MPS-based infinite DMRG (iDMRG) technique [34,35]. The method works directly in the thermodynamic limit. The PI and CDW boundaries are characterized by various excitation gaps obtained by DMRG combined with the infinite MPS representation on the boundaries, see previous work by some of the authors [9]. When tracing the central charge along the PI-CDW transition line, we use DMRG for finite systems with periodic boundary conditions (PBC).

#### A. Phase diagram

According to weak-coupling renormalization-group results [11], a bond alternation  $\delta$  changes the universality class of the BOW-CDW transition in the EHM from Gaussian- to Ising-type. The Ising criticality has been confirmed by DMRG computations [12].

Figure 1 presents the complete ground-state phase diagram of the EHM with bond dimerization, as obtained by the

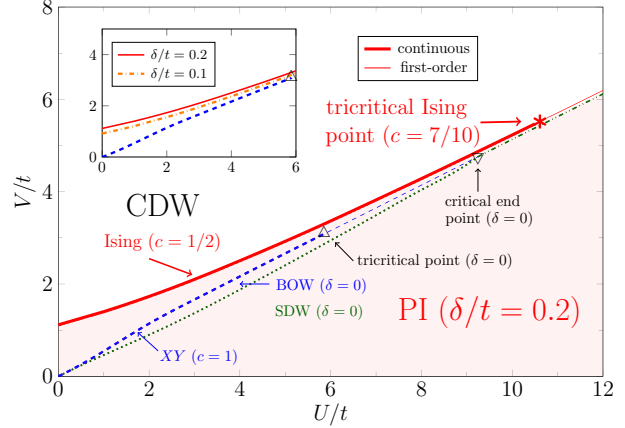


FIG. 1. iDMRG ground-state phase diagram of the 1D EHM with bond dimerization (2). The red solid line gives the PI-CDW phase boundaries for  $\delta/t = 0.2$ . The quantum phase transition is continuous (first order) below (above) the tricritical Ising point  $[U_t, V_t]$  marked by the asterisk. For comparison results for the BOW-CDW (blue dashed line), SDW-BOW (green dotted line), and SDW-CDW (green dashed-dotted line) transitions of the pure EHM ( $\delta = 0$ ) were included [22]. (Inset) PI-CDW transition for  $\delta/t = 0.1$  and  $0.2$  in the weak-coupling regime. As expected, decreasing  $\delta/t$ , the transition lines come closer to BOW-CDW transition line of the pure EHM.

iDMRG technique. The phase boundaries for the pure EHM are also included (blue and green lines). The dimerized PI phase replaces entirely the SDW and BOW states of the EHM. The PI state has the lowest energy also in the weak-coupling regime, and even at  $U/t = 0$ . This finding confirms previous weak-coupling renormalization group results [11]. In the intermediate-to-strong coupling regime, the PI-CDW transition line converges to those of the BOW/SDW-CDW transition for the pure EHM. The transition is continuous up to the tricritical Ising point  $[U_t, V_t](\delta)$ , which converges naturally to the tricritical point of the EHM when  $\delta \rightarrow 0$ . Above  $[U_t, V_t]$ , the PI-CDW transition becomes first order. At very large  $U/t$ , the phase boundaries of the PI/SDW-CDW transitions are almost indistinguishable.

We now characterize the different ground states of the model (2) in some more detail. Since the dimerized PI state can be considered as an SPT state, the entanglement spectrum plays an important role in our analysis. The so-called entanglement spectrum  $\epsilon_\alpha$  can be extracted from the singular value decomposition [9]. Dividing our system into two subblocks,  $\mathcal{H} = \mathcal{H}_L \otimes \mathcal{H}_R$ , and considering the reduced density matrix  $\rho_L = \text{Tr}_R[\rho]$ , the entanglement spectra are given by the singular values  $\lambda_\alpha$  of  $\rho_L$  as  $\epsilon_\alpha = -2 \ln \lambda_\alpha$ . Moreover, the correlation length  $\xi_\chi$  can be determined from the second largest eigenvalue of the transfer matrix for some bond dimension  $\chi$  used in the iDMRG simulation [34,35]. While the physical correlation length diverges at the critical point,  $\xi_\chi$  stays finite, as a consequence of working with a finite bond dimension  $\chi$ . Because of  $\xi_\chi$ 's rapid increase with  $\chi$  near the critical point,  $\xi_\chi$  can be used nevertheless to determine the phase transition. We performed iDMRG simulations with  $\chi$

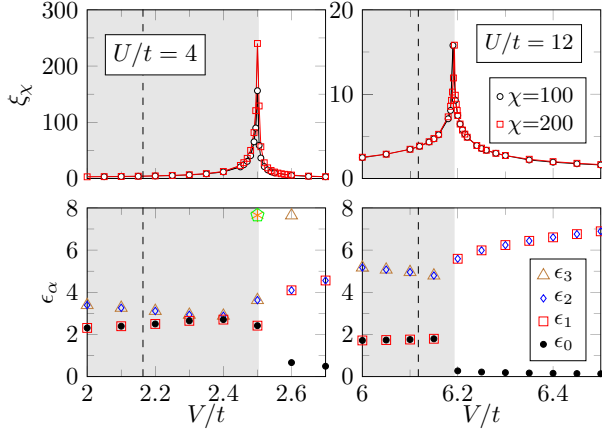


FIG. 2. Correlation length  $\xi_\chi$  (top) and entanglement spectrum  $\epsilon_\alpha$  (bottom) as a function of  $V/t$  for  $U/t = 4$  (left) and  $U/t = 12$  (right), where  $\delta/t = 0.2$ . Data are obtained by iDMRG. Dashed lines give the BOW-CDW (SDW-CDW) transition for  $U/t = 4$  ( $U/t = 12$ ) in the EHM [22].

up to 400, so that the effective correlation length at criticality is less or at most equal 300.

Figure 2 gives  $\xi_\chi$  and  $\epsilon_\alpha$  as functions of  $V/t$  for fixed  $\delta/t = 0.2$ , at two characteristic  $U/t$  values. In the weak-to-intermediate coupling regime,  $U/t = 4$ , we find a distinct peak in the correlation length at  $V_c/t \simeq 2.504$ , which increases rapidly as  $\chi$  grows from 100 to 200, indicating the divergence of the correlation length  $\xi_\chi \rightarrow \infty$  as  $\chi \rightarrow \infty$ , i.e., a quantum phase transition (of Ising type, as will be shown in Sec. III C). In contrast, at strong coupling  $U/t = 12$ , the peak height stays almost constant at  $V_c/t \simeq 6.194$  when  $\chi$  is enhanced. Decreasing the magnitude of  $\delta/t$ , the transition points will approach those of the pure EHM, e.g., for  $\delta/t = 0.1$  and  $U/t = 4$  we find  $V_c/t \simeq 2.372$ , with a simultaneous reduction of the  $\xi_\chi$ 's peak heights. Most notably, the entanglement spectra of the dimerized SPT phase exhibits a distinguishing double degeneracy in the lowest entanglement level [10]; for  $V > V_c$ , in the CDW phase, this level is nondegenerate.

### B. Excitation gaps

Let us now analyze the behavior of the various excitation gaps. Following previous treatment of the SPT phase [9,36], we define the spin-, two-particle charge-, and neutral gaps as

$$\Delta_s = E_0(N, 1) - E_0(N, 0), \quad (4)$$

$$\Delta_c = \frac{1}{2}[E_0(N + 2, 0) + E_0(N - 2, 0) - 2E_0(N, 0)], \quad (5)$$

and

$$\Delta_n = E_1(N, 0) - E_0(N, 0), \quad (6)$$

respectively. Here,  $E_0(N_e, S_{\text{tot}}^z)$  denotes the ground-state energy of the finite system with  $L$  sites, given the number of electrons  $N_e$  and the  $z$  component of total spin  $S_{\text{tot}}^z$ .  $E_1(N_e, S_{\text{tot}}^z)$  is the corresponding energy of the first excited state.

In the pure EHM ( $\delta = 0$ ), at small-to-intermediate  $U/t$  and  $V/t$ , both  $\Delta_c$  and  $\Delta_n$  vanish at the BOW-CDW transition,

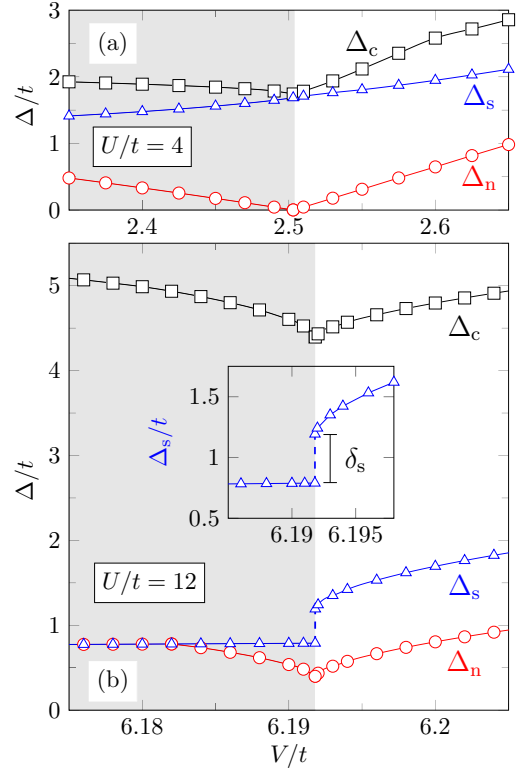


FIG. 3. Charge ( $\Delta_c$ ), spin ( $\Delta_s$ ), and neutral ( $\Delta_n$ ) gaps in dependence on  $V/t$  for (a)  $U/t = 4$  and (b)  $U/t = 12$ . Again,  $\delta/t = 0.2$ . The dimerized PI (CDW) phase is marked in gray (white). Note the jump of the spin gap,  $\delta_s \equiv \Delta_s(V_c^+) - \Delta_s(V_c^-)$ , at  $V_c/t$ .

whereas  $\Delta_s$  stays finite. Turning on the dimerization  $\delta$ , also the charge gap becomes finite, while the neutral gap still closes linearly, reflecting the fact that the transition point belongs to the Ising universality class, see Fig. 3(a) for  $U/t = 4$ , where  $V_c/t \simeq 2.503$ .

By contrast, in the strong-coupling regime, the neutral gap stays finite passing the transition point, see Fig. 3(b) for  $U/t = 12$ . Most strikingly, the spin gap exhibits a jump at the transition point ( $V_c/t \simeq 6.192$ ), which indicates a first-order transition.

### C. Entanglement entropy

We finally determine the universality class of the PI-CDW quantum phase transition. When the system becomes critical, the central charge  $c$  can easily be deduced from the entanglement entropy [36,37]. CFT tells us that the von Neumann entropy for a system with PBC is [38]

$$S_L(\ell) = \frac{c}{3} \ln \left[ \frac{L}{\pi} \sin \left( \frac{\pi \ell}{L} \right) \right] + s_1, \quad (7)$$

where  $s_1$  is a nonuniversal constant. In the face of the doubled unit cell of the SPT phase the related formula for the central charge should be modified as [39]

$$c^*(L) \equiv \frac{3[S_L(L/2 - 2) - S_L(L/2)]}{\ln\{\cos[\pi/(L/2)]\}}. \quad (8)$$

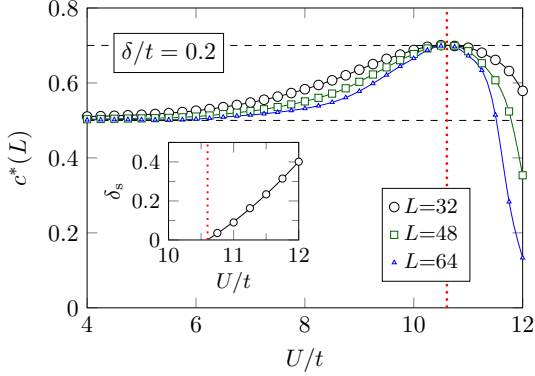


FIG. 4. Central charge  $c^*(L)$  along the PI-CDW transition line for  $\delta/t = 0.2$ . DMRG data (obtained with PBC) indicate the Ising universality class ( $c = 1/2$ ) for  $U < U_t$  and, most notably, a tricritical Ising point with  $c = 7/10$  at  $U_t$  (red dotted line). (Inset) Jump-value of the spin gap for  $U \gtrsim U_t$ . The infinite MPS data point to a first-order transition.

Figure 4 displays  $c^*(L)$  along the PI-CDW transition line, varying  $U$  and  $V$  simultaneously at fixed dimerization strength  $\delta/t = 0.2$ . With increasing  $U$ , we find clear evidence for a crossover from  $c^*(L) \simeq 1/2$  to  $c^*(L) \simeq 7/10$ , which signals Ising tricriticality.

Alternatively, the tricritical Ising point can be estimated from the magnitude of the jump of the spin gap,  $\delta_s$ , see inset of Fig. 3 for  $U/t = 12$ .  $\delta_s$  should be finite for  $U > U_t$ , and is expected to vanish at the tricritical Ising point, where  $U = U_t$ . This is confirmed by the inset of Fig. 4. Obviously,  $\delta_s$  closes at  $U_t/t \simeq 10.6$ , in accord with the critical value estimated from the numerically obtained central charge  $c^*(L)$  in the main panel.

#### IV. FIELD THEORY ANALYSIS

The weak-coupling regime  $U, V \ll t$  of the model (2) can be analyzed by field theory methods [11,12]. A standard bosonization analysis [16,17] leads to the following form of the low-energy Hamiltonian:

$$\begin{aligned} \mathcal{H} &= \sum_{\alpha=c,s} \frac{v_\alpha}{16\pi} [(\partial_x \Phi_\alpha)^2 + (\partial_x \Theta_\alpha)^2] + \mathcal{H}_{\text{int}}, \\ \mathcal{H}_{\text{int}} &= -\lambda_c \cos(\beta_c \Phi_c) \\ &\quad + \lambda_s \left\{ \cos(\Phi_s) + \frac{a_0^2}{16} [(\partial_x \Theta_s)^2 - (\partial_x \Phi_s)^2] \right\} \\ &\quad + \lambda_\delta \cos\left(\frac{\Phi_s}{2}\right) \cos\left(\frac{\beta_c}{2} \Phi_c\right) \\ &\quad + \lambda'_\delta \cos\left(\frac{\Phi_s}{2}\right) \cos\left(\frac{3\beta_c}{2} \Phi_c\right) + \dots \end{aligned} \quad (9)$$

Here,  $a_0$  is the lattice spacing,  $\Phi_{s,c}$  are canonical Bose fields associated with the collective spin and charge degrees of freedom, and  $\Theta_{s,c}$  the associated dual fields fulfilling

$$[\Phi_\alpha(x), \Theta_{\alpha'}(x')] = 4\pi i \delta_{\alpha,\alpha'} \text{sgn}(x - x'). \quad (10)$$

The parameters  $\beta_c, \lambda_{c,s}, \lambda_\delta, \lambda'_\delta, v_{c,s}$  can be determined at weak coupling  $U, V, \delta \ll t$ . Compared to Ref. [12], we have retained one higher harmonic in the interaction potential between spin and charge degrees of freedom. The reason for this will become clear later on.

#### A. Quantum critical line

It was shown in Refs. [11] and [12] that for appropriate choices of the parameters  $U, V$ , and  $\delta$  the spin sector is gapped, while the charge sector undergoes a quantum phase transition. In the vicinity of this critical line, we have

$$\cos\left(\frac{\Phi_s}{2}\right) \neq 0. \quad (11)$$

Integrating out the massive spin degrees of freedom then leads to an effective low-energy description of the charge sector by a triple sine-Gordon model

$$\begin{aligned} \mathcal{H}_c^{\text{eff}} &= \frac{v}{16\pi} [(\partial_x \Phi_c)^2 + (\partial_x \Theta_c)^2] + g_\delta \cos\left(\frac{\beta_c}{2} \Phi_c\right) \\ &\quad + g_c \cos(\beta_c \Phi_c) + g'_\delta \cos\left(\frac{3\beta_c}{2} \Phi_c\right) + \dots \end{aligned} \quad (12)$$

If we neglect the last term, we arrive at the two-frequency sine-Gordon model discussed in Ref. [12]. It exhibits a quantum phase transition in the Ising universality class [40]. In the classical limit  $\beta_c \rightarrow 0$ , this corresponds to values of  $g_c$  and  $g_\delta$  such that the quadratic terms in the expansion of the cosines precisely cancel. The reason for retaining the last term in (12) is now clear: by fine-tuning the parameters  $g_c, g_\delta, g'_\delta$  in the classical limit, we can set the coefficient of the quartic term in the expansion of the interaction potential to zero as well, which corresponds to a phase transition in the tricritical Ising universality class. This scenario is known to persist in the full quantum theory [41].

It is important to note that while the field theories (9) and (12) are initially derived in the limit  $U, V, \delta \ll t$ , they have a wider regime of applicability, provided that their parameters are adjusted appropriately. In the following, we will assume that the description (12) applies along the line of quantum phase transitions even at large values of  $U/t$  and  $V/t$ . This will allow us to make predictions for the large distance behavior of various correlation functions, which then can be tested by numerical computations for the lattice model.

#### B. Density correlations

In the field theory limit, the bosonized form of the electron density is

$$n_j \rightarrow \rho_0(x) + (-1)^j \rho_\pi(x), \quad x = ja_0, \quad (13)$$

where

$$\begin{aligned} \rho_0(x) &= \text{const} - \frac{\beta_c}{2\pi} \partial_x \Phi_c + \hat{A}_0 \partial_x \Phi_c \cos\left(\frac{\Phi_s}{2}\right) + \dots, \\ \rho_\pi(x) &= \hat{A}_\pi \sin\left(\frac{\beta_c}{2} \Phi_c\right) \cos\left(\frac{\Phi_s}{2}\right) + \dots \end{aligned} \quad (14)$$

Here we have absorbed Klein factors into the nonuniversal amplitudes  $\hat{A}_{0,\pi}$ . Importantly, at half-filling, the smooth



component  $\rho_0(x)$  does not contain a  $4k_F$  umklapp contribution [42]. As this is quite important, it is worthwhile to review the derivation of this fact. We note that the Hamiltonian (2) is invariant under the particle-hole transformation

$$\hat{C}\hat{c}_{j,\sigma}\hat{C}^\dagger = (-1)^j\hat{c}_{j,-\sigma}. \quad (15)$$

The electron density operator is odd under (15)

$$\hat{C}(\hat{n}_j - 1)\hat{C}^\dagger = 1 - \hat{n}_j. \quad (16)$$

In the field theory, Eq. (15) is implemented as follows:

$$\begin{aligned} \hat{C}\varphi_c\hat{C}^\dagger &= -\varphi_c, & \hat{C}\bar{\varphi}_c\hat{C}^\dagger &= -\bar{\varphi}_c, \\ \hat{C}\varphi_s\hat{C}^\dagger &= \varphi_s, & \hat{C}\bar{\varphi}_s\hat{C}^\dagger &= \bar{\varphi}_s, \\ \hat{C}\eta_\sigma\hat{C}^\dagger &= \eta_{-\sigma}, & \hat{C}\bar{\eta}_\sigma\hat{C}^\dagger &= \bar{\eta}_{-\sigma}. \end{aligned} \quad (17)$$

Here  $\eta_\uparrow$ ,  $\eta_\downarrow$ ,  $\bar{\eta}_\downarrow$ , and  $\bar{\eta}_\uparrow$  are Klein factors, cf. Ref. [43]. At general band filling, the  $4k_F$  term in the charge density takes the form

$$\rho_{4k_F}(x) = A_{4k_F}\eta_\uparrow\bar{\eta}_\uparrow\eta_\downarrow\bar{\eta}_\downarrow\cos(\beta_c\Phi_c - 4k_Fx) + \dots \quad (18)$$

Equation (17) implies that at half-filling ( $4k_Fx = 0 \pmod{2\pi}$ ), we have

$$C\rho_{4k_F}(x)C^\dagger = \rho_{4k_F}(x), \quad (19)$$

which can be reconciled with Eq. (16) only by taking  $A_{4k_F} = 0$ .

In the vicinity of the quantum critical line, we can again integrate out the gapped spin degrees of freedom and arrive at

$$\begin{aligned} \rho_0(x) &= \text{const} + B_0\partial_x\Phi_c + \dots, \\ \rho_\pi(x) &= B_\pi\sin\left(\frac{\beta_c}{2}\Phi_c\right) + \dots \end{aligned} \quad (20)$$

Finally, we need to relate our charge boson to the primary fields in the tricritical Ising model. This can be done by referring to the Landau-Ginzburg description of the transition, see, e.g., Ref. [44]. Expanding our low-energy effective theory (12) for  $\beta_c \ll 1$ , we obtain the Landau-Ginzburg model

$$\mathcal{L} \sim \frac{v}{16\pi}\Phi_c\left(\partial_x^2 - \frac{\partial_t^2}{v^2}\right)\Phi_c - \lambda_2\Phi_c^2 - \lambda_4\Phi_c^4 - \lambda_6\Phi_c^6 + \dots \quad (21)$$

In this limit, we can then use Ref. [44] to relate local operators in our theory to primary fields in the TIM. In particular, one has

$$\begin{aligned} \Phi_c(x) &\leftrightarrow \sigma(x), \\ \Phi_c^2(x) &\leftrightarrow \epsilon(x), \\ \Phi_c^3(x) &\leftrightarrow \sigma'(x), \\ \Phi_c^4(x) &\leftrightarrow \epsilon'(x), \end{aligned} \quad (22)$$

where  $\sigma$ ,  $\epsilon$ ,  $\sigma'$ , and  $\epsilon'$  are respectively the magnetization field, energy density, submagnetization, and vacancy density in the TIM. Proceeding in the same way for the components of the charge density (20) then suggests the following identifications:

$$\begin{aligned} \rho_\pi(x) &\sim A\sigma(x) + \dots, \\ \rho_0(x) &\sim \text{const} + Ba_0\partial_x\sigma(x) + \dots \end{aligned} \quad (23)$$

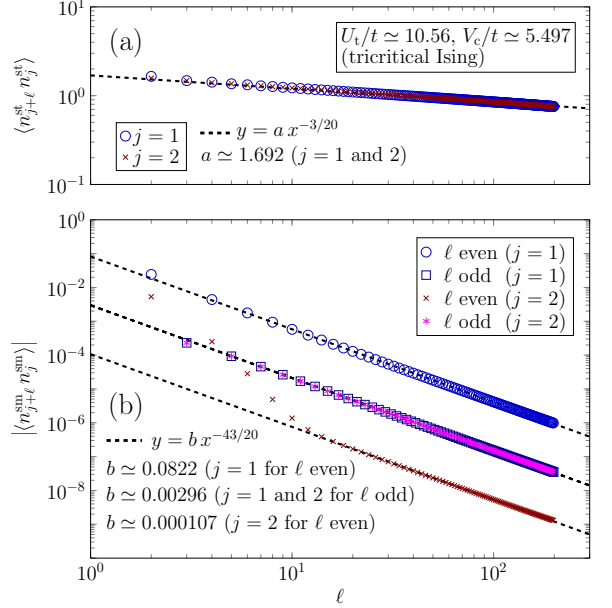


FIG. 5. Density-density correlation functions at the tricritical Ising point for  $\delta/t = 0.2$ . Data obtained by iDMRG with  $\chi = 1600$ . The correlation functions (symbols) show a power-law decay, in accordance with the field theory predictions, Eqs. (26) and (27).

Using the known results for correlation functions in the TIM, we then arrive at the following prediction for the density-density correlator at the Ising tricritical point:

$$\langle (\hat{n}_{j+\ell} - 1)(\hat{n}_j - 1) \rangle \sim (-1)^\ell \frac{A^2}{\ell^{3/20}} + \dots, \quad \ell \gg 1. \quad (24)$$

We may isolate the subleading behavior by considering smooth and staggered combinations of the density on the lattice:

$$\begin{aligned} \hat{n}_j^{\text{st}} &= (-1)^j(\hat{n}_j - \hat{n}_{j+1}) \sim 2A\sigma(x) + \dots, \\ \hat{n}_j^{\text{sm}} &= \frac{\hat{n}_j + \hat{n}_{j+1}}{2} - 1 \sim (B - (-1)^j A)a_0\partial_x\sigma + \dots \end{aligned} \quad (25)$$

The TIM predictions for two point functions of these operators are

$$\begin{aligned} \langle \hat{n}_{j+\ell}^{\text{st}} \hat{n}_j^{\text{st}} \rangle &\sim 4A^2\ell^{-3/20} + \dots, \\ \langle \hat{n}_{j+\ell}^{\text{sm}} \hat{n}_j^{\text{sm}} \rangle &\sim C_{j,\ell}\ell^{-43/20} + \dots, \end{aligned} \quad (26)$$

$$C_{j,\ell} = -\frac{69}{400} \begin{cases} B^2 - A^2/4 & \ell \text{ odd} \\ [B - (-1)^j A/2]^2 & \ell \text{ even.} \end{cases} \quad (27)$$

The predictions (26) and (27) can now be compared with iDMRG simulations of the 1D lattice model (2). Figure 5 shows the iDMRG results for two point functions of the (a) staggered and (b) smooth combinations of the particle density at the TIM critical point of the lattice model. The results for  $\langle \hat{n}_{j+\ell}^{\text{st}} \hat{n}_j^{\text{st}} \rangle$  are seen to be in excellent agreement with the leading  $\ell^{-3/20}$  dependence at long distances predicted by Eq. (26) for both  $j = 1$  and  $2$ . To test the second prediction in Eq. (27), we consider separately the cases of even and odd  $\ell$  for  $j = 1$  and  $j = 2$ , and plot the absolute value of  $\langle \hat{n}_{\ell+1}^{\text{sm}} \hat{n}_1^{\text{sm}} \rangle$

in Fig. 5(b). Again the numerical data are seen to be in excellent agreement with the predicted  $\ell^{-43/20}$  dependence at large separations. The prefactors for the power laws extracted from our iDMRG data are in very good agreement with the prediction of Eq. (27) as well.

### C. BOW correlations

The BOW order parameter is given by  $\hat{m}_{\text{BOW}} = (1/L) \sum_j \hat{m}_j$  with

$$\hat{m}_j = (-1)^j \sum_{\sigma} [\hat{c}_{j\sigma}^{\dagger} \hat{c}_{j+1\sigma} + \text{H.c.}] \quad (28)$$

The BOW order parameter is always nonzero in the vicinity of the transition

$$\langle \hat{m}_{\text{BOW}} \rangle \neq 0. \quad (29)$$

The bosonized expression for  $\hat{m}_{\text{BOW}}$  is

$$\begin{aligned} \hat{m}_j \sim & (-1)^j \text{const} + \hat{C}_{\pi} \cos\left(\frac{\beta_c}{2} \Phi_c\right) \cos\left(\frac{\Phi_s}{2}\right) \\ & + (-1)^j \hat{C}_0 \cos(\beta_c \Phi_c) + \dots \end{aligned} \quad (30)$$

We now proceed in the same way as for the charge density. We integrate out the gapped spin degrees of freedom, then expand for small  $\beta_c$ , and finally use the Landau-Ginzburg description to identify which operators in the TIM dominate the long-distance behavior of the BOW correlations. The main difference compared to the charge density is that the BOW order parameter is even under charge conjugation, and concomitantly we find

$$\hat{m}_j \sim \langle \hat{m}_{\text{BOW}} \rangle + D_0 \epsilon(x) + (-1)^j [D_1 + D_2 \epsilon(x)] + \dots \quad (31)$$

We again form smooth and staggered combinations,

$$\begin{aligned} \hat{m}_j^{\text{st}} &= (-1)^j (\hat{m}_j - \hat{m}_{j+1}) \sim 2[D_1 + D_2 \epsilon(x)] + \dots, \\ \hat{m}_j^{\text{sm}} &= \frac{\hat{m}_j + \hat{m}_{j+1}}{2} \sim \langle \hat{m}_{\text{BOW}} \rangle + D_0 \epsilon(x) + \dots \end{aligned} \quad (32)$$

The TIM predictions for BOW correlations are then

$$\langle \hat{m}_{j+\ell}^{\text{st}} \hat{m}_j^{\text{st}} \rangle \sim 4[D_1^2 + D_2^2 \ell^{-2/5}] + \dots, \quad (33)$$

$$\langle \hat{m}_{j+\ell}^{\text{sm}} \hat{m}_j^{\text{sm}} \rangle \sim \langle \hat{m}_{\text{BOW}} \rangle^2 + D_0^2 \ell^{-2/5} + \dots \quad (34)$$

These predictions can be compared to iDMRG computations in Fig. 6. In order to remove the constant terms in Eqs. (33) and (34), we first fit the numerical results to the functional form  $y = A + Bx^{-2/5}$ . This allows us to extract the constants as shown in the upper panels in Fig. 6. Subtracting the estimated constants from original data, both staggered and smooth correlation functions are seen to decay in a power-law fashion compatible with the TIM prediction.

### D. Spin correlations

As the spin sector is gapped, we expect an exponential decay for the spin two-point function

$$\langle \hat{S}_{j+\ell}^z \hat{S}_j^z \rangle \sim E_0 e^{-\ell/\xi_1} + E_1 (-1)^{\ell} e^{-\ell/\xi_2}. \quad (35)$$

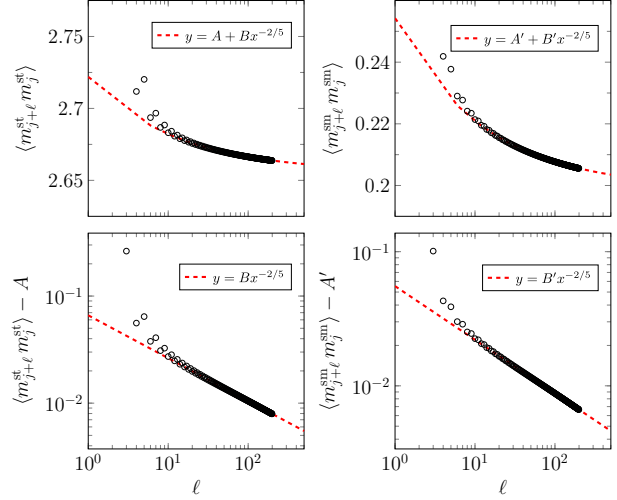


FIG. 6. BOW correlation functions at the tricritical Ising point for  $\delta/t = 0.2$  computed by iDMRG with  $\chi = 1600$ . (Top) The asymptotic values for the two-point functions of staggered and smooth combinations of the BOW density are estimated by fitting to Eqs. (33) and (34). (Bottom) log-log plots of the same correlation functions with the asymptotic values subtracted show power-law decay compatible with Ising tricriticality.

Here we have used that the low energy degrees of freedom in the spin sector occur at wave numbers zero and  $\pi$ . This behavior is again in good agreement with iDMRG computations as shown in Fig. 7. The correlation lengths extracted by fitting the iDMRG results to Eq. (35) are found to be in reasonable agreement with the corresponding eigenvalue of the transfer matrix  $\xi_1 \simeq 1.225$ .

To summarize this section, we have seen that field theory predictions obtained by means of a triple sine-Gordon model description of the tricritical Ising transition are in excellent agreement with iDMRG computations for the lattice model. This firmly establishes that the critical endpoint is in the universality class of the TIM. We note that an analogous field

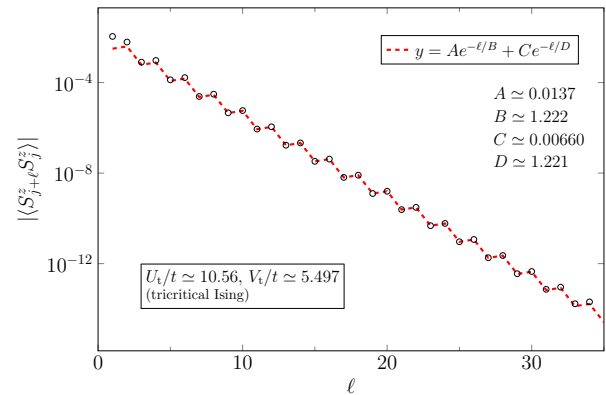


FIG. 7. Spin correlation function (symbols) at the tricritical Ising point for  $\delta/t = 0.2$  using the iDMRG with  $\chi = 1600$ , showing exponential decay. The line is a fit to Eq. (35).

theory description applies along the entire Ising critical line. Here, field theory predictions are again in excellent agreement with iDMRG computations as shown in Appendix.

## V. CONCLUSIONS

We have revisited ground-state properties of the one-dimensional half-filled extended Hubbard model with staggered bond dimerization. We have employed a combination of numerical and analytical techniques to map out the ground-state phase diagram in detail, and identify all quantum critical regions. At fixed dimerization  $\delta$ , there are two distinct phases. A CDW phase at large  $V \gtrsim U$  is separated from a PI phase at  $U \gtrsim V$  by an Ising critical line, that terminates in a critical point which we have shown to be in the universality class of the tricritical Ising model. Our identification was based on a detailed analysis of both entanglement entropy scaling and critical exponents describing the power-law decay of several two-point correlation functions.

Correlation functions of local operators in the EHM with bond dimerization access only the bosonic sector of the TIM CFT. This precludes us from directly investigating the emergence of supersymmetry at low energies/long distances. To “see” the fermionic sector one presumably would have to consider correlation functions of suitably constructed nonlocal operators. It would be interesting to investigate this possibility further. Another issue worth pursuing is to investigate the scaling regime around the TIM critical point in the framework of the EHM with bond dimerization. It would be interesting to investigate whether it is possible to make contact with the field theory predictions of Ref. [45].

## ACKNOWLEDGMENTS

We thank P. Fendley and G. Mussardo for useful discussions. The iDMRG simulations were performed using the ITensor library [46]. This work was supported by Deutsche Forschungsgemeinschaft (Germany), SFB 652, project B5, and by the EPSRC under Grant No. EP/N01930X/1 (FHLE).

## APPENDIX: CORRELATION FUNCTIONS ON THE ISING CRITICAL LINE

The tricritical Ising model describes the end point of a critical line of Ising transitions, cf. Fig. 1. The Ising critical line was previously investigated by DMRG methods in Ref. [12] and the critical exponents were extracted by considering the scaling of the order parameter and spectral gap in the vicinity of the transition. In this Appendix, we complement these results by examining the power law behavior of correlations functions at the transition, i.e., the same diagnostics we used in the main text to identify the TIM critical point.

The identification of operators is analogous to the TIM case. The projections of the particle density and BOW order parameter onto local fields in the Ising CFT are again of the form (23) and (32), but  $\sigma(x)$  and  $\epsilon(x)$  are now the spin field and energy density of the Ising CFT. This leads to the following prediction for the large distance asymptotics of the density-density correlator

$$\langle (\hat{n}_{j+\ell} - 1)(\hat{n}_j - 1) \rangle \sim (-1)^\ell \tilde{A} \ell^{-1/4} + \dots \quad (\text{A1})$$

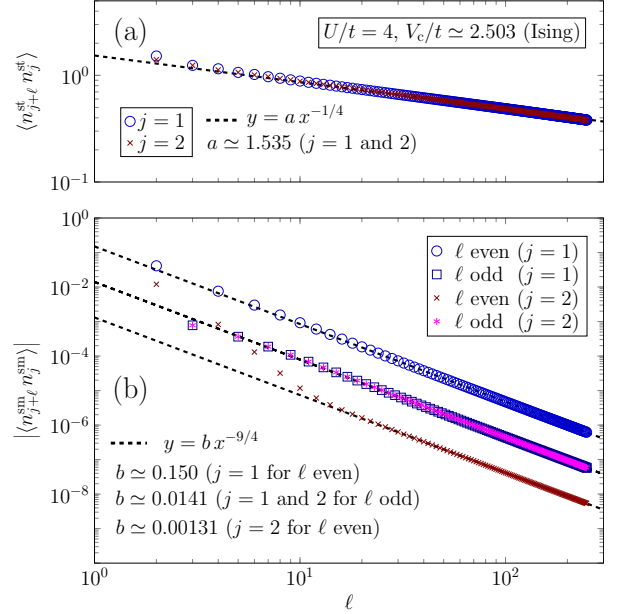


FIG. 8. Density-density correlation functions at the Ising transition point ( $V_c \simeq 2.503$ ) for  $U/t = 4$  and  $\delta/t = 0.2$ , using the iDMRG with  $\chi = 1600$ . (a) The correlator of the staggered combination is in excellent agreement with Eq. (A2) with  $4\tilde{A}^2 \approx 1.535$ . (b) Correlations of the smooth combination  $\hat{n}_j^{\text{sm}}$  are plotted separately for odd and even  $\ell$  with  $j = 1$  and 2. The data are in excellent agreement with the prediction Eq. (A3).

Considering smooth and staggered combinations defined in (25) separately, we obtain

$$\begin{aligned} \langle \hat{n}_{j+\ell}^{\text{st}} \hat{n}_j^{\text{st}} \rangle &\sim 4\tilde{A}^2 \ell^{-1/4} + \dots, \\ \langle \hat{n}_{j+\ell}^{\text{sm}} \hat{n}_j^{\text{sm}} \rangle &\sim \tilde{C}_{j,\ell} \ell^{-9/4} + \dots, \end{aligned} \quad (\text{A2})$$

$$\tilde{C}_{j,\ell} = -\frac{5}{16} \begin{cases} \tilde{B}^2 - \tilde{A}^2/4 & \ell \text{ odd} \\ [\tilde{B} - (-1)^j \tilde{A}/2]^2 & \ell \text{ even}. \end{cases} \quad (\text{A3})$$

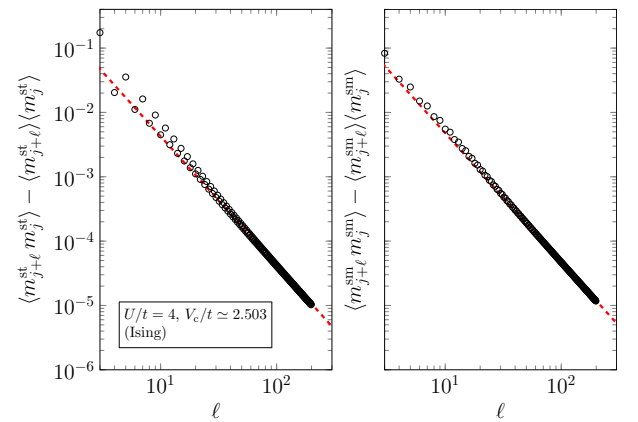


FIG. 9. BOW correlations at the Ising transition point for  $U/t = 4$  and  $\delta/t = 0.2$ . The correlators exhibit a power-law decay consistent with the field theory predictions, Eq. (A4).

These predictions are in excellent agreement with iDMRG computations for the lattice model on the Ising critical line as is shown in Fig. 8.

The field theory predictions for staggered and smooth combinations of the BOW order parameter on the Ising transition line are

$$\begin{aligned} \langle \hat{m}_{j+\ell}^{\text{st}} \hat{m}_j^{\text{st}} \rangle &\sim (-1)^\ell [\tilde{C}_4^2 + \tilde{C}_5 \ell^{-2}] + \dots, \\ \langle \hat{m}_{j+\ell}^{\text{sm}} \hat{m}_j^{\text{sm}} \rangle &\sim \langle \hat{m}_{\text{BOW}} \rangle^2 + \tilde{C}_6 \ell^{-2} + \dots. \end{aligned} \quad (\text{A4})$$

We can remove the constant contributions by considering connected correlators, which in turn exhibit power-law decay to zero at large distances. The iDMRG results shown in Fig. 9

agree perfectly with the predicted  $\ell^{-2}$  power-law decay. As a consistency check we have extracted the value of  $\langle \hat{m}_{\text{BOW}} \rangle$  by fitting the long-distance behavior of two-point function of  $\hat{m}_j^{\text{sm}}$  to the form (A4). We find it to be in excellent agreement with the value obtained by computing the one-point function.

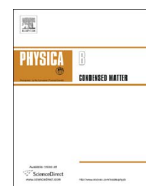
We note that the agreement between our numerical data and field theory predictions is much better along the Ising transition line than at the TIM critical point. There are two reasons for this. First, at fixed  $U/t$ , the Ising transition point ( $V_c/t$ ) can be determined more accurately than the location of the TIM transition, where two parameters ( $U$  and  $V$ ) have to be fine-tuned simultaneously. Second, the corrections to scaling are different in both cases.

- 
- [1] D. Friedan, Z. Qiu, and S. Shenker, *Phys. Rev. Lett.* **52**, 1575 (1984).
- [2] D. Friedan, Z. Qiu, and S. Shenker, *Phys. Lett. B* **151**, 37 (1985).
- [3] M. Blume, *Phys. Rev.* **141**, 517 (1966).
- [4] H. Capel, *Physica (Amsterdam)* **32**, 966 (1966).
- [5] F. C. Alcaraz, J. R. Drugowich de Felicio, R. Köberle, and J. F. Stilck, *Phys. Rev. B* **32**, 7469 (1985).
- [6] A. Feiguin, S. Trebst, A. W. W. Ludwig, M. Troyer, A. Kitaev, Z. Wang, and M. H. Freedman, *Phys. Rev. Lett.* **98**, 160409 (2007).
- [7] A. Rahmani, X. Zhu, M. Franz, and I. Affleck, *Phys. Rev. Lett.* **115**, 166401 (2015).
- [8] X. Zhu and M. Franz, *Phys. Rev. B* **93**, 195118 (2016).
- [9] F. Lange, S. Ejima, and H. Fehske, *Phys. Rev. B* **92**, 041120 (2015).
- [10] F. Pollmann, A. M. Turner, E. Berg, and M. Oshikawa, *Phys. Rev. B* **81**, 064439 (2010).
- [11] M. Tsuchiizu and A. Furusaki, *Phys. Rev. B* **69**, 035103 (2004).
- [12] H. Benthien, F. H. L. Essler, and A. Grage, *Phys. Rev. B* **73**, 085105 (2006).
- [13] M. Nakamura, *J. Phys. Soc. Jpn.* **68**, 3123 (1999).
- [14] M. Nakamura, *Phys. Rev. B* **61**, 16377 (2000).
- [15] S. R. White, *Phys. Rev. Lett.* **69**, 2863 (1992).
- [16] A. O. Gogolin, A. A. Nersisyan, and A. M. Tsvelik, *Bosonization and Strongly Correlated Systems* (Cambridge University Press, Cambridge, 1999).
- [17] F. H. L. Essler, H. Frahm, F. Göhmann, A. Klümper, and V. E. Korepin, *The One-Dimensional Hubbard Model* (Cambridge University Press, Cambridge, 2005).
- [18] P. Sengupta, A. W. Sandvik, and D. K. Campbell, *Phys. Rev. B* **65**, 155113 (2002).
- [19] A. W. Sandvik, L. Balents, and D. K. Campbell, *Phys. Rev. Lett.* **92**, 236401 (2004).
- [20] Y. Z. Zhang, *Phys. Rev. Lett.* **92**, 246404 (2004).
- [21] K.-M. Tam, S.-W. Tsai, and D. K. Campbell, *Phys. Rev. Lett.* **96**, 036408 (2006).
- [22] S. Ejima and S. Nishimoto, *Phys. Rev. Lett.* **99**, 216403 (2007).
- [23] T. Giamarchi, *Quantum Physics in One Dimension* (Oxford University Press, Oxford, 2003).
- [24] F. Gebhard, K. Bott, M. Scheidler, P. Thomas, and S. W. Koch, *Philos. Mag. B* **75**, 1 (1997).
- [25] T. Nakano and H. Fukuyama, *J. Phys. Soc. Jpn.* **50**, 2489 (1981).
- [26] A. M. Tsvelik, *Phys. Rev. B* **45**, 486 (1992).
- [27] G. S. Uhrig and H. J. Schulz, *Phys. Rev. B* **54**, R9624 (1996).
- [28] F. H. L. Essler, A. M. Tsvelik, and G. Delfino, *Phys. Rev. B* **56**, 11001 (1997).
- [29] S. Ejima, F. Gebhard, and S. Nishimoto, *Phys. Rev. B* **74**, 245110 (2006).
- [30] A. Grage, F. Gebhard, and J. Rissler, *J. Stat. Mech.: Theory Exp.* (2005) P08009.
- [31] M. Dzierzawa and C. Mocanu, *J. Phys.: Condens. Matter* **17**, 2663 (2005).
- [32] M. Sugiura and Y. Suzumura, *J. Phys. Soc. Jpn.* **71**, 697 (2002).
- [33] M. Tsuchiizu and E. Orignac, *J. Phys. Chem. Solids* **63**, 1459 (2002).
- [34] I. P. McCulloch, [arXiv:0804.2509](https://arxiv.org/abs/0804.2509).
- [35] U. Schollwöck, *Ann. Phys.* **326**, 96 (2011).
- [36] S. Ejima and H. Fehske, *Phys. Rev. B* **91**, 045121 (2015).
- [37] S. Ejima, F. Lange, and H. Fehske, *Phys. Rev. Lett.* **113**, 020401 (2014).
- [38] P. Calabrese and J. Cardy, *J. Stat. Mech.* (2004) P06002.
- [39] S. Nishimoto, *Phys. Rev. B* **84**, 195108 (2011).
- [40] G. Delfino and G. Mussardo, *Nucl. Phys. B* **516**, 675 (1998).
- [41] G. Z. Tóth, *J. Phys. A: Math. Gen.* **37**, 9631 (2004).
- [42] D. Controzzi and F. H. L. Essler, *Phys. Rev. B* **66**, 165112 (2002).
- [43] F. H. L. Essler, R. G. Pereira, and I. Schneider, *Phys. Rev. B* **91**, 245150 (2015).
- [44] M. Lässig, G. Mussardo, and J. L. Cardy, *Nucl. Phys. B* **348**, 591 (1991).
- [45] L. Lepori, G. Mussardo, and G. Z. Tóth, *J. Stat. Mech.* (2008) P09004.
- [46] <http://itensor.org/>.



Contents lists available at ScienceDirect

Physica B

journal homepage: [www.elsevier.com/locate/physb](http://www.elsevier.com/locate/physb)

# Critical behavior of the extended Hubbard model with bond dimerization



Satoshi Ejima<sup>a,\*</sup>, Florian Lange<sup>a,b</sup>, Fabian H.L. Essler<sup>c</sup>, Holger Fehske<sup>a</sup>

<sup>a</sup> Institut für Physik, Ernst-Moritz-Arndt-Universität Greifswald, 17487 Greifswald, Germany

<sup>b</sup> Computational Condensed Matter Physics Laboratory, RIKEN, Wako, Saitama 351-0198, Japan

<sup>c</sup> The Rudolf Peierls Centre for Theoretical Physics, Oxford University, Oxford OX1 3NP, United Kingdom

## ARTICLE INFO

### Keywords:

Extended Hubbard model  
(tricritical) Ising universality class

## ABSTRACT

Exploiting the matrix-product-state based density-matrix renormalization group (DMRG) technique we study the one-dimensional extended ( $U$ - $V$ ) Hubbard model with explicit bond dimerization in the half-filled band sector. In particular we investigate the nature of the quantum phase transition, taking place with growing ratio  $V/U$  between the symmetry-protected-topological and charge-density-wave insulating states. The (weak-coupling) critical line of continuous Ising transitions with central charge  $c = 1/2$  terminates at a tricritical point belonging to the universality class of the dilute Ising model with  $c = 7/10$ . We demonstrate that our DMRG data perfectly match with (tricritical) Ising exponents, e.g., for the order parameter  $\beta = 1/8$  ( $1/24$ ) and correlation length  $\nu = 1$  ( $5/9$ ). Beyond the tricritical Ising point, in the strong-coupling regime, the quantum phase transition becomes first order.

## 1. Introduction

Half a century has passed since it was proposed, yet the Hubbard model [1] is still a key Hamiltonian for the investigation of strongly correlated electron systems. Originally designed to describe the ferromagnetism of transition metals, in successive studies the Hubbard model has also been used for heavy fermions and high-temperature superconductors. The physics of the model is governed by the competition between the itinerancy of the charge carriers and their local Coulomb interaction. In one dimension (1D), seen from a theoretical point of view, the Hubbard model is a good starting point to explore, for example, Tomonaga-Luttinger liquid behavior (including spin-charge separation).

While the 1D Hubbard model is exactly solvable by Bethe Ansatz [2], most of its extensions are no longer integrable. This is even true if only the Coulomb interaction between electrons on nearest-neighbor lattice sites is added. The ground-state phase diagram of this so-called extended Hubbard model (EHM) is still a hotly debated issue. At half filling, this relates in particular to the recently discovered bond-order-wave (BOW) state located in between spin-density-wave (SDW) and charge-density-wave (CDW) phases [3,4]. To characterize the BOW state and determine its phase boundaries considerable efforts were undertaken in the last few years, using both analytical [5,6] and numerical [7–9] methods.

At present, quantum phase transitions between topologically trivial and nontrivial states arouse great interest [10–12]. In this context,

extensions of the half-filled EHM also attracted attention, mainly with regard to the formation of symmetry-protected-topological (SPT) states [11]. Including an alternating ferromagnetic spin interaction [13] or an explicit dimerization [14] in the EHM, the SDW and BOW phases are completely replaced by an SPT insulator, whereby a quantum phase transition occurs between the SPT and the CDW, the area of which shrinks. Most interestingly, the SPT-CDW continuous Ising transition with central charge  $c = 1/2$  ends at a tricritical point, belonging to the universality class of the tricritical Ising model, a second minimal model with  $c = 7/10$  [15,16]. Above this point, the quantum phase transition becomes first order. In Ref. [14] it has been demonstrated that the transition region of the EHM with bond dimerization can be described by the triple sine-Gordon model by extending the former bosonization analysis [17]. The predictions of field theory regarding power-law (exponential) decay of the density-density (spin-spin) and bond-order correlation functions are shown to be in excellent accordance with the numerical data obtained by a matrix-product-states (MPS) based density-matrix renormalization group (DMRG) technique [18,19].

The Ising criticality of the EHM with explicit dimerization was established in early work [17] that also specifies the critical exponents. The critical exponents at the tricritical point should differ from those at the ordinary Ising transition because the tricritical Ising quantum phase transition belongs to a different universality class.

Simulating the neutral gap and the CDW order parameter by DMRG, in this paper we will determine the critical exponents at both Ising and tricritical Ising transitions. The paper is structured as follows.

\* Corresponding author.

E-mail address: [ejima@physik.uni-greifswald.de](mailto:ejima@physik.uni-greifswald.de) (S. Ejima).

<http://dx.doi.org/10.1016/j.physb.2017.09.001>

Received 22 June 2017; Accepted 1 September 2017

Available online 06 September 2017

0921-4526/ © 2017 Elsevier B.V. All rights reserved.

Section 2 introduces the model Hamiltonians under consideration and discusses their ground-state properties. The critical exponents will be derived in Section 3. Section 4 summarizes our main results.

## 2. Model

### 2.1. Extended Hubbard model

The Hamiltonian of the EHM is defined as

$$\begin{aligned} \hat{H}_{\text{EHM}} = & -t \sum_{j\sigma} (\hat{c}_{j\sigma}^\dagger \hat{c}_{j+1\sigma} + \text{H. c.}) \\ & + U \sum_j \left( \hat{n}_{j\uparrow} - \frac{1}{2} \right) \left( \hat{n}_{j\downarrow} - \frac{1}{2} \right) \\ & + V \sum_j (\hat{n}_j - 1)(\hat{n}_{j+1} - 1), \end{aligned} \quad (1)$$

where  $\hat{c}_{j\sigma}^\dagger$  ( $\hat{c}_{j\sigma}$ ) creates (annihilates) an electron with spin projection  $\sigma = \uparrow, \downarrow$  at Wannier site  $j$ ,  $\hat{n}_{j\sigma} = \hat{c}_{j\sigma}^\dagger \hat{c}_{j\sigma}$ , and  $\hat{n}_j = \hat{n}_{j\uparrow} + \hat{n}_{j\downarrow}$ . In the Hubbard model limit ( $V = 0$ ), at half-filling, no long-range order exists. Instead the system shows fluctuating SDW order. The spin (charge) excitations are gapless (gapped)  $\forall U > 0$  [2]. At finite  $V$ , for  $V/U \lesssim 1/2$ , the ground state is still a SDW. When  $V/U$  becomes larger than  $1/2$  a  $2k_F$ -CDW is formed. As pointed out first by Nakamura [3,4] and confirmed later by various analytical and numerical studies [8,9,20,21], the SDW and CDW phases are separated by a narrow BOW phase below the critical end point,  $(U_{\text{cc}}^{\text{EHM}}, V_{\text{cc}}^{\text{EHM}}) \approx (9.25t, 4.76t)$ . In the BOW phase translational symmetry is spontaneously broken, which implies that the spin gap opens passing the SDW-BOW phase boundary at fixed  $U < U_{\text{cc}}^{\text{EHM}}$ . Increasing  $V$  further, the system enters the CDW phase with finite spin and charge gaps. The BOW-CDW Gaussian transition line with central charge  $c = 1$  terminates at the tricritical point,  $(U_{\text{tr}}^{\text{EHM}}, V_{\text{tr}}^{\text{EHM}}) \approx (5.89t, 3.10t)$  [9]. For  $U_{\text{tr}}^{\text{EHM}} < U < U_{\text{cc}}^{\text{EHM}}$ , the BOW-CDW transition becomes first order, characterized by a jump in the spin gap (see, Fig. 3 in Ref. [9]). Fig. 1 summarizes the rich physics of the half-filled EHM.

The criticality at the continuous BOW-CDW transition line can be verified numerically by extracting, e.g., the central charge from the correlation length ( $\xi_\chi$ ) and von Neumann entropy ( $S_\chi$ ), where  $\xi_\chi$  can be obtained from the second largest eigenvalue of the transfer matrix for some bond dimension  $\chi$  used in an infinite DMRG (iDMRG) simulation [19,22]. Conformal field theory tells us that the von Neumann entropy for a system between two semi-infinite chains is [23]

$$S_\chi = \frac{c}{6} \ln \xi_\chi + s_0 \quad (2)$$

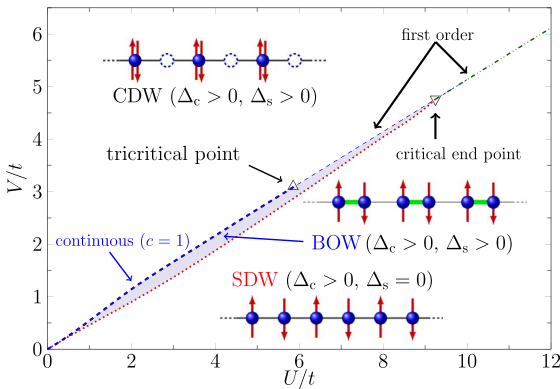


Fig. 1. DMRG ground-state phase diagram of the 1D EHM (1) at half filling [9]. The red dotted line gives the continuous SDW-BOW transition. The bold (thin) blue dashed line marks the continuous (first-order) BOW-CDW transition and the green dashed-dotted line denotes the first-order SDW-CDW transition. (For interpretation of the references to color in this figure legend, the reader is referred to the web version of this article.)

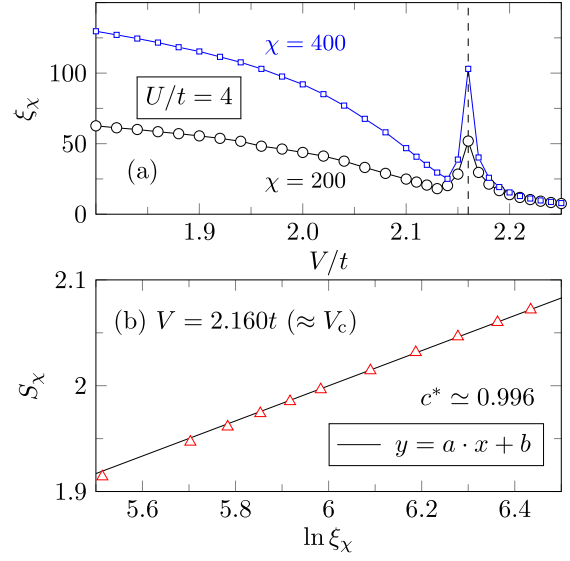


Fig. 2. (a): Correlation length  $\xi_\chi$  of the EHM as a function of  $V/t$  for  $U/t = 4$  obtained from iDMRG. The dashed line indicates the BOW-CDW transition point. (b): von Neumann entropy  $S_\chi$  as a function of logarithm of  $\xi_\chi$  at  $V \approx V_c$  for  $U/t = 4$ . The iDMRG data for  $\ln \xi_\chi > 6$  ( $\chi \geq 1800$ ) provide us the numerically obtained central charge  $c^* \approx 0.996$  by fitting to Eq. (2).

with a non-universal constant  $s_0$ .

Fig. 2(a) shows iDMRG results of  $\xi_\chi$  as a function of  $V/t$  for fixed  $U/t = 4$ . Since the system is critical in the SDW phase and at the BOW-CDW transition point, we find a rapid increase of  $\xi_\chi$  in the SDW phase and a distinct peak at the BOW-CDW critical point ( $V_c/t \approx 2.160$ ) when we increase  $\chi$  from 200 to 400. This indicates the divergence of the correlation length  $\xi_\chi \rightarrow \infty$  as  $\chi \rightarrow \infty$ . Now, plotting the von Neumann entropy  $S_\chi$  as a function of  $\ln \xi_\chi$  and fitting the graph to Eq. (2), the criticality at  $V = V_c$  can be proved, as demonstrated by Fig. 2(b). The obtained  $c^* \approx 0.996$  for iDMRG data with  $\chi \geq 1800$  corroborates the Gaussian transition resulting from a bosonization analysis [5,6]. Note that for the confirmation of the SDW-BOW transition much larger bond dimensions  $\chi$  are required in order to make clear the convergence of  $\xi_\chi$  in the BOW phase of Fig. 2.

### 2.2. EHM with explicit bond dimerization

Let us now add a staggered bond dimerization to the EHM,  $\hat{H} = \hat{H}_{\text{EHM}} + \hat{H}_\delta$ , where

$$\hat{H}_\delta = -t \sum_{j\sigma} \delta (-1)^j (\hat{c}_{j\sigma}^\dagger \hat{c}_{j+1\sigma} + \text{H. c.}). \quad (3)$$

Previous studies of this model have shown that the low lying excitations in the large- $U$  limit are chargeless spin-triplet and spin-singlet excitations [24–30], whereby the dynamics is described by an effective spin-Peierls Hamiltonian. Moreover, at finite  $U$ , the Tomonaga-Luttinger parameters have been explored at and near commensurate fillings by DMRG [31]. Particularly for half filling, it has been proven by perturbative [32,33] and renormalization group [6,34,35] approaches that the system realizes Peierls insulator (PI) and CDW phases in the weak-coupling regime. According to weak-coupling renormalization-group results [6], any finite bond dimerization  $\delta$  will change the universality class of the continuous BOW-CDW transition (realized in the pure EHM) from Gaussian to Ising type. Thereby the PI-CDW transition in the weak-to-intermediate coupling regime belongs to the universality class of the two-dimensional (2D) Ising model [6,17].

Even more interesting physics appears analyzing the intermediate-to-strong-coupling regime [14] by analogy with an effective spin-1

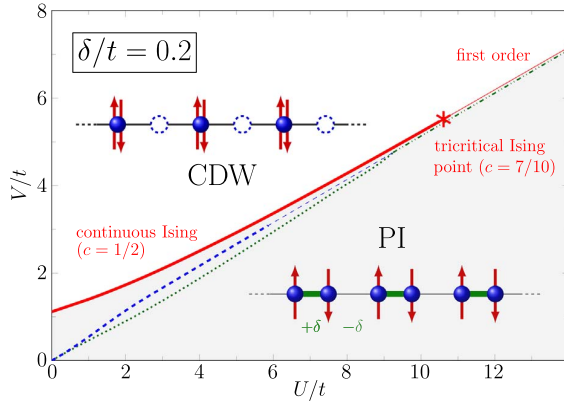


**Fig. 3.** Ground-state phase diagram of the 1D EHM with bond dimerization in the half-filled band sector [14]. The red solid line marks the PI-CDW phase boundaries for  $\delta/t = 0.2$ . The tricritical Ising point  $[U_{tr}, V_{tr}]$  separates continuous Ising and first-order phase transitions. For comparisons, the phase boundaries of the pure EHM ( $\delta = 0$ ) were included. (For interpretation of the references to color in this figure legend, the reader is referred to the web version of this article.)

(EHM) system with alternating ferromagnetic spin interaction [13]: Here the continuous PI-CDW Ising transition line with central charge  $c = 1/2$  terminates at a tricritical point that belongs to the universality class of the 2D dilute Ising model with  $c = 7/10$ . Above the tricritical Ising point the quantum phase transition becomes first order. Displaying the ground-state phase diagram, Fig. 3 summarizes these results. A field theoretical description of the tricritical transition region has been performed in terms of a triple sine-Gordon model [14], based on the bosonization analysis in Ref. [17], providing results for the decay of various correlation functions, such as the density-density, bond-order or spin-spin two-points functions. The predictions of field theory are in excellent agreement with iDMRG data.

### 3. Critical exponents

In the following, we give further evidence for the Ising respectively the tricritical Ising universality classes of the quantum phase transitions in the EHM with bond dimerization by calculating the critical exponents of various physical quantities. When approaching a continuous phase transition by varying a parameter (e.g., a coupling strength)  $g$  of the Hamiltonian, the correlation length diverges as

$$\xi \propto |g - g_c|^{-\nu}. \quad (4)$$

Here,  $g_c$  denotes the (critical) value of  $g$  at the transition point and  $\nu$  is the corresponding critical exponent. Other quantities such as the order parameters or energy gaps also show power-law behavior. In this way the system is characterized by a set of universal exponents near the continuous phase transitions. The exact values of the most common exponents for the 2D Ising and tricritical Ising universality classes are listed in Table 1.

The exponents satisfy the following scaling relation

$$\frac{\nu}{2}(\eta + d - 2) = \beta, \quad (5)$$

**Table 1**

Critical exponents belonging to the Ising and tricritical Ising universality classes in 2D [36–38]. The critical exponent  $\eta$  for the pair correlation function has been confirmed in Ref. [14].

Quantity	Exponent	Ising	tricritical Ising
Magnetization	$\beta$	1/8	1/24
Correlation length	$\nu$	1	5/9
Pair correlation	$\eta$	1/4	3/20

where  $d$  is the spatial dimension (in our case  $d = 2$ ).

For the EHM with bond dimerization,  $\beta$  and  $\nu$  can be extracted from the CDW order parameter and the neutral gap, respectively. The CDW order parameter is defined as

$$m_{\text{CDW}} = \frac{1}{L} \sum_j (-1)^j (\hat{n}_j - 1). \quad (6)$$

The neutral gap is obtained from

$$\Delta_n(L) = E_1(N) - E_0(N), \quad (7)$$

where  $E_0(N)$  [ $E_1(N)$ ] denotes the energy of the ground state [first excited state] of a system with  $L$  sites,  $N$  electrons, and vanishing total spin  $z$  component.

#### 3.1. Ising transition

We now show that the critical exponents  $\beta = 1/8$  and  $\nu = 1$  follow from (i)DMRG simulations by varying  $V$  at fixed  $U$  and  $\delta$ , just as the corresponding phase transition line was obtained in Fig. 3. Note that  $\beta = 1/8$  and  $\nu = 1$  were extracted in Ref. [17] by means of the DMRG method, varying  $\delta$  for fixed  $U$  and  $V$ .

Fig. 4 gives the CDW order parameter as a function of  $V/t$ , fixing  $U/t = 4$  and  $\delta/t = 0.2$ , calculated by iDMRG technique with bond dimensions  $\chi = 800$ . Obviously, in the CDW (PI) realized for  $V > V_c$  ( $V < V_c$ ),  $|m_{\text{CDW}}|$  is finite (zero). Using  $V_c/t \approx 2.5035$ , the iDMRG data are well fitted by  $(V - V_c)^\beta$  near the transition, where the critical exponent  $\beta = 1/8$  can be easily read off from a log-log plot; see inset of Fig. 4.

Extrapolating the values of the neutral gap  $\Delta_n$  to the thermodynamic limit, the critical exponent  $\nu = 1$  is verified, as demonstrated by Fig. 5. Increasing  $V$  at fixed  $U/t = 4$ , the neutral gap decreases linearly and closes at the Ising transition point. If  $V$  grows further,  $\Delta_n$  opens again with linear slope. This is clearly visible in the log-log plots representation, both for  $V > V_c$  and  $V < V_c$ ; see Fig. 5(b).

#### 3.2. Perturbed tricritical Ising model

As quoted above and demonstrated in Ref. [14], the tricritical point in the EHM with bond dimerization belongs to the universality class of the 2D tricritical Ising model with the critical exponents given in Table 1. Let us emphasize that it is exceptionally challenging to verify the critical exponents at the tricritical Ising point numerically, not least because one first has to determine the tricritical point itself, with high precision, varying  $U$  and  $V$  simultaneously [14].

The exponent  $\eta$  characterizes the power-law decay of the CDW order-parameter two-point function at the critical point. As shown in Ref. [14] one has

$$\langle (-1)^\ell (\hat{n}_{j+\ell} - 1)(\hat{n}_j - 1) \rangle \propto \ell^{-3/20}, \quad \ell \gg 1. \quad (8)$$

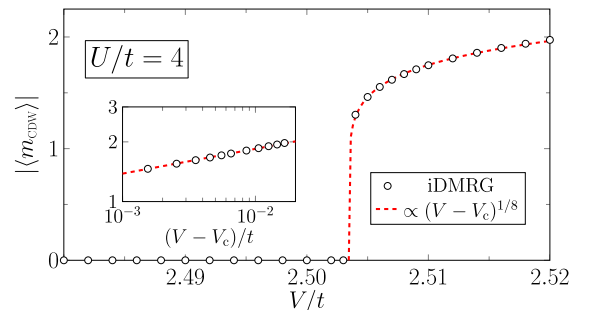


**Fig. 4.** Absolute value of the CDW order parameter in the vicinity of the Ising transition at fixed  $U/t = 4$ . Symbols are iDMRG data; the dashed line displays the fitting function  $|m_{\text{CDW}}| \propto (V - V_c)^\beta$  with critical exponent  $\beta = 1/8$  (Ising universality class). Inset: Log-log plot of the order parameter for  $V > V_{tr}$  demonstrating the power-law decay with exponent  $\beta$ .

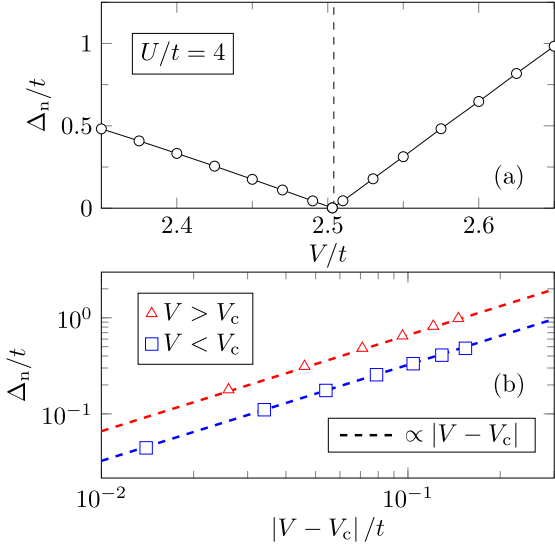


**Fig. 5.** (a): Neutral gap  $\Delta_n$  near the Ising transition at fixed  $U/t = 4$  (symbols are DMRG data taken from Ref. [14]). (b): Log-log plots of  $\Delta_n$  as a function of  $|V - V_c|$ , fitted by  $|V - V_c|^\nu$  with  $\nu = 1$  (Ising universality class).

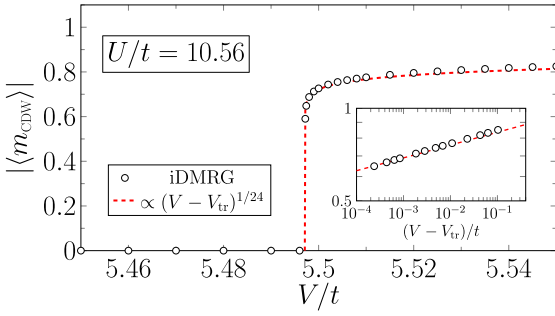


**Fig. 6.** Absolute value of the CDW order parameter in the vicinity of the tricritical Ising point at fixed  $U/t = 10.56$ . Symbols are iDMRG data; the dashed line displays the fitting function  $|\langle m_{\text{CDW}} \rangle| \propto (V - V_{\text{tr}})^\beta$  with critical exponent  $\beta = 1/24$  (tricritical Ising universality class). Inset: Log-log plot of the order parameter for  $V > V_{\text{tr}}$  demonstrating the power-law decay with exponent  $\beta$ .

This establishes that  $\eta = 3/20$ . In order to determine the exponents  $\beta$  and  $\nu$  one needs to consider the off-critical regime. We therefore consider the perturbation of the tricritical Ising conformal field theory by the “energy operator”  $\epsilon(x)$ , which has conformal dimensions  $(\Delta_\epsilon, \bar{\Delta}_\epsilon) = (\frac{1}{10}, \frac{1}{10})$  [36–38]

$$H = H_{\text{CF}} + h \int dx \epsilon(x). \quad (9)$$

The perturbing operator has scaling dimension  $d = 1/5$  and is therefore relevant in the renormalization group (RG) sense. It generates a spectral gap  $M$  that scales as

$$M \sim Ch^{1/(2-d)} = Ch^{5/9}, \quad (10)$$

where  $C$  is a constant. This identifies the critical exponent  $\nu = 5/9$ . The magnetization operator  $\sigma(x)$  in the tricritical Ising model has scaling dimension  $(\Delta_\sigma, \bar{\Delta}_\sigma) = (\frac{3}{80}, \frac{3}{80})$ . In the perturbed theory (9) it acquires a non-zero expectation value that scales as

$$\langle \sigma(x) \rangle \sim Dh^{\Delta_\sigma/(1-\Delta_\epsilon)} = Dh^{1/24}, \quad (11)$$

where  $D$  is a constant. This identifies the critical exponent  $\beta = 1/24$ .

The predictions of perturbed conformal field theory for  $\beta$  and  $\nu$  can be checked against numerical computations as follows. Fixing  $U = 10.56t$  ( $\approx U_{\text{tr}}$ ), we first give the iDMRG results for the CDW order

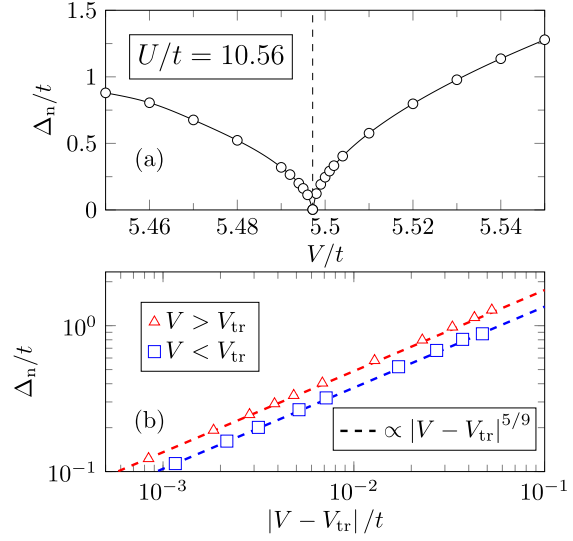


**Fig. 7.** (a): DMRG data for the neutral gap  $\Delta_n$  in the vicinity of the tricritical Ising point where  $U/t = 10.56$ . (b): Log-log plots of  $\Delta_n$  as a function of  $|V - V_{\text{tr}}|$ , fitted by  $|V - V_{\text{tr}}|^\nu$  with  $\nu = 5/9$  (tricritical Ising universality class).

parameter  $|\langle m_{\text{CDW}} \rangle|$  as a function of  $V$ , cf. Fig. 6. Just as in the case of the Ising universality class,  $|\langle m_{\text{CDW}} \rangle|$  is finite (zero) for  $V > V_{\text{tr}}$  ( $V < V_{\text{tr}}$ ). The order parameter  $|\langle m_{\text{CDW}} \rangle|$  now vanishes much more abruptly approaching the quantum phase transition point from above. Fitting the iDMRG data for  $V > V_{\text{tr}}$  to  $(V - V_{\text{tr}})^\beta$  with  $V_{\text{tr}}/t \approx 5.497$  and  $\beta = 1/24$  works perfectly, see the log-log representation Fig. 7.

In order to verify the field theory prediction for  $\nu$  we examine the  $L \rightarrow \infty$  extrapolated values of the neutral gap  $\Delta_n$ . Increasing  $V (< V_{\text{tr}})$  at fixed  $U/t = 10.56$ ,  $\Delta_n$  is reduced but not linearly as in the Ising case (cf. Fig. 4), and closes at  $V \approx V_{\text{tr}}$  before it becomes finite again for  $V > V_{\text{tr}}$ . Again the log-log representation can be used to extract the critical exponent for  $|V - V_{\text{tr}}|^\nu$ ,  $\nu = 5/9$ , for both  $V < V_{\text{tr}}$  and  $V > V_{\text{tr}}$ , in conformity with the tricritical Ising universality class.

#### 4. Summary

To conclude, we have investigated the criticality of the 1D half-filled extended Hubbard model (EHM) with explicit dimerization  $\delta$ . The BOW-CDW Gaussian transition with central charge  $c = 1$  of the pure EHM gives way to an Ising transition with  $c = 1/2$  at any finite  $\delta$ . The Ising transition line terminates at a tricritical point, which belongs to the universality class of the tricritical Ising model in two dimensions. The change of the universality class is verified numerically by (i)DMRG (see also [14]). Furthermore, we demonstrate that not only the Ising but also the tricritical Ising critical exponents  $\beta$  and  $\nu$  can be obtained with high accuracy by simulating the CDW order parameter and the neutral gap.

#### Acknowledgement

We thank M. Tsuchiizu for fruitful discussions. The DMRG simulations were performed using the ITensor library [39]. This work was supported by Deutsche Forschungsgemeinschaft (Germany), SFB 652, project B5 (SE and HF), and by the EPSRC under grant EP/N01930X/1 (FHLE). FL thanks RIKEN for the hospitality sponsored by the IPA program.

#### References

- [1] J. Hubbard, *Proc. R. Soc. Lond. Ser. A* 276 (1963) 238.
- [2] F.H.L. Essler, H. Frahm, F. Göhmann, A. Klümper, V.E. Korepin, *The One-*



- Dimensional Hubbard Model, Cambridge University Press, Cambridge, 2005.
- [3] M. Nakamura, J. Phys. Soc. Jpn. 68 (1999) 3123.
- [4] M. Nakamura, Phys. Rev. B 61 (2000), 16377.
- [5] M. Tsuchiizu, A. Furusaki, Phys. Rev. Lett. 88 (2002), 056402.
- [6] M. Tsuchiizu, A. Furusaki, Phys. Rev. B 69 (2004), 035103.
- [7] E. Jeckelmann, Phys. Rev. Lett. 89 (2002), 236401.
- [8] A.W. Sandvik, L. Balents, D.K. Campbell, Phys. Rev. Lett. 92 (2004), 236401.
- [9] S. Ejima, S. Nishimoto, Phys. Rev. Lett. 99 (2007), 216403.
- [10] Z.-C. Gu, X.-G. Wen, Phys. Rev. B 80 (2009), 155131.
- [11] F. Pollmann, A.M. Turner, E. Berg, M. Oshikawa, Phys. Rev. B 81 (2010), 064439.
- [12] F. Pollmann, E. Berg, A.M. Turner, M. Oshikawa, Phys. Rev. B 85 (2012), 075125.
- [13] F. Lange, S. Ejima, H. Fehske, Phys. Rev. B 92 (2015), 041120.
- [14] S. Ejima, F.H.L. Essler, F. Lange, H. Fehske, Phys. Rev. B 93 (2016), 235118.
- [15] D. Friedan, Z. Qiu, S. Shenker, Phys. Rev. Lett. 52 (1984) 1575.
- [16] D. Friedan, Z. Qiu, S. Shenker, Phys. Lett. B 151 (1985) 37.
- [17] H. Benthien, F.H.L. Essler, A. Grage, Phys. Rev. B 73 (2006), 085105.
- [18] S.R. White, Phys. Rev. Lett. 69 (1992) 2863.
- [19] U. Schollwöck, Ann. Phys. 326 (2011) 96.
- [20] P. Sengupta, A.W. Sandvik, D.K. Campbell, Phys. Rev. B 65 (2002), 155113.
- [21] K.-M. Tam, S.-W. Tsai, D.K. Campbell, Phys. Rev. Lett. 96 (2006), 036408.
- [22] I.P. McCulloch, arXiv:0804.2509.
- [23] P. Calabrese, J. Cardy, J. Stat. Mech. (2004), P06002.
- [24] A.O. Gogolin, A.A. Nersisyan, A.M. Tselik, Bosonization and Strongly Correlated Systems, Cambridge University Press, Cambridge, 1999.
- [25] T. Giamarchi, Quantum Physics in One Dimension, Oxford University Press, Oxford, 2003.
- [26] F. Gebhard, K. Bott, M. Scheidler, P. Thomas, S.W. Koch, Philos. Mag. B 75 (1997) 1.
- [27] T. Nakano, H. Fukuyama, J. Phys. Soc. Jpn. 50 (1981) 2489.
- [28] A.M. Tselik, Phys. Rev. B 45 (1992) 486.
- [29] G.S. Uhrig, H.J. Schulz, Phys. Rev. B 54 (1996), R9624.
- [30] F.H.L. Essler, A.M. Tselik, G. Delfino, Phys. Rev. B 56 (1997), 11001.
- [31] S. Ejima, F. Gebhard, S. Nishimoto, Phys. Rev. B 74 (2006), 245110.
- [32] A. Grage, F. Gebhard, J. Rissler, Theory Exp. (2005), P08009.
- [33] M. Dzierzawa, C. Mocanu, J. Phys.:Condens. Matter 17 (2005) 2663.
- [34] M. Sugiura, Y. Suzumura, J. Phys. Soc. Jpn. 71 (2002) 697.
- [35] M. Tsuchiizu, E. Orignac, J. Phys. Chem. Solids 63 (2002) 1459.
- [36] M. Lässig, G. Mussardo, J.L. Cardy, Nucl. Phys. B 348 (1991) 591.
- [37] P.D. Francesco, P. Mathieu, D. Sénéchal, Conformal Field Theory, Springer, New York, 1997.
- [38] G. Mussardo, Statistical Field Theory, Oxford University Press, Oxford, 2009.
- [39] (<http://itensor.org/>).



## Anyonic Haldane Insulator in One Dimension

Florian Lange,<sup>1,2</sup> Satoshi Ejima,<sup>2</sup> and Holger Fehske<sup>2</sup>

<sup>1</sup>*Computational Condensed Matter Physics Laboratory, RIKEN, Wako, Saitama 351-0198, Japan*

<sup>2</sup>*Institut für Physik, Ernst-Moritz-Arndt-Universität Greifswald, 17489 Greifswald, Germany*

(Received 30 November 2016; published 23 March 2017)

We demonstrate numerically the existence of a nontrivial topological Haldane phase for the one-dimensional extended ( $U$ - $V$ ) Hubbard model with a mean density of one particle per site, not only for bosons but also for anyons, despite a broken reflection parity symmetry. The Haldane insulator, surrounded by superfluid, Mott insulator, and density-wave phases in the  $V$ - $U$  parameter plane, is protected by combined (modified) spatial-inversion and time-reversal symmetries, which is verified within our matrix-product-state based infinite density-matrix renormalization group scheme by analyzing generalized transfer matrices. With regard to an experimental verification of the anyonic Haldane insulator state the calculated asymmetry of the dynamical density structure factor should be of particular importance.

DOI: 10.1103/PhysRevLett.118.120401

Anyons represent a third fundamental class of particles with fractional exchange statistics that interpolates, to some degree, between those of bosons and fermions having symmetric or antisymmetric wave functions under exchange [1,2]. By contrast, the exchange of two anyons creates a phase factor  $e^{i\theta}$  in the many-body wave function, where the statistical parameter  $\theta$  can be of any value in the interval  $(0, \pi)$ . In the beginning anyons were thought to be relevant solely for two-dimensional systems. Describing the fractional quantum Hall effect experiments in particular, the quasiparticles could be viewed as anyons with  $\theta$  fixed by the filling factor [3,4]. With Haldane's generalized Pauli principle and definition of fractional statistics, however, the concept of anyons becomes important in arbitrary dimensions [5].

In one dimension, the physics of anyons might be studied successfully with ultracold atoms in optical lattices [6]. For example, one-dimensional (1D) anyon statistics can be implemented by bosons with occupation-dependent hopping amplitudes generated by assisted Raman tunneling [7,8]. An alternative route to create 1D anyons in an optical lattice exploits lattice-shaking-assisted tunneling against potential offsets generated by a combination of a static potential tilt and strong on-site interactions [9]. Thereby, advantageously, no additional lasers are required, except for those employed on creating optical lattices. However, in spite of the huge experimental efforts, a conclusive detection of 1D anyons in optical lattices has not yet been achieved.

Notwithstanding, from a theoretical point of view, anyons in one dimension have received continuous and legitimate interest on account of their intriguing physical properties. The exact solution of a 1D anyon gas with a delta-function potential has been obtained by a Bethe ansatz technique [10]. Boundary conformal field theory shows that non-Abelian anyons may form topological insulating phases in spin-1/2  $su(2)_k$  chains [11]. For the Abelian 1D anyon-Hubbard

model (AHM), the possibility of a statistically induced quantum phase transition between Mott-insulator (MI) and superfluid phases [7,12] and the asymmetry of the momentum distribution for hard-core [13] and soft-core anyons [14] have been addressed so far. Since the AHM is equivalent to a variant of the Bose-Hubbard model (BHM) with state-dependent bosonic hopping amplitudes [7], the next very interesting question might be whether the symmetry-protected topological (SPT) Haldane state [15,16], observed in the extended BHM (EBHM) with an additional nearest-neighbor particle repulsion [17,18], also shows up in the extended AHM (EAHM). Because of its SPT order, the Haldane phase in the EBHM is separated from the topologically trivial MI phase by a phase transition, as long as the protecting symmetry—being a combination of bond-centered inversion and a local unitary transformation—keeps up [16]. By breaking this symmetry, the two phases can be adiabatically connected without crossing a phase transition. Therefore, a sharp distinction between the two phases is only possible in the presence of the protecting symmetry, even though no spontaneous symmetry breaking occurs. As the hopping phase factor breaks the reflection parity in the system [19], naively one might expect the Haldane state to disappear in the EAHM for any finite fractional phase  $\theta$ . However, this will not happen if the protecting symmetry is appropriately generalized for finite  $\theta$ .

To comment on an anyonic topological Haldane state in one dimension, we scrutinize its protecting symmetry in the framework of the EAHM by analyzing the invariance of the density-dependent hopping amplitudes (as for the EBHM in the limit  $\theta \rightarrow 0$ ). Calculating the generalized transfer matrices [20] from the infinite matrix-product state (iMPS) of the infinite density-matrix renormalization-group (iDMRG) [21–23] simulations, we prove the existence of the Haldane insulator (HI) state and derive the complete ground-state phase diagram of this paradigmatic anyonic

model Hamiltonian at unit filling. In order to discriminate the topological HI phase from the other, more conventional Mott and density-wave (DW) insulating phases in possible future experiments, we also determine the dynamical density response of the system, showing a characteristic asymmetry in the Brillouin zone, which can be attributed to the fractional phase factor of the anyons.

The Hamiltonian of the 1D EAHM consists of three terms,  $\hat{H}_{\text{EAHM}}^{(a)} \equiv \hat{H}_t + \hat{H}_U + \hat{H}_V$ , with

$$\hat{H}_t = -t \sum_j (\hat{a}_j^\dagger \hat{a}_{j+1} + \text{H.c.}), \quad (1)$$

$\hat{H}_U = U \sum_j \hat{n}_j (\hat{n}_j - 1)/2$ , and  $\hat{H}_V = V \sum_j \hat{n}_j \hat{n}_{j+1}$ , describing the nearest-neighbor anyon transfer ( $\propto t$ ), as well as the repulsive on-site ( $\propto U$ ) and nearest-neighbor ( $\propto V$ ) particle interaction, respectively. The anyon creation ( $\hat{a}_j^\dagger$ ), annihilation ( $\hat{a}_j$ ), and particle number ( $\hat{n}_j = \hat{a}_j^\dagger \hat{a}_j$ ) operators at lattice site  $j$  are defined by the generalized commutation relations [7,10]:

$$\hat{a}_j \hat{a}_\ell^\dagger - e^{-i\theta \text{sgn}(j-\ell)} \hat{a}_\ell^\dagger \hat{a}_j = \delta_{j\ell}, \quad (2)$$

$$\hat{a}_j \hat{a}_\ell - e^{i\theta \text{sgn}(j-\ell)} a_\ell a_j = 0, \quad (3)$$

where the sign function  $\text{sgn}(j-\ell) = 0$  for  $j = \ell$  is mandatory, since two anyons on the same site behave as ordinary bosons. Anyons with  $\theta = \pi$  represent so-called ‘‘pseudofermions,’’ namely, they are fermions off site, while being bosons on site.

Performing a fractional Jordan–Wigner transformation [7],

$$\hat{a}_j = \hat{b}_j e^{i\theta \sum_{\ell=1}^{j-1} \hat{n}_\ell}, \quad (4)$$

where  $\hat{b}_j^\dagger$  ( $\hat{b}_j$ ) is a boson creation (annihilation) operator,  $\hat{H}_{\text{EAHM}}^{(a)}$  becomes  $\hat{H}_{\text{EAHM}}^{(b)}$  with density-dependent hopping amplitudes,

$$\hat{H}_t = -t \sum_j (\hat{b}_j^\dagger \hat{b}_{j+1} e^{i\theta \hat{n}_j} + e^{-i\theta \hat{n}_j} \hat{b}_{j+1}^\dagger \hat{b}_j). \quad (5)$$

That is, when a boson hops to the left from site  $j+1$  to site  $j$  it acquires an occupation dependent phase  $e^{i\theta \hat{n}_j}$ . Of course,  $\hat{n}_j = \hat{a}_j^\dagger \hat{a}_j = \hat{b}_j^\dagger \hat{b}_j$ , which means that  $\hat{H}_U$  and  $\hat{H}_V$  are form invariant under the anyon-boson mapping (4).

If we limit the maximum number of particles per site as  $n_p = 2$ , the EBHM, resulting in the limit  $\theta \rightarrow 0$  from  $\hat{H}_{\text{EAHM}}^{(b)}$ , maps to an effective XXZ spin-1 chain [18]:

$$\begin{aligned} \hat{H}_{\text{eff}} = & -t \sum_j (\hat{S}_j^+ \hat{S}_{j+1}^- + \text{H.c.}) + \frac{U}{2} \sum_j (\hat{S}_j^z)^2 \\ & + V \sum_j \hat{S}_j^z \hat{S}_{j+1}^z \end{aligned} \quad (6)$$

with the pseudospin operator  $\hat{S}_j^z = \hat{n}_j - 1$ . Here, we have neglected terms that break the particle-hole symmetry. We note the negative sign of the first term compared to the usual XXZ spin-chain Hamiltonian. This leads to a protecting modified inversion symmetry  $\mathcal{I}'$  for the Haldane state of the EBHM [16]:

$$\mathcal{I}' = e^{i\pi \sum_j \hat{S}_j^z} \mathcal{I} = e^{i\pi \sum_j (\hat{n}_j - 1)} \mathcal{I}. \quad (7)$$

Owing to the occupation-dependent hopping in Eq. (5) the HI phase in the EAHM seems not be protected by the modified inversion symmetry  $\mathcal{I}'$ .

To clarify whether  $\hat{H}_t$  is invariant under certain symmetry operations, let us first consider the inversion symmetry operator  $\mathcal{I}$ , acting on  $\hat{H}_t \rightarrow \hat{H}_t' = \mathcal{I} \hat{H}_t \mathcal{I}^\dagger$  with

$$\hat{H}_t' = -t \sum_j (\hat{b}_{j+1}^\dagger \hat{b}_j e^{i\theta \hat{n}_{j+1}} + e^{-i\theta \hat{n}_{j+1}} \hat{b}_j^\dagger \hat{b}_{j+1}). \quad (8)$$

Applying next a time-reversal transformation  $\mathcal{T}$ ,  $\hat{H}_t' \rightarrow \hat{H}_t'' = \mathcal{T} \hat{H}_t' \mathcal{T}^{-1}$ , we obtain

$$\hat{H}_t'' = -t \sum_j (\hat{b}_{j+1}^\dagger \hat{b}_j e^{-i\theta \hat{n}_{j+1}} + e^{i\theta \hat{n}_{j+1}} \hat{b}_j^\dagger \hat{b}_{j+1}). \quad (9)$$

To see that  $\hat{H}_t$  stays invariant under the combined symmetry operations, we make the following transformation:

$$\hat{b}_j^\dagger \rightarrow e^{i\theta \hat{n}_j (\hat{n}_j - 1)/2} \hat{b}_j^\dagger e^{-i\theta \hat{n}_j (\hat{n}_j - 1)/2} = \hat{b}_j^\dagger e^{i\theta \hat{n}_j}, \quad (10)$$

$$\hat{b}_j \rightarrow e^{i\theta \hat{n}_j (\hat{n}_j - 1)/2} \hat{b}_j e^{-i\theta \hat{n}_j (\hat{n}_j - 1)/2} = e^{-i\theta \hat{n}_j} \hat{b}_j. \quad (11)$$

Since the second term of Eq. (9) transforms as  $e^{i\theta \hat{n}_{j+1}} \hat{b}_{j+1}^\dagger \hat{b}_j \rightarrow \hat{b}_{j+1}^\dagger \hat{b}_j e^{i\theta \hat{n}_j}$ , it is equal to the first term of  $\hat{H}_t$ . Therefore, the Hamiltonian  $\hat{H}_{\text{EAHM}}^{(b)}$  is invariant under the transformation

$$\mathcal{K} = e^{i\theta \sum_j \hat{n}_j (\hat{n}_j - 1)/2} \mathcal{I} \mathcal{T}. \quad (12)$$

We now show that the combination of  $\mathcal{R}^z = e^{i\pi \sum_j \hat{S}_j^z} = e^{i\pi \sum_j (\hat{n}_j - 1)}$  and  $\mathcal{K}$  is related to an SPT phase in the EAHM, and define a corresponding topological order parameter. Following Ref. [24], we use the iMPS representation formed by complex  $\chi \times \chi$  matrices  $\Gamma_\sigma$  and a positive, real, diagonal matrix  $\Lambda$ :

$$|\psi\rangle = \sum_{\dots, \sigma_j, \sigma_{j+1}, \dots} \dots \Lambda \Gamma_{\sigma_j} \Lambda \Gamma_{\sigma_{j+1}} \dots |\dots, \sigma_j, \sigma_{j+1}, \dots\rangle, \quad (13)$$

where the index  $\sigma$  labels the basis states of the local Hilbert spaces. The iMPS is assumed to be in the canonical form:  $\sum_\sigma \Gamma_\sigma \Lambda^2 \Gamma_\sigma^\dagger = \sum_\sigma \Gamma_\sigma^\dagger \Lambda^2 \Gamma_\sigma = 1$ . If a state  $|\psi\rangle$  is invariant under an internal symmetry that is represented by a unitary matrix  $\Sigma_{\sigma\sigma'}$ , then the transformed  $\Gamma_\sigma$  matrices satisfy [16,25]

$$\sum_{\sigma} \Sigma_{\sigma\sigma'} \Gamma_{\sigma'} = e^{i\varphi} U^{\dagger} \Gamma_{\sigma} U, \quad (14)$$

where  $U$  is a unitary matrix that commutes with  $\Lambda$  matrices, and  $e^{i\varphi}$  is a phase factor. Similar relations hold for time reversal symmetry, inversion symmetry, and a combination of both. In those cases  $\Gamma_{\sigma}$  on the left-hand side is replaced by its complex conjugate  $\Gamma_{\sigma}^*$ , its transpose  $\Gamma_{\sigma}^T$ , and its Hermitian transpose  $\Gamma_{\sigma}^{\dagger}$ , respectively. The properties of the matrices  $U$  can be used to classify SPT phases [16,26]. For instance, in the case of time reversal or (modified) inversion symmetry the matrices satisfy  $U_{\mathcal{T}} U_{\mathcal{T}}^* = \pm \mathbb{1}$  or  $U_{\mathcal{T}(\nu)} U_{\mathcal{T}(\nu)}^* = \pm \mathbb{1}$ , and the sign distinguishes between two symmetric phases. In the EAHM, the situation is slightly different because time reversal and inversion are not symmetries of the system; only a combination  $\mathcal{K}$  of them is. For  $\mathcal{R}^z$  and  $\mathcal{K}$  we have  $U_{\mathcal{R}^z}^2 = e^{i\alpha_{\mathcal{R}^z}} \mathbb{1}$  and  $U_{\mathcal{K}}^2 = e^{i\alpha_{\mathcal{K}}} \mathbb{1}$ . From this we can derive an SPT order parameter similar to the case of the  $Z_2 \times Z_2$  spin rotation symmetry of  $\mathcal{R}^z$  and  $\mathcal{R}^x$  in the spin-1 XXZ chain [16]. Since the phase factors  $e^{i\alpha_{\mathcal{R}^z}}$  and  $e^{i\alpha_{\mathcal{K}}}$  can be removed by absorbing them into the corresponding matrices  $U_{\mathcal{R}^z}$  and  $U_{\mathcal{K}}$  they have no physical meaning. However, if both  $\mathcal{R}^z$  and  $\mathcal{K}$  are preserved, the combination  $\mathcal{R}^z \mathcal{K}$  is a symmetry as well and its phase factor is not arbitrary if  $U_{\mathcal{R}^z}$  and  $U_{\mathcal{K}}$  have been fixed. Indeed, one can show that  $U_{\mathcal{R}^z} U_{\mathcal{K}} = \pm U_{\mathcal{K}} U_{\mathcal{R}^z}$ , which defines two different phases. To verify that the EAHM has a nontrivial topological phase protected by  $\mathcal{R}^z$  and  $\mathcal{K}$ , we calculate the order parameter [20]

$$O = \frac{1}{\chi} \text{tr}(U_{\mathcal{K}} U_{\mathcal{R}^z} U_{\mathcal{K}}^{\dagger} U_{\mathcal{R}^z}^{\dagger}), \quad (15)$$

if the state is symmetric under both  $\mathcal{K}$  and  $\mathcal{R}^z$ . Otherwise, if one of the symmetries is broken, the order parameter is zero.

The iDMRG results for the order parameter are shown in Fig. 1. If  $U_{\mathcal{K}}$  and  $U_{\mathcal{R}^z}$  commute ( $O = 1$ ), the system is in a trivial phase, i.e., a site-factorizable MI state, whereas if they anticommute ( $O = -1$ ), the system realizes a nontrivial HI state. Since the order parameter  $O$  changes its sign only if a phase transition takes place, the HI is a well-defined phase of the EAHM. Increasing the number of particles per site  $n_p$  at fixed  $U/t = 5$ , the HI phase ( $O = -1$ ) slightly shifts to larger value of  $V/t$  but, most notably, the Haldane phase still occupies a solid parameter region, see the data for  $n_p = 3$  and 5 in Fig. 1(a). Increasing the fractional angle  $\theta$  for  $n_p = 2$ , the Haldane state region narrows [see Fig. 1(b) for  $\theta = \pi/2$ ] and disappears (at least) for  $\theta = \pi$  [33]. We would like to emphasize that the HI sector marked in Fig. 1 by the gray area agrees with that extracted from the correlation length, the entanglement spectrum, and the numerically obtained central charge [27].

Figure 2 represents the ground-state phase diagram of the 1D EAHM in the  $V$ - $U$  plane, as obtained from large-scale

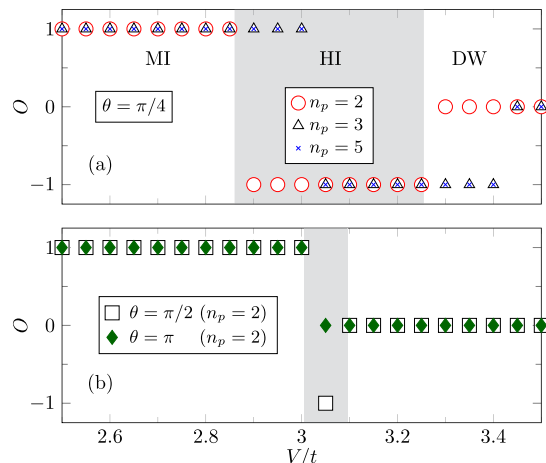


FIG. 1. Order parameter  $O$ , defined by Eq. (15), selecting the topological state in the EAHM at fixed  $U/t = 5$  and  $\theta = \pi/4$  for different  $n_p$  (a), and at fixed  $\theta = \pi/2$  and  $\pi$  for  $n_p = 2$  (b). Data obtained by iDMRG calculations with a (relatively small) bond dimension  $\chi = 100$ .

iDMRG calculations for  $\theta = \pi/4$  and  $n_p = 2$ . The phase boundaries are determined simulating the order parameter  $O$ , as well as the correlation length and the entanglement spectrum [27]. The EAHM exhibits three different

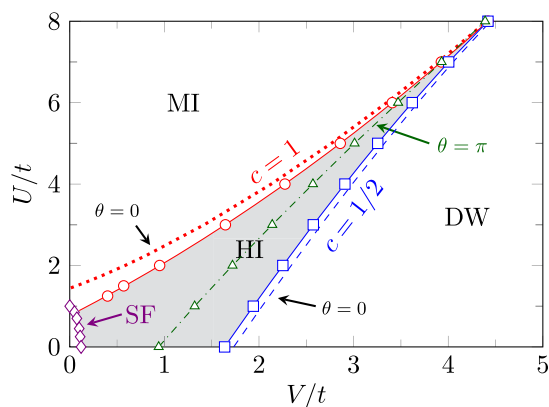


FIG. 2. Ground-state phase diagram of the extended anyon-Hubbard model in one dimension, where the particle density  $\rho = 1$ ,  $n_p = 2$ , and  $\theta = \pi/4$ . Most notably the Haldane insulator (HI), located between Mott insulator (MI) and density wave (DW) insulating phases in the EBHM, survives for any  $\theta > 0$ , i.e., in the anyonic case. Likewise, the superfluid (SF) appears in the very weak-coupling regime. The MI-HI (squares) and HI-DW (circles) transition points can be determined by a divergent correlation length  $\xi_{\chi}$  as  $\chi$  increases; i.e., the model becomes critical with the central charge  $c = 1$  and  $c = 1/2$ , respectively (see Ref. [27]). For comparison, the dotted (dashed) line marks the MI-HI (HI-DW) transition in the EBHM ( $\theta = 0$ ) [34]. The dash-dotted line with triangles up denotes the first-order MI-DW phase transition for  $\theta = \pi$ .

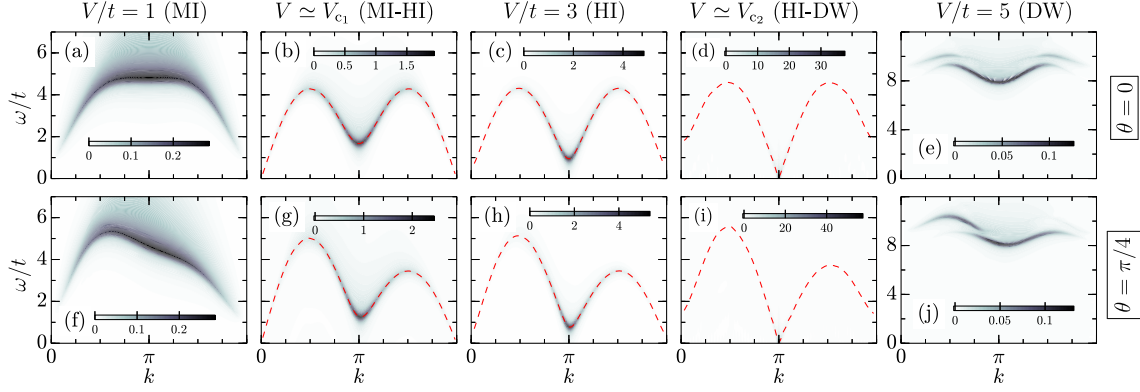


FIG. 3. Intensity plots of the dynamical structure factor  $S(k, \omega)$  in the EBHM ( $\theta = 0$ , upper panels) and in the EAHM ( $\theta = \pi/4$ , lower panels) for characteristic values of  $V/t$  at fixed  $U/t = 5$ . Again, the maximum number of particles per site is limited to  $n_p = 2$ . Dashed lines in panels (b)–(d) and (g)–(i) mark the highest intensity of  $S(k, \omega)$  in the  $k$ - $\omega$  plane.

insulating phases (MI, DW, and HI) and a superfluid state in the weak interaction regime, just as for the EBHM [34] but with the addition that the region of the intervening anyonic HI phase at  $\theta = \pi/4$  is slightly reduced. The HI vanishes in the pseudofermionic case ( $\theta = \pi$ ). According to field theory for the EBHM [18,35], which is based on the bosonization procedure developed for integer-spin chains [36,37], the MI-HI and HI-DW quantum phase transitions belong to the universality class of Tomonaga-Luttinger liquid and Ising model, with central charge  $c = 1$  and  $1/2$ , respectively, see Fig. S1(c) in Ref. [27]. That is, the universality classes are not modified by the fractional angle.

Perhaps the most striking feature of the AHM is the asymmetry of the momentum distribution function in  $k$  space [13,14]. The position of the maximum strongly depends on the fractional phase  $\theta$  [recall that the momentum distribution diverges at  $k = 0$  in the BHM ( $\theta = 0$ )]. We expect that this asymmetry can also be observed in dynamical quantities such as the dynamical structure factor  $S(k, \omega)$ . Hence, if an anyonic system will be realized in optical lattices,  $S(k, \omega)$  might be one of the best physical quantities to look at, comparing theoretical predictions with real experiments, like for 1D Bose–Hubbard type models [38].  $S(k, \omega)$  should be easily accessible by momentum resolved Bragg spectroscopy [39]. Furthermore, it has been recently demonstrated that  $S(k, \omega)$  can also be used to distinguish the topological HI from the conventional MI and DW states [34,40], in analogy to exploiting the dynamical spin-spin structure factor in the spin-1 XXZ chain [41].

The dynamical density structure factor is defined as

$$S(k, \omega) = \sum_n |\langle \psi_n | \hat{n}_k | \psi_0 \rangle|^2 \delta(\omega - \omega_n), \quad (16)$$

where  $|\psi_0\rangle$  ( $|\psi_n\rangle$ ) denotes the ground ( $n$ th excited) state, and  $\omega_n = E_n - E_0$ . To compute this quantity, we follow Ref. [42] and first determine the two-point correlation

function  $\langle \psi_0 | \hat{n}_j(\tau) \hat{n}_0(0) | \psi_0 \rangle$  by real-time evolution of the iMPS  $|\psi_0\rangle$ . Fourier transformation then provides us with accurate numerical results of the dynamical structure factor in the EAHM.

Figure 3 compares the intensity of the dynamical wavevector-resolved density response in the EBHM ( $\theta = 0$ ) with those in the EAHM for  $\theta = \pi/4$ , for  $U/t = 5$ , at five characteristic  $V/t$  values. One point worthy of remark is that each of the phases and phase transitions can be distinguished by looking at  $S(k, \omega)$ . In the MI, at  $V = t$  [Figs. 3(a) and 3(f)], the excitation gap appears at  $k \approx 0$ . With increasing  $V/t$ , the MI-HI transition occurs at  $V \approx V_{c1}$ , where the excitation gap closes at  $k = 0$ , as shown in Figs. 3(b) and 3(g). Deep in the HI phase,  $V = 3t$  [Figs. 3(c) and 3(h)], the spectral weight exclusively concentrates at  $k \approx \pi$ , and there are finite excitation gaps at  $k = 0$  and  $\pi$ . It is of particular interest to see whether the gap  $S(k, \omega)$  closes at the HI-DW transition point. Indeed, the excitation gap at  $V = V_{c2}$  closes, but at momentum  $k = \pi$ , reflecting the lattice-period doubling in the DW phase. Moreover, in the DW phase [Figs. 3(e) and 3(j)], we find a large excitation gap at  $k = \pi$  and two dispersive branches, where a changeover of the intensity maximum occurs at  $k = \pi/2$  ( $k = 3\pi/4$ ) for  $\theta = 0$  ( $\theta = \pi/4$ ). Interestingly, the influence of the occupation-dependent phase of  $\hat{H}_t$  in Eq. (5) shows up in  $S(k, \omega)$  as well, which helps to differentiate the results from those of the EBHM.  $S(k, \omega)$  of the EAHM is asymmetric for any  $0 < \theta < \pi$ , while  $S(k, \omega)$  in the EBHM is always symmetric about  $k = \pi$ .

To summarize, we carried out an unbiased numerical investigation of the extended anyon-Hubbard model in one dimension and determined its ground-state phase diagram with high precision exploiting the behavior of correlation lengths and entanglement spectra. Defining an order parameter that distinguishes trivial and nontrivial topological phases, we were able to show that the EAHM possesses

an anyonic Haldane insulator state sandwiched between superfluid, Mott insulator, and density-wave phases. Both the HI-MI and HI-DW quantum phase transitions are critical with central charge 1 and 1/2, respectively. While the HI state survives the EBHM limit ( $\theta = 0$ ), it vanishes when the system is composed of pseudofermions ( $\theta = \pi$ ). If a 1D interacting anyonic system could be realized experimentally in the future, maybe in an optical-lattice setup with ultracold atoms, we suggest performing momentum-resolved Bragg spectroscopy to look for the pronounced asymmetry of the density response spectra in momentum space that we have demonstrated in our model calculation theoretically.

The iDMRG simulations were performed using the ITensor library [43]. This work was supported by Deutsche Forschungsgemeinschaft (Germany), SFB 652, Project No. B5.

- 
- [1] J. M. Leinaas and J. Myrheim, *Nuovo Cimento B* **37**, 1 (1977).
- [2] F. Wilczek, *Phys. Rev. Lett.* **49**, 957 (1982).
- [3] D. C. Tsui, H. L. Stormer, and A. C. Gossard, *Phys. Rev. Lett.* **48**, 1559 (1982).
- [4] R. B. Laughlin, *Phys. Rev. Lett.* **50**, 1395 (1983).
- [5] F. D. M. Haldane, *Phys. Rev. Lett.* **67**, 937 (1991).
- [6] I. Bloch, J. Dalibard, and W. Zwerger, *Rev. Mod. Phys.* **80**, 885 (2008).
- [7] T. Keilmann, S. Lanzmich, I. McCulloch, and M. Roncaglia, *Nat. Commun.* **2**, 361 (2011).
- [8] S. Greschner and L. Santos, *Phys. Rev. Lett.* **115**, 053002 (2015).
- [9] C. Sträter, S. C. L. Srivastava, and A. Eckardt, *Phys. Rev. Lett.* **117**, 205303 (2016).
- [10] A. Kundu, *Phys. Rev. Lett.* **83**, 1275 (1999).
- [11] W. DeGottardi, *Phys. Rev. B* **90**, 075129 (2014).
- [12] J. Arcila-Forero, R. Franco, and J. Silva-Valencia, *Phys. Rev. A* **94**, 013611 (2016).
- [13] Y. Hao, Y. Zhang, and S. Chen, *Phys. Rev. A* **79**, 043633 (2009).
- [14] G. Tang, S. Eggert, and A. Pelster, *New J. Phys.* **17**, 123016 (2015).
- [15] Z.-C. Gu and X.-G. Wen, *Phys. Rev. B* **80**, 155131 (2009).
- [16] F. Pollmann, A. M. Turner, E. Berg, and M. Oshikawa, *Phys. Rev. B* **81**, 064439 (2010).
- [17] E. G. D. Torre, E. Berg, and E. Altman, *Phys. Rev. Lett.* **97**, 260401 (2006).
- [18] E. Berg, E. G. D. Torre, T. Giamarchi, and E. Altman, *Phys. Rev. B* **77**, 245119 (2008).
- [19] F. Wilczek, *Fractional Statistics and Anyon Superconductivity* (World Scientific, Singapore, 1990).
- [20] F. Pollmann and A. M. Turner, *Phys. Rev. B* **86**, 125441 (2012).
- [21] S. R. White, *Phys. Rev. Lett.* **69**, 2863 (1992).
- [22] U. Schollwöck, *Ann. Phys. (Berlin)* **326**, 96 (2011).
- [23] I. P. McCulloch, arXiv:0804.2509.
- [24] G. Vidal, *Phys. Rev. Lett.* **98**, 070201 (2007).
- [25] D. Pérez-García, M. M. Wolf, M. Sanz, F. Verstraete, and J. I. Cirac, *Phys. Rev. Lett.* **100**, 167202 (2008).
- [26] X. Chen, Z.-C. Gu, and X.-G. Wen, *Phys. Rev. B* **84**, 235128 (2011).
- [27] See Supplemental Material at <http://link.aps.org/supplemental/10.1103/PhysRevLett.118.120401>, which includes Refs. [28–32], for further quantities to determine and characterize the phase boundaries and quantum phase transitions.
- [28] H. Li and F. D. M. Haldane, *Phys. Rev. Lett.* **101**, 010504 (2008).
- [29] I. Affleck, T. Kennedy, E. H. Lieb, and H. Tasaki, *Phys. Rev. Lett.* **59**, 799 (1987).
- [30] F. Verstraete, M. A. Martín-Delgado, and J. I. Cirac, *Phys. Rev. Lett.* **92**, 087201 (2004).
- [31] S. Nishimoto, *Phys. Rev. B* **84**, 195108 (2011).
- [32] S. Ejima, H. Fehske, F. Gebhard, K. zu Münster, M. Knap, E. Arrigoni, and W. von der Linden, *Phys. Rev. A* **85**, 053644 (2012).
- [33] Note that our iDMRG scheme holds for arbitrary  $\theta$ . Additional iDMRG calculations confirm that the HI phase exists not only for the specific fractional angles  $\theta$  used in Fig. 1 but also for other values of  $\theta \in (0, \pi)$  (not shown). The critical  $\theta_c$ , where the HI phase disappears, depends on the model parameters  $U$ ,  $V$ , and  $n_p$ .
- [34] S. Ejima, F. Lange, and H. Fehske, *Phys. Rev. Lett.* **113**, 020401 (2014).
- [35] Y.-W. Lee, Y.-L. Lee, and M.-F. Yang, *Phys. Rev. B* **76**, 075117 (2007).
- [36] H. J. Schulz, *Phys. Rev. B* **34**, 6372 (1986).
- [37] A. M. Tsvelik, *Phys. Rev. B* **42**, 10499 (1990).
- [38] D. Clément, N. Fabbri, L. Fallani, C. Fort, and M. Inguscio, *Phys. Rev. Lett.* **102**, 155301 (2009).
- [39] P. T. Ernst, S. Götze, J. S. Krauser, K. Pyka, D.-S. Lühmann, D. Pfannkuche, and K. Sengstock, *Nat. Phys.* **6**, 56 (2010).
- [40] S. Ejima and H. Fehske, *J. Phys. Conf. Ser.* **592**, 012134 (2015).
- [41] S. Ejima and H. Fehske, *Phys. Rev. B* **91**, 045121 (2015).
- [42] H. N. Phien, G. Vidal, and I. P. McCulloch, *Phys. Rev. B* **86**, 245107 (2012).
- [43] <http://itensor.org/>.

## Supplementary material

As discussed in the main text, we find compelling evidence for the existence of the symmetry-protected topological Haldane insulator phase in the one-dimensional (1D) extended anyon-Hubbard model (EAHM), by calculating an order parameter from the largest eigenvalues of the generalized transfer matrix within an infinite density-matrix renormalization group (iDMRG) scheme.

Here we show that for the EAHM (with maximum number of particles per site  $n_p = 2$ ) further quantities can be exploited in order to determine and characterize the phase boundaries and quantum phase transitions with high precision.

The entanglement analysis in particular provides us with valuable information about the existence of a symmetry protected Haldane insulator (HI) in the EAHM. Furthermore, it allows to determine the phase boundaries between the HI and other insulating phases. Dividing a system into two subblocks,  $\mathcal{H} = \mathcal{H}_L \otimes \mathcal{H}_R$ , and considering the reduced density matrix  $\rho_L = \text{Tr}_R[\rho]$ , the entanglement spectra [S1] can be extracted from the singular values  $\lambda_\alpha$  of  $\rho_L$  as  $\epsilon_\alpha = -2 \ln \lambda_\alpha$ . In addition, the correlation length  $\xi_\chi$  can be obtained from the second largest eigenvalue of the transfer matrix for some fixed bond dimension  $\chi$  in an iDMRG simulation [S2, S3]. While  $\xi_\chi$  stays finite as a consequence of the fixed bond dimension  $\chi$ , the physical correlation length will diverge at the critical point. Nevertheless,  $\xi_\chi$  is useful to pinpoint a phase boundary because it rapidly increases with  $\chi$  close to the quantum phase transition point, see also Ref. [S4] for the corresponding discussion in the AKLT model [S5].

Figures S1(a) and (b) show  $\xi_\chi$  and  $\epsilon_\alpha$  as functions of  $V/t$  for fixed  $U/t = 5$ . The strong upturn of  $\xi_\chi$  indicates the formation of a HI phase in the EAHM for  $\theta > 0$ . We find distinct peaks at  $V_{c_1} \simeq 2.859t$  and  $V_{c_2} \simeq 3.255t$ , which become more pronounced as  $\chi$  grows from 100 to 200, signaling a divergence of  $\xi_\chi \rightarrow \infty$  as  $\chi \rightarrow \infty$ . At the same time, the entanglement spectra develops a characteristic double degeneracy in all entanglement levels for  $V_{c_1} < V < V_{c_2}$ , indicating a symmetry-protected topological phase between MI and DW states.

The universality class of these quantum phase transitions can be explored by calculating the central charge numerically, just as in case of the EBHM [S6]. When the system gets critical the central charge can be determined very accurately by DMRG, utilizing the relation [S7]

$$c^*(L) \equiv \frac{3[S_L(L/2 - 1) - S_L(L/2)]}{\ln[\cos(\pi/L)]}. \quad (\text{S1})$$

In this way, the MI-SF transition in the BHM [S8], and especially, the universality class of the MI-HI and HI-DW quantum phase transitions in the EBHM have been determined in the past [S6].

Figure S1(c) displays  $c^*(L)$  for the 1D EAHM, where the model parameters are the same as in Figs. S1(a) and

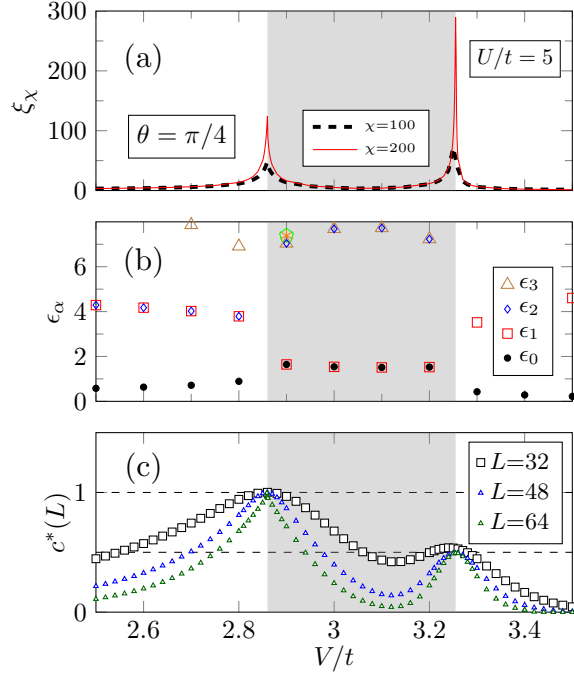


FIG. S1. (Color online). Correlation length  $\xi_\chi$  [panel (a)] and entanglement spectrum  $\epsilon_\alpha$  [panel (b)] as a function of  $V/t$  for  $U/t = 5$  and  $\theta = \pi/4$  from iDMRG. Panel (c) displays the central charge  $c^*(L)$  for the same parameter set, signaling a MI-HI (HI-DW) quantum phase transition with  $c = 1$  ( $c = 1/2$ ). Here data obtained by the finite-system DMRG with periodic boundary conditions.

(b). Running the DMRG we adopt periodic boundary conditions for system sizes up to  $L = 64$ . For  $U/t = 5$  and  $V \simeq V_{c_1}$  [ $V \simeq V_{c_2}$ ], we find  $c^*(L = 64) \simeq 0.996$  [ $c^*(L = 64) \simeq 0.494$ ], which points to the universality class of the Luttinger liquid (Ising) model, in accordance with what was obtained for the corresponding quantum phase transitions in the EBHM ( $\theta = 0$ ).

- [S1] H. Li and F. D. M. Haldane, Phys. Rev. Lett. **101**, 010504 (2008).
- [S2] I. P. McCulloch, arXiv:0804.2509.
- [S3] U. Schollwöck, Ann. Phys. **326**, 96 (2011).
- [S4] F. Verstraete, M. A. Martín-Delgado, and J. I. Cirac, Phys. Rev. Lett. **92**, 087201 (2004).
- [S5] I. Affleck, T. Kennedy, E. H. Lieb, and H. Tasaki, Phys. Rev. Lett. **59**, 799 (1987).
- [S6] S. Ejima, F. Lange, and H. Fehske, Phys. Rev. Lett. **113**, 020401 (2014).
- [S7] S. Nishimoto, Phys. Rev. B **84**, 195108 (2011).
- [S8] S. Ejima, H. Fehske, F. Gebhard, K. zu Münster, M. Knap, E. Arrigoni, and W. von der Linden, Phys. Rev. A **85**, 053644 (2012).



## Strongly repulsive anyons in one dimension

Florian Lange, Satoshi Ejima, and Holger Fehske

*Institut für Physik, Ernst-Moritz-Arndt Universität Greifswald, D-17489 Greifswald, Germany*

(Received 24 April 2017; published 23 June 2017)

To explore the static properties of the one-dimensional anyon-Hubbard model for a mean density of one particle per site, we apply perturbation theory with respect to the ratio between kinetic energy and interaction energy in the Mott insulating phase. The strong-coupling results for the ground-state energy, the single-particle excitation energies, and the momentum distribution functions up to 6th order in hopping are benchmarked against the numerically exact (infinite) density-matrix renormalization group technique. Since these analytic expressions are valid for any fractional phase  $\theta$  of anyons, they will be of great value for a sufficiently reliable analysis of future experiments, avoiding extensive and costly numerical simulations.

DOI: [10.1103/PhysRevA.95.063621](https://doi.org/10.1103/PhysRevA.95.063621)

### I. INTRODUCTION

Particles are usually classified as either bosons or fermions, depending on whether the wave function is symmetric or antisymmetric with respect to the exchange of two identical particles. Some systems, however, may realize quasiparticles with fractional statistics, called anyons, that acquire a complex phase factor  $e^{i\theta}$  with  $0 < \theta < \pi$  under exchange [1,2]. Most notably, anyons have been used in the description of the fractional quantum Hall effect [3,4]. While anyons are usually restricted to two-dimensional systems, fractional statistics can in principle be defined in arbitrary dimensions [5].

One-dimensional (1D) anyon models can be expressed in terms of bosonic operators by using a generalized Jordan-Wigner transformation. There are several proposals to utilize this equivalence to realize an anyon-Hubbard model (AHM) by loading ultracold atoms in optical lattices. The fractional exchange statistics is thereby translated into an occupation-dependent hopping phase that experimentally may be implemented by assisted Raman tunneling [6,7] or lattice-shaking-assisted tunneling against potential offsets [8]. One of the advantages of any optical lattice setup is the high degree of control of system parameters including the statistical angle  $\theta$ . As yet, however, an experimental realization of anyons in optical lattices has not been archived.

Since the introduction of the AHM [6], several theoretical and numerical studies have been carried out, *inter alia*, exploring the effect of fractional statistics on momentum distributions [9] and the position of the quantum phase transition between the Mott insulator (MI) and superfluid (SF) [6,10] as well as revealing additional phases such as an exotic two-component partially paired phase [7]. It has been shown that the various superfluid phases of the AHM can be qualitatively understood within a generalized Gutzwiller mean-field ansatz [9,11]. Here, we instead focus on the MI phase, using strong-coupling perturbation theory as it has been applied to the Bose-Hubbard model (BHM) [12–14]. In addition to the perturbative analysis, we study the model numerically with the density-matrix renormalization group (DMRG) [15–17] and a variational matrix-product state (MPS) ansatz for dispersion relations [18,19].

The outline of this paper is as follows: In Sec. II we introduce the 1D AHM and apply the anyon-boson mapping by the fractional version of the Jordan-Wigner transformation to

the AHM in order to rewrite the Hamiltonian with the bosonic operators. In Sec. III we describe the strong-coupling analysis for the ground-state energy, the momentum-dependent single-hole and single-particle excitation energies, and the momentum distribution functions. To evaluate the validity of the proposed strong-coupling approach we perform an extensive comparison with unbiased data obtained by the MPS-based (infinite) DMRG (iDMRG) technique. Finally, Sec. IV summarizes our results and gives a brief outlook.

### II. ANYONIC HUBBARD MODEL

On a linear chain of  $L$  sites with periodic boundary conditions (PBCs), the Hamiltonian of the 1D AHM is defined as  $\hat{H}_{\text{AHM}}^{(a)} \equiv t\hat{T}_a + U\hat{D}$ , with

$$\hat{T}_a = - \sum_{j=1}^L (\hat{a}_j^\dagger \hat{a}_{j+1} + \hat{a}_{j+1}^\dagger \hat{a}_j) \quad (1)$$

and

$$\hat{D} = \frac{1}{2} \sum_{j=1}^L \hat{n}_j (\hat{n}_j - 1), \quad (2)$$

describing the nearest-neighbor anyon transfer ( $\propto t$ ) and the on-site anyon repulsion ( $\propto U$ ), respectively. Here,  $\hat{a}_j^\dagger$ ,  $\hat{a}_j$ , and  $\hat{n}_j = \hat{a}_j^\dagger \hat{a}_j$  are the anyon creation, annihilation, and particle number operators on site  $j$ , respectively, which fulfill the generalized commutation relations [6]

$$\hat{a}_j \hat{a}_\ell^\dagger - e^{-i\theta \text{sgn}(j-\ell)} \hat{a}_\ell^\dagger \hat{a}_j = \delta_{j\ell}, \quad (3)$$

$$\hat{a}_j \hat{a}_\ell - e^{i\theta \text{sgn}(j-\ell)} \hat{a}_\ell \hat{a}_j = 0. \quad (4)$$

Since  $\text{sgn}(0) = 0$ , regular bosonic commutation relations apply for particles on the same site. Anyons with the fractional angle  $\theta = \pi$  represent the so-called “pseudo-fermions,” namely, they behave as ordinary fermions off site, while being bosons on site.

Carrying out a fractional Jordan-Wigner transformation [6],

$$\hat{a}_j = \hat{b}_j e^{i\theta \sum_{\ell=1}^{j-1} \hat{n}_\ell}, \quad (5)$$

$\hat{T}_a$  of Eq. (1) can be rewritten with boson creation ( $\hat{b}_j^\dagger$ ) and annihilation ( $\hat{b}_j$ ) operators as

$$\hat{T}_b = - \sum_j (\hat{b}_j^\dagger \hat{b}_{j+1} e^{i\theta \hat{n}_j} + e^{-i\theta \hat{n}_j} \hat{b}_{j+1}^\dagger \hat{b}_j). \quad (6)$$

To be more precise, when an anyon hops to the left from site  $j+1$  to site  $j$ , an occupation-dependent phase  $e^{i\theta \hat{n}_j}$  is picked up in the bosonic operator description. Note that  $\hat{n}_j = \hat{a}_j^\dagger \hat{a}_j = \hat{b}_j^\dagger \hat{b}_j$ , so that the on-site repulsion term  $\hat{D}$  is form-invariant under the anyon-boson mapping (5). In order to study the model deep in the Mott-insulating regime, we apply an  $x = t/U$  strong-coupling expansion to  $\hat{H}_{\text{AHM}}^{(b)} = t\hat{T}_b + U\hat{D}$ . Throughout this work, we restrict ourselves to unit filling.

### III. STRONG-COUPLING EXPANSIONS

#### A. Ground state

At integer filling  $\rho = N/L$ , the AHM has a unique ground state,

$$|\phi_0\rangle = \frac{1}{(\rho!)^{L/2}} \prod_i (\hat{b}_i^\dagger)^\rho |\text{vac}\rangle, \quad (7)$$

in the limit  $x \rightarrow 0$ . The state  $|\phi_0\rangle$  can be used as a starting point for a perturbative calculation of the ground state in the MI phase.

Executing the unitary Harris-Lange transformation [20], the strong-coupling Hamiltonian of the AHM is derived in a similar way as for the BHM [12]:

$$\hat{h} = e^{\hat{S}} \hat{H} e^{-\hat{S}} = U\hat{D} + t \sum_{r=0}^{\infty} x^r \hat{h}_r, \quad (8)$$

$$\hat{S} = -\hat{S}^\dagger = \sum_{r=1}^{\infty} x^r \hat{S}_r. \quad (9)$$

Practically, we keep a finite order in the expansion of  $\hat{S}$ . Retaining  $\hat{S}_r$  for  $1 \leq r \leq n$  denotes the “ $n$ th-order expansion.” The operators  $\hat{S}_n$  are defined by requiring that in the  $n$ th order for  $S$ , the transformed Hamiltonian conserves the number of double occupancies to  $(n-1)$ th order, that is,  $[\hat{h}_r, \hat{D}] = 0$  for  $1 \leq r \leq n-1$ . Higher-order terms in the expansion of  $\hat{h}$  are neglected, so  $|\phi_0\rangle$  is an eigenstate of the strong-coupling Hamiltonian.

Following this recipe, the leading-order terms for  $\hat{S}_r$  and  $\hat{h}_r$  are obtained as

$$\hat{S}_1 = \sum_{D_1, D_2} \frac{\hat{P}_{D_1} \hat{T} \hat{P}_{D_2}}{D_1 - D_2}, \quad (10)$$

$$\begin{aligned} \hat{S}_2 = & \sum_{D_1, D_2} \frac{-\hat{P}_{D_1} \hat{T} \hat{P}_{D_1} \hat{T} \hat{P}_{D_2} + \hat{P}_{D_1} \hat{T} \hat{P}_{D_2} \hat{T} \hat{P}_{D_2}}{(D_1 - D_2)^2} \\ & + \sum_{D_1, D_2, D_3} \frac{\hat{P}_{D_1} \hat{T} \hat{P}_{D_3} \hat{T} \hat{P}_{D_2} [D_1 - D_3 + D_2 - D_3]}{2(D_1 - D_2)(D_1 - D_3)(D_2 - D_3)}, \end{aligned} \quad (11)$$

$$\hat{h}_0 = \sum_D \hat{P}_D \hat{T} \hat{P}_D, \quad (12)$$

$$\hat{h}_1 = \sum_{D_1, D_2} \frac{\hat{P}_{D_1} \hat{T} \hat{P}_{D_2} \hat{T} \hat{P}_{D_1}}{D_1 - D_2}, \quad (13)$$

where  $\hat{P}_D$  is the projection operator onto the subspace of eigenstate with  $D$  interactions,  $\hat{D} = \sum_{D=0}^{\infty} D \hat{P}_D$ . In the above sums it is implicitly suggested that all indices  $D_i \geq 0$  are different from each other. Higher orders are generated recursively as described in Ref. [21], where the necessary bookkeeping can be done by a computer algebra program. The resulting expansion differs from the one for the BHM only by the hopping operator  $\hat{T}$ .

Within the strong-coupling expansion the ground state  $|\psi_0\rangle$  and ground-state energy  $E_0$  of the original Hamiltonian are

$$|\psi_0\rangle = e^{\hat{S}} |\phi_0\rangle, \quad \hat{h} |\phi_0\rangle = E_0 |\phi_0\rangle, \quad (14)$$

where  $|\phi_0\rangle$  is the ground state of  $\hat{h}_{-1} = \hat{D}$ , see Eq. (7). Since the Harris-Lange transformation is unitary the operators and ground-state expectation values are translated with  $|\psi_0\rangle \mapsto |\phi_0\rangle$ ,  $\hat{H} \mapsto \hat{h}$ , and  $\hat{A} \mapsto \tilde{A} = e^{\hat{S}} \hat{A} e^{-\hat{S}}$ .

Calculating the various observables in the strong-coupling expansion then amounts to evaluating chains of hopping operators in the unperturbed ground state  $|\phi_0\rangle$  which are weighted depending on how they change the number of double occupancies at each step. In doing so, one only has to sum over connected hopping processes that can be evaluated using finite clusters. The difference between the AHM and the BHM enters the strong-coupling expansion through the phase factors picked up by the hopping processes or an explicit  $\theta$  dependence of the observables.

The ground-state energy is simply given by

$$E_0 = \langle \phi_0 | \hat{h} | \phi_0 \rangle. \quad (15)$$

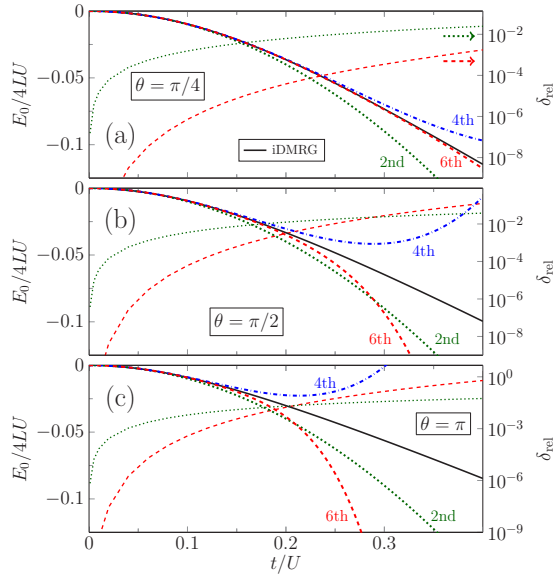


FIG. 1. Ground-state energy  $E_0/4LU$  as a function of interaction strength  $t/U$ .  $n$ th-order strong-coupling results  $E_0^{[n]}$  of Eq. (16) are compared with the quasixact iDMRG data  $E_0^{\text{ex}}$  for  $\chi = 100$  (solid lines). The relative errors  $\delta_{\text{rel}} = |(E_0^{\text{ex}} - E_0^{[n]})/E_0^{\text{ex}}|$  are given in semilogarithmic representation corresponding to the right y axis.

Up to 6th order in  $x$ , we obtain for the rescaled ground-state energy per site

$$\begin{aligned} \frac{E_0^{[6]}}{4UL} &= -x^2 + [6 - 5 \cos(\theta)]x^4 \\ &+ \frac{1}{9}[-872 + 1168 \cos(\theta) - 228 \cos(2\theta)]x^6 \\ &+ O(x^8), \end{aligned} \quad (16)$$

in agreement with Refs. [12,13] in the BHM limit  $\theta \rightarrow 0$ .

Figure 1 compares the strong-coupling perturbation theory with iDMRG results for various  $\theta$ . Similar to the case in the BHM [12], for small  $\theta$  [e.g., Fig. 1(a) for  $\theta = \pi/4$ ], the strong-coupling series expansion is in reasonable accordance with the numerically exact result, as indicated clearly by the relative errors in Fig. 1. For 6th order in  $x$ , the deviation starts in the intermediate-coupling regime at  $t/U \simeq 0.35$ . As expected, the quality of the perturbation analysis improves as higher-order corrections are taken into account. This is valid for all  $\theta$  as demonstrated in Fig. 1.

Figure 1 also shows that the range of validity of the strong-coupling theory becomes worse with increasing  $\theta$ .

The deviation starts already at  $t/U \simeq 0.12$  in the case of  $\theta = \pi$ , see Fig. 1(c).

### B. Excitation energies

Similar to the ground state  $|\phi_0\rangle$ , Eq. (7), the energy levels of a single-hole excitation,  $E_h(k)$ , and of a single-particle excitation,  $E_p(k)$ , can be extracted from the strong-coupling expansion to high order in  $x$ , since the perturbation analysis for these energy levels also starts from nondegenerate states, i.e., in the case of  $\rho = 1$ ,

$$|\phi_h(k)\rangle = \sqrt{\frac{1}{L}} \sum_{\ell=1}^L e^{-ik\ell} \hat{b}_\ell |\phi_0\rangle, \quad (17)$$

$$|\phi_p(k)\rangle = \sqrt{\frac{1}{L}} \sqrt{\frac{1}{2}} \sum_{\ell=1}^L e^{ik\ell} \hat{b}_\ell^\dagger |\phi_0\rangle. \quad (18)$$

Therefore, the single-hole and single-particle excitation energies can be obtained from

$$E_h(k) = \langle \phi_h(k) | \hat{h} | \phi_h(k) \rangle - E_0, \quad (19)$$

$$E_p(k) = \langle \phi_p(k) | \hat{h} | \phi_p(k) \rangle - E_0. \quad (20)$$

Carrying out the above perturbation analysis up to and including 6th order in  $x$ , we obtain

$$\begin{aligned} \frac{E_h^{[6]}(k)}{t} &= -2 \cos(k) + x \{ 8 - 4 \cos(2k + \theta) \} + x^2 \{ 8 \cos(k) + 4 \cos(k + \theta) - 4 \cos(3k + \theta) - 8 \cos(3k + 2\theta) \} \\ &+ x^3 \{ -56 + 56 \cos(\theta) + 64 \cos(2k + \theta) - 4 \cos(4k + \theta) - 24 \cos(4k + 2\theta) - 16 \cos(4k + 3\theta) \} \\ &+ x^4 \left\{ -\frac{256}{3} \cos(k) + \frac{88}{3} \cos(k - \theta) - \frac{104}{3} \cos(k + \theta) + 16 \cos(k + 2\theta) - 8 \cos(3k) + 100 \cos(3k + \theta) \right. \\ &+ 216 \cos(3k + 2\theta) - 32 \cos(3k + 3\theta) - 4 \cos(5k + \theta) - 48 \cos(5k + 2\theta) - 96 \cos(5k + 3\theta) \\ &\left. - 32 \cos(5k + 4\theta) \right\} \\ &+ x^5 \left\{ \frac{2896}{3} - \frac{4480}{3} \cos(\theta) + \frac{1072}{3} \cos(2\theta) + \frac{784}{3} \cos(2k) + 28 \cos(2k - \theta) - \frac{3392}{3} \cos(2k + \theta) \right. \\ &+ \frac{928}{3} \cos(2k + 2\theta) + \frac{160}{3} \cos(2k + 3\theta) - 16 \cos(4k) + \frac{208}{3} \cos(4k + \theta) + 864 \cos(4k + 2\theta) \\ &+ \frac{1520}{3} \cos(4k + 3\theta) - 128 \cos(4k + 4\theta) - 4 \cos(6k + \theta) - 80 \cos(6k + 2\theta) - 320 \cos(6k + 3\theta) \\ &\left. - 320 \cos(6k + 4\theta) - 64 \cos(6k + 5\theta) \right\} \end{aligned} \quad (21)$$

and

$$\begin{aligned} \frac{E_p^{[6]}(k)}{t} &= \frac{1}{x} - 4 \cos(k + \theta) + x \{ 5 - 4 \cos(2k + \theta) \} \\ &+ x^2 \{ 8 \cos(k) + 22 \cos(k + \theta) - 12 \cos(k + 2\theta) - 4 \cos(3k + \theta) - 8 \cos(3k + 2\theta) \} \\ &+ x^3 \left\{ -\frac{1969}{20} + \frac{364}{5} \cos(\theta) + 70 \cos(2k + \theta) - 18 \cos(2k + 2\theta) + 12 \cos(2k + 3\theta) - 4 \cos(4k + \theta) \right. \\ &\left. - 24 \cos(4k + 2\theta) - 16 \cos(4k + 3\theta) \right\} \end{aligned}$$

$$\begin{aligned}
& + x^4 \left\{ -\frac{13384}{75} \cos(k) + 84 \cos(k - \theta) + \frac{2189}{150} \cos(k + \theta) + \frac{10331}{75} \cos(k + 2\theta) - \frac{294}{5} \cos(k + 3\theta) \right. \\
& - 8 \cos(3k) + 102 \cos(3k + \theta) + 204 \cos(3k + 2\theta) - 10 \cos(3k + 3\theta) - 12 \cos(3k + 4\theta) \\
& \left. - 4 \cos(5k + \theta) - 48 \cos(5k + 2\theta) - 96 \cos(5k + 3\theta) - 32 \cos(5k + 4\theta) \right\} \\
& + x^5 \left\{ \frac{794483}{600} - \frac{101513}{50} \cos(\theta) + \frac{22907}{75} \cos(2\theta) + \frac{14296}{75} \cos(2k) + 68 \cos(2k - \theta) - \frac{668719}{750} \cos(2k + \theta) \right. \\
& - \frac{14284}{375} \cos(2k + 2\theta) + \frac{1896}{125} \cos(2k + 3\theta) + \frac{3663}{25} \cos(2k + 4\theta) - \frac{294}{5} \cos(2k + 5\theta) - 16 \cos(4k) \\
& + 70 \cos(4k + \theta) + 858 \cos(4k + 2\theta) + 526 \cos(4k + 3\theta) - 154 \cos(4k + 4\theta) + 12 \cos(4k + 5\theta) \\
& \left. - 4 \cos(6k + \theta) - 80 \cos(6k + 2\theta) - 320 \cos(6k + 3\theta) - 320 \cos(6k + 4\theta) - 64 \cos(6k + 5\theta) \right\}. \quad (22)
\end{aligned}$$

In the BHM limit ( $\theta = 0$ ), we obtain Eqs. (A1) and (A2), which agree with Eqs. (24) and (25) of Ref. [12], respectively, when correcting some misprints; see Appendix A.

To calculate the dispersion relations of the particle and hole excitations numerically, we use the variational MPS ansatz introduced in Refs. [18,19] that works directly in the thermodynamic limit. In the following, we give a rough description of the method. Starting point is an infinite MPS (iMPS) approximation of the ground state

$$|\psi_0\rangle = v_L^\dagger \left( \prod_{j \in \mathbb{Z}} \sum_{s_j} A^{s_j} \right) v_R |s\rangle, \quad (23)$$

where  $|s\rangle = |\dots, s_j, s_{j+1}, \dots\rangle$ , the indices  $s_n$  label the states of the local Hilbert spaces,  $A^s$  are site-independent  $\chi \times \chi$  complex matrices, and  $v_L$  and  $v_R$  are  $\chi$ -dimensional vectors. The boundary vectors  $v_L$  and  $v_R$  will not affect the bulk properties and can therefore be ignored. It is assumed that the transfer matrix  $\sum_s A^s \otimes \bar{A}^s$  has one eigenvalue 1 and that its other eigenvalues are smaller in magnitude. To calculate  $|\psi_0\rangle$ , we use the iDMRG. The ansatz for the elementary excitations is a momentum superposition of local perturbations which are introduced by replacing the matrices  $A^s$  at a single site with matrices  $B^s$ :

$$|\phi_k(B)\rangle = \sum_{j \in \mathbb{Z}} e^{ikj} \sum_{\{s\}} v_L^\dagger (\dots A^{s_{j-1}} B^{s_j} A^{s_{j+1}} \dots) v_R |s\rangle. \quad (24)$$

This includes all excitations that are induced by one-site operators but can also describe, to some degree, those corresponding to operators with larger support. Increasing the bond dimension  $\chi$  of  $|\psi_0\rangle$  results, in addition to a better approximation for the ground-state energy, in a more general ansatz for the excitations. One can define matrices  $\mathbf{N}_k$  and  $\mathbf{H}_k$  such that

$$\langle \phi_k(B) | \phi_{k'}(B') \rangle = 2\pi \delta(k - k') B^\dagger \mathbf{N}_k B', \quad (25)$$

$$\langle \phi_k(B) | \hat{H} - E_0 | \phi_{k'}(B') \rangle = 2\pi \delta(k - k') B^\dagger \mathbf{H}_k B', \quad (26)$$

where  $E_0$  is the (infinite) ground-state energy and the matrices  $B^s$  have been combined and reshaped into a vector. The approximate excitation energies for any momentum  $k$  can then be obtained by solving the generalized eigenvalue problem for

the effective Hamiltonian  $\mathbf{H}_k$  and the normalization matrix  $\mathbf{N}_k$ . As described in detail in Ref. [19],  $B$  must be appropriately parametrized to exclude zero modes which would result in  $|\phi_k(B)\rangle = 0$  and to impose orthogonality to the ground state. A linear parametrization fulfilling these requirements can be chosen such that the normalization matrix becomes the identity and only a regular eigenvalue problem needs to be solved. Since the number of particles is a good quantum number, we can separately target particle and hole excitations to obtain both  $E_p$  and  $E_h$ .

In Fig. 2 we compare the strong-coupling results up to 6th order in  $x$  with the lowest excitation energy obtained by the above-mentioned iMPS technique. First of all,  $E_{h/p}$  are clearly symmetric about  $q = 0$  in the BHM limit  $\theta = 0$ , although they become asymmetric for  $0 < \theta < \pi$  reflecting the influence of the fractional angle  $\theta$ . By considering the strong-coupling expansions up to 1st order only, this asymmetry of the excitation energies can be understood well: the minimum of excitation energy,  $\min\{E_p(k)\}$  [ $\min\{E_h(k)\}$ ], shifts from  $k = 0$  to  $-\pi < k < 0$ , consistent with the positive sign of  $\theta$  in cosine terms up to 1st order. Quantitatively, the 6th-order expansions agree perfectly with iMPS data up to  $x \lesssim 0.1$ . The deviation between both results starts about  $x \sim 0.15$  especially in  $E_p(k)$ . The single-particle excitation from the perturbation theory is clearly higher than the lowest excitation energy by iMPS, e.g., for  $-\pi < k < -\pi/2$  and  $\pi/2 < k < \pi$  with  $\theta = 0$ . Most probably, the lowest excitation by iMPS stems from a many-particle excitation such as two particles and one hole that are forced into an artificial bound state by the iMPS ansatz [19]. Moreover, plotting the higher excitation energies, it is obvious that a continuum of excitations starts to arise in this regime. Figure 3 demonstrates a typical example for  $E_p(k)$  with the parameter sets of Fig. 2. Because of the finite bond dimension  $\chi$ , the continuous part of the spectrum is approximated by a finite number of discrete energy levels. With increasing  $x$  further, the results of strong-coupling expansions start to oscillate, see Fig. 2 for  $x \gtrsim 0.2$ .

From the single-hole and single-particle dispersions we can obtain the phase boundaries between MI and SF in the grand-canonical ensemble. The chemical potentials  $\mu^\pm$  at which the phase transitions for fixed  $t/U$  take place are determined by the minimum energies for adding a particle or hole to the MI ground state:  $\mu^+ = \min\{E_p(k)\}$  and  $\mu^- = -\min\{E_h(k)\}$ . In

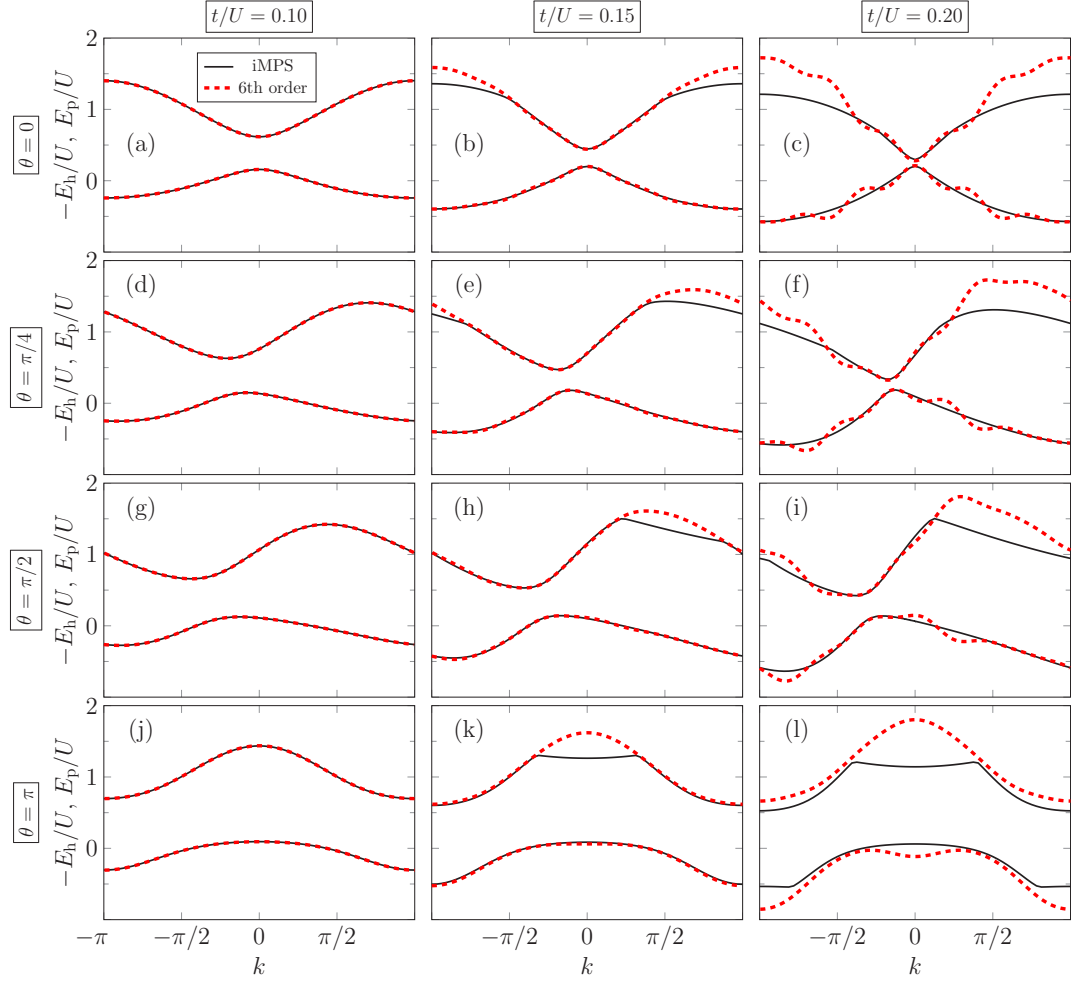


FIG. 2. Sixth-order strong-coupling expansions (dashed lines) of the single-hole and single-particle excitation energies, Eqs. (21) and (22), compared with numerical data by iMPS with the variational ansatz (solid lines).

general, the minima of the strong-coupling expressions (21) and (22) have to be found numerically. However, in the BHM

limit ( $\theta = 0$ ) we have  $\mu^+ = E_p(0)$  and  $\mu^- = -E_h(0)$  and thus the gap is given by  $\Delta = \mu^+ - \mu^- = E_p(0) + E_h(0)$ . In this way, we can reproduce the single-particle gap in the BHM

$$\frac{\Delta}{U} = 1 - 6x + 5x^2 + 6x^3 + \frac{287}{20}x^4 + \frac{5821}{50}x^5 - \frac{602243}{1000}x^6 + \dots, \quad (27)$$

in agreement with Ref. [14].

As in the case of the BHM [22,23],  $\mu^\pm$  in the AHM can be also determined numerically by DMRG using the following definitions of the chemical potentials for finite system sizes:

$$\pm\mu^\pm(L) = E_0(L, N \pm 1) - E_0(L, N), \quad (28)$$

where  $E_0(L, N \pm 1)$  and  $E_0(L, N)$  denote the corresponding ground-state energies.

Figure 4 shows the ground-state phase diagram of the 1D AHM, exhibiting MI and SF regions as a function of the chemical potential  $\mu/U$  and the anyon transfer amplitude  $t/U$ . The strong-coupling expansions of the chemical potentials via Eqs. (21) and (22) up to 6th order are compared with DMRG

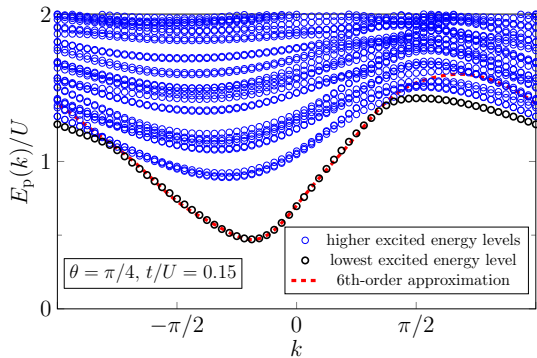


FIG. 3. Excitation energies for one additional particle, the parameters being the same as in Fig. 2(e). The disagreement between perturbation theory and variational iMPS ansatz can be explained by the onset of the multiparticle continuum.

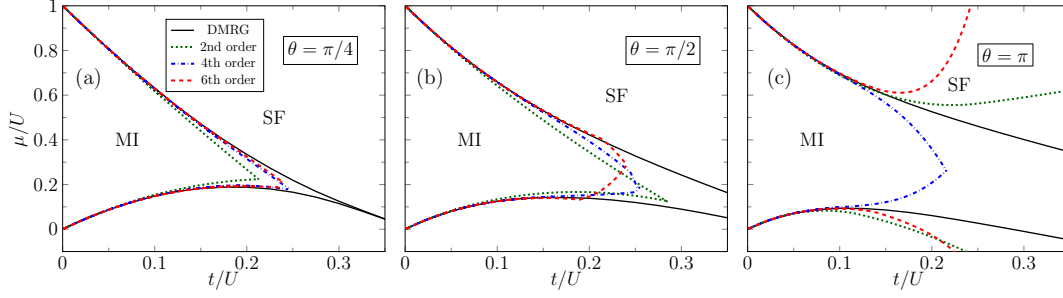


FIG. 4. Phase diagram of the one-dimensional anyon-Hubbard model ( $n_p \leq 5$ ) for the fractional angle  $\theta = \pi/4$  [panel (a)],  $\pi/2$  [panel (b)], and  $\pi$  [panel (c)] with Mott insulator (MI) and superfluid (SF) regions. The MI-SF boundaries (black lines) were determined by DMRG with system sizes up to  $L = 128$ , open boundary conditions, and  $n_p \leq 5$ . The strong-coupling expansions up to 6th order in  $x$  show reasonable agreements with the numerical data.

results. For small  $\theta \lesssim \pi/2$ , both methods essentially agree up to  $x \lesssim 0.2$  [see Figs. 4(a) and 4(b)], while in the case of the pseudofermions [ $\theta = \pi$  in Fig. 4(c)] even 6th-order results start to deviate around  $x \sim 0.12$ . In the intermediate-coupling regime ( $t/U \gtrsim 0.20$ ) sudden changes will appear in the perturbation results, especially for  $\theta = \pi/4$  (not shown). This is because the perturbation expansions fall into the wrong minima as will be discussed in Appendix B.

### C. Momentum distribution function

Anyons might be characterized most significantly by momentum distribution functions as has been demonstrated for both hardcore [24] and softcore [9] anyons. For the current model, we can define two different types of single-particle correlation functions

$$C_b(r) = \langle \hat{b}_j^\dagger \hat{b}_{j+r} \rangle, \quad (29)$$

$$C_a(r) = \langle \hat{a}_j^\dagger \hat{a}_{j+r} \rangle, \quad (30)$$

corresponding to boson or anyon representations. Results for the boson correlation function should be relevant for the proposed realization of the model in optical lattices. The anyon correlation function can be expressed in terms of the boson operators as follows:

$$\langle \hat{a}_j^\dagger \hat{a}_\ell \rangle \rightarrow \begin{cases} \langle \hat{b}_j^\dagger e^{i\theta \hat{n}_j} [\prod_{j < m < \ell} e^{i\theta \hat{n}_m}] \hat{b}_\ell \rangle & \text{for } j < \ell, \\ \langle e^{-i\theta \hat{n}_\ell} \hat{b}_\ell [\prod_{\ell < m < j} e^{-i\theta \hat{n}_m}] \hat{b}_j^\dagger \rangle & \text{for } j > \ell, \\ \langle \hat{n}_j \rangle & \text{for } j = \ell. \end{cases} \quad (31)$$

Within the strong-coupling expansion, the above correlators are translated according to

$$\langle \hat{b}_j^\dagger \hat{b}_\ell \rangle \mapsto \langle \phi_0 | e^{\hat{S}} \hat{b}_j^\dagger \hat{b}_\ell e^{-\hat{S}} | \phi_0 \rangle, \quad (32)$$

$$\langle \hat{a}_j^\dagger \hat{a}_\ell \rangle \mapsto \langle \phi_0 | e^{\hat{S}} \hat{a}_j^\dagger \hat{a}_\ell e^{-\hat{S}} | \phi_0 \rangle. \quad (33)$$

In Appendix C we compare the perturbation results for the two-point correlation functions up to 4th order in  $x$  with the iDMRG data.

The Fourier-transformed single-particle density matrices give the momentum distribution functions for bosons and

anyons as

$$n_b(k) = \frac{1}{L} \sum_{j,\ell} e^{ik(j-\ell)} \langle \hat{b}_j^\dagger \hat{b}_\ell \rangle, \quad (34)$$

$$n_a(k) = \frac{1}{L} \sum_{j,\ell} e^{ik(j-\ell)} \langle \hat{a}_j^\dagger \hat{a}_\ell \rangle. \quad (35)$$

Up to and including 4th order in  $x$ , we obtain for the momentum distribution functions of bosons

$$\begin{aligned} n_b^{[4]}(k) = & 1 + x\{4 \cos(k) + 4 \cos(k + \theta)\} \\ & + x^2\{4 \cos(2k) + 24 \cos(2k + \theta) \\ & + 8 \cos(2k + 2\theta)\} \\ & + x^3\{-36 \cos(k) + 12 \cos(k - \theta) \\ & - 8 \cos(k + \theta) + 16 \cos(k + 2\theta) \\ & + 4 \cos(3k) + 60 \cos(3k + \theta) \\ & + 96 \cos(3k + 2\theta) + 16 \cos(3k + 3\theta)\} \\ & + x^4\left\{\frac{152}{3} \cos(2k) + \frac{64}{3} \cos(2k - \theta) \right. \\ & - 400 \cos(2k + \theta) + \frac{152}{3} \cos(2k + 2\theta) \\ & + 64 \cos(2k + 3\theta) + 4 \cos(4k) \\ & + 112 \cos(4k + \theta) + 432 \cos(4k + 2\theta) \\ & \left. + 320 \cos(4k + 3\theta) + 32 \cos(4k + 4\theta)\right\}, \quad (36) \end{aligned}$$

and for anyons

$$\begin{aligned} n_a^{[4]}(k) = & 1 + 8x \cos(k) + x^2\{24 \cos(2k) + 12 \cos(2k - \theta)\} \\ & + x^3\{-96 \cos(k) + 40 \cos(k + \theta) \\ & + 40 \cos(k - \theta) + 64 \cos(3k) \\ & + 16 \cos(3k - 2\theta) + 96 \cos(3k - \theta)\} \\ & + x^4\left\{-\frac{1408}{3} \cos(2k) + \frac{272}{3} \cos(2k - 2\theta) \right. \\ & \left. - \frac{176}{3} \cos(2k - \theta) + 224 \cos(2k + \theta) \right\} \end{aligned}$$

$$\left. \begin{aligned} &+ 160 \cos(4k) + 480 \cos(4k - \theta) \\ &+ 240 \cos(4k - 2\theta) + 20 \cos(4k - 3\theta) \end{aligned} \right\}. \quad (37)$$

Taking the limit  $\theta \rightarrow 0$  in Eqs. (36) or (37), we obtain the momentum distribution function in the BHM

$$\begin{aligned} n_{\text{BHM}}^{[4]}(k) &= 1 + 8x \cos(k) + 36x^2 \cos(2k) \\ &+ x^3 \{-16 \cos(k) + 176 \cos(3k)\} \\ &+ x^4 \left\{ -\frac{640}{3} \cos(2k) + 900 \cos(4k) \right\}, \end{aligned} \quad (38)$$

in agreement with the former studies of the strong-coupling expansions in the BHM up to and including 3rd order in  $x$  [25].

Using DMRG with PBCs, the momentum distribution functions of anyons and bosons can be extracted from Eqs. (34) and (35) after calculating the two-point correlation functions, as demonstrated in Fig. 5 by the comparison with the strong-coupling expansions (36) and (37). While for  $t/U = 0.05$  analytical and numerical methods agree [Fig. 5(a)], small deviations appear for  $t/U \gtrsim 0.1$  [Fig. 5(b)]. For  $t/U \sim 0.20$  [Fig. 5(c)] the oscillations become significant in the 4th-order strong-coupling expansions which are clearly an artifact.

Analogous to the momentum-dependent excitation energies in Sec. III B, the characteristic asymmetry in the momentum distribution functions can be understood by considering the main  $\theta$ -dependent contributions in the strong-coupling expansion of  $n_{a/b}(k)$ . In the BHM limit ( $\theta = 0$ ),  $n_b(k) [= n_a(k)]$  is always symmetric about  $k = 0$ , where the position of the maximum is located. These peak positions of  $n_b(k)$  [ $n_a(k)$ ] shift to the negative [positive] momentum with increasing  $\theta$  for  $0 < \theta < \pi$ , which is consistent with the sign of  $\theta$  in the cosine term of the main  $\theta$ -dependent contribution of  $n_{b/a}(k)$ , i.e., the positive [negative] sign of  $\theta$  in  $n_b^{[1]}(k)$  [ $n_a^{[2]}(k)$ ] of Eq. (36) [Eq. (37)]. Moreover, the peak positions of  $n_b(k)$  depend more strongly on  $\theta$  than those of  $n_a(k)$ , this is because the  $\theta$ -dependent main contribution in  $n_a(k)$  shows up first in the 2nd-order expansion, while in the case of  $n_b(k)$  it can

already be seen in the 1st-order expansion. To 1st order, the peak of  $n_b(k)$  is located at  $k = -\theta/2$ , that is, its position depends linearly on the fractional angle. When increasing  $\theta$  from 0 to  $\pi$ , the boson momentum distribution becomes flatter because of cancellations in the 1st-order terms. Close to the pseudofermion limit, a second peak appears for  $0 < k < \pi$  that can be attributed mainly to 2nd-order contributions. At  $\theta = \pi$ , the cancellation of 1st-order terms becomes exact for all  $k$  and one ends up with  $n_b(k) = 1 - 12x^2 \cos(2k) + O(x^3)$ . Our results for the boson momentum distribution function in the MI are in contrast to the results of Ref. [9] for the SF where, depending on the filling, a single peak at either  $k \sim 0$  or  $k \sim -\theta$  has been found.

#### IV. SUMMARY AND OUTLOOK

We studied the MI phase of the anyon-Hubbard model at filling factor one for arbitrary fractional angle  $\theta$  using strong-coupling perturbation theory. Explicit expressions for the  $\theta$  dependence of the ground-state energy per site, the single-particle and single-hole excitation energies, as well as the momentum distribution functions were obtained for up to 6th order in  $t/U$  (hopping/interaction).

In the BHM both single-particle and single-hole dispersions have their minimum at  $k = 0$ . For finite  $\theta$ , the minimum of the dispersion is shifted differently for single-particle and single-hole excitations, that is, there is an indirect gap for particle-hole excitations.

The momentum distribution functions become asymmetric for  $0 < \theta < \pi$  with the peak shifted to negative (positive) momentum in the boson (anyon) description of the model. A stronger  $\theta$  dependence is found for the boson momentum distribution than for the anyon one. In particular, the boson momentum distribution function becomes almost flat in the pseudofermion limit  $\theta = \pi$ .

While the series generated by the strong-coupling expansion might be asymptotic, the results for finite order agree well with numerically exact MPS calculations for small hopping  $t$ . Increasing  $t$ , however, the accuracy starts to deteriorate and the perturbative description is no longer sensible. At fixed order,

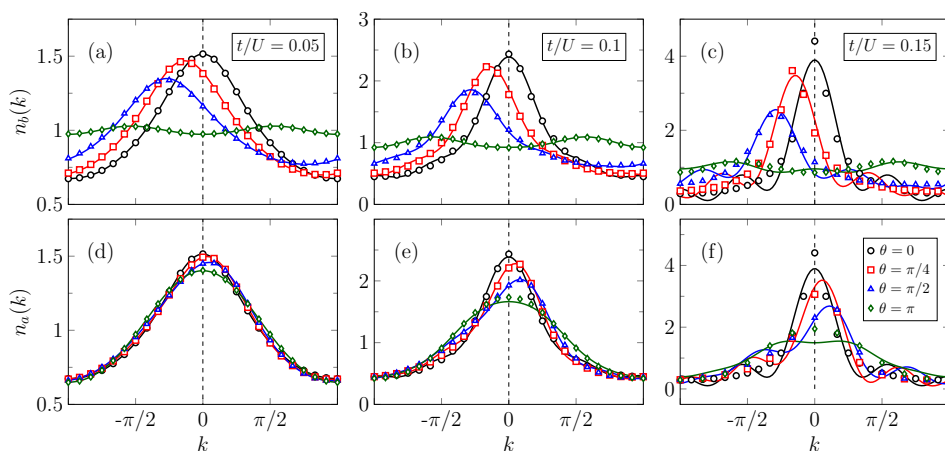


FIG. 5. Momentum distribution function  $n_b(k)$  (upper panels) and  $n_a(k)$  (lower panels) within the first Mott for various  $\theta$  from DMRG with  $L = 48$  and PBCs (symbols) compared with 4th-order strong-coupling expansions (solid lines).

the region of validity of the perturbative expansion seemingly decreases when the fractional angle  $\theta$  is increased even though the MI region becomes larger.

Obviously, there are several other directions to extend our work. The perturbation results in this paper are limited to the Mott insulator for  $\rho = 1$ . First natural extension might be the strong-coupling study in higher integer fillings. Another possibility is the inclusion of a nearest-neighbor interaction which leads to additional Haldane-insulator and density-wave phases [26], the latter being susceptible to a perturbative treatment. Furthermore, the strong-coupling approach could be applied to the AHM in higher dimensions. In this case perturbation theory should be particularly useful since no quasixact results from MPS-based methods are available. Finally, for the comparison with future experiments it would be desirable to investigate the dynamical quantities, such as the single-particle spectral functions, the dynamical structure factor, and the dynamical current and kinetic-energy correlation functions as demonstrated in the BHM [12,27,28].

#### ACKNOWLEDGMENTS

We thank F. Gebhard for valuable discussions. DMRG simulations were performed using the ITensor library [29]. This work was supported by Deutsche Forschungsgemeinschaft (Germany) through SFB 652.

#### APPENDIX A: EXCITATION ENERGIES IN THE BOSE-HUBBARD LIMIT

Taking the limit  $\theta = 0$  in Eqs. (21) and (22) we obtain the single-hole and single-particle excitation energies in the momentum space for the BHM as

$$\begin{aligned} \frac{E_h(k)}{t} = & 8x - \frac{512}{3}x^5 + \left(-2 + 12x^2 - \frac{224}{3}x^4\right)\cos(k) \\ & + (-4x + 64x^3 - \frac{1436}{3}x^5)\cos(2k) \\ & + (-12x^2 + 276x^4)\cos(3k) \\ & + (-44x^3 + 1296x^5)\cos(4k) \\ & - 180x^4\cos(5k) - 788x^5\cos(6k) + O(x^6), \quad (\text{A1}) \end{aligned}$$

and

$$\begin{aligned} \frac{E_p(k)}{t} = & \frac{1}{x} + 5x - \frac{513}{20}x^3 - \frac{80139}{200}x^5 \\ & + \left(-4 + 18x^2 - \frac{137}{150}x^4\right)\cos(k) \\ & + \left(-4x + 64x^3 - \frac{426161}{750}x^5\right)\cos(2k) \\ & + (-12x^2 + 276x^4)\cos(3k) \\ & + (-44x^3 + 1296x^5)\cos(4k) \\ & - 180x^4\cos(5k) - 788x^5\cos(6k) + O(x^6). \quad (\text{A2}) \end{aligned}$$

Direct comparison of Eqs. (A1) and (A2) with iMPS results is demonstrated in Fig. 2. Note that in Eqs. (24) and (25) of Ref. [12] the coefficient of the  $x^5 \cos(6k)$  term in  $E_h(k)$  as well as the coefficients of the  $x^5 \cos(2k)$  and the  $x^5 \cos(6k)$  terms

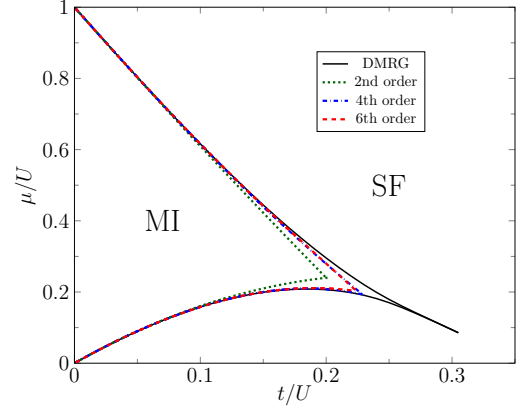


FIG. 6. Ground-state phase diagram of the Bose-Hubbard model ( $\theta = 0$ ). The strong-coupling results (A1) and (A2) show a reasonable agreement with the DMRG data (black solid line).

in  $E_p(k)$  are flawed; these errors were corrected in Eqs. (A1) and (A2).

Plotting chemical potentials,  $\mu_+ = \min\{E_p(k)\}$  and  $\mu_- = -\min\{E_h(k)\}$ , the phase diagram of the BHM can be extracted from the strong-coupling expansions, Eqs. (A1) and (A2), and compared with the DMRG prediction (see Fig. 6).

#### APPENDIX B: MINIMA OF EXCITATION ENERGIES

In Fig. 4, chemical potentials  $\mu^\pm$ , obtained from strong-coupling expansions, show a sudden increase for large  $t/U$  ( $\gtrsim 0.24$ ), especially for  $\theta = \pi/4$  [see, e.g., the results of Fig. 7(a), which were not included in Fig. 4]. In this section we explain the origin of this shortcoming in detail.

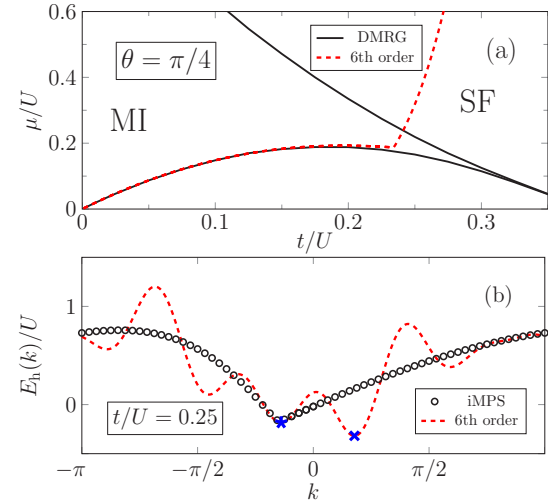


FIG. 7. (a) Zoomed view of Fig. 4(a) showing the artificial upturn of the 6th-order perturbation result  $\mu^-$  at  $\theta = \pi/4$ . (b) Single-hole excitation energy  $E_h(k)$  in the momentum space for  $\theta = \pi/4$  and  $t/U = 0.25$  by the 6th-order strong-coupling expansion (dashed line) compared with the iMPS results (circles). Star and cross symbols denote the correct and wrong minima to estimate chemical potential  $\mu^-$ , see text.



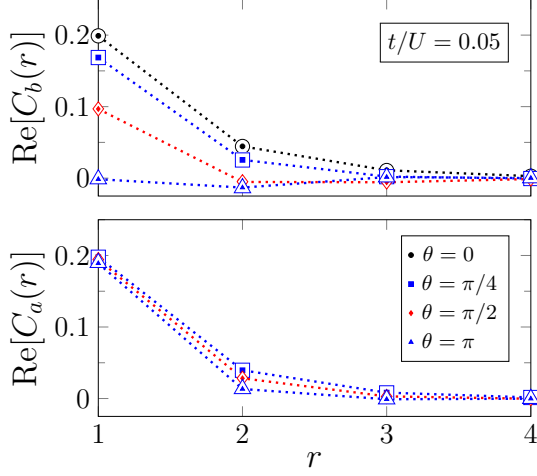


FIG. 8. Strong-coupling results of the boson (upper panel) and anyon (lower panel) correlation functions  $C_{b/a}(r)$  (closed symbols) for the distance  $r = 1$  to 4, compared with the iDMRG data for  $\chi = 100$  (open symbols).

Figure 7(b) shows the single-hole excitation energies by the 6th-order strong-coupling expansion (21) for  $t/U = 0.25$  and  $\theta = \pi/4$  compared with iMPS results. In this intermediate-coupling region the perturbation results oscillate strongly, so that the position of the minimum for  $E_h^{[6]}(k)$  to estimate  $\mu^- = \min\{E_h^{[6]}(k)\}$  shift from negative (star symbol) to positive (cross symbol) momentum, while iMPS data still indicate that the minimum should be located at the negative momentum as in the case of  $t/U < 0.25$ . This sudden change of the location of minima leads to the artificial upturns of the strong-coupling expansions in the intermediate-coupling region of Fig. 4.

### APPENDIX C: CORRELATION FUNCTION

In this Appendix we will give the strong-coupling expressions for the boson and anyon correlation functions. Note that in the anyonic case Eq. (31) should be taken into account. As explained in the main text, we employ the Harris-Lange

transformation and obtain  $C_{b/a}(r)$  for the distance  $r = 1$  to 4 up to 4th order in  $x = t/U$  as

$$C_b(1) = x(2 + 2e^{-i\theta}) + x^3(-18 + 6e^{i\theta} - 4e^{-i\theta} + 8e^{-2i\theta}), \quad (C1)$$

$$C_b(2) = x^2(2 + 12e^{-i\theta} + 4e^{-2i\theta}) + x^4\left(\frac{76}{3} + \frac{32}{3}e^{i\theta} - 200e^{-i\theta} + \frac{76}{3}e^{-2i\theta}\right), \quad (C2)$$

$$C_b(3) = x^3(2 + 30e^{-i\theta} + 48e^{-2i\theta} + 8e^{-3i\theta}), \quad (C3)$$

$$C_b(4) = x^4(56e^{-i\theta} + 216e^{-2i\theta} + 160e^{-3i\theta} + 16e^{-4i\theta}), \quad (C4)$$

and

$$C_a(1) = 4x + x^3(-48 + 20e^{-i\theta} + 20e^{i\theta}), \quad (C5)$$

$$C_a(2) = x^2(12 + 6e^{i\theta}) + x^4\left(-\frac{704}{3} + \frac{136}{3}e^{2i\theta} - \frac{88}{3}e^{i\theta} + 112e^{-i\theta}\right), \quad (C6)$$

$$C_a(3) = x^3(32 + 8e^{2i\theta} + 48e^{i\theta}), \quad (C7)$$

$$C_a(4) = x^4(80 + 240e^{i\theta} + 120e^{2i\theta} + 10e^{3i\theta}). \quad (C8)$$

Finally, the Fourier transforms of Eqs. (C1)–(C4) [(C5)–(C8)] provide us with the momentum distribution function (36) [(37)].

These two-point functions can be compared directly with the iDMRG data for  $\chi = 100$ . Figure 8 demonstrates for the real part that strong-coupling and iDMRG results are in excellent agreement for all fractional angles  $\theta$  at  $x = 0.05$ .

- [1] J. M. Leinaas and J. Myrheim, *Nuovo Cimento B* **37**, 1 (1977).
- [2] F. Wilczek, *Phys. Rev. Lett.* **49**, 957 (1982).
- [3] D. C. Tsui, H. L. Stormer, and A. C. Gossard, *Phys. Rev. Lett.* **48**, 1559 (1982).
- [4] R. B. Laughlin, *Phys. Rev. Lett.* **50**, 1395 (1983).
- [5] F. D. M. Haldane, *Phys. Rev. Lett.* **67**, 937 (1991).
- [6] T. Keilmann, S. Lanzmich, I. McCulloch, and M. Roncaglia, *Nat. Commun.* **2**, 361 (2011).
- [7] S. Greschner and L. Santos, *Phys. Rev. Lett.* **115**, 053002 (2015).
- [8] C. Sträter, S. C. L. Srivastava, and A. Eckardt, *Phys. Rev. Lett.* **117**, 205303 (2016).
- [9] G. Tang, S. Eggert, and A. Pelster, *New J. Phys.* **17**, 123016 (2015).
- [10] J. Arcila-Forero, R. Franco, and J. Silva-Valencia, *Phys. Rev. A* **94**, 013611 (2016).
- [11] W. Zhang, S. Greschner, E. Fan, T. C. Scott, and Y. Zhang, *Phys. Rev. A* **95**, 053614 (2017).
- [12] S. Ejima, H. Fehske, F. Gebhard, K. zu Münster, M. Knap, E. Arrigoni, and W. von der Linden, *Phys. Rev. A* **85**, 053644 (2012).
- [13] B. Damski and J. Zakrzewski, *Phys. Rev. A* **74**, 043609 (2006).
- [14] N. Elstner and H. Monien, *arXiv:cond-mat/9905367*.
- [15] S. R. White, *Phys. Rev. Lett.* **69**, 2863 (1992).
- [16] I. P. McCulloch, *arXiv:0804.2509*.
- [17] U. Schollwöck, *Ann. Phys. (NY)* **326**, 96 (2011).
- [18] J. Haegeman, B. Pirvu, D. J. Weir, J. I. Cirac, T. J. Osborne, H. Verschelde, and F. Verstraete, *Phys. Rev. B* **85**, 100408 (2012).
- [19] J. Haegeman, T. J. Osborne, and F. Verstraete, *Phys. Rev. B* **88**, 075133 (2013).
- [20] A. B. Harris and R. V. Lange, *Phys. Rev.* **157**, 295 (1967).
- [21] P. G. J. van Dongen, *Phys. Rev. B* **49**, 7904 (1994).

- [22] T. D. Kühner, S. R. White, and H. Monien, *Phys. Rev. B* **61**, 12474 (2000).
- [23] S. Ejima, H. Fehske, and F. Gebhard, *Europhys. Lett.* **93**, 30002 (2011).
- [24] Y. Hao, Y. Zhang, and S. Chen, *Phys. Rev. A* **78**, 023631 (2008).
- [25] J. K. Freericks, H. R. Krishnamurthy, Y. Kato, N. Kawashima, and N. Trivedi, *Phys. Rev. A* **79**, 053631 (2009).
- [26] F. Lange, S. Ejima, and H. Fehske, *Phys. Rev. Lett.* **118**, 120401 (2017).
- [27] S. Ejima, H. Fehske, and F. Gebhard, *J. Phys.: Conf. Ser.* **391**, 012143 (2012).
- [28] K. zu Münster, F. Gebhard, S. Ejima, and H. Fehske, *Phys. Rev. A* **89**, 063623 (2014).
- [29] <http://itensor.org/>.

**Finite-temperature dynamic structure factor of the spin-1 XXZ chain with single-ion anisotropy**

Florian Lange, Satoshi Ejima, and Holger Fehske

*Institut für Physik, Ernst-Moritz-Arndt-Universität Greifswald, D-17489 Greifswald, Germany*

(Received 4 December 2017; published 12 February 2018)

Improving matrix-product state techniques based on the purification of the density matrix, we are able to accurately calculate the finite-temperature dynamic response of the infinite spin-1 XXZ chain with single-ion anisotropy in the Haldane, large- $D$ , and antiferromagnetic phases. Distinct thermally activated scattering processes make a significant contribution to the spectral weight in all cases. In the Haldane phase, intraband magnon scattering is prominent, and the on-site anisotropy causes the magnon to split into singlet and doublet branches. In the large- $D$  phase response, the intraband signal is separated from an exciton-antiexciton continuum. In the antiferromagnetic phase, holons are the lowest-lying excitations, with a gap that closes at the transition to the Haldane state. At finite temperatures, scattering between domain-wall excitations becomes especially important and strongly enhances the spectral weight for momentum transfer  $\pi$ .

DOI: [10.1103/PhysRevB.97.060403](https://doi.org/10.1103/PhysRevB.97.060403)

The spin- $S$  XXZ Heisenberg chain, defined by the Hamilton operator

$$\hat{H}_{\text{XXZ}} = \sum_j \left[ \frac{J}{2} (\hat{S}_j^+ \hat{S}_{j+1}^- + \hat{S}_j^- \hat{S}_{j+1}^+) + J_z \hat{S}_j^z \hat{S}_{j+1}^z \right], \quad (1)$$

is perhaps the most fundamental model in the study of low-dimensional magnetism. Here, the experimentally quite often realized and, regarding the nature of the excitations, very different cases  $S = 1/2$  and  $S = 1$  are of particular importance. Haldane's conjecture [1] states that, at the isotropic point, the ground state of a chain with integer spin is gapped while that of a half-integer spin chain is gapless. Motivated by this, there has been a continued interest in the distinct properties of the spin-1 chain. Unlike its spin-1/2 counterpart, however, for which numerous exact results can be obtained via the Bethe ansatz, the spin-1 chain is not integrable and one often has to rely on numerical calculations. Nevertheless, the ground-state phase diagram of the spin-1 chain is now well established. For an antiferromagnetic interaction ( $J_z > 0$ ) and when taking an additional single-ion anisotropy into account, the model exhibits Haldane, large- $D$ , and antiferromagnetic (Néel) phases. These phases are realized by different compounds with  $\text{Ni}^{2+}$  ions, opening up the possibility to directly compare the theoretical predictions with experimental data. Examples are  $\text{Ni}(\text{C}_2\text{H}_8\text{N}_2)_2\text{NO}_2(\text{ClO}_4)$  (the so-called NENP) [2,3] and  $\text{SrNi}_2\text{V}_2\text{O}_8$  [4,5] for the Haldane phase,  $\text{NiCl}_24\text{SC}(\text{NH}_2)_2$  (DTN) [6,7] for the large- $D$  phase, and  $\text{NiCl}_3\text{C}_6\text{H}_5\text{CH}_2\text{CH}_2\text{NH}_3$  [8] for the antiferromagnetic phase. Inelastic neutron scattering provides maybe the most comprehensive experimental characterization of such materials. In this case, the measured quantity is the dynamic spin structure factor which contains detailed information about the systems' excitation spectrum.

From the theory side, a very reliable calculation of the magnetic response of one-dimensional spin systems can be performed, at zero temperature, by means of the numerical density-matrix renormalization group technique [9,10].

However, to more closely approximate the conditions in real experiments, it is desirable to take finite-temperature effects into account, such as the shift and broadening of spectral lines or the intraband scattering recently predicted for the Haldane chain with  $J_z/J = 1$  [11]. A standard approach for the calculation of finite-temperature dynamics is based on evolving the purification of the density matrix in real time [12,13]. The main limitation of this method is the reachable time scale because of the entanglement growth out of equilibrium. A partial remedy for this is given by using time-translation invariance [14] and a backwards time evolution on the auxiliary sites [15].

In this Rapid Communication, we combine these techniques with the infinite boundary conditions (IBCs) originally introduced for zero-temperature calculations [16–18], to obtain the finite-temperature, momentum- and energy-resolved spin structure factor of the anisotropic spin-1 chain directly in the thermodynamic limit. An improved scheme for the evaluation of the time-dependent correlation functions thereby allows us to significantly reduce the numerical effort when exploiting time-translation invariance.

Hereinafter, we will first recapitulate the main previous results for the antiferromagnetic spin-1 chain with single-ion anisotropy. Then our numerical approach will be outlined, and finally we will present and discuss our findings for the dynamic spin structure factor in three different parameter regimes, corresponding to the Haldane, large- $D$ , and antiferromagnetic quantum phases.

The Hamilton operator of the spin-1 XXZ chain with single-ion anisotropy  $D$  is

$$\hat{H} = \hat{H}_{\text{XXZ}} + D \sum_j (\hat{S}_j^z)^2. \quad (2)$$

Assuming a positive exchange parameter  $J > 0$ , the ground-state phase diagram of the model (2) for  $J_z/J > 0$  consists of three gapped phases [19]. At the isotropic point ( $D = 0$ ,  $J_z/J = 1$ ), the ground state belongs to the symmetry-protected topological Haldane phase [20,21]. A transition

to the topologically trivial large- $D$  phase that includes the product state with  $S^z = 0$  at every site takes place for strong on-site positive anisotropy  $D/J$ . Lastly, a long-range ordered antiferromagnetic phase exists at negative  $D/J$  or exchange anisotropy  $J_z > J$ .

Tackling (2) at finite temperatures  $T = 1/\beta$ , within the so-called purification method, the density matrix  $\rho$  of the system is regarded as the reduced density matrix of a pure state  $|\psi\rangle$  in an enlarged Hilbert space with twice as many sites,  $\rho = \text{Tr}_Q |\psi\rangle\langle\psi|$ , where trace is taken over the space  $Q$  spanned by the auxiliary sites. To obtain the equilibrium density matrix at  $T$ , one first constructs a matrix-product state (MPS) representation of a state  $|\psi_\infty\rangle$  corresponding to the infinite-temperature density matrix and then carries out an imaginary time evolution  $|\psi_\beta\rangle = e^{-\beta\hat{H}/2} |\psi_\infty\rangle$  on the physical subsystem. A possible choice for  $|\psi_\infty\rangle$  in the grand canonical ensemble is a state where each physical site is in a maximally entangled state with an auxiliary site. When the physical and auxiliary sites are arranged alternately, such a state has a simple MPS representation that can be easily constructed. Then, for any nearest-neighbor Hamiltonian, the time evolution can be carried out with, for example, a Suzuki-Trotter decomposition and swap gates [22].

To avoid boundary effects, the purification method can be applied directly in the thermodynamic limit by using infinite MPS (iMPS) that are invariant under the translation by a unit cell. This also reduces the number of MPS parameters since only a small unit cell is needed. For the time evolution, one can employ the infinite time-evolving block decimation method [23,24]. However, since the imaginary time evolution is not unitary, the canonical form of the iMPS is lost after each time step, which leads to a rapidly growing error due to large truncations. One should therefore make use of a reorthogonalization procedure [25] to restore the canonical form.

Dynamic properties can be calculated similarly to the  $T = 0$  case by switching to real-time evolution, but a fast growth of the entanglement usually restricts the simulations to short time scales. Several methods have been devised to extend the range of the simulations. A significant improvement is achieved evolving the auxiliary system in reverse time to slow down the entanglement growth [15]. Additionally, time-translation invariance can be used to spread the time evolution to two MPS and increase the simulated time approximately by a factor of 2 [14,15]. In equilibrium, the reverse time evolution on the auxiliary system completely cancels the effect of the physical time evolution for any inverse temperature  $\beta$ . When a local perturbation is applied to  $|\psi_\beta\rangle$ , only the tensors of the MPS in the region over which the perturbation has spread need to be updated during the time evolution. It is therefore possible to use IBCs to avoid finite-size effects in the calculation of dynamic correlation functions. IBCs are also advantageous when calculating correlation functions by using time-translation invariance. In that case, both operators are fixed so that a separate simulation would be necessary for each distance if open boundary conditions are used. For IBCs, however, we can exploit the spatial translation invariance to shift both states relative to each other and obtain the correlation function at arbitrary distance. An MPS with IBCs can be

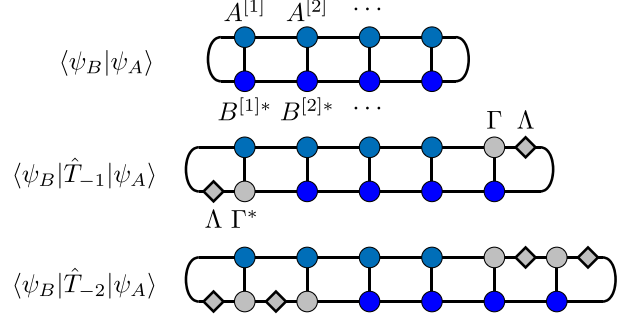


FIG. 1. Graphical representation of Eq. (4). The blue symbols represent the tensors in the finite window that distinguishes between  $|\psi_A\rangle$  and  $|\psi_B\rangle$  while the gray tensors represent the iMPS unit cell.

written as

$$|\psi\rangle = \sum_{\sigma} \dots \Lambda \Gamma^{\sigma_0} A^{[1]\sigma_1} \dots A^{[N]\sigma_N} \Gamma^{\sigma_{N+1}} \Lambda \dots |\sigma\rangle, \quad (3)$$

where  $\sigma_j$  labels the basis states of the local Hilbert space at site  $j$ . The infinitely repeated iMPS unit cell is defined by  $\Gamma$  and  $\Lambda$ , and only the tensors  $A^{[j]}$  in a finite window are updated during the time evolution. For two different states  $|\psi_A\rangle$  and  $|\psi_B\rangle$  with tensors  $A^{[j]}$  and  $B^{[j]}$ , respectively, and the same iMPS unit cell, we have

$$\begin{aligned} \langle\psi_B|\hat{T}_{-r}|\psi_A\rangle &= \sum_{\{\sigma\}} \text{Tr} \left[ A^{[1]\sigma_1} \dots A^{[N]\sigma_N} \left( \prod_{d=1}^r \Gamma^{\sigma_{N+d}} \Lambda \right) \right. \\ &\quad \left. \times B^{[N]\sigma_{N+r}} \dots B^{[1]\sigma_{r+1}} \left( \prod_{d=1}^r \Gamma^{\sigma_{r+d}} \Lambda \right) \right], \end{aligned} \quad (4)$$

where  $\hat{T}_r$  is the translation operator for a shift by  $r$  sites and  $N$  is the number of sites in the window. Graphically, this can be represented as shown in Fig. 1. To calculate the dynamic correlation function for some operator  $\hat{O}$ , one can identify  $|\psi_A\rangle = e^{-i(t/2)\hat{H}} \hat{O}_j |\psi_\beta\rangle$  and  $|\psi_B\rangle = e^{+i(t/2)\hat{H}} \hat{O}_j |\psi_\beta\rangle$  so that Eq. (4) gives  $\langle\hat{O}_{j+r}^\dagger(t)\hat{O}_j(0)\rangle$ , provided one also applies the auxiliary time evolution. In our simulations, the expectation values are taken in the grand canonical ensemble. While we restrict ourselves to gapped phases, the purification method can be applied to gapless phases as well. In that case, the bond dimension required to approximate the equilibrium density matrix with a fixed accuracy would scale polynomially with the inverse temperature  $\beta$  instead of saturating at large  $\beta$  as for gapped phases [26].

The longitudinal and transversal dynamic spin structures factors we are interested in are defined as

$$S^{zz}(k, \omega) = \int_{-\infty}^{\infty} dt \sum_r e^{i(kr - \omega t)} \langle \hat{S}_{j+r}^z(t) \hat{S}_j^z(0) \rangle, \quad (5)$$

$$S^{+-}(k, \omega) = \frac{1}{2} \int_{-\infty}^{\infty} dt \sum_r e^{i(kr - \omega t)} \langle \hat{S}_{j+r}^+(t) \hat{S}_j^-(0) \rangle. \quad (6)$$

We calculate the time-dependent correlation functions in Eqs. (5) and (6) with the method described above and, to reach

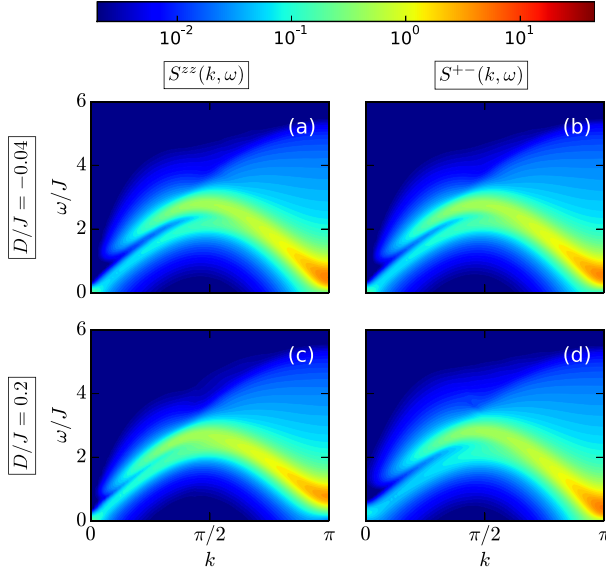


FIG. 2. Finite-temperature dynamic structure factor in the Haldane phase ( $J_z = J$ ) in units of  $J^{-1}$ . The temperature  $T/J = 0.4$ ; the on-site anisotropy  $D/J = -0.04$  in (a), (b) and  $D/J = 0.2$  in (c), (d). All spectral functions are convoluted with a Gaussian of width  $0.1J$ .

a higher resolution, extrapolate the data to larger times using linear prediction [10]. The MPS simulations usually take a couple of days to finish on a modern cluster when using a parallel time-evolving block decimation implementation.

For the Haldane phase, we assume an isotropic exchange ( $J_z/J = 1$ ) and two realistic values of the single-ion anisotropy,  $D/J = -0.04$  and  $D/J = 0.2$ , corresponding to the compounds  $\text{SrNi}_2\text{V}_2\text{O}_8$  [5] and NENP [27], respectively. Since these values are close to the isotropic point already studied in Ref. [11], we restrict ourselves to a single intermediate temperature  $T/J = 0.4$ . Figure 2 gives the results for the dynamic structure factors (5) and (6) (see also Ref. [28] for constant-momentum cuts). The on-site anisotropy causes the magnon to split into a singlet branch ( $S^z = 0$ ) and a doublet branch ( $S^z = \pm 1$ ), which show up in  $S^{zz}(k, \omega)$  and  $S^{+-}(k, \omega)$ , respectively. For positive  $D$ , the singlet gap is larger than the doublet gap, while the situation is reversed for negative  $D$ . At finite temperature, there is an additional spectral weight below the magnon bands, which in the longitudinal (transversal) structure factor is caused by intraband (interband) scattering. The splitting of the magnon branch shifts the position of the interband signal in  $S^{+-}(k, \omega)$  compared to the intraband response seen in  $S^{zz}(k, \omega)$ , so that the spectral weight for zero momentum transfer is centered at a small finite energy. For the considered  $D$  values we find only a small effect of the anisotropy and essentially reproduce the result of Ref. [11] with the system size  $L = 32$  and open boundary conditions. Note, however, that the edge-state modes of Ref. [11] are absent because our simulations are done in the thermodynamic limit.

We now choose an anisotropy  $D/J = 2$  strong enough for the system to be in the topologically trivial large- $D$  phase (see Fig. 3). The lowest-lying excitations in the large- $D$  phase can be viewed as single up or down spins that move in a

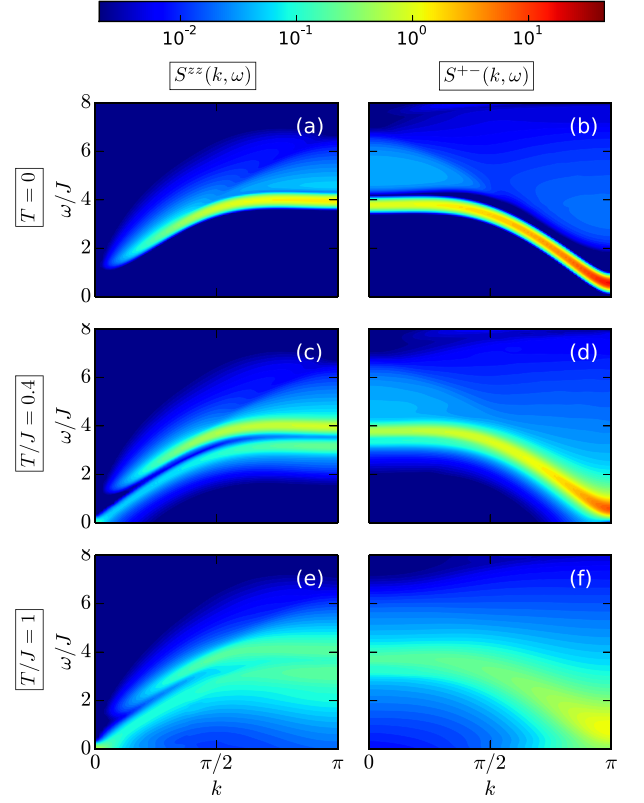


FIG. 3. Dynamic spin structure factor in the large- $D$  phase for  $D/J = 2$ . Again,  $J_z/J = 1$ . (a), (b) Zero-temperature data obtained by pure-state MPS techniques are contrasted with the results for (c), (d)  $T/J = 0.4$  and (e), (f) 1.

background of sites with  $S^z = 0$ . These excitations have been called excitons and antiexcitons [29]. At zero temperature, the longitudinal structure factor  $S^{zz}(k, \omega)$  consists of an exciton-antiexciton continuum and possibly a bound state due to the attractive interaction between opposite spins [29]. For the parameters taken in Fig. 3, a bound state occurs at momenta  $k \gtrsim \pi/2$ . When the temperature is increased, the dynamic structure factor broadens and the contributions of the bound state and the continuum become indistinguishable. Similar to the thermal intraband magnon scattering in the Haldane phase, intraband scattering of excitons and antiexcitons at finite temperature produces additional spectral weight at low energies that is separated from the exciton-antiexciton continuum. When  $D/J$  is lowered, the single-exciton gap decreases, which results in a smaller distance between the intraband-scattering peak and the exciton-antiexciton continuum. In the zero-temperature transversal structure factor  $S^{+-}(k, \omega)$ , most of the spectral weight is concentrated in the single-exciton branch that lies below the three-particle continuum. At finite temperature, the single-exciton line broadens and eventually merges with the continuum. Since only matrix elements between states whose total  $S^z$  differ by one contribute to  $S^{+-}(k, \omega)$ , no intraband scattering is observed in the transversal structure factor. For small momenta  $k \approx 0$ , however, an additional peak appears slightly below the single-exciton line that is likely caused by

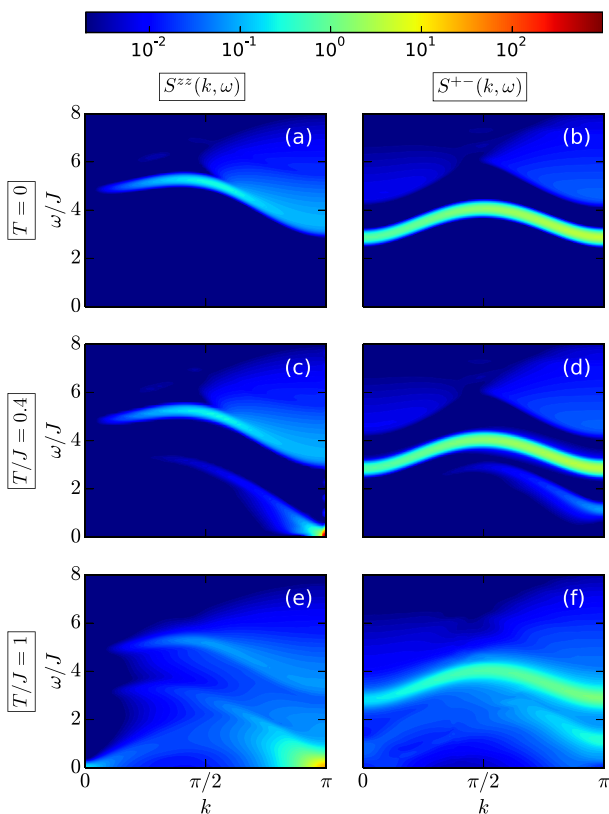


FIG. 4. Dynamic spin structure factor in the antiferromagnetic phase. Model parameters are  $D/J = 0.2$  and  $J_z/J = 2$ . We use  $T/J = 0, 0.4$ , and  $1$  as in Fig. 3.

transitions between excitons and exciton-antiexciton bound states.

For the dynamic magnetic response in the antiferromagnetic phase, both magnons and domain-wall excitations that connect two parts of the chain with different antiferromagnetic order are relevant. Following Ref. [30], we call these domain-wall states holons and spinons. The spin configuration of a holon (spinon) state can be schematically written as  $|\cdots + - + \sigma - + - \cdots\rangle$  with  $\sigma = 0$  ( $\sigma = \pm 1$ ), where  $0$  denotes a site with  $S^z = 0$  and  $\pm$  a site with  $S^z = \pm 1$ . Holons are the lowest-lying excitations and their energy gap closes at the transition to the Haldane phase [30]. Scattering between domain-wall

excitations becomes important at finite temperature, similar to the Villain mode [31] in the antiferromagnetic phase of spin-1/2 chains. The MPS simulations take states with an odd number of domain walls into account. In principle, it should be possible to exclude these states from the calculation by adding a small staggered magnetic field.

Figure 4 shows the dynamic spin structure factors for  $D/J = 0.2$  and  $J_z/J = 2$ . In the zero-temperature longitudinal structure factor  $S^{zz}(k, \omega)$ , a bound state can be seen for  $k \lesssim \pi/2$ . It merges with the two-holon continuum for higher momenta. The small spectral weight above the bound state for  $k \lesssim \pi/2$  corresponds to the two-spinon continuum. At finite temperatures, additional spectral weight shows up at low energies, which again can be related to intraband scattering. Holons are expected to provide the largest contribution. Most strikingly, the thermal intraband scattering leads to a strong increase of the longitudinal structure factor  $S^{zz}(k, \omega)$  around  $k = \pi$  and  $\omega = 0$  [see Figs. 4(c) and 4(e)]. When the temperature is increased, two separate peaks below the zero-temperature response become visible. From the dispersion relations of these excitations, one can deduce that the upper peak corresponds to holon intraband scattering and the lower one to either spinon or magnon intraband scattering. The transversal structure factor  $S^{+-}(k, \omega)$  at zero temperature consists primarily of the single-magnon line and the spinon-holon continuum. Additional low-energy contributions occur for finite temperature. At low temperatures, the scattering between holons and spinons should be most significant. The momentum dependence of the spectral weight is weaker than for the intraband holon-scattering signal in  $S^{zz}(k, \omega)$ .

To summarize, applying infinite boundary conditions to the time-dependent density-matrix renormalization group technique at finite temperatures, the dynamic spin structure factor has been analyzed for the Haldane, large- $D$ , and antiferromagnetic (Néel) phases of the spin-1 XXZ chain with on-site anisotropy. In each case, the finite-temperature result differs markedly from the one at zero temperature because of thermally activated scattering processes. Our results reveal that further high-resolution inelastic neutron scattering experiments would be highly desirable to detect the thermally enhanced spectral weight and prove the differences in the magnetic response between the various spin-1 chain compounds.

MPS simulations were performed using the ITensor library [32]. F.L. was supported by Deutsche Forschungsgemeinschaft through Project No. FE 398/8-1.

- [1] F. D. M. Haldane, *Phys. Rev. Lett.* **50**, 1153 (1983).
- [2] J. P. Renard, M. Verdaguer, L. P. Regnault, W. A. C. Erkelens, J. Rossat-Mignod, and W. G. Stirling, *Europhys. Lett.* **3**, 945 (1987).
- [3] L. P. Regnault, I. Zaliznyak, J. P. Renard, and C. Vettier, *Phys. Rev. B* **50**, 9174 (1994).
- [4] A. K. Bera, B. Lake, A. T. M. N. Islam, B. Klemke, E. Faulhaber, and J. M. Law, *Phys. Rev. B* **87**, 224423 (2013).
- [5] A. K. Bera, B. Lake, A. T. M. N. Islam, O. Janson, H. Rosner, A. Schneidewind, J. T. Park, E. Wheeler, and S. Zander, *Phys. Rev. B* **91**, 144414 (2015).
- [6] V. S. Zapf, D. Zocco, B. R. Hansen, M. Jaime, N. Harrison, C. D. Batista, M. Kenzelmann, C. Niedermayer, A. Lacerda, and A. Paduan-Filho, *Phys. Rev. Lett.* **96**, 077204 (2006).
- [7] S. A. Zvyagin, J. Wosnitzer, C. D. Batista, M. Tsukamoto, N. Kawashima, J. Krzystek, V. S. Zapf, M. Jaime, N. F. Oliveira, and A. Paduan-Filho, *Phys. Rev. Lett.* **98**, 047205 (2007).
- [8] F. Lipps, A. H. Arkenbout, A. Polyakov, M. Günther, T. Salikhov, E. Vavilova, H. H. Klauss, B. Büchner, T. M. Palstra, and V. Kataev, *Fiz. Nizk. Temp.* **43**, 1626 (2017) [*Low Temp. Phys.* **43**, 1298 (2017)].
- [9] S. R. White, *Phys. Rev. Lett.* **69**, 2863 (1992).

- [10] S. R. White and I. Affleck, *Phys. Rev. B* **77**, 134437 (2008).
- [11] J. Becker, T. Köhler, A. C. Tiegel, S. R. Manmana, S. Wessel, and A. Honecker, *Phys. Rev. B* **96**, 060403 (2017).
- [12] M. Suzuki, *J. Phys. Soc. Jpn.* **54**, 4483 (1985).
- [13] F. Verstraete, J. J. García-Ripoll, and J. I. Cirac, *Phys. Rev. Lett.* **93**, 207204 (2004).
- [14] T. Barthel, *New J. Phys.* **15**, 073010 (2013).
- [15] D. Kennes and C. Karrasch, *Comput. Phys. Commun.* **200**, 37 (2016).
- [16] H. N. Phien, G. Vidal, and I. P. McCulloch, *Phys. Rev. B* **86**, 245107 (2012).
- [17] A. Milsted, J. Haegeman, T. J. Osborne, and F. Verstraete, *Phys. Rev. B* **88**, 155116 (2013).
- [18] V. Zauner, M. Ganahl, H. G. Evertz, and T. Nishino, *J. Phys.: Condens. Matter* **27**, 425602 (2015).
- [19] W. Chen, K. Hida, and B. C. Sanctuary, *Phys. Rev. B* **67**, 104401 (2003).
- [20] Z.-C. Gu and X.-G. Wen, *Phys. Rev. B* **80**, 155131 (2009).
- [21] F. Pollmann, A. M. Turner, E. Berg, and M. Oshikawa, *Phys. Rev. B* **81**, 064439 (2010).
- [22] E. M. Stoudenmire and S. R. White, *New J. Phys.* **12**, 055026 (2010).
- [23] G. Vidal, *Phys. Rev. Lett.* **91**, 147902 (2003).
- [24] G. Vidal, *Phys. Rev. Lett.* **98**, 070201 (2007).
- [25] R. Orús and G. Vidal, *Phys. Rev. B* **78**, 155117 (2008).
- [26] T. Barthel, [arXiv:1708.09349](https://arxiv.org/abs/1708.09349).
- [27] T. Delica, K. Kopinga, H. Leschke, and K. K. Mon, *Europhys. Lett.* **15**, 55 (1991).
- [28] See Supplemental Material at <http://link.aps.org/supplemental/10.1103/PhysRevB.97.060403>, which includes Refs. [33,34], for constant-momentum cuts of the dynamic structure factor and a comparison with sigma-model results.
- [29] N. Papanicolaou and P. Spathis, *J. Phys.: Condens. Matter* **2**, 6575 (1990).
- [30] A. F. Albuquerque, C. J. Hamer, and J. Oitmaa, *Phys. Rev. B* **79**, 054412 (2009).
- [31] J. Villain, *Physica B+C* **79**, 1 (1975).
- [32] <http://itensor.org/>.
- [33] T. Jolicoeur and O. Golinelli, *Phys. Rev. B* **50**, 9265 (1994).
- [34] F. H. L. Essler and R. M. Konik, *Phys. Rev. B* **78**, 100403 (2008).

## Supplemental material

### Constant-momentum cuts

To allow a better comparison with other theoretical results and experimental data, we plot the dynamic spin structure factor at selected constant momentum transfer. Fig. S1 shows the spectral functions in the Haldane phase for  $k = \pi/2$  and temperature  $T/J = 0.4$ , where both a coherent magnon mode and an intraband signal can be observed. For single-ion anisotropy  $D/J = 0.2$ , the dynamic structure factor differs noticeably from the isotropic case. In particular, only a single peak appears in the longitudinal part  $S^{zz}(k, \omega)$  [Fig. S1(a)]. The effect of an anisotropy  $D/J = -0.04$  is instead negligible.

Constant-momentum cuts of the dynamic structure factor in the large- $D$  phase are presented in Fig. S2. At finite temperature, an intraband signal is clearly visible in the longitudinal response  $S^{zz}(k, \omega)$  [panels (a) and (b)]. On the other hand, only a small additional peak directly below the exciton line shows up for small momentum in the transverse response  $S^{+-}(k, \omega)$  [Fig. S2(c)]. The thermal shift of the exciton mode in  $S^{+-}(k, \omega)$  depends on the momentum. For  $k = 0$  and  $k = \pi/2$ , the peak moves to lower energy, while it moves to higher energy for  $k = \pi$ .

Fig. S3 shows the dynamic structure factor for  $J_z/J = 2$  and  $D/J = 0.2$  in the antiferromagnetic phase. Because of the relatively large gap, the quasi-particle peaks are only weakly affected when the temperature is changed from  $T = 0$  to  $T/J = 0.4$ . Further increasing the temperature to  $T/J = 1$ , however, leads to a noticeable broadening. As in the other phases, low energy contributions to the structure factor show up at finite temperature that can be attributed to thermally activated scattering

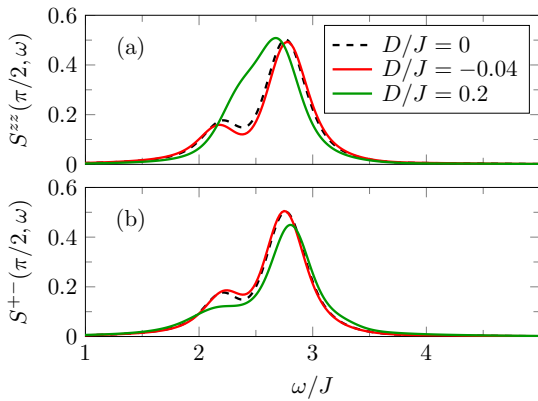


FIG. S1. Finite-temperature dynamic spin structure factor in the Haldane phase at fixed momentum  $k = \pi/2$  and temperature  $T/J = 0.4$  for different values of the single-ion anisotropy  $D$ . Like in the main text, all spectral functions are convoluted with a Gaussian of width  $0.1J$  and shown in units of  $J^{-1}$ .

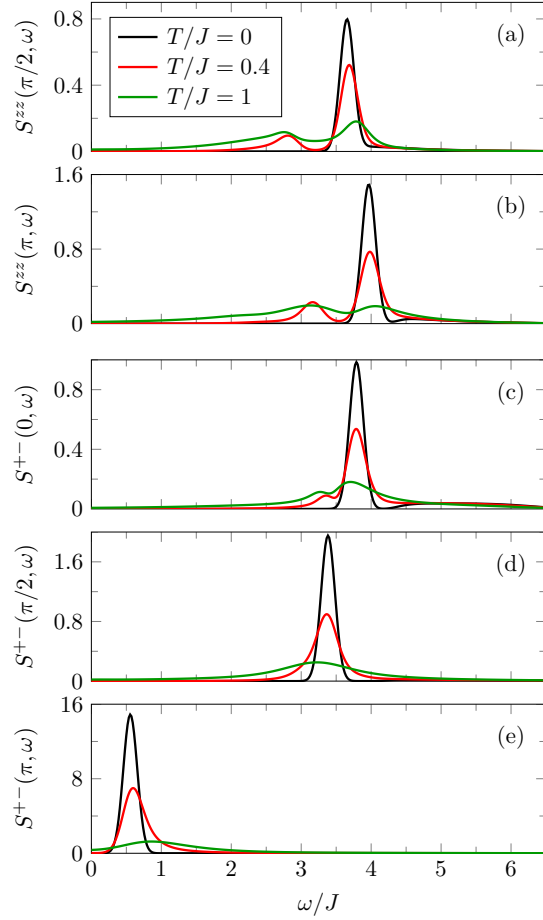


FIG. S2. Momentum cuts of the dynamic spin structure factor in the large- $D$  phase for  $D/J = 2$  and  $J_z/J = 1$ .

processes. In particular, we see two additional peaks in the longitudinal structure factor  $S^{zz}(k, \omega)$  at momentum  $k = \pi/2$  [Fig. S3(a)].

### Comparison with nonlinear sigma model predictions

We now consider the isotropic Heisenberg chain ( $J_z/J = 1$ ,  $D = 0$ ) for which analytical predictions based on the nonlinear sigma model (NLSM) are available. Figure S4 shows the single-magnon peak in the dynamic spin structure factor at momentum  $k = \pi$ . When the temperature is increased, the magnon line shifts and broadens, and the line shape becomes asymmetric, with a larger spectral weight at high energies. Such an asymmetry has also been obtained in the  $O(3)$  NLSM [S2]. We compare the thermal shift of the magnon line in our numerical results with the NLSM calculation of Ref. [S1]. To take the asymmetric line shape into account, we define the line position as the energy corresponding to the full width at half



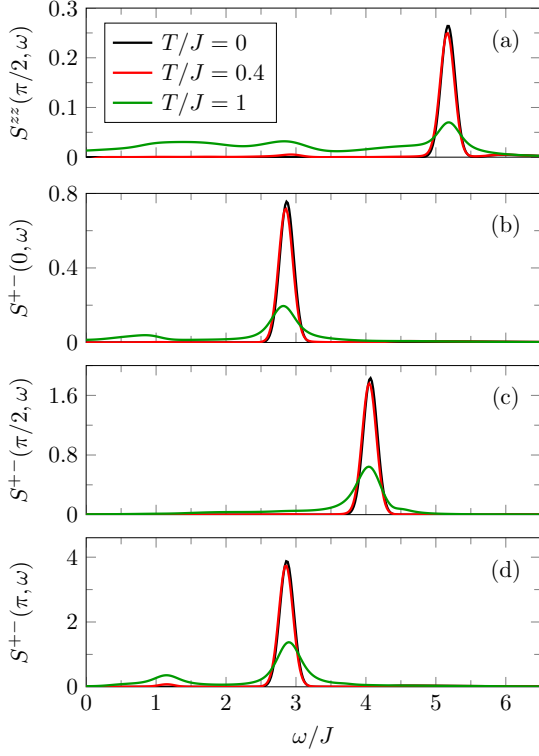


FIG. S3. Momentum cuts of the dynamic structure factor in the antiferromagnetic phase for  $D/J = 0.2$  and  $J_z/J = 2$ .

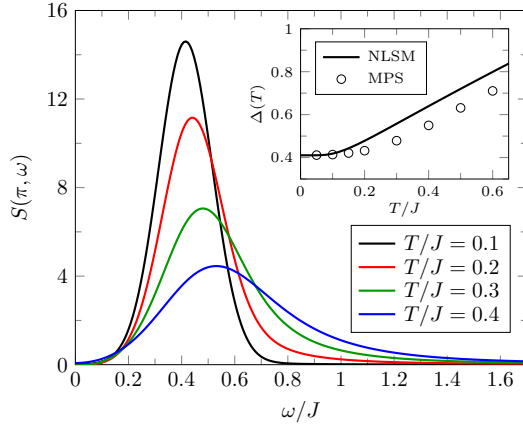


FIG. S4. Dynamic structure factor in the isotropic Heisenberg chain for momentum  $k = \pi$  and several temperatures. The inset compares the position of the numerically obtained single-magnon line (open symbols) with a nonlinear sigma model prediction [S1].

maximum. Our results for the thermal shift agree qualitatively with the activated behaviour predicted by the NLSM. However, the NLSM description seems to overestimate the energy shift already for low temperatures. In contrast to the present results, a quantum Monte Carlo study [S3] has found an almost perfect agreement with the NLSM results for temperatures up to  $T/J \approx 0.4$ .

- 
- [S1] T. Jolicoeur and O. Golinelli, Phys. Rev. B **50**, 9265 (1994).
  - [S2] F. H. L. Essler and R. M. Konik, Phys. Rev. B **78**, 100403 (2008).
  - [S3] J. Becker, T. Köhler, A. C. Tiegeler, S. R. Manmana, S. Wessel, and A. Honecker, Phys. Rev. B **96**, 060403 (2017).



## Dynamic response of spin-2 bosons in one-dimensional optical lattices

Florian Lange, Satoshi Ejima, and Holger Fehske  
*Institut für Physik, Universität Greifswald, 17489 Greifswald, Germany*

We investigate the spin-2 chain model corresponding to the small hopping limit of the spin-2 Bose-Hubbard model using density-matrix-renormalization-group and time-evolution techniques. We calculate both static correlation functions and the dynamic structure factor. The dynamic structure factor in the dimerized phase differs significantly between parameters near the SU(5)-symmetric point and those deeper in the phase where the dimerization is strong. In the former case, most of the spectral weight is concentrated in a single excitation line, while in the latter case, a broad excitation continuum shows up. For the trimerized phase, we find gapless excitations at momenta  $k = \pm 2\pi/3$  in agreement with previous results, although the visibility of these excitations in the dynamic spin response depends strongly on the specific parameters. We also consider parameters for specific atoms which may be relevant for future optical-lattice experiments.

### I. INTRODUCTION

After the realization of the Bose-Hubbard model and its superfluid-Mott insulator transition [1], there have been many proposals to extend experiments with optical lattices to other systems [2, 3]. One approach is to make use of the hyperfine spin of alkali atoms to add a spin-1 or spin-2 degree of freedom to the particles [4, 5], as has already been done in experiments with Bose-Einstein condensates [6–9]. Such systems are expected to be described by generalizations of the Bose-Hubbard model with additional spin-dependent interactions. These interactions could give reason to much richer phase diagrams, which makes the models interesting also from a theoretical point of view [10–12].

The Mott insulating phases in a deep optical lattice can be studied more easily in effective models of localized spins [13]. Here, we are interested in the spin-2 chain corresponding to spin-2 bosons in a one-dimensional lattice at unit filling. In a mean-field approximation this model realizes ferromagnetic, nematic and cyclic phases that each break the spin-rotation symmetry in a different way [11, 14]. However, a more reliable density-matrix-renormalization-group (DMRG) study showed that in one-dimension the nematic and cyclic phases are replaced, respectively, by dimerized and trimerized phases conserving the spin-rotation symmetry [15]. This is in agreement with the Mermin-Wagner theorem which forbids the spontaneous breaking of the continuous spin-rotation symmetry in the case of nematic or cyclic order.

While the phase diagram has been established, the static and dynamic properties of the spin-2 chain are much less explored, also in comparison with its spin-1 counterpart. Especially the dynamic response should be of interest in case the model could be realized experimentally. For this reason, the primary objective of this paper is to calculate the dynamic spin structure factor, which gives valuable insight into the excitation spectrum of this system, and should be accessible in future experiments [16]. We restrict ourselves to the dimerized and trimerized phases specific to one dimension.

### II. MODEL AND METHOD

Bosonic atoms with a fixed hyperfine spin  $S = 2$  in an optical lattice are expected to be described by the spin-2 Bose-Hubbard model

$$\hat{H}_B = -t \sum_{j\sigma} (\hat{b}_{j\sigma}^\dagger \hat{b}_{j+1,\sigma} + \text{H.c.}) + \sum_j \sum_{n=0,2,4} g_n \hat{P}_j^n, \quad (1)$$

where  $\hat{b}_{j\sigma}^\dagger$  ( $\hat{b}_{j\sigma}$ ) are bosonic creation (annihilation) operators and  $\sigma \in \{-2, -1, 0, 1, 2\}$  is the  $z$  projection of the hyperfine spin. The interaction term consists of projection operators  $\hat{P}_j^n$  onto the subspace of states with total spin  $n$  at site  $j$ . It describes  $s$ -wave scattering between the particles, and the interaction strengths  $g_n$  are, up to constant factor, the scattering lengths for the corresponding channel [14].

We study the limit of small hopping at unit filling and assume that the interaction strengths are such that the ground state has a uniform density. The effective spin-2 chain for this limit in second-order perturbation theory is

$$\hat{H} = \sum_j \sum_{n=0,2,4} \epsilon_n \hat{P}_{j,j+1}^n. \quad (2)$$

Here,  $\hat{P}_{j,j+1}^n$  is the projection operator onto the subspace of states with total spin  $n$  between sites  $j$  and  $j+1$ , and  $\epsilon_n = -4t^2/g_n$ . We assume  $\epsilon_n < 0$  since other parameter regions are not accessible with spin-2 bosons. The phase diagram for this model obtained in Ref. [15] can be summarized as follows (cf. Fig. 1): If the term proportional to  $\epsilon_0$  is dominant, the system is in a spontaneously dimerized gapped phase. The  $\epsilon_2$  term instead favors a gapless phase which has a trimerized ground state for finite systems. Lastly, a sufficiently large  $\epsilon_4$  term leads to ferromagnetic order.

The dimerized and trimerized phases both have the full spin-rotation symmetry in the ground state. In the dimerized phase, the symmetry under translation by one site is spontaneously broken while the symmetry under bond-centered reflection is conserved. This is captured by the order parameter

$$\mathcal{O}_D = |\langle \hat{h}_j - \hat{h}_{j+1} \rangle| / |\langle \hat{h}_j + \hat{h}_{j+1} \rangle|, \quad (3)$$

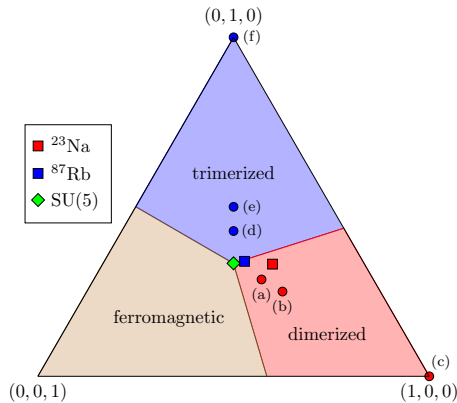


FIG. 1. Schematic phase diagram of the model (2) as a ternary plot of the variables  $(\epsilon_0, \epsilon_2, \epsilon_4)/(\epsilon_0 + \epsilon_2 + \epsilon_4)$  [15]. The circles labeled by (a)-(f) indicate the model-parameter values used in the corresponding panels of Fig. 4.

where  $\hat{h}_j = \sum_{n=0,2,4} \epsilon_n \hat{P}_{j,j+1}^n$  is the nearest-neighbor term in the Hamiltonian acting on the sites  $j$  and  $j+1$ . A dimerized phase also occurs in the model describing spin-1 bosons, the spin-1 bilinear-biquadratic chain [17]. It has long been debated for this model whether there is a direct transition to the ferromagnet or an intermediate disordered nematic phase exists [18–20]. Recent numerical calculations indicate the absence of a nematic phase but find a very small dimerization near the transition [21]. Here, we take a similar view for the spin-2 model, although the distinction between a weakly dimerized phase and a uniform nematic phase is difficult to detect numerically.

The name of the trimerized phase originates from the period-3 structure seen for finite systems in the bond observables such as nearest-neighbor spin correlations [15]. In the thermodynamic limit, this structure disappears and the lattice symmetry is unbroken. Additionally the excitation gap vanishes unlike in the dimerized phase. The trimerized phase does not occur in spin-1 bosons but resembles the gapless phase in a different parameter region of the bilinear-biquadratic chain. It was shown numerically to be described by the  $SU(3)_1$  Wess-Zumino-Witten field theory with central charge  $c = 2$  [22]. In the same work, exact-diagonalization spectra were provided which exhibit minima at  $k = \pm 2\pi/3$ . The excitations at these momenta are expected to become gapless in the thermodynamic limit, which can serve as a signature of the phase in the dynamic spin response.

At the point  $\epsilon_0 = \epsilon_2 = \epsilon_4$ , where the three phases meet, the symmetry of the Hamiltonian (2) becomes  $SU(5)$  and the ground state is highly degenerate [11, 12]. The degeneracy is lifted, however, when moving into the dimerized or the trimerized phase. Only a twofold degeneracy due to the broken translation symmetry remains in the dimerized phase. In the spinful Bose-Hubbard model, from which the effective Hamiltonian (2) is derived, the

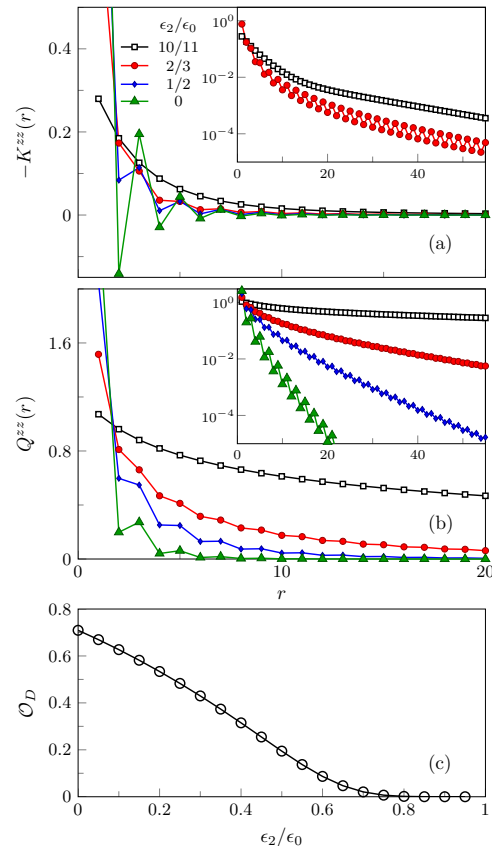


FIG. 2. Spin-spin (a) and quadrupolar (b) correlation functions defined in Eq. (4) and (5) for the dimerized phase. A bond dimension of  $\chi = 4000$  was used in the iDMRG calculations. The insets display the same results using a semi-logarithmic representation. In (c), the dimerization order parameter  $\mathcal{O}_D$  (3) is shown as a function of  $\epsilon_2/\epsilon_0$ .

$SU(5)$ -symmetric point corresponds to the absence of any spin-dependent interactions.

Accurate numerical results for the ground states of one-dimensional systems can be obtained with the DMRG which is based on a matrix-product-state (MPS) ansatz [23, 24]. Here, we employ the infinite DMRG (iDMRG) that works directly in the thermodynamic limit and approximates the ground state by an infinite MPS (iMPS) [25, 26]. Similarly to the finite-system DMRG, the accuracy of the approximation is determined by the so-called bond-dimension  $\chi$ . For details of the numerical method, see Ref. [24]. The iMPS ansatz is well suited to describe gapped ground states but cannot capture the power-law decay of correlations in critical phases. Nevertheless, even for gapless states the correlation functions are correctly reproduced up to a finite distance that increases with the bond dimension  $\chi$  [26]. It is therefore possible to obtain reliable information about the critical properties with the iDMRG method [27].

Static correlation functions can be calculated directly

from the iMPS ground state. To obtain the dynamic structure factors, we use the iMPS as input for a time-evolving-block-decimation simulation [28] with infinite boundary conditions [29]. We spread the time evolution to two separate states in order to reach longer times and thereby a better resolution in frequency space [30, 31]. Furthermore, we use linear prediction to extrapolate the calculated dynamic correlation functions to longer times [32]. This can be done reliably, if the spectrum consists of a small number of sharp excitation peaks.

### III. STATIC CORRELATIONS

Figure 2 shows the iDMRG results for the static spin-spin correlation function

$$K^{zz}(r) = \langle \hat{S}_{j+r}^z \hat{S}_j^z \rangle, \quad (4)$$

and for the quadrupolar correlation function

$$Q^{zz}(r) = \langle [(\hat{S}_{j+r}^z)^2 - 2][(\hat{S}_j^z)^2 - 2] \rangle, \quad (5)$$

in the dimerized phase [see Fig. 2(b)]. The latter is of interest, since quadrupolar ordering occurs in the nematic phase for similar parameters in higher-dimensional versions of the model [11]. For simplicity, we consider only parameter points on the line  $\epsilon_2 = \epsilon_4$ . Since the dimerized phase is gapped, the correlations fall off exponentially at long distances. Near the SU(5) point  $\epsilon_2/\epsilon_0 = 1$ , however, the correlation length is quite large, as can be seen in the quadrupolar correlations  $Q^{zz}(r)$ . Both functions  $K^{zz}(r)$  and  $Q^{zz}(r)$  are more or less smooth for  $\epsilon_2/\epsilon_0 \lesssim 1$  but develop a period-2 structure when  $\epsilon_2/\epsilon_0$  is decreased. This is indicative of the dimerization, which can be more clearly detected by the order parameter  $\mathcal{O}_D$  defined in Eq. (3) [see Fig. 2(c)]. We find that  $\mathcal{O}_D$  is almost zero for  $\epsilon_2/\epsilon_0 \gtrsim 0.7$  but quickly increases for smaller values. Similar behavior of the order parameter  $\mathcal{O}_D$  and dominance of quadrupolar correlations have also been observed in the spin-1 bilinear-biquadratic chain near the transition between ferromagnet and dimerized phase [20, 21].

Results for the trimerized phase are displayed in Fig. 3. Here, we choose  $\epsilon_0 = \epsilon_4$  and analyze the dependence on  $0 \leq \epsilon_0/\epsilon_2 < 1$ . The spin-spin correlations again fall off smoothly near the SU(5) point but now show a period-3 structure deeper in the phase. In contrast to the dimerized phase, the correlations decrease with a power-law, as can be seen in the inset of Fig. 3. Note that the quadrupolar correlation functions do not decrease noticeably slower than the spin-spin correlations (not shown).

The DMRG implementation explicitly enforces the U(1) symmetry of  $S^z$ -conservation but not the full SU(2) symmetry of spin rotations. Nevertheless, the ground state approximation fulfills the spin-rotation symmetry to high accuracy in the dimerized phase. In the gapless trimerized phase, the iDMRG converges to a state with broken spin symmetry. However, the dipolar and

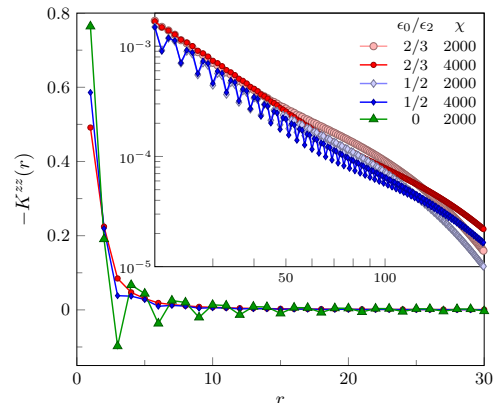


FIG. 3. Spin-spin correlation function (4) in the trimerized phase. The inset uses a log-log scale for the same data.

quadrupolar order parameters vanish, i.e.,  $\langle \hat{S}_j^\alpha \rangle = 0$ ,  $\langle \hat{Q}_j^{\alpha,\beta} \rangle = 0$ , where  $\hat{Q}_j^{\alpha,\beta} = \hat{S}_j^\alpha \hat{S}_j^\beta + \hat{S}_j^\beta \hat{S}_j^\alpha - 4$ . The symmetry breaking shows up only in higher powers of the spin operators, e.g.  $\langle (\hat{S}_j^z)^3 \rangle \neq \langle (\hat{S}_j^x)^3 \rangle$ . This is likely related to the fact that the trimerized phase replaces the cyclic phase in higher dimensions, where the spin-rotation symmetry breaks without dipolar and quadrupolar order occurring [11, 33]. These discrepancies become smaller increasing the bond dimension  $\chi$ , and are expected to vanish for  $\chi \rightarrow \infty$ . Since we are mainly interested in the dynamic spin-spin correlations, the artificial symmetry breaking should not be problematic.

### IV. DYNAMIC SPIN STRUCTURE FACTOR

The dynamic spin structure factor for a periodic chain with  $N$  sites is defined by

$$S(k, \omega) = \sum_{n \neq 0} |\langle n | \tilde{S}_k^z | 0 \rangle|^2 \delta(\omega - (E_n - E_0)), \quad (6)$$

where  $\tilde{S}_k^z = (1/\sqrt{N}) \sum_j e^{ikj} \hat{S}_j^z$ , and  $E_0$  ( $E_n$ ) is the energy of the ground state ( $n$ th excited state). Since the Hamiltonian conserves the spin-rotation symmetry, it is not necessary to consider the other spin components separately. In our numerical calculations, we consider the thermodynamic limit  $N \rightarrow \infty$ .

At the SU(5)-symmetric point  $\epsilon_0 = \epsilon_2 = \epsilon_4$ , the Hamiltonian can be written as  $\hat{H} = (\epsilon_0/2) \sum_j (1 + \hat{\mathcal{P}}_{j,j+1})$ , where  $\hat{\mathcal{P}}_{j,j+1}$  exchanges the states of sites  $j$  and  $j+1$ . We therefore have elementary excitations with dispersion

$$\omega(k)/|\epsilon_0| = 1 - \cos(k), \quad (7)$$

which show up in  $S(k, \omega)$  as delta peaks. In the following we will analyze how the dynamic spin response changes when moving away from this point into either the dimerized or the trimerized phase, again concentrating on parameters  $\epsilon_2 = \epsilon_4$  and  $\epsilon_0 = \epsilon_4$ .

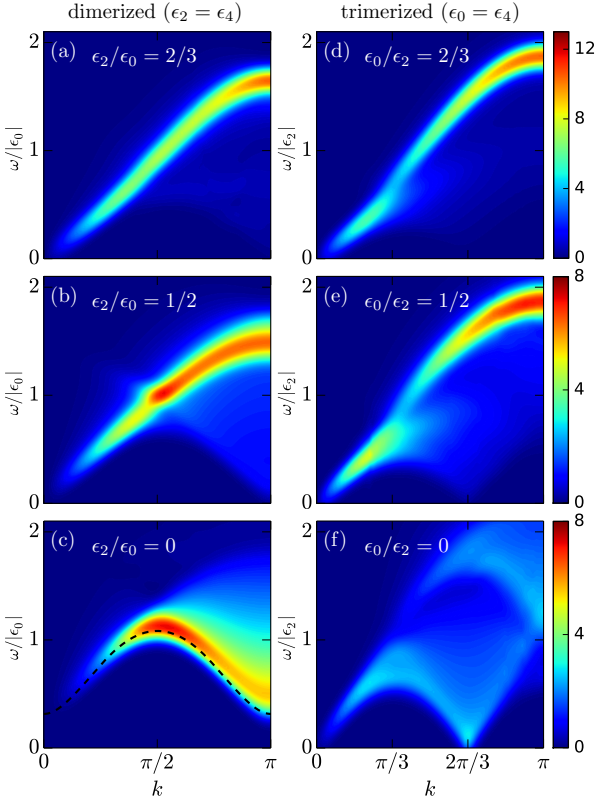


FIG. 4. Dynamic structure factor  $S(k, \omega)$  (6) in the dimerized [(a)-(c)] and trimerized phases [(d)-(f)]. The parameters used are indicated in the phase diagram of Fig. 1. In panel (c), the exact onset of the excitation continuum according to Eq. (8) is marked by the dashed line. The spectral functions are convolved with a Gaussian function with  $\sigma = 0.075|\epsilon_0|$  ( $\sigma = 0.075|\epsilon_2|$ ) in the dimerized (trimerized) phase.

### A. Dimerized phase

Let us begin by discussing the dimerized phase. It is reasonable to assume that the dynamic structure factor close to the SU(5) point shows a dispersion similar to Eq. (7). On the other hand, the excitation spectrum at the point  $\epsilon_2 = \epsilon_4 = 0$  is known exactly, and it differs significantly from the one at the SU(5) point. In particular, it is built from pairs of excitations, which lead to a continuum in  $S(k, \omega)$ . Their dispersion is given by [34]

$$\omega(k)/|\epsilon_0| = \sqrt{A + B \sin^2(k)}, \quad (8)$$

where  $A \approx 0.290$  and  $B \approx 9.725$ . Our iDMRG results indicate that the ground state for  $\epsilon_2 = 0$  is strongly dimerized, nearly consisting of fully decoupled pairs of nearest-neighbor singlets. In fact, the exact dispersion (8) roughly agrees with a simple estimate based on a decoupled site moving as a domain wall through such a fully dimerized state.

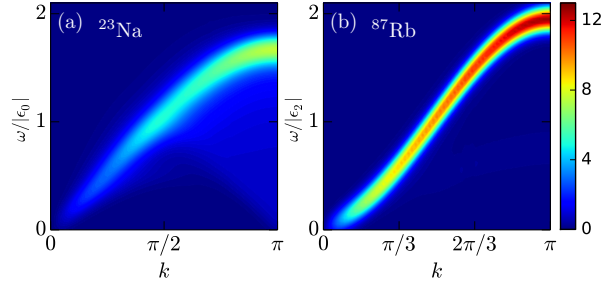


FIG. 5. Dynamic structure factor for parameters calculated using the scattering lengths of Ref. [35], namely  $(\epsilon_0, \epsilon_2, \epsilon_4)/(\epsilon_0 + \epsilon_2 + \epsilon_4) \approx (0.43, 0.33, 0.24)$  and  $(0.36, 0.34, 0.30)$  for  $^{23}\text{Na}$  and  $^{87}\text{Rb}$ , respectively. The Gaussian broadening is as in Fig. 4.

Determining numerically the dynamic structure factor  $S(k, \omega)$ , we can demonstrate how the excitation spectrum changes between the two limits [Fig. 4(a)-(c)]. Near the SU(5) point, up to at least  $\epsilon_2/\epsilon_0 = 2/3$ , the dynamic structure factor  $S(k, \omega)$  is indeed dominated by a single excitation line, although a broad continuum below it is also visible. The dispersion becomes linear at small momenta but otherwise stays qualitatively similar to the cosine form of Eq. (7). It is in fact very similar to the dispersion  $\omega(k) \propto \sqrt{[1 - \cos(k)]^2 + A \sin^2(k)}$  resulting from a generalized spin-wave analysis around a nematically ordered mean-field state of a spin-1 chain [36, 37], even though our ground state has no nematic order and we consider a spin-2 model.

Going to smaller values of  $\epsilon_2/\epsilon_0$ , the dynamic response changes more significantly. The energy gap becomes noticeably larger and the spectral weight gets spread over a wide excitation continuum, particularly for  $|k| > \pi/2$ . The onset of the continuum in the limit  $\epsilon_2 = 0$  is in excellent agreement with the exact dispersion (8). Comparing with Fig. 2, we find that the change in  $S(k, \omega)$  coincides with an increase in the dimerization strength  $\mathcal{O}_D$ .

### B. Trimerized phase

Let us now discuss the dynamic structure factor in the trimerized phase [Fig. 4(d)-(f)]. According to a previous analysis this phase is characterized by gapless excitations with spin  $S = 0, 1, 2$  at momenta  $k = \pm 2\pi/3$  [22]. Numerically, we find that for  $\epsilon_0/\epsilon_2 = 2/3$ , the spectral weight is still concentrated in a single line with a dispersion similar to that found in the dimerized phase. Further away from the SU(5) point, for  $\epsilon_0/\epsilon_2 = 1/2$ , a continuum of excitations appears at lower energies. In particular, the gap closes at  $k = 2\pi/3$  as anticipated in Ref. [22]. Moving towards the limit  $\epsilon_0 = 0$ , the response at  $k = 2\pi/3$  becomes more pronounced.

### C. Relation to experiments

The parameters describing an optical lattice system will depend on the scattering lengths of the particles. With the values given in Ref. [35], one expects that  $^{23}\text{Na}$  atoms develop a dimerized and  $^{87}\text{Rb}$  atoms a trimerized state [15]. We have included results for these parameters as examples for the two phases. One should note, however, that experiments have found a very short lifetime for  $^{23}\text{Na}$  gases in the manifold with hyperfine spin  $S = 2$ , which makes an actual realization of the corresponding spin Hamiltonian unlikely [38]. Systems of  $^{87}\text{Rb}$  atoms are more promising [39] although, to our knowledge, the model (2) has not implemented so far. There are different estimates for the scattering length of  $^{87}\text{Rb}$  in the literature [5, 39] but the deviations are rather small and we do not expect them to notably affect the dynamic response function.

For the  $^{23}\text{Na}$  parameters [Fig. 5(a)], the dynamic structure factor  $S(k, \omega)$  seems to exhibit signatures of both the weak and the strong dimerization limit, i.e., there is a clear excitation line but also significant spectral weight in the continuum below it. In agreement with this, the dimerization order parameter takes an intermediate value  $\mathcal{O}_D \approx 0.14$ . For  $^{87}\text{Rb}$  [Fig. 5(b)], we do not see the low-energy excitations at  $k = 2\pi/3$  characteristic for the trimerized phase. Instead, the dynamic structure factor resembles that at the  $\text{SU}(5)$ -symmetric point with dispersion (7). Perhaps this is not surprising since, as shown in Fig. 1, the  $^{87}\text{Rb}$  parameters lie close to the  $\text{SU}(5)$  point.

### V. CONCLUSION

We have used time-dependent matrix-product-state techniques to study the dynamic structure factor of a

spin-2 chain describing spinful bosons in optical lattices. The spectra in the dimerized and the trimerized phases are known to be qualitatively different. While the dimerized phase is gapped, the trimerized one has gapless excitations at momenta  $k = \pm 2\pi/3$ . In the dynamic spin structure factor, however, these differences become apparent only deeper into the respective phases. Near the  $\text{SU}(5)$  point, where dimerized, trimerized and ferromagnetic phases meet, the observed spectra are quite similar, with a single dominant excitation line and, in the dimerized phase, only a very small gap. As parameters further away from this point correspond to relatively strong spin-dependent interactions in the underlying spin-2 Bose-Hubbard model, they may be difficult to realize experimentally. Using the scattering lengths of Ref. [35], we have carried out simulations for  $^{87}\text{Rb}$  and  $^{23}\text{Na}$ . The dynamic structure factor for the potentially feasible  $^{87}\text{Rb}$  systems indeed shows only a single branch with a dispersion similar to the one at the  $\text{SU}(5)$  point.

So far we have considered only systems at zero temperature in the limit of a deep optical lattice. In a real experiment, however, temperature and hopping will be finite and it would be interesting to see how this affects the system's properties. While it is possible to do this with matrix-product-state techniques, the required computational effort would be significantly higher than in the present work.

### ACKNOWLEDGMENTS

FL was supported by Deutsche Forschungsgemeinschaft (Germany) through project FE 398/8-1. DMRG simulations were performed using the ITensor library [40].

- 
- [1] M. Greiner, O. Mandel, T. Esslinger, T. W. Hänsch, and I. Bloch, *Nature* **415**, 39 (2002).
  - [2] C. Gross and I. Bloch, *Science* **357**, 995 (2017).
  - [3] J. Simon, W. S. Bakr, R. Ma, M. E. Tai, P. M. Preiss, and M. Greiner, *Nature* **472**, 307 (2011).
  - [4] E. Demler and F. Zhou, *Phys. Rev. Lett.* **88**, 163001 (2002).
  - [5] D. M. Stamper-Kurn and M. Ueda, *Rev. Mod. Phys.* **85**, 1191 (2013).
  - [6] J. Stenger, S. Inouye, D. M. Stamper-Kurn, H.-J. Miesner, A. P. Chikkatur, and W. Ketterle, *Nature* **396**, 345 (1998).
  - [7] H. Schmaljohann, M. Erhard, J. Kronjäger, M. Kottke, S. van Staa, L. Cacciapuoti, J. J. Arlt, K. Bongs, and K. Sengstock, *Phys. Rev. Lett.* **92**, 040402 (2004).
  - [8] M.-S. Chang, C. D. Hamley, M. D. Barrett, J. A. Sauer, K. M. Fortier, W. Zhang, L. You, and M. S. Chapman, *Phys. Rev. Lett.* **92**, 140403 (2004).
  - [9] T. Kuwamoto, K. Araki, T. Eno, and T. Hirano, *Phys. Rev. A* **69**, 063604 (2004).
  - [10] R. V. Pai, K. Sheshadri, and R. Pandit, *Phys. Rev. B* **77**, 014503 (2008).
  - [11] R. Barnett, A. Turner, and E. Demler, *Phys. Rev. Lett.* **97**, 180412 (2006).
  - [12] H. Yang and H. Katsura, *Phys. Rev. Lett.* **122**, 053401 (2019).
  - [13] A. Imambekov, M. Lukin, and E. Demler, *Phys. Rev. A* **68**, 063602 (2003).
  - [14] K. Eckert, Ł. Zawitkowski, M. J. Leskinen, A. Sanpera, and M. Lewenstein, *New J. Phys.* **9**, 133 (2007).
  - [15] P. Chen, Z.-L. Xue, I. P. McCulloch, M.-C. Chung, and S.-K. Yip, *Phys. Rev. A* **85**, 011601(R) (2012).
  - [16] D. Baillie and P. B. Blakie, *Phys. Rev. A* **93**, 033607 (2016).
  - [17] M. N. Barber and M. T. Batchelor, *Phys. Rev. B* **40**, 4621 (1989).
  - [18] A. V. Chubukov, *Phys. Rev. B* **43**, 3337 (1991).
  - [19] K. Buchtá, G. Fátá, O. Legeza, and J. Sólyom, *Phys. Rev. B* **72**, 054433 (2005).

- [20] A. Läuchli, G. Schmid, and S. Trebst, *Phys. Rev. B* **74**, 144426 (2006).
- [21] S. Hu, A. M. Turner, K. Penc, and F. Pollmann, *Phys. Rev. Lett.* **113**, 027202 (2014).
- [22] P. Chen, Z.-L. Xue, I. P. McCulloch, M.-C. Chung, C.-C. Huang, and S.-K. Yip, *Phys. Rev. Lett.* **114**, 145301 (2015).
- [23] S. R. White, *Phys. Rev. Lett.* **69**, 2863 (1992).
- [24] U. Schollwöck, *Ann. Phys.* **326**, 96 (2011).
- [25] I. P. McCulloch, arXiv:0804.2509.
- [26] G. Vidal, *Phys. Rev. Lett.* **98**, 070201 (2007).
- [27] S. Ejima, T. Yamaguchi, F. H. L. Essler, F. Lange, Y. Ohta, and H. Fehske, *SciPost Phys.* **5**, 59 (2018).
- [28] G. Vidal, *Phys. Rev. Lett.* **91**, 147902 (2003).
- [29] H. N. Phien, G. Vidal, and I. P. McCulloch, *Phys. Rev. B* **86**, 245107 (2012).
- [30] T. Barthel, *New J. Phys.* **15**, 073010 (2013).
- [31] F. Lange, S. Ejima, and H. Fehske, *Phys. Rev. B* **97**, 060403(R) (2018).
- [32] S. R. White and I. Affleck, *Phys. Rev. B* **77**, 134437 (2008).
- [33] F. Zhou and G. W. Semenoff, *Phys. Rev. Lett.* **97**, 180411 (2006).
- [34] A. Klümper, *J. Phys. A: Math. Gen.* **23**, 809 (1990).
- [35] C. V. Ciobanu, S.-K. Yip, and T.-L. Ho, *Phys. Rev. A* **61**, 033607 (2000).
- [36] V. M. Matveev, *Zh. Eksp. Teor. Fiz.* **65**, 1626 (1973), [*Sov. Phys. JETP* **38**, 813 (1973)].
- [37] N. Papanicolaou, *Nucl. Phys. B* **305**, 367 (1988).
- [38] A. Görlitz, T. L. Gustavson, A. E. Leanhardt, R. Löw, A. P. Chikkatur, S. Gupta, S. Inouye, D. E. Pritchard, and W. Ketterle, *Phys. Rev. Lett.* **90**, 090401 (2003).
- [39] A. Widera, F. Gerbier, S. Fölling, T. Gericke, O. Mandel, and I. Bloch, *New J. Phys.* **8**, 152 (2006).
- [40] <http://itensor.org/>.



## Spin transport through a spin- $\frac{1}{2}$ XXZ chain contacted to fermionic leads

Florian Lange,<sup>1,2</sup> Satoshi Ejima,<sup>1,2</sup> Tomonori Shirakawa,<sup>2,3,4,5</sup> Seiji Yunoki,<sup>2,4,5</sup> and Holger Fehske<sup>1</sup>

<sup>1</sup>*Institut für Physik, Ernst-Moritz-Arndt-Universität Greifswald, 17489 Greifswald, Germany*

<sup>2</sup>*Computational Condensed Matter Physics Laboratory, RIKEN Cluster for Pioneering Research (CPR), Saitama 351-0198, Japan*

<sup>3</sup>*International School for Advanced Studies (SISSA), via Bonomea 265, 34136, Trieste, Italy*

<sup>4</sup>*Computational Quantum Matter Research Team, RIKEN Center for Emergent Matter Science (CEMS), Saitama 351-0198, Japan*

<sup>5</sup>*Computational Materials Science Research Team, RIKEN Center for Computational Science (R-CCS), Hyogo 650-0047, Japan*



(Received 23 April 2018; published 14 June 2018)

We employ matrix-product state techniques to numerically study the zero-temperature spin transport in a finite spin- $\frac{1}{2}$  XXZ chain coupled to fermionic leads with a spin bias voltage. Current-voltage characteristics are calculated for parameters corresponding to the gapless XY phase and the gapped Néel phase. In both cases, the low-bias spin current is strongly suppressed unless the parameters of the model are fine tuned. For the XY phase, this corresponds to a conducting fixed point where the conductance agrees with the Luttinger-liquid prediction. In the Néel phase, fine tuning the parameters similarly leads to an unsuppressed spin current with a linear current-voltage characteristic at low bias voltages. However, with increasing the bias voltage, there occurs a sharp crossover to a region where the current-voltage characteristic is no longer linear and a smaller differential conductance is observed. We furthermore show that the parameters maximizing the spin current minimize the Friedel oscillations at the interface, in agreement with the previous analyses of the charge current for inhomogeneous Hubbard and spinless fermion chains.

DOI: [10.1103/PhysRevB.97.245124](https://doi.org/10.1103/PhysRevB.97.245124)

### I. INTRODUCTION

Besides the more usual semiconductor- and metal-based spintronics, there have been proposals to use magnetic insulators in spin-based devices [1–3]. An advantage of these systems would be the absence of scattering due to conduction electrons, which may allow spin-current transmission over longer distances. Experiments have demonstrated the possibility to electrically induce a magnon spin current at a Pt/Y<sub>3</sub>Fe<sub>5</sub>O<sub>12</sub> interface by using the spin-Hall effect [1]. More recently, a spin current has been driven through the spin- $\frac{1}{2}$ -chain material Sr<sub>2</sub>CuO<sub>3</sub> by applying a temperature gradient [3]. This was interpreted as a spinon spin current induced by the spin-Seebeck effect.

A lot of research has been reported on the spin transport in the antiferromagnetic spin- $\frac{1}{2}$  XXZ chain, especially concerning the question whether the dynamics are ballistic or diffusive in the linear-response regime. At zero temperature, it is known from the exact Bethe-ansatz calculations that the spin transport is ballistic in the gapless phase and diffusive in the gapped phase [4]. There is considerable analytical and numerical evidence that this also holds true at any finite temperature [5–9]. A possible exception is the SU(2) isotropic point for which differing results have been obtained.

Here we study the finite-bias spin transport for a specific setup with fermionic leads at zero temperature. To this end, we employ the density-matrix renormalization group (DMRG) [10] and the real-time evolution of matrix-product states (MPS) via the time-evolving block decimation (TEBD) [11]. The difference from previous studies of transport in finite spin chains is our choice of the leads. In Refs. [12–14] boundary driving modeled by a Lindblad equation was considered, which

allows the direct calculation of the nonequilibrium steady state with matrix-product-operator techniques. Interestingly, a negative differential conductance was observed for strong driving in the gapped phase. Other studies have explored the transport in inhomogeneous XXZ chains [15] and fermionic quantum wires coupled to noninteracting leads, which map to an XXZ chain through a Jordan-Wigner transformation [16–20].

In setups with leads, the transport may be influenced by backscattering at the interfaces which, for repulsive interactions, can completely inhibit transport at low voltages and temperatures [21,22]. In general, the strength of the backscattering will depend in a nontrivial way on the parameters on either side of the interface. In particular, it has been shown for typical models of fermionic chains that conducting fixed points with perfect conductance exist [19,23,24].

The primary concern of this paper is to numerically explore the possibility of such conducting fixed points for our specific setup of the junction. We consider both the gapless XY and the gapped Néel phase of the spin- $\frac{1}{2}$  XXZ chain. In the latter case, the energy gap leads to insulating behavior at zero temperature. One may then ask how the insulating state breaks down at finite bias voltage and how the transport depends on the length of the chain. The charge transport in a similar setup with a Mott-insulating Hubbard chain has been addressed, e.g., in Ref. [25]. Here we show that conducting fixed points exist not only for gapless but, in a sense, also for gapped spin chains. However, beyond a low-bias region with nearly ideal conductance the current-voltage curves at these fixed points are qualitatively different in the two regimes, with a smaller conductance in the gapped phase.

The rest of this paper is organized as follows. In Sec. II we introduce the model and describe the numerical method employed. We then demonstrate in Sec. III the existence of nontrivial conducting fixed points. To this end, we calculate steady-state spin currents and Friedel oscillations at the interface. In Sec. IV, current-voltage curves for the gapless and the gapped regime are examined. Finally, Sec. V summarizes our main results.

## II. MODEL AND METHOD

We consider the spin transport through a spin-chain material sandwiched between two conducting leads. The transport is assumed to occur in the spin-chain direction and all interchain couplings are neglected. Thereby, we end up with a one-dimensional Hamiltonian

$$\hat{H}_0 = \hat{H}_S + \hat{H}_{L_1} + \hat{H}_{L_2} + \hat{H}_{S-L_1} + \hat{H}_{S-L_2}, \quad (1)$$

with  $\hat{H}_S$  describing a single spin chain,  $\hat{H}_{L_1(L_2)}$  the left (right) lead, and  $\hat{H}_{S-L_1(S-L_2)}$  the coupling between the spin chain and the left (right) lead. From now on, we restrict ourselves to the spin- $\frac{1}{2}$  XXZ case so that

$$\hat{H}_S = J \sum_{j=1}^{N_S-1} \left[ \frac{1}{2} (\hat{S}_j^+ \hat{S}_{j+1}^- + \hat{S}_j^- \hat{S}_{j+1}^+) + \Delta \hat{S}_j^z \hat{S}_{j+1}^z \right], \quad (2)$$

where  $N_S$  is the number of sites of the spin chain,  $\hat{S}_j^\alpha$  is the  $\alpha$  ( $= x, y, z$ ) component of the spin- $\frac{1}{2}$  operator at site  $j$ , and  $\hat{S}_j^\pm = \hat{S}_j^x \pm i \hat{S}_j^y$ . The fermionic leads are modeled by semi-infinite tight-binding chains at half-filling. Thus, the Hamiltonian for the left (right) lead is

$$\hat{H}_{L_1(L_2)} = -t \sum_{\sigma=\uparrow,\downarrow} \sum_{\substack{j < 0 \\ (j > N_S)}} [\hat{c}_{j\sigma}^\dagger \hat{c}_{j+1,\sigma} + \hat{c}_{j+1,\sigma}^\dagger \hat{c}_{j\sigma}], \quad (3)$$

where  $\hat{c}_{j\sigma}$  is the annihilation operator of an electron at site  $j$  with spin  $\sigma$  ( $= \uparrow, \downarrow$ ). For simplicity, the couplings between the spin chain and the leads are assumed to be identical to the exchange interaction inside the spin chain. By defining the spin operators  $\hat{S}_j^+ = \hat{c}_{j\uparrow}^\dagger \hat{c}_{j\downarrow}$ ,  $\hat{S}_j^- = \hat{c}_{j\downarrow}^\dagger \hat{c}_{j\uparrow}$ , and  $\hat{S}_j^z = \frac{1}{2} (\hat{c}_{j\uparrow}^\dagger \hat{c}_{j\uparrow} - \hat{c}_{j\downarrow}^\dagger \hat{c}_{j\downarrow})$  at tight-binding site  $j$ , the coupling terms can be written as

$$\hat{H}_{S-L_1} = J \left[ \frac{1}{2} (\hat{S}_0^+ \hat{S}_1^- + \hat{S}_0^- \hat{S}_1^+) + \Delta \hat{S}_0^z \hat{S}_1^z \right] \quad (4)$$

and

$$\hat{H}_{S-L_2} = J \left[ \frac{1}{2} (\hat{S}_{N_S}^+ \hat{S}_{N_S+1}^- + \hat{S}_{N_S}^- \hat{S}_{N_S+1}^+) + \Delta \hat{S}_{N_S}^z \hat{S}_{N_S+1}^z \right]. \quad (5)$$

We calculate the steady-state spin current that is generated by applying a spin bias voltage  $V$ . As in Ref. [25], it is assumed that the potential drops off linearly in the spin chain, which adds the following term in the Hamiltonian (see also Fig. 1):

$$\hat{H}_V = \sum_j V_j \hat{S}_j^z, \quad (6)$$

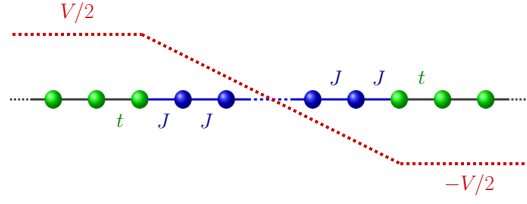


FIG. 1. Schematic depiction of the setup defined by the Hamiltonian  $\hat{H}_0 + \hat{H}_V$  according to Eqs. (1) and (6). Blue (green) circles indicate the spin chain (left and right leads). The red dashed line denotes the spin bias potential, which linearly decreases inside the spin chain.

where

$$V_j = \begin{cases} \frac{V}{2}, & j \leq 0, \\ -\frac{V}{N_S+1} j + \frac{V}{2}, & 1 \leq j \leq N_S, \\ -\frac{V}{2}, & j \geq N_S + 1. \end{cases} \quad (7)$$

The operator of the local spin current is defined as

$$\hat{j}_j^z = \begin{cases} -\frac{i t}{2} \hat{c}_j^\dagger \sigma_z \hat{c}_{j+1} + \text{H.c.}, & j < 0 \text{ or } j > N_S, \\ \frac{i t}{2} \hat{S}_j^+ \hat{S}_{j+1}^- + \text{H.c.}, & 0 \leq j \leq N_S, \end{cases} \quad (8)$$

where  $\hat{c}_j^\dagger = (\hat{c}_{j\uparrow}^\dagger, \hat{c}_{j\downarrow}^\dagger)$  and  $\sigma_z$  is the  $z$  component of Pauli matrices [26]. Our transport simulations are carried out in the zero-temperature limit. Then the system is initially in the ground state at time  $\tau = 0$ . More precisely, the time evolution is started from the ground state of  $\hat{H}_0$ , where the spin chain and the leads are already coupled, and the spin bias voltage  $V$  is applied at  $\tau = 0$ . As discussed in Refs. [18,27], other setups are possible. For example, if one starts with the two leads decoupled from the spin chain and turns on the coupling, the transient behavior is different but the same steady-state properties are obtained. If, instead, the system is in the ground state with a finite spin bias  $V$  and the bias is switched off at  $\tau = 0$ , different steady-state currents are expected for large  $V$  [27].

For the numerical calculation of the steady-state current, we mostly follow the MPS-based approach of Refs. [18,25,27]. The DMRG and parallel TEBD are used, respectively, to calculate the ground state of  $\hat{H}_0$  and simulate the time evolution after the spin bias (described by  $\hat{H}_V$ ) is switched on at  $\tau = 0$ . We employ a standard Suzuki-Trotter approximation where the Hamiltonian is decomposed into terms acting on even and odd bonds. Specifically, a second-order decomposition with time step  $\delta\tau = 0.05/t$  is used. The leads have to be truncated to finite length  $N_L$ , which gives rise to a discretization in the energy spectrum. The error due to this may be reduced by choosing appropriate boundary conditions with bond-dependent hopping strength that increase the energy resolution in the relevant energy region [17,18]. Here, however, we find the leads with uniform hopping  $t$  to be sufficient.

In our calculation of the steady-state current, the accuracy is mainly limited by the accessible timescale. The finite size of the leads obviously restricts the simulations to the time until the current reflected at the open boundaries of the leads returns to the spin chain. Additionally, the entanglement growth of

an out-of-equilibrium state requires an increase of the bond dimension  $m$  during the course of the time evolution, which eventually makes an accurate MPS representation of the state too costly. In the current setup, the von-Neumann entanglement entropy of the state after the perturbation grows linearly with the time [25], which requires an exponential increase of the bond dimension  $m$  for a fixed truncation error. The rate of the entanglement growth depends strongly on the applied voltage  $V$ . Simulation for large  $V$  are typically more expensive. We fix the truncation error to a maximum discarded weight  $10^{-6}$ , which, in the worst cases, requires bond dimensions as large as  $m = 2200$ .

In principle, an MPS representation with one tensor for each site  $j$  in Eq. (1) could be used for all of our simulations. However, for small  $V$ , where larger lead sizes are necessary to get accurate results, we find it advantageous to split the tight-binding leads into two branches with different  $z$  component of the spin and employ a tree-tensor-network description [28] analogous to Ref. [29]. This algorithm scales as  $m^4$  at the interfaces, instead of  $m^3$ , but the representation of the tight-binding leads becomes much more efficient, allowing us to simulate larger leads. In addition, the worse scaling of the bond dimension  $m$  is softened by the fact that the entanglement entropy at equilibrium is smallest at the interfaces, as already observed in Ref. [25].

### III. CONDUCTING FIXED POINT

Both the tight-binding chain and the spin- $\frac{1}{2}$  XXZ chain in the gapless regime are ballistic spin conductors at zero temperature. However, when these systems form a junction as described in Eq. (1), the transport may be suppressed by scattering at the interfaces. For different, purely fermionic junctions a field-theoretical analysis has shown that the relevant backscattering that leads to insulating behavior at low temperatures vanishes for certain values of the model parameters [19,23,24]. At these conducting fixed points, the effective low-energy field theory is an inhomogeneous Luttinger liquid (LL). One may expect to find similar conducting fixed points for the spin-chain junction, since the gapless XXZ chain and the spin sector of the tight-binding leads are separately described by Luttinger liquids [30]. In this section we numerically show that such conducting fixed points indeed exist. The LL description of our model is given in the Appendix. A proper field-theoretical treatment of the junction between spin-chain and tight-binding lead is left for a future investigation.

#### A. Spin current

To search for conducting fixed points, we simulate the spin transport at finite spin bias for the two-lead setup described in Eq. (1). Let us first illustrate the procedure used to obtain the steady-state spin current. Figure 2(a) shows the spin current profile for different time  $\tau$  after the spin bias is switched on at  $\tau = 0$ . The current starts to flow in the spin chain and spreads over to the leads, where the wave front moves with the Fermi velocity  $2t$ . While the spin current in the spin chain becomes position and time independent in a true steady state, we find it fluctuating even at the maximum simulated time. Therefore, here the steady-state value is estimated from

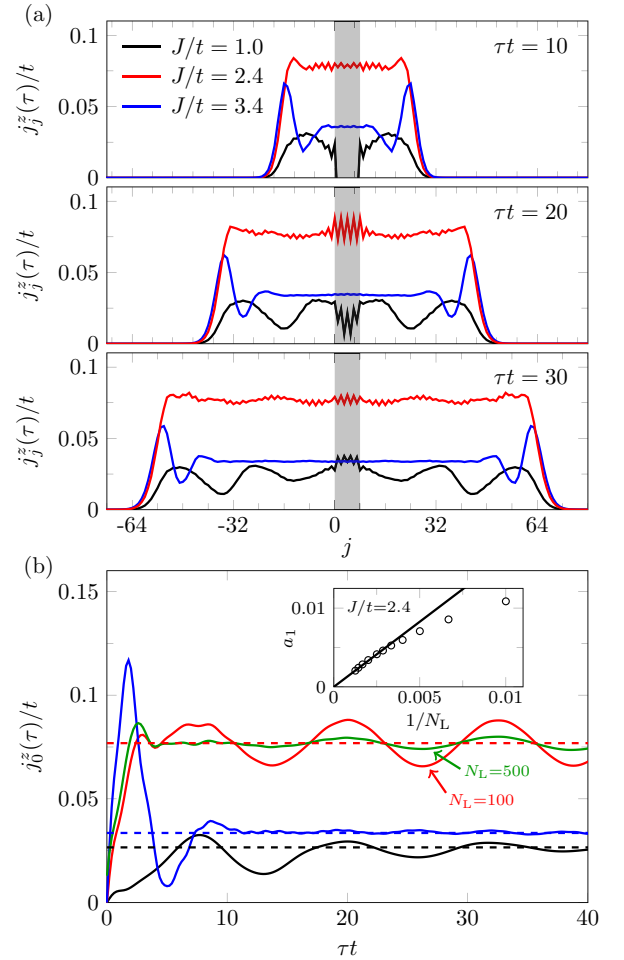


FIG. 2. Time evolution of the spin current  $j_j^z(\tau)$  in a junction composed of an isotropic spin chain ( $\Delta = 1$ ) of  $N_S = 8$  sites (shaded region) coupled to tight-binding leads of  $N_L = 100$  sites for spin bias  $V/t = 1$  and several values of  $J/t$ . (a) Spin current profile at three different times  $\tau t = 10, 20$ , and  $30$ . (b) Time dependence of the spin current  $j_0^z(\tau)$  between the spin chain and the left lead (solid lines) and estimated steady-state value (dashed lines). The result for  $J/t = 2.4$  with a larger size of the leads  $N_L = 500$  is indicated by the green line. In the inset, the amplitude  $a_1$  of the current oscillations [see Eq. (9)] is shown for several different lead sizes  $N_L$ . The solid line is a fit to  $a_1 \propto 1/N_L$ .

the time dependence of the spin current  $j_0^z(\tau)$  between the spin chain and the lead, as demonstrated in Fig. 2(b) for the isotropic chain. After a transient time of  $\tau t \approx 10$ , the spin current oscillates around its steady-state value with a period of approximately  $4\pi/V$ . This kind of oscillation has been explained as a Josephson current that arises because of the finite size of the leads and the corresponding gap between the single-particle energy levels [18]. We calculate the steady-state value of the spin current either by simply averaging  $j_0^z(\tau)$  over multiple periods of the oscillation or by adapting it to

$$j_0^z(\tau) = a_0 + a_1 \cos(\tau V/2 + a_2), \quad (9)$$

where  $a_0$ ,  $a_1$ , and  $a_2$  are fit parameters [18].

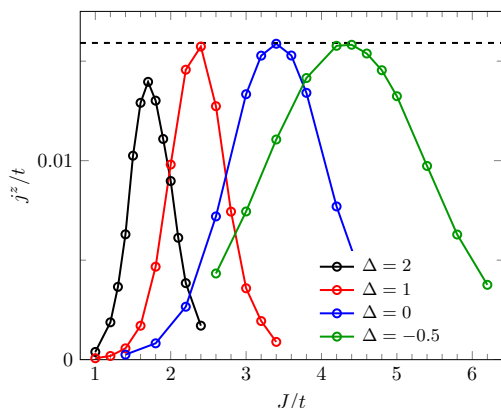


FIG. 3. Steady-state current  $j^z$  as a function of  $J/t$  for four different values of  $\Delta$ . Other parameters are  $N_S = 8$ ,  $N_L = 500$ , and  $V/t = 0.2$ . The dashed line shows the current  $V/(4\pi)$  expected for a Luttinger liquid with smooth interfaces.

The spin current generally depends on both the anisotropy  $\Delta$  and the ratio  $J/t$  of the exchange interaction in the spin chain and the hopping amplitude in the leads. For most of the parameter space, the spin current is expected to be strongly suppressed because of the backscattering at the interfaces. As we will show, however, the system can be tuned to a conducting fixed point for each  $\Delta$  by varying  $J/t$ . In the isotropic chain ( $\Delta = 1$ ) considered in Fig. 2, for example, the corresponding value is  $(J/t)_c \approx 2.4$ . The current there is much larger than for the other values shown,  $J/t = 1$  and  $J/t = 3.4$ , which lie away from the conducting fixed point.

The ratio  $J/t$  affects not only the steady-state value of the spin current but also the oscillation of the current as a function of time  $\tau$ . For a fixed size of the leads with  $N_L = 100$ , the current oscillation at the interface is strongest at  $J/t = (J/t)_c$  where it appears nearly undamped [see Fig. 2(b)]. For either larger or smaller value of  $J/t$ , on the other hand, the oscillation decays relatively quickly with increasing  $\tau$ . By using the tree-tensor-network method, we also consider a junction with much larger leads of  $N_L = 500$  sites. In this case, the current oscillation at the conducting fixed point becomes significantly smaller, as shown in Fig. 2(b), which confirms that it is mostly caused by the discretization of the single-particle energy levels in the leads. It is expected that the amplitude of the oscillations is proportional to the gap between single particle levels and thereby inverse proportional to  $N_L$  [18]. As shown in the inset of Fig. 2, this agrees with our results for  $N_L \gtrsim 400$ , while deviations are seen for smaller leads. The steady-state values of the spin current estimated from the simulations are the same for each  $N_L$ .

Figure 3 shows the dependence of the steady-state spin current  $j^z$  on the ratio  $J/t$  at the fixed spin bias voltage  $V/t = 0.2$  for several values of  $\Delta$ . In each case, a clear maximum of the spin current appears. We first address the gapless phase for  $\Delta = 1, 0$ , and  $-0.5$  where the LL description is applicable. For parameters in this regime, the maximum current obtained is close to  $V/(4\pi)$ , which, as discussed in the Appendix, is the current for a LL with adiabatic contacts. This indicates

that a conducting fixed point with ideal linear conductance exists at the ratio  $(J/t)_c$  which maximizes the current. As  $\Delta$  is decreased,  $(J/t)_c$  becomes larger. In addition, the current peak as a function of  $J/t$  broadens, which suggests that the backscattering becomes less relevant. A current maximum remains, however, even for negative  $\Delta$ .

Figure 3 also shows the results for  $\Delta = 2$  in the gapped phase. While a sharp peak is still observed, the maximum value of the spin current does not reach the ideal value in this case. The vanishing of the Friedel oscillations (see Sec. III B) for the parameters at the current peak indicates that the relevant backscattering at the interfaces can still be tuned to zero. Therefore, the deviation from the ideal conductance appears to be caused by different reasons, most likely related to properties in the bulk of the spin chain, which for  $\Delta > 1$  is no longer described by a LL model. How the spin transport differs in the gapped and gapless phases of the antiferromagnetic XXZ chain will be analyzed in Sec. IV.

### B. Friedel oscillations

Besides its effect on the transport, the backscattering at inhomogeneities is known to induce characteristic Friedel oscillations of the local density or magnetization with twice the Fermi wave number  $k_F$  [31]. The Friedel oscillations at the interface vanish, however, if the backscattering amplitude is tuned to zero. The calculation of the magnetization profile therefore constitutes a different, perhaps a more efficient way to search a conducting fixed point [19]. As a consistency check for the results of the spin-transport simulations above, we now investigate the dependence of the Friedel oscillations on  $J/t$  for fixed  $\Delta$  with no spin bias applied. Since the magnetization is uniform in the spin-flip symmetric case, we examine the local susceptibility [19] instead by adding a small uniform magnetic field described by  $\delta\hat{H} = h \sum_j \hat{S}_j^z$ . For these calculations, we consider a single interface between the tight-binding lead and the spin chain because the Friedel oscillations typically decay over a distance longer than the spin-chain length accessible in our transport simulations. Furthermore, we consider finite temperatures by using the grand-canonical purification method [32], which avoids problems in the convergence of the DMRG ground-state calculations. The purification method allows us to keep track of the growth of the Friedel oscillations starting from the interface and the open ends of the system as the temperature is lowered successively. We terminate the simulations when the finite system size begins to affect the results. The finite-temperature calculations also allow us to study the gapped phase of the spin chain where the ground state is antiferromagnetically long-range ordered.

Figure 4 shows the magnetization profile around the interface for the magnetic field strength  $h/J = 0.05$ . Here we fix  $h/J$  instead of  $h/t$  because for the values of the anisotropy  $\Delta$  considered, the Friedel oscillations are much stronger in the spin chain than in the lead. Since the spin chain without magnetic field corresponds to a half-filled chain of fermions, the local magnetization oscillates with wave number  $2k_F = \pi$ . As expected, the effect is larger at low temperatures. For the fixed exchange anisotropy, the strength of the Friedel oscillations has a minimum as a function of  $J/t$ . This behavior can be observed in both the gapless and gapped regimes. For

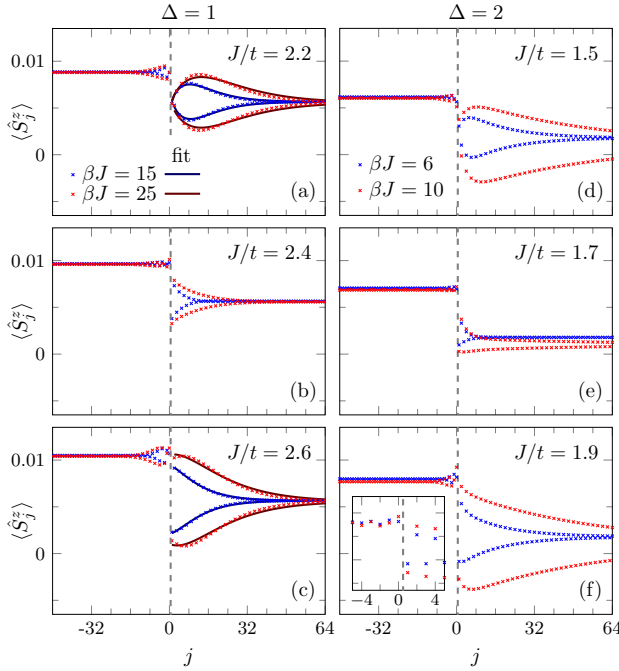


FIG. 4. Magnetization profile  $\langle \hat{S}_j^z \rangle$  around the interface for an applied magnetic field  $h/J = 0.05$ . The dashed line indicates the interface between the tight-binding lead ( $j \leq 0$ ) and the spin chain ( $j > 0$ ). The systems sizes are  $N_L = 400$  and  $N_S = 400$  for  $\Delta = 1$  and  $N_L = 400$  and  $N_S = 800$  for  $\Delta = 2$ . The inset in (f) is a magnified view of the region close to the interface, highlighting the Friedel oscillations with wave number  $\pi$ . Solid black lines in (a) and (c) are fits of the data in the form of Eq. (10). The results are obtained by finite temperature calculations at the inverse temperature  $\beta$ .

the former case, we have attempted a fit to the oscillation profile

$$\chi(j + \tilde{a}_0) = \tilde{a}_1 T^{\bar{K}-1} j(-1)^j \left[ \frac{v}{T} \sinh\left(\frac{2\pi T j}{v}\right) \right]^{-K} \times P_{-\bar{K}}[\coth(2\pi T j/v)] \quad (10)$$

derived for the susceptibility of a chain of spinless fermions with an abrupt jump of the parameters [19,23]. Here  $P_l(z)$  is the Legendre function,  $K$  and  $v$  are the LL parameter and the spin velocity, respectively, and  $\bar{K}$  is determined by the LL parameters on both sides of the interface (see the Appendix). Free parameters of the fit are a position offset  $\tilde{a}_0$  and the amplitude  $\tilde{a}_1$ . The fits for the even and odd sites separately are shown in Figs. 4(a) and 4(c) for the oscillations in the spin chain with  $\Delta = 1$ , where  $K = 1/2$  and  $v = J\pi/2$ , and we set  $\bar{K} = 1/2$ , corresponding to an isotropic spin chain with a jump in the exchange parameter. Very good agreement is found with our numerical data, suggesting that Eq. (10) or a similar relation is also applicable to the junction with the fermionic lead.

To measure the overall strength of the Friedel oscillations, we introduce a quantity

$$O_F = \sum_{j=1}^{N'} \left| \langle \hat{S}_{j+1}^z \rangle - \langle \hat{S}_j^z \rangle \right|, \quad (11)$$

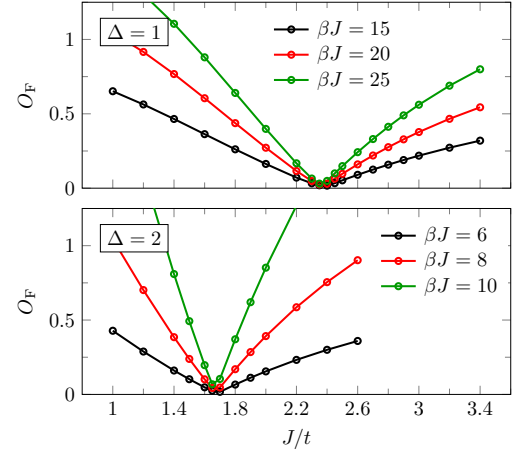


FIG. 5. Strength of the Friedel oscillations  $O_F$  defined in Eq. (11) around the interface inside the spin chain at the inverse temperature  $\beta$ . The system sizes are the same as in Fig. 4.

where  $N'$  is chosen so that the Friedel oscillations due to the open boundary at the end of the spin chain are excluded. By calculating  $O_F$ , we search for a value of  $J/t$  that minimizes the Friedel oscillations for a fixed anisotropy  $\Delta$ .

The results for  $\Delta = 1$  and  $\Delta = 2$  are shown in Fig. 5. In all cases studied, including the gapped regime, we find a clear minimum of the Friedel oscillation strength, where approximately  $O_F = 0$ , which suggests that the relevant backscattering vanishes. When the temperature is lowered, the position of the minimum moves to smaller  $J/t$ . The temperature dependence seems to be stronger for small  $\Delta$ . By identifying the position of the minimum for  $T \rightarrow 0$  as the conducting fixed point, we obtain  $(J/t)_c \approx 2.4$  for  $\Delta = 1$ . This value agrees with the results of the spin-transport simulations for  $N_S = 8$ , despite the fact that we now consider the limit of a large spin chain. Identifying  $(J/t)_c$  similarly in the gapped phase, we obtain  $(J/t)_c \approx 1.7$  for  $\Delta = 2$ , which also coincides with the value of  $J/t$  where the spin current becomes maximum in Fig. 3. When calculating  $(J/t)_c$  as a function of the anisotropy  $\Delta$ , we find no qualitative difference across the phase boundary at  $\Delta = 1$ .

#### IV. CURRENT-VOLTAGE CHARACTERISTICS

Having established the existence of conducting fixed points with a finite linear conductance in the previous section, we now turn our attention to the spin-bias dependence of the spin current. To examine how the current-voltage curve is modified by the backscattering at the interfaces and the presence of a finite energy gap, the system parameters at and away from the line of conducting fixed points are considered for both the gapless and gapped phases of the antiferromagnetic spin- $\frac{1}{2}$  XXZ chain.

##### A. Gapless regime

First, we study the gapless XY phase where the spin chain can be described by a LL model. As mentioned in the Appendix, a spin conductance  $G = 1/(4\pi)$  is expected unless the transport is hindered by the backscattering at the interfaces. We have already confirmed that this ideal value can be obtained

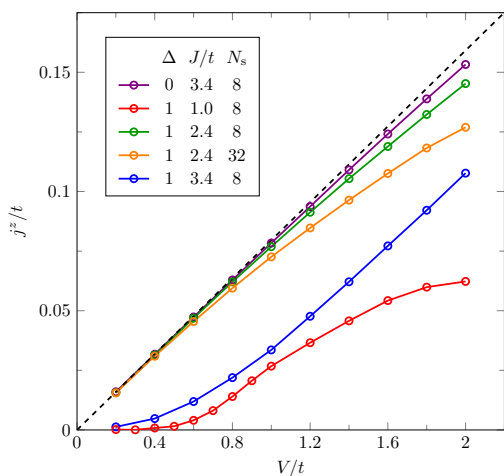


FIG. 6. Current-voltage curve in the two-lead setup described in Eq. (1) for different parameters in the gapless phase. The dashed line is the conductance  $G = 1/(4\pi)$  of a Luttinger liquid smoothly connected to noninteracting leads.

approximately at low spin bias  $V/t = 0.2$  by tuning  $J/t$  to a conducting fixed point  $(J/t)_c$  for a given anisotropy  $\Delta$ . By calculating the current-voltage curve, we can determine at what energy scale the LL description becomes invalid and the linear behavior breaks down. Figure 6 shows the results for the isotropic spin chain ( $\Delta = 1$ ) and the XX spin chain ( $\Delta = 0$ ) where the conducting fixed points are  $(J/t)_c \approx 2.4$  and  $(J/t)_c \approx 3.4$ , respectively (see Figs. 3 and 5). In both cases, the current-voltage curve for  $J/t \approx (J/t)_c$  shows good agreement with the LL prediction up to at least  $V/t = 1$ , despite the strong inhomogeneity at the interfaces. For  $\Delta = 1$ , increasing the length of the spin chain to  $N_S = 32$  leads to stronger deviations at large  $V$  while the currents for  $V/t \lesssim 0.4$  remain nearly unchanged. Possible length-dependent corrections to the conductance have been considered, for example, in Refs. [33,34].

Away from the conducting fixed points, the low-bias conductance is strongly reduced by backscattering. This is demonstrated in Fig. 6 for an isotropic chain and values  $J/t = 1$  and 3.4 that are significantly smaller or larger than  $(J/t)_c \approx 2.4$ . In a LL with an impurity, the differential conductance eventually approaches the ideal value  $1/(4\pi)$  with a power law as the bias is increased [35]. This is consistent with our results for  $J/t = 3.4$  where an approximately linear current-voltage relation is restored for  $V/t \gtrsim 1.2$ . For  $J/t = 1$ , on the other hand, the differential conductance drops off again at  $V/t \approx 1$ , likely because the bias voltage considered is already comparable or larger than the exchange constant  $J$ . In any case, the current should vanish in the large- $V$  limit for the chosen setup because of the finite bandwidth of the leads. This does not apply, however, to the setup where the spin voltage  $V$  is present initially and then turned off at  $\tau = 0$  [18,27].

### B. Gapped regime

In Sec. III it was shown that the finite-temperature Friedel oscillations around the interfaces can be tuned to zero by

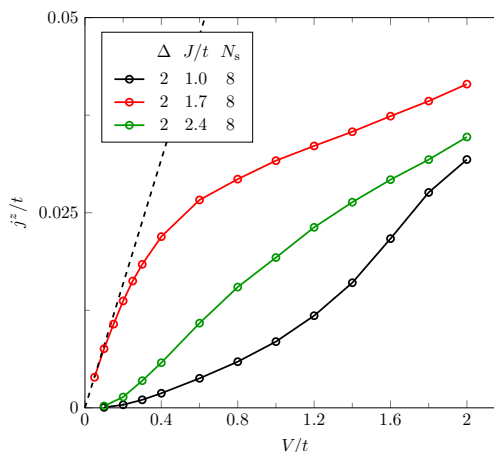


FIG. 7. Current-voltage curve for a spin chain with  $N_S = 8$ , anisotropy  $\Delta = 2$ , and different values of  $J/t$ . The dashed line corresponds to the ideal conductance  $G = 1/(4\pi)$  obtained in the Luttinger-liquid regime.

varying  $J/t$  even in the gapped phase. Therefore, a fixed point  $(J/t)_c$  with vanishing relevant backscattering seems to exist in this regime as well. One may then ask how the current-voltage curve there differs from that at a conducting fixed point in the gapless phase. In the following, we examine this for the anisotropy parameter  $\Delta = 2$  where the Friedel oscillations disappear at  $J/t \approx 1.7$ .

Figure 7 displays the current-voltage curve of a spin chain with  $N_S = 8$  sites for  $J/t = 1.7$  as well as for smaller and larger values of  $J/t$ . For  $J/t = 1.7$ , the conductance appears to approach  $1/(4\pi)$  as the voltage  $V$  is decreased to zero, indicating that almost ideal spin transport can be achieved at low energy. At larger voltage, on the other hand, the differential conductance drops off sharply, which is not observed in the LL phase. This crossover occurs approximately at  $V/t \approx 0.4$ . As in the LL regime, the spin current at small bias voltage is strongly reduced away from  $(J/t)_c$ . Since the XXZ spin chain with  $\Delta > 1$  is a spin insulator, the spin transport at fixed  $V$  should become more and more suppressed with increasing the system size  $N_S$ . The effect of  $N_S$  on the current-voltage curve for  $J/t = 1.7$  is shown in Fig. 8. As expected, the spin current becomes noticeably smaller when going to larger system sizes  $N_S$ . There is still a crossover below which the perfect spin conductance seems to be approached. However, this crossover is shifted to very small bias voltage  $V$  with increasing  $N_S$ .

Similar behavior, i.e., unsuppressed current for small systems at low energy, occurs in the charge transport through Hubbard chains with an odd number of sites [36]. Perhaps more relevant to our model, such effect has been predicted for one-dimensional charge-density-wave insulators adiabatically contacted to noninteracting leads, by using field theoretical methods [20]. This model may be interpreted as a XXZ spin chain with the anisotropy  $\Delta$  set to zero outside a finite region with  $\Delta > 1$  that corresponds to the charge-density-wave part. In contrast to our results, a negative differential conductance was obtained. However, this may be related to the different choice of the leads.

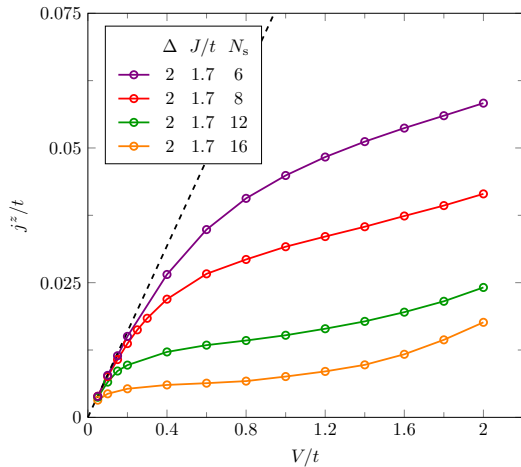


FIG. 8. Same as in Fig. 7 but for a spin chain with  $J/t = 1.7$  and various chain lengths.

For sufficiently long spin chains, we observe an upturn of the spin current at large spin bias. A setup analogous to ours has been considered in the calculation of the charge current through a Mott-insulating Hubbard chain connected to noninteracting leads [25]. It was shown that the current-voltage curve can be described by a function  $j(V) = aVe^{-V_c/V}$ , where  $a$  and  $V_c$  are constants. In particular,  $V_c$  is approximately proportional to the square of the charge gap of the disconnected Hubbard chain. This relation was previously obtained for the current in a periodic chain and explained in terms of a Landau-Zener mechanism [37]. The upturn observed for  $N_S = 16$  in Fig. 8 suggests that a similar activated behavior occurs in our model for long enough chains where the low-voltage transport is suppressed. However, our available data are not sufficient to check the specific functional form and the dependence on the spin gap of the isolated spin chain.

## V. CONCLUSION

We have numerically studied the finite-bias spin transport in a spin- $\frac{1}{2}$  XXZ chain connected to half-filled tight-binding leads at zero temperature, focusing on the effect of scattering at the interfaces. By calculating the steady-state spin current and the Friedel oscillations, it was shown that in the Luttinger-liquid regime, conducting fixed points with the ideal linear conductance exist, similarly as in related models for inhomogeneous quantum wires. Our results furthermore indicate that conducting fixed points also appear in the gapped phase. There, the nearly ideal spin transport can only be observed in a small bias voltage region, which shrinks when the length of the spin chain is increased.

Our interpretation of the numerical data is partially based on the field-theoretical description which has been derived for a different type of junction consisting only of fermionic chains. It would be interesting to find the effective low-energy field theory for the specific junction considered here, including explicit expressions for the scattering at the interfaces, and determine whether there are qualitative differences with the previously studied models.

More difficult to treat numerically, but closer to actual experiments, is the finite temperature case. For the finite-temperature simulations, one could employ a similar TEBD method where the MPS describes a purification of the density matrix instead of a pure state. With the approach in Ref. [38], it may also be possible to study a setup where a spin current is driven by a temperature gradient, mimicking the experiment in Ref. [3].

In this paper we have only considered junctions composed of spin- $\frac{1}{2}$  chains. A possible extension would be to study analogous systems for spin ladders or chains with higher local spin. The spin-1 Heisenberg chain, for example, might be interesting since it is experimentally realizable and differs from the spin- $\frac{1}{2}$  chain in several aspects: Its elementary excitations are magnons instead of spinons, it is nonintegrable, and it exhibits symmetry-protected edge states at open boundaries. For a setup with leads, the question then arises how the contact is affected by these edge states. This will be addressed in a forthcoming study.

## ACKNOWLEDGMENTS

DMRG simulations were performed using the ITensor library [39]. F. L. was supported by Deutsche Forschungsgemeinschaft through project FE 398/8-1 and by the International Program Associate (IPA) program in RIKEN. This work was supported by Grant-in-Aid for Scientific Research from MEXT Japan under Grant No. 17K05523 and also in part by RIKEN Center for Computational Science through the HPCI System Research projects hp120246, hp140130, and hp150140. T.S. acknowledges the Simons Foundation for funding.

## APPENDIX: LUTTINGER LIQUID DESCRIPTION

The low-energy physics of the spin- $\frac{1}{2}$  XXZ chain in the XY phase ( $-1 \leq \Delta \leq 1$ ) are described by the Luttinger-liquid (LL) model [30]

$$\hat{H}_S = \frac{1}{2} \int dx \left[ \frac{v}{K} (\partial_x \phi)^2 + vK (\partial_x \theta)^2 \right], \quad (\text{A1})$$

where the bosonic fields obey the commutation relations  $[\phi(x), \partial_{x'} \theta(x')] = i\delta(x - x')$  and the LL parameter  $K = \pi/[2 \arccos(-\Delta)]$  and the spin velocity  $v = J\pi\sqrt{1 - \Delta^2}/[2 \arccos(\Delta)]$  are known from the Bethe-ansatz solution [40]. In this representation, the long-wavelength part of the magnetization is related to the fields by

$$\hat{S}^z(x) \simeq -\frac{1}{\sqrt{\pi}} \partial_x \phi. \quad (\text{A2})$$

The charge transport in a system of spinless fermions with a nearest-neighbor interaction corresponds directly to the spin transport in the spin- $\frac{1}{2}$  XXZ chain since the models are related by a Jordan-Wigner transformation. For an infinite homogeneous chain, the spin conductance  $G$  is given by [22]

$$G = \frac{K}{2\pi}. \quad (\text{A3})$$

In general, however, this expression is no longer valid when leads are taken into account. The effective low-energy Hamiltonian of the tight-binding leads in our setup described by

Eq. (1) consists of two components of the form of Eq. (A1) for the charge and spin sectors. Requiring the representation of the leads to be consistent with Eqs. (A2) and (A3) fixes the spin LL parameter to  $K = 1/2$ . This is also the value for the spin chain at the SU(2) symmetric point  $\Delta = 1$ .

A single junction between spin chain and lead has some similarity with the single-channel Kondo model, except that the impurity site is now also coupled to a spin chain. We assume that, analogously to the Kondo model, the charge and spin sectors are decoupled in the low-energy theory [41]. Focusing only on the spin part and ignoring any possible boundary terms, the naive field-theoretical description of our system becomes an inhomogeneous LL with the position-dependent LL parameter  $K(x)$  and spin velocity  $v(x)$ . It has been shown that the conductance of such a system is obtained by replacing the LL parameter in Eq. (A3) with its asymptotic value in the leads  $K(x \rightarrow \pm\infty)$  [42,43]. For the noninteracting leads, the spin conductance therefore is  $G = 1/(4\pi)$ , independent of the parameters in the spin chain.

By using an inhomogeneous LL model to describe a one-dimensional junction one assumes that backscattering at the interfaces can be neglected. This is justified for adiabatic contacts but not for the abrupt transition between the spin chain and the lead described in Eq. (1). For a chain of spinless fermions with uniform LL parameter  $K$ , the effect of backscattering at an inhomogeneity on the linear conductance  $G$  is well known [21,22]: At zero temperature,  $G$  vanishes if the interactions are repulsive (i.e.,  $K < 1$ ), while  $G$  is not reduced for attractive interactions (i.e.,  $K > 1$ ). An abrupt change in the system parameters of a quantum wire has a similar impact on the conductance, as has been studied for both

spinless [19,23] and spinful [24] fermions using bosonization and quantum Monte Carlo methods. In those cases, whether the transport is suppressed at low temperatures depends on the LL parameters on each side of the interface. For the spinless model, the zero-temperature conductance vanishes for  $\bar{K} < 1$ , where  $\bar{K} = 2(\frac{1}{K_1} + \frac{1}{K_2})^{-1}$ , and  $K_1$  and  $K_2$  are the LL parameters on the left and right sides of the interface [19]. However, it was also shown that, even for abrupt junctions, conducting fixed points may be obtained by tuning certain system parameters such as the hopping and interaction strengths [19,24]. At these conducting fixed points, the amplitude of the relevant backscattering becomes zero and thus the ideal conductance determined by the LL parameters of the leads is recovered at zero temperature. Note that there is still irrelevant scattering at the interfaces, which can affect the conductance at finite temperatures.

In the spin-chain junction described in Eq. (1), the couplings between the subsystems are different than in the previously studied fermionic models. Therefore, it is not clear that the field-theoretical results in the previous studies apply similarly in our system. However, we demonstrate in the main text for several values of  $\Delta$  that conducting fixed points with ideal spin transport exist. Since these fixed points are obtained by varying a single model parameter, there appears to be only one relevant perturbation at the interfaces, similarly as in the purely fermionic chains. For  $\Delta = 1$ , this may be expected by noticing that the spin-chain junction corresponds to a strong-coupling limit of the inhomogeneous half-filled Hubbard chain for which conducting fixed points have been reported in Ref. [24]. By analogy with the fermionic models, we refer to the relevant perturbation at the interfaces as “backscattering.”

- 
- [1] Y. Kajiwara, K. Harii, S. Takahashi, J. Ohe, K. Uchida, M. Mizuguchi, H. Umezawa, H. Kawai, K. Ando, K. Takanashi, S. Maekawa, and E. Saitoh, *Nature (London)* **464**, 262 (2010).
- [2] K. Uchida, H. Adachi, T. Ota, H. Nakayama, S. Maekawa, and E. Saitoh, *Appl. Phys. Lett.* **97**, 172505 (2010).
- [3] D. Hirobe, M. Sato, T. Kawamata, Y. Shiomi, K. Uchida, R. Iguchi, Y. Koike, S. Maekawa, and E. Saitoh, *Nat. Phys.* **13**, 30 (2016).
- [4] B. S. Shastry and B. Sutherland, *Phys. Rev. Lett.* **65**, 243 (1990).
- [5] X. Zotos, *Phys. Rev. Lett.* **82**, 1764 (1999).
- [6] F. Heidrich-Meisner, A. Honecker, D. C. Cabra, and W. Brenig, *Phys. Rev. B* **68**, 134436 (2003).
- [7] M. Žnidarič, *Phys. Rev. Lett.* **106**, 220601 (2011).
- [8] C. Karrasch, J. Hauschild, S. Langer, and F. Heidrich-Meisner, *Phys. Rev. B* **87**, 245128 (2013).
- [9] T. Prosen, *Phys. Rev. Lett.* **106**, 217206 (2011).
- [10] S. R. White, *Phys. Rev. Lett.* **69**, 2863 (1992).
- [11] G. Vidal, *Phys. Rev. Lett.* **91**, 147902 (2003).
- [12] T. Prosen and M. Žnidarič, *J. Stat. Mech.* (2009) P02035.
- [13] G. Benenti, G. Casati, T. Prosen, D. Rossini, and M. Žnidarič, *Phys. Rev. B* **80**, 035110 (2009).
- [14] G. Benenti, G. Casati, T. Prosen, and D. Rossini, *Europhys. Lett.* **85**, 37001 (2009).
- [15] K. A. van Hoogdalem and D. Loss, *Phys. Rev. B* **84**, 024402 (2011).
- [16] P. Schmitteckert, *Phys. Rev. B* **70**, 121302 (2004).
- [17] D. Bohr, P. Schmitteckert, and P. Wölfle, *Europhys. Lett.* **73**, 246 (2006).
- [18] A. Branschädel, G. Schneider, and P. Schmitteckert, *Ann. Phys. (Berlin)* **522**, 657 (2010).
- [19] N. Sedlmayr, J. Ohst, I. Affleck, J. Sirker, and S. Eggert, *Phys. Rev. B* **86**, 121302 (2012).
- [20] V. V. Ponomarenko and N. Nagaosa, *Phys. Rev. Lett.* **83**, 1822 (1999).
- [21] C. L. Kane and M. P. A. Fisher, *Phys. Rev. Lett.* **68**, 1220 (1992).
- [22] C. L. Kane and M. P. A. Fisher, *Phys. Rev. B* **46**, 15233 (1992).
- [23] N. Sedlmayr, D. Morath, J. Sirker, S. Eggert, and I. Affleck, *Phys. Rev. B* **89**, 045133 (2014).
- [24] D. Morath, N. Sedlmayr, J. Sirker, and S. Eggert, *Phys. Rev. B* **94**, 115162 (2016).
- [25] F. Heidrich-Meisner, I. González, K. A. Al-Hassanieh, A. E. Feiguin, M. J. Rozenberg, and E. Dagotto, *Phys. Rev. B* **82**, 205110 (2010).
- [26] R. A. Bari, D. Adler, and R. V. Lange, *Phys. Rev. B* **2**, 2898 (1970).
- [27] M. Einhellinger, A. Cojuhovski, and E. Jeckelmann, *Phys. Rev. B* **85**, 235141 (2012).



- [28] V. Murg, F. Verstraete, O. Legeza, and R. M. Noack, *Phys. Rev. B* **82**, 205105 (2010).
- [29] A. Holzner, A. Weichselbaum, and J. von Delft, *Phys. Rev. B* **81**, 125126 (2010).
- [30] T. Giamarchi, *Quantum Physics in One Dimension* (Clarendon, Oxford, 2003).
- [31] S. Rommer and S. Eggert, *Phys. Rev. B* **62**, 4370 (2000).
- [32] F. Verstraete, J. J. García-Ripoll, and J. I. Cirac, *Phys. Rev. Lett.* **93**, 207204 (2004).
- [33] N. Sedlmayr, P. Adam, and J. Sirker, *Phys. Rev. B* **87**, 035439 (2013).
- [34] K. A. Matveev and A. V. Andreev, *Phys. Rev. Lett.* **107**, 056402 (2011).
- [35] M. P. A. Fisher and L. I. Glazman, in *Mesoscopic Electron Transport*, edited by L. L. Sohn, L. P. Kouwenhoven, and G. Schön (Springer Netherlands, Dordrecht, 1997), pp. 331–373.
- [36] A. Oguri, *Phys. Rev. B* **63**, 115305 (2001).
- [37] T. Oka, R. Arita, and H. Aoki, *Phys. Rev. Lett.* **91**, 066406 (2003).
- [38] C. Karrasch, R. Ilan, and J. E. Moore, *Phys. Rev. B* **88**, 195129 (2013).
- [39] <http://itensor.org/>.
- [40] A. Luther and I. Peschel, *Phys. Rev. B* **12**, 3908 (1975).
- [41] I. Affleck, *Nucl. Phys. B* **336**, 517 (1990).
- [42] D. L. Maslov and M. Stone, *Phys. Rev. B* **52**, R5539 (1995).
- [43] I. Safi and H. J. Schulz, *Phys. Rev. B* **52**, R17040 (1995).





## Driving XXZ spin chains: Magnetic-field and boundary effects

F. LANGE<sup>(a)</sup>, S. EJIMA<sup>(b)</sup>, H. FEHSKE<sup>(c)</sup>*Institut für Physik, Universität Greifswald - D-17487 Greifswald, Germany*received 17 October 2018; accepted in final form 11 December 2018  
published online 11 January 2019PACS 72.25.Mk – Spin transport through interfaces  
PACS 75.10.Pq – Spin chain models  
PACS 75.76.+j – Spin transport effects

**Abstract** – Using the time-evolving block decimation, we study the spin transport through spin-(1/2) and spin-1 XXZ chains subjected to an external magnetic field and contacted to noninteracting fermionic leads. For generic system-lead couplings, the spin conductance exhibits several resonances as a function of the magnetic-field strength. In the spin-(1/2) but not the spin-1 case, the coupling to the leads can be fine-tuned to reach a conducting fixed point, where the peak structure is washed out and the spin conductance is large throughout the gapless Luttinger-liquid phase. For the Haldane phase of the spin-1 chain, we analyse how the spin transport is affected by spin-(1/2) edge states, and argue that two-impurity Kondo physics is realised.

Copyright © EPLA, 2019

The transport properties of interacting nanostructures connected to leads are currently of great interest and hence have been the subject of many numerical and analytical studies [1–6]. For the most part, the focus has been on the charge transport, which is easier to access experimentally. However, there are also proposals to use a spin battery to drive a spin current through a contacted system [7]. Here, motivated by the recent development of antiferromagnetic spintronics [8], we numerically investigate such a setup for general XXZ spin chains. We use the density-matrix renormalisation group (DMRG) [9] in conjunction with the time-evolving block decimation [10] to calculate the spin conductance at zero temperature and small spin bias. While isolated XXZ chains have already been studied extensively [11–14], we explicitly include the leads in our simulations, which should significantly affect the transport behaviour. There are numerous studies on the spin transport in related models of open spin chains, where the baths are accounted for through driving terms at the outer sites, see refs. [15] and [16], for example. Our model differs in that we use a closed-system description with tight-binding leads. We extend our previous work [17] on the spin-(1/2) XXZ chain by also considering the topological spin-1 Haldane chain [18], and adding an external magnetic field. The spin chain realises different quantum phases, both gapped and gapless, depending

on the magnitude of the local spins and the strength of the magnetic field. One might expect the system to be conducting in the gapless and insulating in the gapped regimes. As we will demonstrate, however, this only holds in specific cases with fine-tuned parameters. In general, the effects of the contacts and the finite size of the spin chain need to be taken into account.

After describing the theoretical model, we discuss separately the spin-(1/2) chain with easy-axis anisotropy and the spin-1 chain with isotropic exchange. For the latter, special attention is paid to the Haldane phase, where the spin-(1/2) edge states contribute to the transport.

**Setup.** – We consider a junction composed of a spin chain and two fermionic leads. It is assumed that the system and the leads are initially in the ground state of the Hamilton operator  $\hat{H}_0 = \hat{H}_S + \hat{H}_L + \hat{H}_{S-L} + \hat{H}_h$ . There, the system part

$$\hat{H}_S = J \sum_{j=1}^{N_S-1} \left[ \frac{1}{2} \left( \hat{S}_j^+ \hat{S}_{j+1}^- + \hat{S}_j^- \hat{S}_{j+1}^+ \right) + \Delta \hat{S}_j^z \hat{S}_{j+1}^z \right] \quad (1)$$

is the usual XXZ chain Hamiltonian and the lead part

$$\hat{H}_L = -t \sum_{a=l,r} \sum_{\sigma=\uparrow,\downarrow} \sum_{j>0} \left[ \hat{c}_{j\sigma a}^\dagger \hat{c}_{j+1,\sigma a} + \hat{c}_{j+1,\sigma a}^\dagger \hat{c}_{j\sigma a} \right] \quad (2)$$

describes two half-infinite tight-binding chains of spinful fermions. Throughout this work, the ratio between the exchange constant and the hopping parameter is assumed

<sup>(a)</sup>E-mail: langef@uni-greifswald.de<sup>(b)</sup>E-mail: ejima@physik.uni-greifswald.de<sup>(c)</sup>E-mail: fehske@physik.uni-greifswald.de

F. Lange *et al.*

to be  $J/t = 1$ . Furthermore, the chemical potential in the leads shall be zero. The lead with  $a = l$  ( $r$ ) is exchange-coupled to the first (last) site of the spin chain:

$$\begin{aligned} \hat{H}_{S-L} = & \frac{J'}{2} \left[ \hat{c}_{1\uparrow l}^\dagger \hat{c}_{1\downarrow l} \hat{S}_1^- + \hat{c}_{1\downarrow l}^\dagger \hat{c}_{1\uparrow l} \hat{S}_1^+ \right. \\ & + \Delta (\hat{c}_{1\uparrow l}^\dagger \hat{c}_{1\uparrow l} - \hat{c}_{1\downarrow l}^\dagger \hat{c}_{1\downarrow l}) \hat{S}_1^z \left. \right] \\ & + \frac{J'}{2} \left[ \hat{c}_{1\uparrow r}^\dagger \hat{c}_{1\downarrow r} \hat{S}_{N_S}^- + \hat{c}_{1\downarrow r}^\dagger \hat{c}_{1\uparrow r} \hat{S}_{N_S}^+ \right. \\ & + \Delta (\hat{c}_{1\uparrow r}^\dagger \hat{c}_{1\uparrow r} - \hat{c}_{1\downarrow r}^\dagger \hat{c}_{1\downarrow r}) \hat{S}_{N_S}^z \left. \right]. \quad (3) \end{aligned}$$

Lastly, a homogeneous magnetic field in both the system and the leads is taken into account by

$$\hat{H}_h = -h \left[ \sum_{j=1}^{N_S} \hat{S}_j^z + \frac{1}{2} \sum_{a=l,r} \sum_{j>0} (\hat{c}_{j\uparrow a}^\dagger \hat{c}_{j\uparrow a} - \hat{c}_{j\downarrow a}^\dagger \hat{c}_{j\downarrow a}) \right]. \quad (4)$$

The Hamiltonian  $\hat{H}_0$  is perturbed by an additional magnetic field that acts only in the left lead so that the time evolution is governed by  $\hat{H} = \hat{H}_0 + \hat{H}_V$ , where

$$\hat{H}_V = \frac{V}{2} \sum_{j>0} (\hat{c}_{j\uparrow l}^\dagger \hat{c}_{j\uparrow l} - \hat{c}_{j\downarrow l}^\dagger \hat{c}_{j\downarrow l}). \quad (5)$$

This term adds a spin bias  $V$  between the leads and drives a spin current through the system. The spin current  $j^z$  in the nonequilibrium steady state defines the spin conductance  $G = j^z/V$ . For the spin current at the interface with left lead, we use the definition  $j^z = \frac{iJ}{2} (\hat{c}_{1\uparrow l}^\dagger \hat{c}_{1\downarrow l} \hat{S}_1^- - \hat{c}_{1\downarrow l}^\dagger \hat{c}_{1\uparrow l} \hat{S}_1^+)$ .

To calculate the steady-state spin current that develops after the spin bias is switched on, we follow the approach described in ref. [5]. Instead of the usual matrix-product states, however, we use a tree-tensor network representation where each lead is split into two branches corresponding to the two values of the spin index [19,20]. Since such a tensor network is loopless, we can employ more or less the same techniques as in the matrix-product state approach. First, the ground state of  $\hat{H}_0$  is calculated with the DMRG. This state is then evolved in time according to  $\hat{H}$  with the time-evolving block decimation. In these simulations, the leads have to be truncated to a finite number of sites, and, therefore, no true steady state can be reached. Nevertheless, one can extract an accurate estimate for the spin conductance by extrapolating the behaviour of the spin current to the steady state. For the finite leads, we apply damped boundary conditions, where the hopping parameter is smoothly set to zero near the boundaries away from the system, which allows for a variable magnetization in the spin chain and the surrounding region [3]. The leads in our simulations have up to 600 sites, and the maximum bond dimension during the time evolution is 500.

**Spin-(1/2).** – The first case we study is the spin-(1/2) XXZ chain with anisotropy parameter  $\Delta = 2$ .

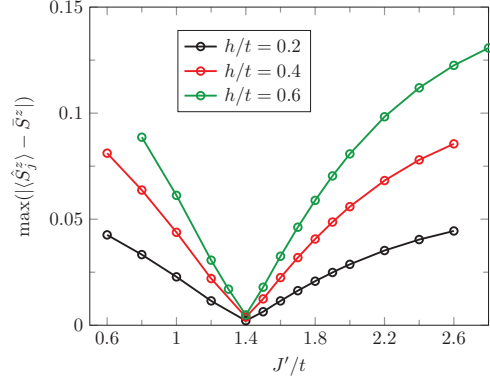


Fig. 1: Maximum of the Friedel oscillations in the spin-(1/2) XXZ chain for  $\Delta = 2$  and  $\beta t = 4$ .

In the absence of an external magnetic field, the system is deep in the gapped Néel phase where the zero-temperature spin transport is diffusive. At some finite magnetic-field strength  $h_c$ , a quantum phase transition to a gapless Luttinger-liquid (LL) phase takes place and the spin transport becomes ballistic [11,21]. For  $\Delta = 2$ , we have  $h_c/J \simeq 0.40$ . The LL parameter is  $K = 1/4$  at  $h = h_c$  (following the convention of ref. [22]) and increases as  $h$  grows further, approaching  $K = 1$  at the transition to the fully polarised ferromagnetic phase [22].

The maximum linear spin conductance of the junction is given by the leads as  $G_0 = 1/(4\pi)$ . Because of scattering at the contacts, this ideal spin conductance may only be achieved when the model parameters are fine-tuned to a conducting fixed point, even if the spin chain is in the LL phase [17]. This situation is similar to the transport in fermionic junctions with abrupt change in the parameter, where such conducting fixed points have been studied previously [6,23,24]. Here, we investigate how the contacts affect the magnetic-field dependence of the spin conductance.

To confirm that a conducting fixed point exists and to determine the corresponding parameter  $J'/t$ , we analyse the Friedel oscillations in the spin chain near the interfaces. Vanishing Friedel oscillations are expected for perfect contacts, for which the linear spin conductance becomes  $G_0$  in the gapless phase [6,17]. While we are interested in the zero-temperature case, we find it easier to carry out the simulations for finite temperature with the purification method [25]. As a simple measure for the strength of the oscillations, the maximum deviation from the average magnetization in the bulk is used. The results for inverse temperature  $\beta t = 4$  are shown in fig. 1. For all field strengths  $h/t$  considered, the oscillations approximately vanish at  $J'/t = 1.4$  which indicates the existence of a conducting fixed point, with no discernible magnetic-field dependence. The temperature dependence of the position of the minimum is negligible for the parameters used.

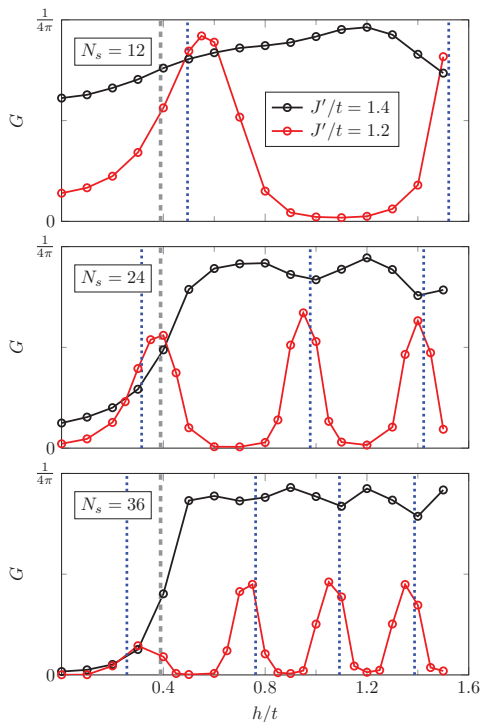


Fig. 2: Spin conductance  $G = j^z/V$  for a spin-(1/2)-chain junction with  $\Delta = 2$ , and spin bias  $V/t = 0.1$ . The grey lines indicate the critical magnetic field  $h_c/t \simeq 0.40$ , the blue lines the positions of the level crossings in an isolated spin chain.

We now discuss the effect of the magnetic field and the system-lead coupling on the spin transport. In fig. 2, the dependence of the spin conductance on the magnetic-field strength  $h$  is shown for fixed spin bias  $V/t = 0.1$  and system sizes  $N_S = 12, 24$  and  $36$ . Two values of the system-lead coupling are considered:  $J'/t = 1.4$ , where a conducting fixed point is expected, and  $J'/t = 1.2$ . For  $J'/t = 1.4$ , conductance stays approximately constant above the critical field  $h_c$ , except for some fluctuations. The spin conductance there is close to the ideal value  $G_0$ . Below  $h_c$ , the spin current at fixed  $V$  becomes suppressed with increasing chain length  $N_S$ . In the limit of a large spin chain and small bias, the spin conductance at the conducting fixed point should be a step function so that the strength of the magnetic field switches between insulating and conducting behaviour:  $\lim_{V \rightarrow 0} \lim_{N_S \rightarrow \infty} G = G_0 \Theta(h - h_c)$ . Very large spin chains are out of reach of our simulations but the results for  $N_S = 36$  already resemble this limiting behaviour. For a slightly smaller coupling  $J'/t = 1.2$ , away from the conducting fixed point, the effect of the magnetic field is qualitatively different. Outside of multiple peaks, the spin current is strongly suppressed even for  $h > h_c$ . The number of peaks increases with  $N_S$  and their height decreases at fixed  $V$ . At the first maximum for  $N_S = 12$ , the spin conductance is close to

the ideal value  $G_0$  while for  $N_S = 36$  the maximum is approximately  $G_0/2$ . The positions of the current peaks depend strongly on the system size and lie roughly at those values of the magnetic field where the ground state of the isolated spin chain becomes degenerate. This is in accordance with the picture that even for strong system-lead coupling the spin chain effectively decouples from the leads. Similar results were found in refs. [3] and [26] for chains of spinless fermions with varying chemical potential. Here, however, the leads are spinful, and states with different magnetization become degenerate. The effective low-energy theory near the degeneracy points therefore resembles the two-channel Kondo model, with the two lowest-lying states of the chain corresponding to a spin-1/2 [27]. In the zero-bias limit, the two-channel Kondo model exhibits perfect spin conductance [28]. The smaller conductance observed in fig. 2 may be attributed to additional perturbations in our system and the finite bias  $V$ . In a certain sense, the resonances in the current *vs.* magnetic-field curves correlate with the Coulomb blockade physics known from charge transport through low-dimensional nanostructures [29], the  $z$ -component of the total spin in our model corresponding to the particle number.

**Spin-1.** – We now consider a spin-1 chain with  $\Delta = 1$ , *i.e.*, the Haldane chain. Below the critical magnetic field  $h_c/J \simeq 0.41$ , the model is in the topological Haldane phase with a finite gap for excitations. For  $h > h_c$ , a gapless LL phase is realised. The LL parameter is  $K = 1$  at the transition, and increases with  $h$  [12]. In contrast to the spin-(1/2) chain, the model is nonintegrable so that the linear-response spin transport is expected to be ballistic only at zero temperature [13]. For small system sizes, the transport behaviour may nevertheless be quite similar to that in an integrable spin-(1/2) chain even at finite low temperatures [14]. The leads of the junction are the same as in the previous section.

Let us first discuss the junction for parameters in the LL regime of the spin chain. While the bulk of the system for  $h > h_c$  can be described by the LL model, the effect of the contacts may be different from the spin-(1/2) case. Indeed, we find that the Friedel oscillations of the magnetization near the interfaces cannot be tuned to zero by adjusting the system-lead coupling  $J'$ . Since the absence of the oscillations indicated a conducting fixed point in the spin-(1/2) model, this suggests that here no such fixed point occurs. We have checked this by calculating the spin conductance for different values of  $J'$  and  $h$ . The results are displayed in figs. 3 and 4. Like in the spin-(1/2) junction away from the conducting fixed point, there are multiple peaks in the spin conductance, which are related to degeneracies in the spectrum of the spin chain. As demonstrated in fig. 4, however, the minima of the current cannot be removed by tuning the coupling parameter  $J'/t$ , confirming the absence of a conducting fixed point in the spin-1 junction. Although no conducting fixed point is observed, the system-lead coupling still has a significant

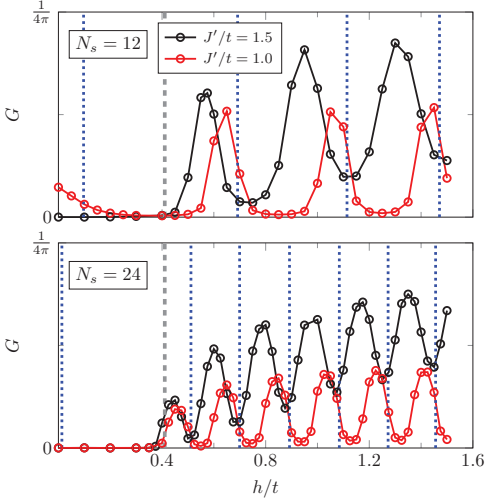


Fig. 3: Spin conductance for a spin-1-chain junction with  $\Delta = 1$ . The spin bias is  $V/t = 0.1$ . At the critical magnetic field  $h_c/t \simeq 0.41$  (grey line), the transition between Haldane and Luttinger-liquid phases takes place in the thermodynamic limit.

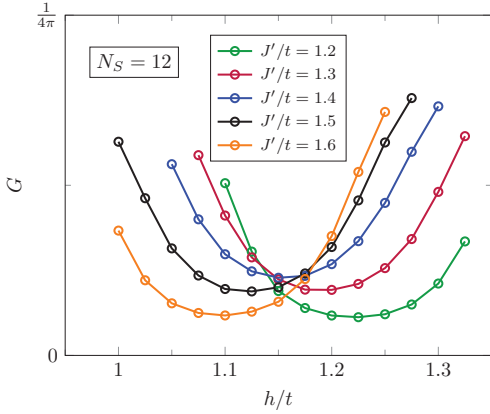


Fig. 4: Local minimum of the spin conductance for different coupling constants  $J'/t$ . The other parameters are the same as in fig. 3.

effect on the conductance as can be seen by comparing the results for  $J'/t = 1.5$  and  $J'/t = 1.0$  in fig. 3. For  $J'/t = 1.5$ , the current values at the minima and maxima become visibly larger with  $h$ , while the effect is much weaker for  $J'/t = 1.0$ . A possible explanation for the growth of the current with  $h$  is the increase of the LL parameter  $K$  with  $h$ , which could lead to a less severe effect of the inhomogeneity at the interfaces [1]. Like in the spin-(1/2) case, we can compare the position of the conductance peaks with the positions of the level crossings in the isolated spin chain. Good agreement is found for the distance between the peaks, but there is a noticeable overall shift to smaller  $h$ .

Table 1: Strength of the effective exchange coupling between the edge spins calculated from the spin gap for open boundary conditions.

$N_S$	$\tilde{J}/J$
12	0.09714
24	0.01341
36	0.00186
48	0.00025

For magnetic fields below  $h_c$ , in the Haldane regime of the spin chain, the spin conductance vanishes for most of the parameters in fig. 3. For  $N_S = 12$  and  $J'/t = 1.0$ , however, there is a clear conductance maximum at  $h = 0$ . As discussed in the following section, this is likely related to the spin-(1/2) edge states in the Haldane phase.

**Haldane phase.** – For appropriate combination of system size  $N_S$  and system-lead coupling  $J'$ , a conductance maximum was found around zero magnetic field in the Haldane phase (see fig. 3). To explain this maximum, one may use an effective low-energy model, where the Hilbert space of the spin chain is reduced to the subspace of the quasidegenerate ground states.

A Haldane chain with open boundary conditions has spin-(1/2) degrees of freedom at the edges, which lead to a fourfold-degenerate ground state in the thermodynamic limit. When the system size is finite, the edge states are coupled and the degeneracy is partially lifted. An effective low-energy model for the spin chain is  $\hat{H} = \tilde{J}\hat{S}_1 \cdot \hat{S}_2$ , where  $\hat{S}_{1/2}$  are spin-(1/2) operators representing the edge states [30]. The coupling  $\tilde{J}$  decreases approximately exponentially with the system size  $N_S$  (table 1). For even (odd)  $N_S$  the coupling is antiferromagnetic (ferromagnetic). Here, we restrict ourselves to even  $N_S$ . Adding the leads results in a spin-(1/2) junction with  $N_S = 2$ , exchange coupling  $\tilde{J}$  and some effective coupling to leads  $\tilde{J}' \propto J'$ . By calculating the matrix elements of the spin-1 operators  $\hat{S}_{1,N_S}$  in the subspace of the quasidegenerate ground states of the isolated spin chain, one obtains the coupling  $\tilde{J}' \simeq 1.064J'$  for  $N_S \rightarrow \infty$  [9,31]. The resulting spin-(1/2) Hamiltonian is a two-impurity two-channel Kondo model [32,33]. For  $\tilde{J} > 0$ , the model has two phases with an impurity phase transition at  $\tilde{J} = \tilde{J}_c$ . In the Kondo-singlet phase ( $\tilde{J} < \tilde{J}_c$ ) each spin-1/2 is screened by the corresponding lead and the two spins effectively decouple. In the local-singlet phase ( $\tilde{J} > \tilde{J}_c$ ), the two spins form a singlet and decouple from the leads.

The phase transition  $\tilde{J} = \tilde{J}_c$  is called the non-Fermi-liquid fixed point. There, the system has some unusual properties such as a residual impurity entropy  $\frac{1}{2}\ln(2)$  and a logarithmic divergence in the temperature dependence of the staggered susceptibility [32,34]. Since these quantities are difficult to access with the DMRG, we search for a phase transition in the spin-1 model by calculating

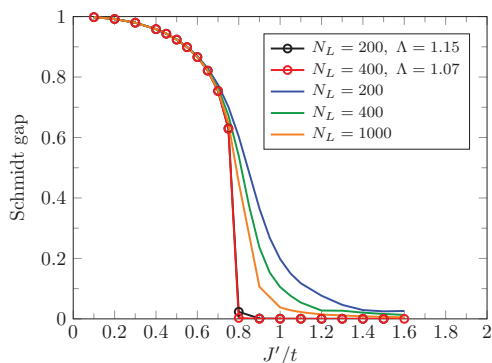


Fig. 5: Schmidt gap for a junction with  $N_S = 12$  and different lead sizes  $N_L$  at the bond between the spin chain and the left lead. Results are shown for uniform leads and for logarithmic discretisation.

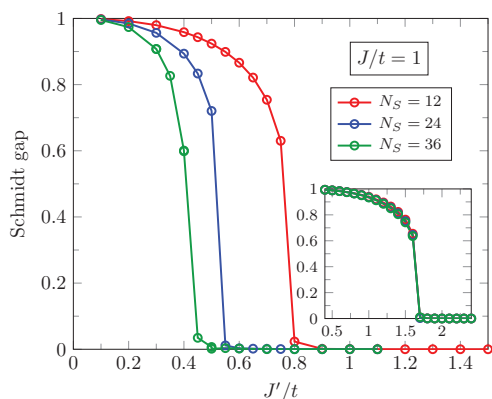


Fig. 6: Schmidt gap for a spin-1 chain with  $\Delta = 1$  at the bond between the spin chain and the left lead. Compared are results for different chain lengths  $N_S$ . The inset shows the results of a similar calculation for the spin-(1/2) chain with  $\Delta = 1$ .

appropriate entanglement spectra instead [35]. To distinguish between the local-singlet and the Kondo-singlet phase, it is sufficient to look at the Schmidt gap which is defined as the difference between the two largest eigenvalues of the reduced density matrix [35].

As already exploited in ref. [36], a logarithmic discretization of the leads works well for the calculation of the Schmidt gap (fig. 5). The discretization intervals are then defined by the points  $\epsilon_n = \pm 2t\Lambda^{-n}$  for  $n = 0, 1, \dots$  and some discretization parameter  $\Lambda > 1$  [34]. The chain representation of the leads is obtained with the Lanczos algorithm. If not mentioned otherwise, leads with  $N_L = 200$  sites and discretization parameter  $\Lambda = 1.15$  are used. Figure 6 displays the Schmidt gap for the bond between the spin chain and the left lead in a spin-1 chain. There is a sharp transition between finite and zero Schmidt gap whose position changes when the size of the spin chain is varied at fixed exchange coupling  $J$ . If, on the other hand,

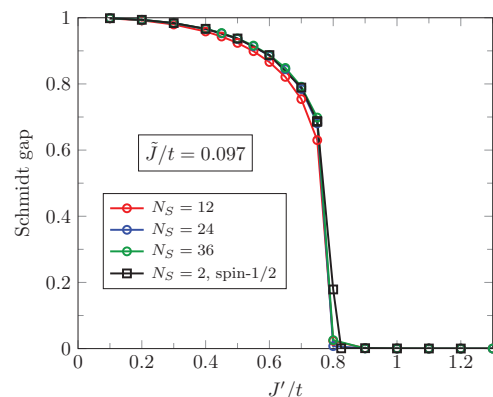


Fig. 7: Schmidt gap for a spin-1 chain with  $\Delta = 1$  for different system sizes and fixed exchange constant for the edge spins  $\tilde{J}/t \simeq 0.097$ , which corresponds to  $N_S = 12$  and  $J/t = 1$  (table 1). The results for the assumed effective spin-(1/2) chain model are also shown.

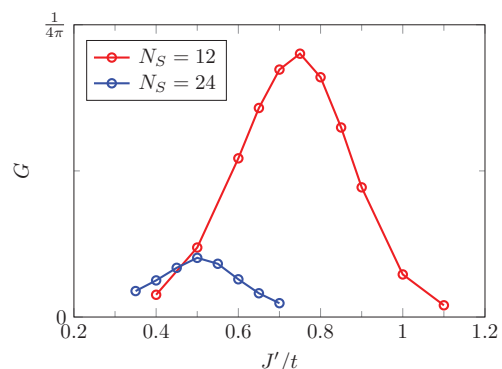


Fig. 8: Spin conductance for a spin-1 junction with  $J/t = 1$  and  $\Delta = 1$ . The spin bias is  $V/t = 0.1$ .

$J/t$  is adjusted to keep the effective spin-(1/2) model constant the position of the jump stays approximately the same (fig. 7). The results for the spin-1 chain also agree with a calculation directly in the expected effective spin-(1/2) model, which suggests that the observed transition is indeed related to the edge states even though we have no direct confirmation that two-impurity Kondo physics are realised. An analogous calculation of the Schmidt gap can be done for a spin-(1/2) chain (inset of fig. 6), where the jump in the Schmidt gap corresponds to the conducting fixed point. In contrast to the spin-1 case, the position of the jump is approximately independent of the chain length  $N_S$  for sufficiently large  $N_S$ .

To see how the spin transport is related to the edge states, the spin conductance is investigated for a spin-1 junction,  $h = 0$ , and different coupling strengths  $J'/t$  (fig. 8). The spin current is very small except for a peak at approximately the position of the jump in the

Schmidt gap ( $J'/t \simeq 0.75$  for  $N_S = 12$  and  $J'/t \simeq 0.50$  for  $N_S = 24$ ). With increasing system size  $N_S$  the maximum of the conductance at fixed  $V$  decreases because of the exponential suppression of the interaction between the edge spins. For low spin bias  $V$ , spin transport in the Haldane chain seems to be possible only near the phase transition between Kondo-singlet and local-singlet phases of the edge states. The spin chain also should be relatively short to have a reasonably strong coupling between the edge states.

When the coupling  $J'/t$  is smaller than the critical value and the system is in the local-singlet phase, the maximum of the conductance is shifted to a small finite  $h$ . This may be explained within an effective single-impurity two-channel Kondo model for a pseudospin formed from the singlet state and the lowest triplet state of the edge spins [33]. Accordingly, the conductance maximum lies roughly at  $h = J'$ , where the singlet and lowest triplet state have the same energy. In fig. 3, this corresponds to the blue lines below the critical field  $h_c$ .

**Conclusion.** – We have numerically studied the spin transport for junctions in which a spin-(1/2) or spin-1 XXZ chain is coupled at both ends to noninteracting fermionic leads. The focus was on the effect of the contacts and an external magnetic field that switches between gapped and gapless phases of the spin chain. When the strength of the magnetic field is varied, the spin conductance generally shows several resonances that correspond to degeneracy points in the spectrum of an isolated spin chain. The height of these current maxima decreases with the system size, indicating that spin transport becomes suppressed for long chains. By fine-tuning the system-lead coupling, a conducting fixed point may be reached. There, instead of showing multiple pronounced peaks, the conductance develops a plateau when the magnetic field is increased and the system passes into the gapless phase. Whether a conducting fixed point exists will depend on the spin chain in the junction. Our results indicate that such a point occurs for the spin-(1/2) XXZ chain but not for the spin-1 Haldane chain. A difference is also observed regarding the Friedel oscillations at the contacts, which vanish at the conducting fixed point of the spin-(1/2) chain but appear to be always finite in the spin-1 case. Lastly, we have discussed the transport in the gapped Haldane phase at zero magnetic field. The spin conductance there shows a clear maximum as a function of the system-lead coupling. By examining the entanglement gap at the interface, we have provided evidence that this conductance maximum corresponds to the non-Fermi-liquid fixed point of an effective two-impurity Kondo model formed by the spin-(1/2) edge states.

\*\*\*

We thank F. GÖHMANN, T. SHIRAKAWA and S. YUNOKI for enlightening discussions. DMRG simulations were performed using the ITensor library [37]. FL was supported

by the Deutsche Forschungsgemeinschaft through project FE 398/8-1.

## REFERENCES

- [1] KANE C. L. and FISHER M. P. A., *Phys. Rev. B*, **46** (1992) 15233.
- [2] JAUHO A.-P., WINGREEN N. S. and MEIR Y., *Phys. Rev. B*, **50** (1994) 5528.
- [3] BOHR D., SCHMITTECKERT P. and WÖLFLE P., *Europhys. Lett.*, **73** (2006) 246.
- [4] ANDERS F. B., *Phys. Rev. Lett.*, **101** (2008) 066804.
- [5] BRANSCHÄDEL A., SCHNEIDER G. and SCHMITTECKERT P., *Ann. Phys. (Berlin)*, **522** (2010) 657.
- [6] SEDLMAYR N., OHST J., AFFLECK I., SIRKER J. and EGGERT S., *Phys. Rev. B*, **86** (2012) 121302.
- [7] WANG D.-K., SUN Q.-F. and GUO H., *Phys. Rev. B*, **69** (2004) 205312.
- [8] JUNGWIRTH T., MARTI X., WADLEY P. and WUNDERLICH J., *Nat. Nanotechnol.*, **11** (2016) 231.
- [9] WHITE S. R., *Phys. Rev. Lett.*, **69** (1992) 2863.
- [10] VIDAL G., *Phys. Rev. Lett.*, **91** (2003) 147902.
- [11] SHASTRY B. S. and SUTHERLAND B., *Phys. Rev. Lett.*, **65** (1990) 243.
- [12] KONIK R. M. and FENDLEY P., *Phys. Rev. B*, **66** (2002) 144416.
- [13] ZOTOS X., *J. Phys. Soc. Jpn. Suppl.*, **74** (2005) 173.
- [14] PSAROUDAKI C., HERBRYCH J., KARADAMOGLU J., PRELOVŠEK P., ZOTOS X. and PAPANICOLAOU N., *Phys. Rev. B*, **89** (2014) 224418.
- [15] PROSEN T. and ŽNIDARIČ M., *J. Stat. Mech.: Theory Exp.*, **2009** (2009) P02035.
- [16] LENARČIČ Z. and PROSEN T., *Phys. Rev. E*, **91** (2015) 030103.
- [17] LANGE F., EJIMA S., SHIRAKAWA T., YUNOKI S. and FEHSKE H., *Phys. Rev. B*, **97** (2018) 245124.
- [18] HALDANE F. D. M., *Phys. Rev. Lett.*, **50** (1983) 1153.
- [19] MURG V., VERSTRAETE F., LEGEZA O. and NOACK R. M., *Phys. Rev. B*, **82** (2010) 205105.
- [20] HOLZNER A., WEICHSELBAUM A. and VON DELFT J., *Phys. Rev. B*, **81** (2010) 125126.
- [21] ZOTOS X., NAEF F. and PRELOVSEK P., *Phys. Rev. B*, **55** (1997) 11029.
- [22] GIAMARCHI T., *Quantum Physics in One Dimension* (Clarendon Press, Oxford) 2003, <http://dx.doi.org/10.1093/acprof:oso/9780198525004.001.0001>.
- [23] SEDLMAYR N., MORATH D., SIRKER J., EGGERT S. and AFFLECK I., *Phys. Rev. B*, **89** (2014) 045133.
- [24] MORATH D., SEDLMAYR N., SIRKER J. and EGGERT S., *Phys. Rev. B*, **94** (2016) 115162.
- [25] VERSTRAETE F., GARCÍA-RIPOLL J. J. and CIRAC J. I., *Phys. Rev. Lett.*, **93** (2004) 207204.
- [26] VASSEUR G., WEINMANN D. and JALABERT R. A., *Eur. Phys. J. B*, **51** (2006) 267.
- [27] MITCHELL A. K., LOGAN D. E. and KRISHNAMURTHY H. R., *Phys. Rev. B*, **84** (2011) 035119.
- [28] MITCHELL A. K., LANDAU L. A., FRITZ L. and SELA E., *Phys. Rev. Lett.*, **116** (2016) 157202.
- [29] VAN HOUTEN H., BEENAKKER C. W. J. and STARING A. A. M., *Coulomb-Blockade Oscillations in*



- Semiconductor Nanostructures* (Springer US, Boston, Mass.) 1992, pp. 167–216, [https://doi.org/10.1007/978-1-4757-2166-9\\_5](https://doi.org/10.1007/978-1-4757-2166-9_5).
- [30] SØRENSEN E. S. and AFFLECK I., *Phys. Rev. B*, **49** (1994) 15771.
- [31] SØRENSEN E. S. and AFFLECK I., *Phys. Rev. B*, **51** (1995) 16115.
- [32] AFFLECK I., LUDWIG A. W. W. and JONES B. A., *Phys. Rev. B*, **52** (1995) 9528.
- [33] JAYATILAKA F. W., GALPIN M. R. and LOGAN D. E., *Phys. Rev. B*, **84** (2011) 115111.
- [34] BULLA R., COSTI T. A. and PRUSCHKE T., *Rev. Mod. Phys.*, **80** (2008) 395.
- [35] BAYAT A., JOHANNESSON H., BOSE S. and SODANO P., *Nat. Commun.*, **5** (2014) 3784.
- [36] SHIRAKAWA T. and YUNOKI S., *Phys. Rev. B*, **93** (2016) 205124.
- [37] <http://itensor.org/>.



# Block-Lanczos density-matrix renormalization-group study of the spin transport in Heisenberg chains coupled to leads

Florian Lange, Satoshi Ejima, and Holger Fehske

Institut für Physik, Universität Greifswald, 17489 Greifswald,  
Germany

## 1 Introduction

This report summarizes results of a block-Lanczos density-matrix renormalization-group (DMRG) study on the spin transport in a spin-chain junction. Specifically, we consider a spin-1/2 Heisenberg chain contacted at each end to two-dimensional (2D) non-interacting leads with spin-orbit coupling. The idea behind the model is as follows: an electric field in the leads causes a spin current to flow in the transverse direction because of the intrinsic spin-Hall effect. At the first interface, this conduction-electron spin current is then converted to a spinon spin-current that passes through the spin chain. When the spin current reaches the second lead it is converted back to an electron spin-current that, via the inverse spin-Hall effect, induces a transverse charge current. The model therefore describes two phenomena relevant for spintronics, conversion between spin- and charge currents, and injection of spin current from a conductor into a magnetic insulator (and vice versa).

Magnetic insulators are potentially useful for spintronics applications because of the greater decay length of spin currents compared to conductors. Motivated by this, there have been several experiments on the spin-current generation in various insulating materials [1–4]. Kajiwara *et al.* achieved the injection of spin currents into the ferrimagnetic insulator yttrium iron garnet (YIG) from an attached platinum (Pt) film, where a spin current was generated electrically using the spin Hall effect [1]. More recently, a spin current was induced in the spin-1/2-chain material  $\text{Sr}_2\text{CuO}_3$  by using the spin Seebeck effect at an interface with a Pt film [4]. Our setup is somewhat similar but does not directly correspond to either experiment. Rather, it serves as a toy model for the spin transport between a one-dimensional (1D) magnetic insulator and 2D conductors. An advantage of our model is that it can be brought to a purely 1D form by using a Lanczos recursive method [5, 6]. It is then amenable to numerical techniques based on matrix-product states (MPS) [7, 8], which allow for simulations without uncontrolled approximations. We focus on junctions consisting of Heisenberg spin chains and 2D Rashba systems [9], which are paradigmatic models for 1D magnetism and the intrinsic spin-Hall effect, respectively. Since both systems have already been investigated thoroughly,

our aim is to analyze particularly the interface effects. Unfortunately, it will turn out that simulating the spin-current generation by the spin Hall effect in a Rashba lead is difficult numerically which is why we will simplify the model and neglect the spin-orbit coupling in the current-generating lead. We will still consider the effect of Rashba spin-orbit coupling in the second lead, however.

The combined Lanczos-DMRG approach employed here could also be applied to various models of similar nature, as long as the interacting region is 1D and the leads are non-interacting. Another purpose of this study is therefore to assess the utility of the numerical method in simulating such systems.

The outline of this report is as follows. In Sec. 2, the model is introduced. Section 3 describes the block-Lanczos transformation which is applied to facilitate the use of MPS methods. The results of the MPS calculations are presented in Sec. 4. Section 5 contains a summary and a discussion of the results.

## 2 Model

### 2.1 Junction setup

We study a junction of a 1D interacting region and two non-interacting leads [see Fig. 1]. The interacting part is modeled by a spin-1/2 Heisenberg chain of length  $N_S$

$$\hat{H}_S = J \sum_{j=1}^{N_S-1} \hat{\mathbf{S}}_j \hat{\mathbf{S}}_{j+1}, \quad (1)$$

with, unless specified differently, antiferromagnetic exchange coupling ( $J > 0$ ). For the lead Hamiltonians  $\hat{H}_{L_1}$  and  $\hat{H}_{L_2}$ , we consider 2D Rashba systems

$$\hat{H}_R = \sum_{\langle ij \rangle} \left( \hat{c}_{i\uparrow}^\dagger, \hat{c}_{i\downarrow}^\dagger \right) \{ -t - i\lambda[(x_j - x_i)\sigma_y - (y_j - y_i)\sigma_x] \} \begin{pmatrix} \hat{c}_{j\uparrow} \\ \hat{c}_{j\downarrow} \end{pmatrix}, \quad (2)$$

where  $\hat{c}_{j\sigma}$  are fermionic annihilation operators,  $\lambda$  parameterizes the spin-orbit coupling,  $\sigma_x$  and  $\sigma_y$  are Pauli matrices. The sites are elements of an infinite square lattice with an open edge and lattice constant  $a = 1$ . At each end, the spin chain is coupled by an exchange interaction to a site at the open edge of one of the leads. Denoting the indices of these sites by  $j_0$ , the coupling terms are of the form

$$\hat{H}_c(a, j) = J' \left[ \frac{1}{2} (\hat{c}_{j_0\uparrow a}^\dagger \hat{c}_{j_0\uparrow a} - \hat{c}_{j_0\downarrow a}^\dagger \hat{c}_{j_0\downarrow a}) \hat{S}_j^z + \frac{1}{2} (\hat{c}_{j_0\uparrow a}^\dagger \hat{c}_{j_0\downarrow a} \hat{S}_j^- + \hat{c}_{j_0\downarrow a}^\dagger \hat{c}_{j_0\uparrow a} \hat{S}_j^+) \right], \quad (3)$$

where an additional index  $a \in \{l, r\}$  was introduced to distinguish between the two leads. With Eq. (3), the complete Hamiltonian can be written as

$$\hat{H} = \hat{H}_S + \hat{H}_{L_1} + \hat{H}_{L_2} + \hat{H}_c(l, 1) + \hat{H}_c(r, N_S). \quad (4)$$

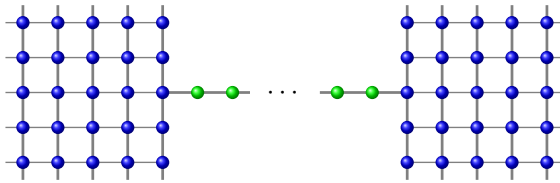


Figure 1: Schematic of the junction with two Rashba leads. The green balls represent spin chain sites, the blue ones lead sites.

## 2.2 Rashba spin-orbit coupling

The system described by Eq. (2) is a discretization of the continuous 2D Rashba model with single-particle Hamiltonian

$$\hat{\mathcal{H}}_R = \frac{\hat{\mathbf{p}}^2}{2m^*} + \frac{\alpha}{\hbar}(\boldsymbol{\sigma} \times \hat{\mathbf{p}}) \cdot \mathbf{z}, \quad (5)$$

where  $\hat{\mathbf{p}}$  is the momentum operator,  $\boldsymbol{\sigma}$  the vector of Pauli matrices,  $m^*$  an effective mass and  $\mathbf{z}$  the unit vector pointing in the  $z$  direction which is perpendicular to the system plane [9]. In the long-wavelength limit  $|\mathbf{k}| \rightarrow 0$ , the models are directly related through  $t = \hbar^2/(2m^*)$  and  $\lambda = \alpha/2$ .

The Rashba Hamiltonian (5) has attracted a lot of theoretical attention since a linear-response calculation indicated the existence of an intrinsic spin Hall effect, i.e., the generation of a transverse spin current by an electric field [10]. Later, it was shown that previously neglected contributions lead to a vanishing spin Hall conductivity [11, 12]. On the other hand, numerical simulations have confirmed the spin Hall effect for mesoscopic systems in the discrete Rashba model [13]. The inverse spin Hall effect, which describes the induction of a transverse charge current by a spin current, appears to be finite in both the continuous and the discrete case [14, 15]. It should be noted that the total magnetization is not a conserved quantity in the Rashba model, which makes the definition of a spin current problematic. To avoid this issue the spin Hall effect has also been defined in terms of the magnetization induced at the edges of a system [16].

In the envisioned junction, the spin Hall effect is used to induce a spin accumulation at the first interface and drive a spin current. When the spin current reaches the second lead, the inverse spin Hall effect supposedly causes a charge current that serves as a measurable signal. The latter part, however, will be complicated by the Rashba precession. One can interpret the Rashba term as a momentum-dependent magnetic field proportional to  $\hat{\mathbf{p}} \times \mathbf{z}$  that causes an electron's spin to precess around it. For our setup this means that, along a given direction from the injection point, the spin current and therefore the induced transverse charge current will oscillate as a function of the covered distance. A similar combination of the anomalous Hall effect and spin precession has been termed *spin-injection Hall effect* [17].

### 3 Block-Lanczos Transformation

The Lanczos algorithm is a way to obtain a unitary transformation that tridiagonalizes a given Hermitian matrix  $H^0$  [18]. One starts with a single unit vector  $v_1$  which is the first column of the transformation matrix  $P = (v_1, v_2, \dots)$ . All remaining  $v_j$  are then obtained by setting  $v_j \leftarrow H^0 v_{j-1}$  and orthogonalizing against previous vectors<sup>1</sup>. We use a block version of the Lanczos method [19], in which one chooses the first  $M$  orthonormal vectors  $v_1, v_2, \dots, v_M$  and sets  $v_n \leftarrow H^0 v_{n-M}$ , again followed by an orthogonalization. From this construction and the hermicity of  $H^0$  it follows that  $P^\dagger H^0 P$  is a band matrix with bandwidth  $M$ :

$$\tilde{H}^0 = P^\dagger H^0 P = \begin{pmatrix} E_1 & T_1 & 0 & 0 & \cdots \\ T_1^\dagger & E_2 & T_2 & 0 & \cdots \\ 0 & T_2^\dagger & E_3 & T_3 & \cdots \\ 0 & 0 & T_3^\dagger & E_4 & \cdots \\ \vdots & \vdots & & \ddots & \ddots \end{pmatrix}, \quad (6)$$

where  $E_j$  and  $T_j$  are Hermitian and lower-triangular  $M \times M$  matrices, respectively.

If the block-Lanczos transformation is applied to the matrix describing a single-particle Hamiltonian  $\hat{H}^0$  of a quantum system, i.e.,  $\hat{H}^0 = \hat{\mathbf{c}}^\dagger H^0 \hat{\mathbf{c}}$  where  $\hat{\mathbf{c}}^\dagger = (\hat{c}_1^\dagger, \hat{c}_2^\dagger, \dots, \hat{c}_N^\dagger)$  is a vector of creation operators, the banded structure of  $\tilde{H}^0$  means that, in terms of the new operators  $\hat{\mathbf{a}}^\dagger = (\hat{a}_1^\dagger, \hat{a}_2^\dagger, \dots, \hat{a}_N^\dagger) = \hat{\mathbf{c}}^\dagger P$ ,  $\hat{H}^0$  describes an open chain with short-ranged hopping and a site-dependent potential. In detail:

$$\hat{H}^0 = \hat{\mathbf{a}}^\dagger \tilde{H}^0 \hat{\mathbf{a}} = \sum_{n=1}^{N-M} \sum_{d=1}^M \left( \tilde{H}_{n,n+d}^0 \hat{a}_n^\dagger \hat{a}_{n+d} + \text{h. c.} \right) + \sum_{n=1}^N \tilde{H}_{nn}^0 \hat{a}_n^\dagger \hat{a}_n, \quad (7)$$

where  $N$  is the order of the matrix  $H^0$  and the number of single-particle states. The first  $M$  operators  $\hat{a}_1^\dagger, \hat{a}_2^\dagger, \dots, \hat{a}_M^\dagger$  can be fixed through the choice of initial vectors. Increasing the bandwidth  $M$  thus allows for a greater flexibility in the transformation but it also increases the maximum hopping range.

For an interacting Hamiltonian  $\hat{H} = \hat{H}^0 + \hat{V}$ , in which the interaction is a function of only  $M$  fermion operators, i.e.,  $\hat{V} = \hat{V}(\hat{c}_{j_1}^\dagger, \dots, \hat{c}_{j_M}^\dagger, \hat{c}_{j_1}, \dots, \hat{c}_{j_M})$ , we can use a block-Lanczos transformation with block size  $M$  and set  $\hat{a}_n^\dagger = \hat{c}_{j_n}^\dagger$  for  $n = 1, 2, \dots, M$ . The interaction is then restricted to the first  $M$  sites after the transformation and the chain representation of  $\hat{H}$  contains only short-ranged terms. An exact solution of the problem will still be impossible in general but the 1D form makes the model suitable for a numerical treatment with MPS techniques. The (block-)Lanczos method has been used in this manner mostly in the context of impurity problems [5, 6]. Our application to the spin-chain junction is analogous, with the sites coupled to the spin chain taking the role of the impurities.

<sup>1</sup> In exact arithmetic, orthogonalization is only necessary against the previous two vectors but reorthogonalization against other vectors may be carried out for numerical stability.

### 3.1 Infinite boundary conditions

In the following discussion, we assume that the Hamiltonian is originally defined on a lattice in real space and has only short-ranged hopping terms. The interaction  $\hat{V}$  shall act on one site whose corresponding fermion operators will be invariant under the transformation. While we are ultimately interested in the thermodynamic limit, the matrix  $H^0$  and thus the system size need to be finite in a numerical calculation. However, for a given  $j_{\max}$  one can always choose the original system large enough so that the new operators  $\hat{a}_j^\dagger$  with  $j \leq j_{\max}$  are not affected by its finite size. This follows from

$$v_j \in \text{span} \{ (H^0)^n v_l \mid 1 \leq l \leq M, 0 \leq n \leq r-1 \} \quad (8)$$

for  $j \leq rM$ , which implies that  $\hat{a}_j^\dagger$  is supported only on sites connected to the interacting site through at most  $r-1$  hopping operations. Of course, finite-size effects will eventually appear if the transformation is carried out to completion. We can, however, stop the Lanczos recursion before that happens and work with a truncated transformation by ignoring the remaining sites in the chain representation. For a fixed number of chain sites these *infinite boundary conditions* will be closer to the thermodynamic limit regarding the physics at the interacting site [5]. On the downside,  $P$  is no longer unitary which complicates the measurements for the original lattice. The one-body expectation values in both representations are related by

$$\langle \hat{c}_j^\dagger \hat{c}_i \rangle = \sum_{nm} P_{mj}^\dagger P_{in} \langle \hat{a}_m^\dagger \hat{a}_n \rangle \quad (9)$$

for the full transformation. Typical quantities in the original system thus have to be reconstructed from a large number of correlation functions in the effective 1D model. If the Lanczos recursion is stopped prematurely, the above relation is not fulfilled because states are missing on the right-hand side. It is still possible to calculate the change in the expectation values that is induced by a perturbation at the interacting site, e.g. an injected current. The reason is that, for sufficiently many sites in the effective 1D model, the only missing terms in Eq. (9) are then between sites that are both outside the range of the perturbation, or whose distance so big, that the contribution from the correlation function can be neglected. We thus expect the following relation to hold during the time evolution:

$$\langle \hat{c}_j^\dagger \hat{c}_i \rangle(\tau) - \langle \hat{c}_j^\dagger \hat{c}_i \rangle(0) \approx \sum_{nm} P_{mj}^\dagger P_{in} [\langle \hat{a}_m^\dagger \hat{a}_n \rangle(\tau) - \langle \hat{a}_m^\dagger \hat{a}_n \rangle(0)], \quad (10)$$

where  $\tau$  denotes the time at which the expectation value is calculated. Another, more accurate way to calculate expectation values away from the interacting site is to increase the block size  $M$  and include additional sites in the Lanczos basis for measurements. This has been used in Ref. [6] to calculate two-point correlation functions between impurity and conduction sites. Here, this scheme is not suitable since we want to carry out measurements at a lot of different positions which would require the simulations to be repeated many times.

### 3.2 Application to the Rashba model

We now apply the block-Lanczos transformation to a 2D Rashba lead. To keep the exchange interaction with the spin chain local, both spin states of the

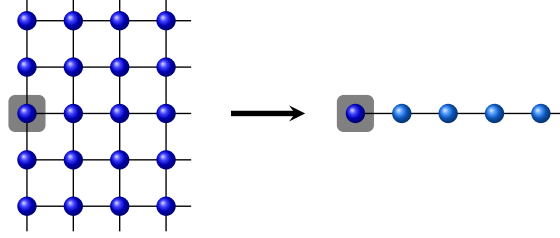


Figure 2: The block-Lanczos transformation maps the two-dimensional Rashba lead to a chain with nearest-neighbor hopping. Since the only site affected by the interaction with the system (shaded circle) is invariant under the transformation, the interaction remains local in the one-dimensional representation.

affected site are included in the Lanczos basis and the block size is therefore  $M = 2$ . Different transformations and effective 1D models are obtained depending on the position of the interacting site. Here, the site is assumed to lie on the open edge of the lead [see Fig. 2].

It turns out, that  $\hat{H}_R$  expressed in terms of the new fermion operators  $\hat{a}_j^\dagger$  describes two decoupled tight-binding chains with the same bond-dependent hopping parameters  $\tilde{t}_j$ . Defining  $\hat{a}_{j\uparrow} = \hat{a}_{2j-1}$  and  $\hat{a}_{j\downarrow} = \hat{a}_{2j}$  allows us to write

$$\hat{H}_R = \sum_{j \geq 1} \tilde{t}_j \sum_{\sigma=\uparrow,\downarrow} \left( \hat{a}_{j\sigma}^\dagger \hat{a}_{j+1,\sigma} + \text{h.c.} \right), \quad (11)$$

so that even for finite Rashba spin-orbit interaction the only difference to a regular tight-binding chain is the position-dependent hopping  $\tilde{t}_j$ . A chemical potential stays the same under the Lanczos transformation but the density changes unless the system is at half-filling. The conservation of the new spin introduced in Eq. (11) can be exploited in numerical simulations. Note, however, that it corresponds to the physical spin only at the first site. This is demonstrated for  $\lambda/t = 0.4$  in the inset of Fig. 3, where it can be seen that the expectation value of  $\hat{S}^z = (1/2) \sum_j (\hat{c}_{j\uparrow}^\dagger \hat{c}_{j\uparrow} - \hat{c}_{j\downarrow}^\dagger \hat{c}_{j\downarrow})$  oscillates as a function of the site index.

The simple form (11) of the Hamiltonian in the block-Lanczos basis means that the Krylov subspaces generated by the  $|\uparrow\rangle = \hat{a}_{1\uparrow}^\dagger |0\rangle$  single-particle state at the interacting site are orthogonal to those generated by the  $|\downarrow\rangle = \hat{a}_{1\downarrow}^\dagger |0\rangle$  state. To prove this, one needs to show that  $\langle \uparrow | \hat{H}_R^n | \downarrow \rangle = 0$  for  $n \in \mathbb{N}_0$ , which follows from the time-reversal symmetry of the Hamiltonian:

$$\langle \uparrow | \hat{H}_R^n | \downarrow \rangle = \langle \tilde{\downarrow} | \hat{T} \hat{H}_R^n \hat{T}^{-1} | \tilde{\uparrow} \rangle = -\langle \uparrow | \hat{H}_R^n | \downarrow \rangle, \quad (12)$$

where  $|\tilde{\uparrow}\rangle = \hat{T}|\uparrow\rangle$ ,  $|\tilde{\downarrow}\rangle = \hat{T}|\downarrow\rangle$  and  $\hat{T}$  is the time-reversal operator. The Lanczos method with block size  $M = 1$  therefore would have been sufficient to obtain the transformation. This is also true if there is both Rashba and Dresselhaus spin-orbit coupling, but not in the presence of a magnetic field.

Figure 3 shows the position dependence of the hopping amplitudes in Eq. (11) for the infinite boundary conditions described in the previous section. Already after a few sites ( $j \approx 8$ ), the hopping amplitude approaches a constant value that depends on the spin-orbit interaction  $\lambda$ . This asymptotic value agrees with the



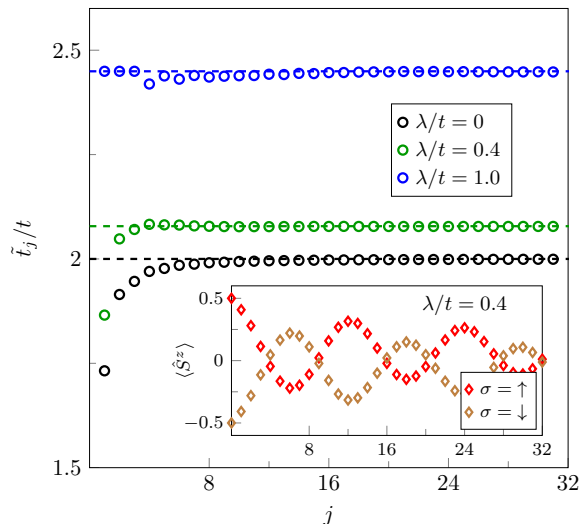


Figure 3: Hopping parameters  $\tilde{t}_j$  in the effective one-dimensional model for the Rashba Hamiltonian described by Eq. (2). The spin-orbit interaction changes the asymptotic value  $\tilde{t}_\infty$  (dashed lines) given by Eq. (13) and slightly affects the position dependence for small  $j$ . In the inset, the expectation value of the  $z$  component of the total spin is shown for the Lanczos basis states corresponding to  $\lambda/t = 0.4$ .

hopping

$$\tilde{t}_\infty = 2t \cos(k_m) + \sqrt{2}\lambda \sin(k_m), \quad (13)$$

where  $k_m = \arctan(\lambda/\sqrt{2}t)$ , that leads to the same bandwidth as in the original model (2). Note that if we applied the transformation to a finite system the hopping parameter would become non-uniform again for sufficiently large site indices.

From Eq. (11) and Fig. 3, one can see that, regardless of the spin-orbit coupling strength  $\lambda$ , the effective model is quite similar to a regular tight-binding chain with uniform hopping amplitude. The differences due to the Rashba spin-orbit coupling only become apparent when transforming back to the original representation.

## 4 Matrix-product-state calculations

With the 2D Rashba system mapped to a chain representation, we are in the position to study the junction by means of MPS techniques. The first task is to inject a spin current from the first lead into the spin chain, which could be achieved by exploiting the spin Hall effect and applying an electric field in the lead. To simulate an electric field in the Rashba system, we need to either switch on a static potential at the start of the time evolution or add a time-dependent phase factor to the hopping terms. In both cases, the perturbation would be

highly non-local in the block-Lanczos basis, rendering MPS simulations inefficient. This can in principle be avoided by working in a mixed momentum and real space representation instead of the Lanczos basis, and using a tree-tensor network ansatz as in multi-channel impurity problems [20]. The non-interacting Hamiltonian then describes multiple decoupled chains for each momentum in, for example, the  $y$  direction. Only short-ranged terms appear in each chain even when a time-dependent vector potential is introduced to drive a charge current. However, the coupling to the spin chain becomes long ranged which complicates time-evolution simulations. In addition, the description of the interface between lead and spin chain is more demanding in the tree-tensor network approach and constitutes a bottleneck in the calculations. It may therefore be more advisable to simplify the model with the specific questions we want to address in mind.

A main goal of our simulations is to determine under which conditions efficient spin transport through the spin chain junction is possible. If we assume that the means by which the spin current is generated is not essential for this question, we can induce the spin current by ignoring the spin-orbit coupling and adding a simple potential that couples to the total magnetization in the current-generating lead. Explicitly, the perturbation is

$$\hat{H}_V = -\frac{V_S}{2} \sum_{j \in L_1} (\hat{c}_{j\uparrow}^\dagger \hat{c}_{j\uparrow} - \hat{c}_{j\downarrow}^\dagger \hat{c}_{j\downarrow}), \quad (14)$$

where  $V_S$  is the spin voltage and the sum runs over sites in the first lead. Our approach is thus analogous to typical charge-transport calculations. In the presence of spin-orbit coupling, the term (14) would not correspond to a uniform potential after the mapping since the Lanczos basis then no longer consists of  $\hat{S}^z$  eigenstates. The spin-orbit coupling in the second lead, on the other hand, is not problematic because the effective 1D model has the same form as without spin-orbit coupling in the absence of a perturbing field [see Eq. (11)]. We analyze the effect of a Rashba term in the second lead in Sec. 4.2.

#### 4.1 Spin conductance

To obtain the zero-temperature spin conductance of the junction, we first calculate the ground state with the DMRG and then simulate the time evolution with switched-on spin voltage using the time-evolving block decimation algorithm [21]. More details on the numerical method are given in Refs. [22, 23], where a similar setup with uniform 1D leads was studied. In these works it was found that the spin conductance depends sensitively on the model parameters near the interfaces. In particular, there can be conducting fixed points where the spin conductance at zero temperature is ideal, i.e., it is equal to that of a homogeneous tight-binding chain [24, 25]. Using the specific 2D leads (in their 1D representation) should not qualitatively affect these results but the added site dependence of the hopping parameters near the interface could move the system away from or towards a conducting fixed point. We have confirmed this for some values of the model parameters by explicit numerical calculations whose results are displayed in Fig. 4. At a small but finite spin voltage  $V_S/J = 0.1$ , the spin conductance  $G_S$  shows a sharp peak as a function of the interface-coupling strength  $J'$ . This is observed for both types of leads but the position of the maximum is indeed different. For the block-Lanczos leads the peak is shifted to

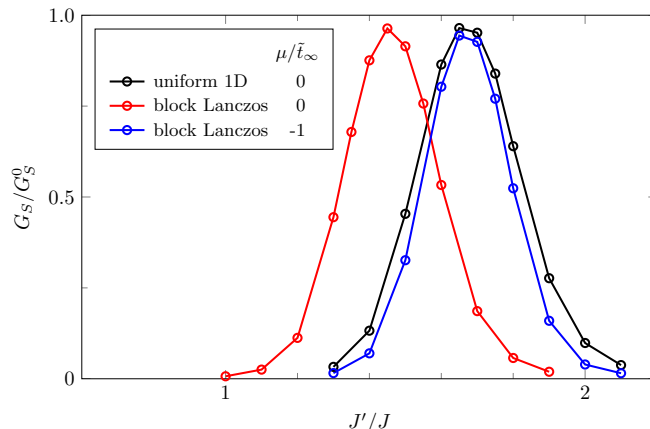


Figure 4: Spin conductance  $G_S$  at zero temperature for  $N_S = 12$  and spin voltage  $V_S/J = 0.1$ . The hopping amplitudes  $\tilde{t}_j$  [see Eq.(11)] in the leads are either assumed to be uniform or obtained by a block-Lanczos transformation of the Hamiltonian (2) without spin-orbit coupling ( $\lambda = 0$ ). In both cases, the overall energy scale is chosen so that  $\tilde{t}_\infty = \lim_{j \rightarrow \infty} \tilde{t}_j = J$ . Each lead is truncated to a finite length of 400 sites in the MPS simulations.

smaller  $J'$ , as may be expected because of the reduced hopping strength near the spin chain. The maximum value of  $G_S$  is in both cases approximately the ideal value  $G_S^0 = 1/(4\pi)$  for the linear conductance. In Refs. [22, 23], only half-filled leads were considered. As can be seen in Fig. 4, conducting fixed points occur for finite chemical potential  $\mu$  as well, though their position is  $\mu$  dependent.

Finally, let us briefly comment on the case of ferromagnetic exchange interaction. Numerical calculations indicate that the spin currents are much smaller than for antiferromagnetic spin-1/2 chains. This may be explained by considering the Kondo model, i.e. a single spin coupled to a fermionic bath. It is known that for ferromagnetic interaction, the Kondo spin effectively decouples from the lead in the low temperature limit [26]. Adding spin sites that interact ferromagnetically with the first spin will not change this behavior. Accordingly, we expect the linear spin conductance of the junction to vanish at zero temperature.

## 4.2 Lead dynamics

Until now, we only considered expectation values in the effective 1D model, which is sufficient to characterize the spin transport through the spin chain. As described in Sec. 3.1, however, the block-Lanczos transformation can be reversed to obtain expectation values of observables defined on the original real-space lattice. To this end, we calculate the single-particle expectation values  $\langle \hat{a}_{i\sigma}^\dagger \hat{a}_{j\sigma} \rangle$  in the 1D representation for all sites  $i, j \leq L$  for some finite number  $L$ . This can be done by two nested sweeps in the MPS program so that the computational cost scales quadratically with  $L$ .

As an example, we investigate the magnetization  $m_j = \frac{1}{2} \langle \hat{c}_{j\uparrow}^\dagger \hat{c}_{j\uparrow} - \hat{c}_{j\downarrow}^\dagger \hat{c}_{j\downarrow} \rangle$  in the second lead after the spin current is injected. Figure 5 shows  $m_j$  for

2D leads with and without spin-orbit coupling. The spin current entering the system leads to a small position-dependent magnetization that depends strongly on both the chemical potential  $\mu$  and the strength of the spin-orbit coupling  $\lambda$ . Most strikingly, the Rashba precession for  $\lambda \neq 0$  leads to oscillations as a function of the position. Near half-filling, the induced magnetization is largest along the diagonal directions, while it becomes more uniformly spread when the chemical potential is increased. This can be understood by looking at the shape of the Fermi surface for  $\lambda = 0$ . At half-filling, it takes a diamond form, so that the energy gradient  $\nabla_{\mathbf{k}}E(\mathbf{k})|_{|\mathbf{k}|=k_F}$ , i.e., the group velocity, points in one of the diagonal directions. In the limit of a nearly empty band  $k_F \rightarrow 0$ , on the other hand, the Fermi surface becomes a circle and  $\nabla_{\mathbf{k}}E(\mathbf{k})|_{|\mathbf{k}|=k_F}$  is proportional to the momentum  $\mathbf{k}$ . For small finite  $\lambda$ , this picture remains qualitatively valid and the observed angular dependence of the magnetization is indeed similar.

Above, it was assumed that the spin current in the spin chain is polarized in the  $z$  direction, i.e., orthogonal to the plane of the 2D lead. If we choose a different polarization the spin current through the chain will have the same magnitude because of the pseudo-spin-rotation symmetry of the 1D representation, but the expectation values in the original lattice will differ. Instead of carrying out a separate MPS simulation, one could calculate these quantities by evaluating formula (10) with the same correlation functions  $\langle \hat{a}_m^\dagger \hat{a}_n \rangle$  and a different transformation matrix  $P' = PR$ , where  $R$  is a unitary matrix that describes the rotation of the pseudo spins.

In addition to the magnetization, we also calculated the charge-current densities which show a non-trivial behavior for finite  $\lambda$  because of the inverse spin Hall effect (not shown). Unfortunately, the obtained currents densities are rather small and their position dependence is strongly affected by both the chemical potential  $\mu$  and spin-orbit-coupling strength  $\lambda$ , which makes an interpretation difficult. For this reason, and because the observed inverse spin Hall effect is mostly a property of the non-interacting Rashba model while the spin chain only plays a secondary role, we have not pursued the analysis of the charge current further.

## 5 Summary

We have applied the block-Lanczos DMRG technique to investigate the spin transport in a two-terminal setup consisting of a spin chain and 2D tight-binding leads. As long as the spin chain couples only to a single site of each lead, the Lanczos transformation yields an effective 1D model where the leads are semi-infinite chains with nearest-neighbor hopping. While the hopping amplitudes are not uniform, their bond dependence is negligible except in the vicinity of the chain edge. The Lanczos transformation done here can be regarded as a specific case of the chain mappings for non-interacting baths based on orthogonal polynomials [27]. Since it is known that these mappings result for typical environments with finite bandwidth in asymptotically homogeneous chains [28], the effective Hamiltonian we obtained is not surprising and its explicit calculation mostly amounts to determining the strength of the inhomogeneities near the spin chain. These inhomogeneities can appreciably affect the spin transport in the junction because the parameters at the interface need to be fine-tuned to get a sizeable spin current at low temperatures. Qualitatively, however, the

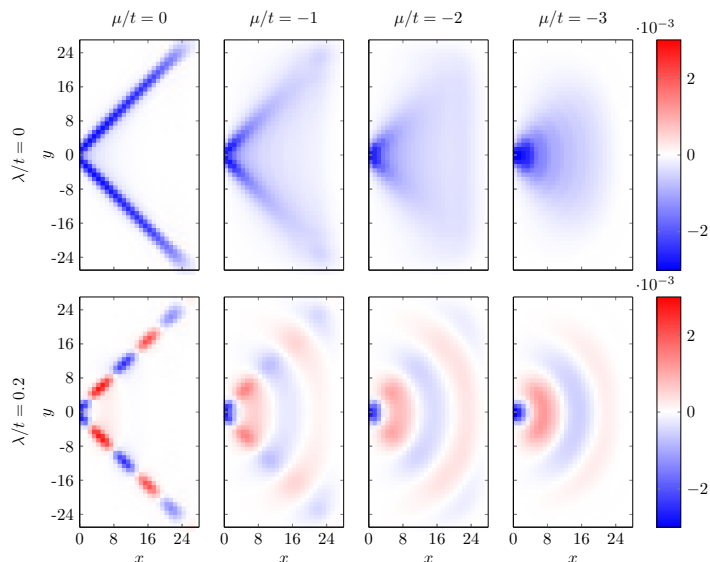


Figure 5: Magnetization in the second lead after injecting a spin current polarized in the  $z$  direction. Both leads have hopping amplitude  $t$  in their two-dimensional representation, and chemical potential  $\mu$ . In the second lead, there is also Rashba spin-orbit coupling of strength  $\lambda$ . The coupling to the spin chain  $J'$  is tuned to the approximate conducting fixed point which is  $J'/J = 1.45, 1.5, 1.7, 1.95$  for  $\mu/t = 0, -1, -2, -3$ , respectively. Other parameters are as in Fig. 4, i.e.,  $J/t = 0.5$  and  $N_S = 12$ . The measurements were carried at time  $\tau = 70 t^{-1}$  after a spin voltage  $V_S/t = 0.25$  was switched on in the first lead at  $\tau = 0$ .

behavior of the spin conductance is the same as when the hopping strength is assumed to be uniform. The Lanczos transformation thus does reveal any new phenomena in the setup studied here regarding the spin conductance. One could apply the method also to more complicated interfaces, e.g. multiple parallel spins. In that case, the lead part would become a ladder model after the transformation, with the number of legs equal to the number of spin chains. As realizations of spin chains in solids typically consist of many weakly coupled chains, the block-Lanczos method could be a way towards a more realistic junction model.

Interestingly, the form of the effective Hamiltonian does not change when Rashba spin-orbit coupling is taken into account. The spin-orbit coupling accordingly does not have a significant impact on the spin chain in the absence of perturbations in the leads. Phenomena characteristic of the Rashba model, like the spin Hall effect, are hidden in the definition of the Lanczos basis states. As a consequence, a spin current entering the lead appears more or less the same in the 1D representation regardless of the strength of the spin-orbit coupling  $\lambda$ . The inverse Hall effect and the Rashba precession in the original real-space lattice, on the other hand, occur only for finite  $\lambda$ . By reversing the Lanczos

transformation one can calculate quantities in real space and thereby observe these effects. However, since the tight-binding leads by themselves are non-interacting, such an approach only makes sense if the interacting region plays an important role. Otherwise, many-body techniques such as the DMRG are not necessary and more efficient tools, e.g., based on Green's functions, are available.

## Acknowledgments

DMRG simulations were performed using the ITensor library [29]. F. L. was supported by Deutsche Forschungsgemeinschaft through project FE 398/8-1 and by the International Program Associate (IPA) program in RIKEN.

## References

- [1] Y. Kajiwara, K. Harii, S. Takahashi, J. Ohe, K. Uchida, M. Mizuguchi, H. Umezawa, H. Kawai, K. Ando, K. Takanashi, S. Maekawa, and E. Saitoh, *Nature* **464**, 262 (2010).
- [2] K. Uchida, J. Xiao, H. Adachi, J. Ohe, S. Takahashi, J. Ieda, T. Ota, Y. Kajiwara, H. Umezawa, H. Kawai, G. E. W. Bauer, S. Maekawa, and E. Saitoh, *Nat. Mater.* **9**, 894 (2010).
- [3] S. Seki, T. Ideue, M. Kubota, Y. Kozuka, R. Takagi, M. Nakamura, Y. Kaneko, M. Kawasaki, and Y. Tokura, *Phys. Rev. Lett.* **115**, 266601 (2015).
- [4] D. Hirobe, M. Sato, T. Kawamata, Y. Shiomi, K. Uchida, R. Iguchi, Y. Koike, S. Maekawa, and E. Saitoh, *Nat. Phys.* **13**, 30 (2016).
- [5] C. A. Büsser, G. B. Martins, and A. E. Feiguin, *Phys. Rev. B* **88**, 245113 (2013).
- [6] T. Shirakawa and S. Yunoki, *Phys. Rev. B* **90**, 195109 (2014).
- [7] S. R. White, *Phys. Rev. Lett.* **69**, 2863 (1992).
- [8] U. Schollwöck, *Ann. Phys.* **326**, 96 (2011).
- [9] E. I. Rashba, *Fiz. Tverd. Tela* **2**, 1224 (1960), *Sov. Phys. Solid State* **2**, 1109 (1960).
- [10] J. Sinova, D. Culcer, Q. Niu, N. A. Sinitsyn, T. Jungwirth, and A. H. MacDonald, *Phys. Rev. Lett.* **92**, 126603 (2004).
- [11] J. Inoue, T. Kato, Y. Ishikawa, H. Itoh, G. E. W. Bauer, and L. W. Molenkamp, *Phys. Rev. Lett.* **97**, 046604 (2006).
- [12] E. I. Rashba, *Phys. Rev. B* **70**, 201309 (2004).
- [13] L. Sheng, D. N. Sheng, and C. S. Ting, *Phys. Rev. Lett.* **94**, 016602 (2005).
- [14] P. Schwab, R. Raimondi, and C. Gorini, *Europhys. Lett.* **90**, 67004 (2010).

- [15] E. M. Hankiewicz, L. W. Molenkamp, T. Jungwirth, and J. Sinova, *Phys. Rev. B* **70**, 241301 (2004).
- [16] J. Sinova, S. Murakami, S.-Q. Shen, and M.-S. Choi, *Solid State Commun.* **138**, 214 (2006).
- [17] J. Wunderlich, A. C. Irvine, J. Sinova, B. G. Park, L. P. Zârbo, X. L. Xu, B. Kaestner, V. Novák, and T. Jungwirth, *Nat. Phys.* **5**, 675 (2009), article.
- [18] Y. Saad, *Iterative Methods for Sparse Linear Systems*, 2nd ed. (Society for Industrial and Applied Mathematics, Philadelphia, PA, USA, 2003).
- [19] A. Ruhe, *Math. Comput.* **33**, 680 (1979).
- [20] A. Holzner, A. Weichselbaum, and J. von Delft, *Phys. Rev. B* **81**, 125126 (2010).
- [21] G. Vidal, *Phys. Rev. Lett.* **91**, 147902 (2003).
- [22] F. Lange, S. Ejima, T. Shirakawa, S. Yunoki, and H. Fehske, *Phys. Rev. B* **97**, 245124 (2018).
- [23] F. Lange, S. Ejima, and H. Fehske, *Europhys. Lett.* **125**, 17001 (2019).
- [24] N. Sedlmayr, J. Ohst, I. Affleck, J. Sirker, and S. Eggert, *Phys. Rev. B* **86**, 121302 (2012).
- [25] D. Morath, N. Sedlmayr, J. Sirker, and S. Eggert, *Phys. Rev. B* **94**, 115162 (2016).
- [26] P. W. Anderson, *J. Phys. C* **3**, 2436 (1970).
- [27] I. de Vega, U. Schollwöck, and F. A. Wolf, *Phys. Rev. B* **92**, 155126 (2015).
- [28] A. W. Chin, Á. Rivas, S. F. Huelga, and M. B. Plenio, *J. Math. Phys.* **51**, 092109 (2010), <https://doi.org/10.1063/1.3490188> .
- [29] <http://itensor.org/>.





# Bibliography

- [1] X. Chen, Z.-C. Gu, and X.-G. Wen, *Phys. Rev. B* **82**, 155138 (2010).
- [2] M. Oshikawa, in *Understanding quantum phase transitions*, Condensed Matter Physics (Taylor and Francis, Hoboken, NJ, 2010).
- [3] X.-G. Wen, *Adv. Phys.* **44**, 405 (1995).
- [4] H. Li and F. D. M. Haldane, *Phys. Rev. Lett.* **101**, 010504 (2008).
- [5] T. Senthil, *Annu. Rev. Condens. Matter Phys.* **6**, 299 (2015).
- [6] X. Chen, Z.-C. Gu, and X.-G. Wen, *Phys. Rev. B* **83**, 035107 (2011).
- [7] N. Schuch, D. Pérez-García, and I. Cirac, *Phys. Rev. B* **84**, 165139 (2011).
- [8] A. Klümper, A. Schadschneider, and J. Zittartz, *Europhys. Lett.* **24**, 293 (1993).
- [9] F. Pollmann, A. M. Turner, E. Berg, and M. Oshikawa, *Phys. Rev. B* **81**, 064439 (2010).
- [10] X. Chen, Z.-C. Gu, and X.-G. Wen, *Phys. Rev. B* **84**, 235128 (2011).
- [11] L. Fidkowski and A. Kitaev, *Phys. Rev. B* **83**, 075103 (2011).
- [12] S. R. White, *Phys. Rev. Lett.* **69**, 2863 (1992).
- [13] U. Schollwöck, *Ann. Phys.* **326**, 96 (2011).
- [14] M. B. Hastings, *J. Stat. Mech.* **2007**, P08024 (2007).
- [15] E. Jeckelmann, *Phys. Rev. B* **66**, 045114 (2002).
- [16] G. Vidal, *Phys. Rev. Lett.* **91**, 147902 (2003).
- [17] S. R. White and A. E. Feiguin, *Phys. Rev. Lett.* **93**, 076401 (2004).
- [18] A. Holzner, A. Weichselbaum, I. P. McCulloch, U. Schollwöck, and J. von Delft, *Phys. Rev. B* **83**, 195115 (2011).
- [19] F. Verstraete, J. J. García-Ripoll, and J. I. Cirac, *Phys. Rev. Lett.* **93**, 207204 (2004).
- [20] E. M. Stoudenmire and S. R. White, *New J. Phys.* **12**, 055026 (2010).
- [21] F. D. M. Haldane, *Phys. Rev. Lett.* **50**, 1153 (1983).
- [22] M. den Nijs and K. Rommelse, *Phys. Rev. B* **40**, 4709 (1989).

- [23] T. Kennedy, *J. Phys.: Condens. Matter* **2**, 5737 (1990).
- [24] F. Pollmann, E. Berg, A. M. Turner, and M. Oshikawa, *Phys. Rev. B* **85**, 075125 (2012).
- [25] W. J. L. Buyers, R. M. Morra, R. L. Armstrong, M. J. Hogan, P. Gerlach, and K. Hirakawa, *Phys. Rev. Lett.* **56**, 371 (1986).
- [26] J.-P. Renard, L.-P. Regnault, and M. Verdaguer, in *Magnetism: Molecules to Materials* (John Wiley & Sons, Ltd, 2003).
- [27] M. Greiner, O. Mandel, T. Esslinger, T. W. Hänsch, and I. Bloch, *Nature* **415**, 39 (2002).
- [28] I. Bloch, J. Dalibard, and W. Zwerger, *Rev. Mod. Phys.* **80**, 885 (2008).
- [29] M. Endres, M. Cheneau, T. Fukuhara, C. Weitenberg, P. Schauß, C. Gross, L. Mazza, M. C. Bañuls, L. Pollet, I. Bloch, and S. Kuhr, *Science* **334**, 200 (2011).
- [30] T. A. Hilker, G. Salomon, F. Grusdt, A. Omran, M. Boll, E. Demler, I. Bloch, and C. Gross, *Science* **357**, 484 (2017).
- [31] D.-W. Zhang, Y.-Q. Zhu, Y. X. Zhao, H. Yan, and S.-L. Zhu, *Adv. Phys.* **67**, 253 (2018).
- [32] O. Dutta, M. Gajda, P. Hauke, M. Lewenstein, D.-S. Lühmann, B. A. Malomed, T. Sowiński, and J. Zakrzewski, *Rep. Prog. Phys.* **78**, 066001 (2015).
- [33] E. G. Dalla Torre, E. Berg, and E. Altman, *Phys. Rev. Lett.* **97**, 260401 (2006).
- [34] E. Berg, E. G. Dalla Torre, T. Giamarchi, and E. Altman, *Phys. Rev. B* **77**, 245119 (2008).
- [35] M. Tsuchiizu and A. Furusaki, *Phys. Rev. B* **69**, 035103 (2004).
- [36] S. Moudgalya and F. Pollmann, *Phys. Rev. B* **91**, 155128 (2015).
- [37] R. Verresen, R. Moessner, and F. Pollmann, *Phys. Rev. B* **96**, 165124 (2017).
- [38] T. Keilmann, S. Lanzmich, I. McCulloch, and M. Roncaglia, *Nat. Commun.* **2**, 361 (2011).
- [39] J. Becker, T. Köhler, A. C. Tiegel, S. R. Manmana, S. Wessel, and A. Honecker, *Phys. Rev. B* **96**, 060403 (2017).
- [40] Y. Zhu, *Modern Techniques for Characterizing Magnetic Materials* (Springer US, Boston, MA, 2005).
- [41] A. M. Rey, P. B. Blakie, G. Pupillo, C. J. Williams, and C. W. Clark, *Phys. Rev. A* **72**, 023407 (2005).
- [42] T. A. Corcovilos, S. K. Baur, J. M. Hitchcock, E. J. Mueller, and R. G. Hulet, *Phys. Rev. A* **81**, 013415 (2010).

- 
- [43] Y. Kajiwara, K. Harii, S. Takahashi, J. Ohe, K. Uchida, M. Mizuguchi, H. Umezawa, H. Kawai, K. Ando, K. Takanashi, S. Maekawa, and E. Saitoh, *Nature* **464**, 262 (2010).
- [44] D. Hirobe, M. Sato, T. Kawamata, Y. Shiomi, K. Uchida, R. Iguchi, Y. Koike, S. Maekawa, and E. Saitoh, *Nat. Phys.* **13**, 30 (2016).
- [45] I. P. McCulloch, arXiv:0804.2509.
- [46] J. Eisert, M. Cramer, and M. B. Plenio, *Rev. Mod. Phys.* **82**, 277 (2010).
- [47] P. Calabrese and J. Cardy, *J. Stat. Mech.* **2004**, P06002 (2004).
- [48] F. Verstraete and J. I. Cirac, *Phys. Rev. B* **73**, 094423 (2006).
- [49] G. Vidal, *Phys. Rev. Lett.* **98**, 070201 (2007).
- [50] M. Fannes, B. Nachtergaele, and R. F. Werner, *Comm. Math. Phys.* **144**, 443 (1992).
- [51] F. Pollmann, S. Mukerjee, A. M. Turner, and J. E. Moore, *Phys. Rev. Lett.* **102**, 255701 (2009).
- [52] P. Calabrese and J. Cardy, *J. Stat. Mech.* **2005**, P04010 (2005).
- [53] A. Perales and G. Vidal, *Phys. Rev. A* **78**, 042337 (2008).
- [54] P. Calabrese and J. Cardy, *J. Phys. A* **42**, 504005 (2009).
- [55] B. Bruognolo, A. Weichselbaum, J. von Delft, and M. Garst, *Phys. Rev. B* **94**, 085136 (2016).
- [56] M. P. Zaletel, R. S. K. Mong, C. Karrasch, J. E. Moore, and F. Pollmann, *Phys. Rev. B* **91**, 165112 (2015).
- [57] J. Haegeman, C. Lubich, I. Oseledets, B. Vandereycken, and F. Verstraete, *Phys. Rev. B* **94**, 165116 (2016).
- [58] N. Hatano and M. Suzuki, in *Quantum Annealing and Other Optimization Methods* (Springer Berlin Heidelberg, Berlin, Heidelberg, 2005).
- [59] M. Kliesch, D. Gross, and J. Eisert, *Phys. Rev. Lett.* **113**, 160503 (2014).
- [60] T. Barthel, arXiv:1708.09349.
- [61] S. Sachdev, *Quantum Phase Transitions* (Cambridge Univ. Press, Cambridge, 1999).
- [62] D. Pérez-García, M. M. Wolf, M. Sanz, F. Verstraete, and J. I. Cirac, *Phys. Rev. Lett.* **100**, 167202 (2008).
- [63] F. Pollmann and A. M. Turner, *Phys. Rev. B* **86**, 125441 (2012).
- [64] H. J. Schulz, *Phys. Rev. B* **34**, 6372 (1986).

- [65] W. Chen, K. Hida, and B. C. Sanctuary, *Phys. Rev. B* **67**, 104401 (2003).
- [66] A. M. Tsvelik, *Phys. Rev. B* **42**, 10499 (1990).
- [67] R. Vicente, A. Escuer, J. Ribas, and X. Solans, *Inorg. Chem.* **31**, 1726 (1992).
- [68] M. Atala, M. Aidelsburger, J. T. Barreiro, D. Abanin, T. Kitagawa, E. Demler, and I. Bloch, *Nat. Phys.* **9**, 795 (2013), article.
- [69] A. Kitazawa, K. Nomura, and K. Okamoto, *Phys. Rev. Lett.* **76**, 4038 (1996).
- [70] P. Di Francesco, P. Mathieu, and D. Sénéchal, *Conformal field theory* (Springer, New York, NY, 1997).
- [71] S. Nishimoto, *Phys. Rev. B* **84**, 195108 (2011).
- [72] N. Laflorencie, E. S. Sørensen, M.-S. Chang, and I. Affleck, *Phys. Rev. Lett.* **96**, 100603 (2006).
- [73] H. Benthien, F. H. L. Essler, and A. Grage, *Phys. Rev. B* **73**, 085105 (2006).
- [74] M. Nakamura, *J. Phys. Soc. Jpn.* **68**, 3123 (1999).
- [75] J. M. Leinaas and J. Myrheim, *Il Nuovo Cimento B (1971-1996)* **37**, 1 (1977).
- [76] A. Kundu, *Phys. Rev. Lett.* **83**, 1275 (1999).
- [77] S. Greschner and L. Santos, *Phys. Rev. Lett.* **115**, 053002 (2015).
- [78] C. Sträter, S. C. L. Srivastava, and A. Eckardt, *Phys. Rev. Lett.* **117**, 205303 (2016).
- [79] X. Chen, Z.-C. Gu, Z.-X. Liu, and X.-G. Wen, *Phys. Rev. B* **87**, 155114 (2013).
- [80] A. K. Bera, B. Lake, F. H. L. Essler, L. Vanderstraeten, C. Hubig, U. Schollwöck, A. T. M. N. Islam, A. Schneidewind, and D. L. Quintero-Castro, *Phys. Rev. B* **96**, 054423 (2017).
- [81] T. Barthel, U. Schollwöck, and S. R. White, *Phys. Rev. B* **79**, 245101 (2009).
- [82] H. N. Phien, G. Vidal, and I. P. McCulloch, *Phys. Rev. B* **86**, 245107 (2012).
- [83] D. Kennes and C. Karrasch, *Comput. Phys. Commun.* **200**, 37 (2016).
- [84] T. Barthel, *New J. Phys.* **15**, 073010 (2013).
- [85] A. Milsted, J. Haegeman, T. J. Osborne, and F. Verstraete, *Phys. Rev. B* **88**, 155116 (2013).
- [86] V. Zauner, M. Ganahl, H. G. Evertz, and T. Nishino, *J. Phys.: Condens. Matter* **27**, 425602 (2015).
- [87] S. R. White and I. Affleck, *Phys. Rev. B* **77**, 134437 (2008).
- [88] X. Zotos, *J. Phys. Soc. Jpn.* **74**, 173 (2005).

- 
- [89] H.-J. Mikeska and A. K. Kolezhuk, in *Quantum Magnetism* (Springer Berlin Heidelberg, Berlin, Heidelberg, 2004).
- [90] B. S. Shastry and B. Sutherland, Phys. Rev. Lett. **65**, 243 (1990).
- [91] X. Zotos, Phys. Rev. Lett. **82**, 1764 (1999).
- [92] F. Heidrich-Meisner, A. Honecker, D. C. Cabra, and W. Brenig, Phys. Rev. B **68**, 134436 (2003).
- [93] M. Žnidarič, Phys. Rev. Lett. **106**, 220601 (2011).
- [94] C. Karrasch, J. Hauschild, S. Langer, and F. Heidrich-Meisner, Phys. Rev. B **87**, 245128 (2013).
- [95] T. Prosen, Phys. Rev. Lett. **106**, 217206 (2011).
- [96] E. Ilievski and J. De Nardis, Phys. Rev. Lett. **119**, 020602 (2017).
- [97] A. Branschädel, G. Schneider, and P. Schmitteckert, Ann. Phys. **522**, 657 (2010).
- [98] M. Einhellinger, A. Cojuhovski, and E. Jeckelmann, Phys. Rev. B **85**, 235141 (2012).
- [99] C. L. Kane and M. P. A. Fisher, Phys. Rev. Lett. **68**, 1220 (1992).
- [100] C. L. Kane and M. P. A. Fisher, Phys. Rev. B **46**, 15233 (1992).
- [101] N. Sedlmayr, J. Ohst, I. Affleck, J. Sirker, and S. Eggert, Phys. Rev. B **86**, 121302 (2012).
- [102] D. Morath, N. Sedlmayr, J. Sirker, and S. Eggert, Phys. Rev. B **94**, 115162 (2016).
- [103] D. L. Maslov and M. Stone, Phys. Rev. B **52**, R5539 (1995).
- [104] I. Safi and H. J. Schulz, Phys. Rev. B **52**, R17040 (1995).
- [105] T. Giamarchi, *Quantum physics in one dimension*, Internat. Ser. Mono. Phys. (Clarendon Press, Oxford, 2004).
- [106] D. Bohr, P. Schmitteckert, and P. Wölfle, Europhys. Lett. **73**, 246 (2006).
- [107] J.-M. Bischoff and E. Jeckelmann, Phys. Rev. B **96**, 195111 (2017).
- [108] H. Van Houten, C. W. J. Beenakker, and A. A. M. Staring, in *Single Charge Tunneling: Coulomb Blockade Phenomena In Nanostructures* (Springer US, Boston, MA, 1992).









# Scientific contributions

## Publications

- (a) “*Exotic criticality in the dimerized spin-1 XXZ chain with single-ion anisotropy*”, S. Ejima, T. Yamaguchi, F. H. L. Essler, F. Lange, Y. Ohta and H. Fehske, *SciPost Phys.* **5**, 059 (2018).
- (b) “*Quantum phase transitions in the dimerized extended Bose-Hubbard model*”, K. Sugimoto, S. Ejima, F. Lange and H. Fehske, *Phys. Rev. A* **99**, 012122 (2019). Copyright (2019) by the American Physical Society.
- (c) “*Ising tricriticality in the extended Hubbard model with bond dimerization*”, S. Ejima, F. H. L. Essler, F. Lange, and H. Fehske, *Phys. Rev. B* **93**, 235118 (2016). Copyright (2016) by the American Physical Society.
- (d) “*Critical behavior of the extended Hubbard model with bond dimerization*”, S. Ejima, F. Lange, F. H. L. Essler, H. Fehske, *Physica B* **536**, 474 (2018). Copyright (2017) by Elsevier.
- (e) “*Anyonic Haldane Insulator in One Dimension*”, F. Lange, S. Ejima, and H. Fehske, *Phys. Rev. Lett.* **118**, 120401 (2017). Copyright (2017) by the American Physical Society.
- (f) “*Strongly repulsive anyons in one dimension*”, F. Lange, S. Ejima, and H. Fehske, *Phys. Rev. A* **95**, 063621 (2017). Copyright (2017) by the American Physical Society.
- (g) “*Finite-temperature dynamic structure factor of the spin-1 XXZ chain with single-ion anisotropy*”, F. Lange, S. Ejima, and H. Fehske, *Phys. Rev. B* **97**, 060403(R) (2018). Copyright (2018) by the American Physical Society.
- (h) “*Dynamic response of spin-2 bosons in one-dimensional optical lattices*”, F. Lange, S. Ejima, and H. Fehske, submitted to *Phys. Rev. A*
- (i) “*Spin transport through a spin-1/2 XXZ chain contacted to fermionic leads*”, F. Lange, S. Ejima, and H. Fehske, *Phys. Rev. B* **97**, 245124 (2018). Copyright (2018) by the American Physical Society.
- (j) “*Driving XXZ spin chains: Magnetic-field and boundary effects*”, F. Lange, S. Ejima, and H. Fehske, *Europhys. Lett.* **125**, 17001 (2019). Copyright (2019) by the Europhysics Letters Association.
- (k) “*Block-Lanczos density-matrix renormalization-group study of the spin transport in Heisenberg chains coupled to leads*”, F. Lange, S. Ejima, and H. Fehske, to be submitted

## Posters

- (a) “*Strongly repulsive anyons in one dimension*”, Korrelationstage, Dresden, 2015
- (b) “*Spin transport through a contacted Heisenberg chain*”, Joint meeting of the DPG and EPS Condensed Matter Divisions, Berlin, 2018
- (c) “*Ising tricriticality in the extended Hubbard model with bond dimerization*”, Joint meeting of the DPG and EPS Condensed Matter Divisions, Berlin, 2018





# Erklärung

Hiermit erkläre ich, dass diese Arbeit bisher von mir weder an der Mathematisch-Naturwissenschaftlichen Fakultät der Universität Greifswald noch einer anderen wissenschaftlichen Einrichtung zum Zwecke der Promotion eingereicht wurde.

Ferner erkläre ich, dass ich diese Arbeit selbständig verfasst und keine anderen als die darin angegebenen Hilfsmittel und Hilfen benutzt und keine Textabschnitte eines Dritten ohne Kennzeichnung übernommen habe.

---

(Florian Lange)

Greifswald, 1. August 2019



# Acknowledgement

First, I would like to express my sincere thanks to Prof. Holger Fehske for being a thoughtful and encouraging supervisor. In addition, I am grateful for his guidance regarding my future career. I also thank the members of the Computational Condensed Matter Physics Laboratory at RIKEN for the hospitality during my stay. Finally, I thank the members of the work group in Greifswald, especially Dr. Satoshi Ejima for the pleasant and fruitful collaboration over the last years.